8. SITE 792[1]

Shipboard Scientific Party[2]

HOLE 792A

Date occupied: 16 May 1989

Date departed: 17 May 1989

Time on hole: 15 hr, 49 min

Position: 30°23.97'N, 140°22.81'E

Bottom felt (rig floor; m, drill pipe measurement): 1797.8

Distance between rig floor and sea level (m): 10.50

Water depth (drill pipe measurement from sea level, m): 1787.3

Total depth (rig floor, m): 1892.8

Penetration (m): 95.00

Number of cores (including cores with no recovery): 10

Total length of cored section (m): 95.00

Total core recovered (m): 72.09

Core recovery (%): 75.9

Oldest sediment cored:
Depth (mbsf): 95.00
Nature: vitric sand and foraminifer-nannofossil vitric silty clay
Age: Pleistocene
Measured velocity (km/s): 1.59

HOLE 792B

Date occupied: 17 May 1989

Date departed: 17 May 1989

Time on hole: 14 hr, 45 min

Position: 32°23.96'N, 140°22.81'E

Bottom felt (rig floor; m, drill pipe measurement): 1798.2

Distance between rig floor and sea level (m): 10.50

Water depth (drill pipe measurement from sea level, m): 1787.7

Total depth (rig floor, m): 1944.6

Penetration (m): 146.4

Number of cores (including cores with no recovery): 11

Total length of cored section (m): 100.70

Total core recovered (m): 43.59

Core recovery (%): 43.3

Oldest sediment cored:
Depth (mbsf): 146.40
Nature: biogenic, silica-rich, lithic-vitric silty clay and nannofossil-
rich vitric silty clay
Age: late Pliocene
Measured velocity (km/s): 1.59

HOLE 792C

Date occupied: 17 May 1989

Date departed: 18 May 1989

Time on hole: 9 hr, 35 min

Position: 32°23.94'N, 140°22.78'E

Bottom felt (rig floor; m, drill pipe measurement): 1798.2

Distance between rig floor and sea level (m): 10.50

Water depth (drill pipe measurement from sea level, m): 1787.7

Total depth (rig floor, m): 1944.6

Penetration (m): 146.4

Number of cores (including cores with no recovery): 1

Total length of cored section (m): 9.60

Total core recovered (m): 0.59

Core recovery (%): 6.1

Oldest sediment cored:
Depth (mbsf): 146.40
Nature: nannofossil-rich vitric silty clay
Age: late Pliocene

HOLE 792D

Date occupied: 18 May 1989

Date departed: 18 May 1989

Time on hole: 6 hr, 50 min

Position: 32°23.93'N, 140°22.80'E

Bottom felt (rig floor; m, drill pipe measurement): 1798.2

Distance between rig floor and sea level (m): 10.50

Water depth (drill pipe measurement from sea level, m): 1787.7

Total depth (rig floor, m): 1944.6

Penetration (m): 146.4

Number of cores (including cores with no recovery): 1

Total length of cored section (m): 9.60

Total core recovered (m): 0.84

Core recovery (%): 8.8

Oldest sediment cored:
Depth (mbsf): 146.4
Nature: nannofossil-rich vitric silty clay
Age: late Pliocene

HOLE 792E

Date occupied: 19 May 1989

Date departed: 26 May 1989

Time on hole: 7 days, 6 hr, 5 min

Position: 32°23.96'N, 140°22.79'E

Bottom felt (rig floor; m, drill pipe measurement): 1798.2

Distance between rig floor and sea level (m): 10.50

Water depth (drill pipe measurement from sea level, m): 1787.7

Total depth (rig floor, m): 2684.1

Penetration (m): 885.9

Number of cores (including cores with no recovery): 78

Total length of cored section (m): 750.30

Total core recovered (m): 361.89

Core recovery (%): 48.2

Oldest sediment cored:
Depth (mbsf): 800.20
Nature: hydrothermally altered volcanic pebble-granule conglomerate and other volcaniclastic rocks of uncertain grain size
Age: late Oligocene
Measured velocity (km/s): 2.01

Basement:
Depth (mbsf): 804.00
Nature: porphyritic andesite
Measured velocity (km/s): 4.59

Principal results: Site 792 is located on the western half of the Izu-Bonin forearc sedimentary basin, about 60 km east of the arc volcano Aoga Shima and 170 km west of the axis of the Izu-Bonin Trench. It is upslope of a fork in the Aoga Shima Canyon where the forearc sediments lap onto the edge of a basement high. The principal objectives of this site were to determine (1) the stratigraphy of the forearc basin, and hence the temporal variations in sedimentation, depositional environment, and paleoceanography, and the history of the intensity and chemistry of the arc volcanism; (2) the uplift and subsidence history across the forearc; (3) the nature of the igneous basement and the formation of the 200-km-wide forearc crust; and (4) the microstructural deformation and large-scale rotation and translation of the forearc terrane since the Eocene. We selected the site on the basis of multichannel seismic records and a short shipboard seismic survey; the location chosen lies on *Fred Moore* 3505, Line 10, at 0134Z. Site 792 was occupied from 1636 hr (UTC) on 16 May, to 2140 hr on 25 May 1989.

Hole 792A was spudded for advanced piston corer (APC) operations at 2130Z on 17 May 1989. We cored 95 m at a recovery rate of 76% before an overpull resulted in a severed piston rod, thus ending operations at the hole. Hole 792B re-cored the mud line, washed to 50 m below sea level (mbsf), and continued with the APC to 69.2 mbsf; at this point we switched to the extended core barrel (XCB) and cored to 146.4 mbsf, with overall recovery of 43%. Holes 792B-D all ended operations in the interval from 137 to 146 mbsf, owing to separation of the XCB cutting shoe in each case. We spudded Hole 792E with a rotary core barrel (RCB) at 0207Z on 19 May, washed to 135.6 mbsf, and then cored to 885.9 mbsf; recovery was 52% in the sediments above 804 mbsf, and 16% in the underlying basement. As we pulled the pipe from the hole to prepare for logging it became stuck, the bit resting at 286 mbsf. After attempts to save the bottom-hole assembly (BHA) proved fruitless, we ran a full suite of standard geophysical and geochemical logs above 878 mbsf. The first use of formation microscanner (FMS) logging in the Ocean Drilling Program (ODP) was successfully completed, and a vertical seismic profile (VSP) was also collected. Finally, we severed the pipe with explosives at 134 mbsf.

We defined six lithostratigraphic units at Site 792:

1. Unit I (0–183.7 mbsf): upper Pliocene to Holocene nannofossil-rich, vitric silty clay and clayey silt, interbedded with vitric silts and sands and minor pumiceous and scoriaceous gravels.
2. Unit II (183.7–357.4 mbsf): middle and upper Miocene sandy mudstone, muddy sandstone, and silty claystone (all with nannofossil-rich intervals), and vitric sand- and siltstone.
3. Unit III (357.4–429.3 mbsf): lower Miocene to upper Oligocene intensely bioturbated, nannofossil-rich claystone and nannofossil chalk, and rare crystal-vitric silt- and sandstone.
4. Unit IV (429.3–783.4 mbsf): upper Oligocene vitric sandstone and sandy conglomerate with claystone intraclasts, with minor silty claystone and claystone that contain nannofossil-rich intervals.

5. Unit V (783.4–804 mbsf): altered volcanic sandstone with claystone intraclasts.
6. Unit VI (804–885.9 mbsf): porphyritic andesite with minor basaltic andesite and dacite.

Units I–IV were dated by means of nannofossils, foraminifers, and paleomagnetics, with the addition of radiolarians for Units I–II. Four lacunae occur, at 1–2.2, 3.5–6, 8–9, and 13–19 Ma. The second and fourth lacunae correspond to the basal boundaries of the first two units. Average sedimentation rates in the intervals between these lacunae are (in order of increasing age) 90 and 122 m/m.y. (Unit I), and 43 and 23 m./m.y. (Unit II), respectively. Sedimentation rates for Unit III are 14 and 4 m/m.y., respectively, for intervals above and below a normal fault that cuts out strata from 23 to 24 Ma. Sedimentation rates for Unit IV (27–29 Ma) were about 300 m/m.y. and greater prior to 28 Ma, but slowed to 40 m/m.y. thereafter. Benthic foraminifers indicate that depositional water depths shallowed from 3.5–4.5 km in the late Oligocene to <2.3 km since the middle Pleistocene, which is evidence for 1–2 km of basement uplift since 29 Ma.

The >200 ash layers in Unit I are evidence of ongoing explosive volcanism since the late Pliocene. Unit II records hemipelagic and turbidite deposition of biogenic and volcanic components, mixed by burrowers. Unit III marks a period of slow bathyal deposition without significant volcanic input. Unit IV consists of thick- to thin-bedded turbidites and debris-flow deposits, and fine-grained hemipelagic sediments. The volcanogenic detritus includes the products of concurrent volcanism and erosion of older volcanic terranes. Bedding is subhorizontal, with maximum dips <5°–10°. Extensional microfaults, conjugate high-angle fractures, slickensided horizontal shears, clastic injections, and dewatering veinlets in Units III and IV are all evidence of postdepositional extensional deformation. Zeolites and gypsum fill many of the veins and fractures. Correlation to multichannel seismic data suggests that we drilled through a major unconformity somewhere between 690 and 730 mbsf at this site. Although there is no lithologic change in this interval, physical property and logging data suggest a significant boundary at 715 mbsf. The age of Unit IV strata from 715 to 770 mbsf is constrained by biostratigraphic results to <34 Ma. This implies that the >1-km-thick forearc basin section, which laps onto the unconformity below the level reached at Site 792, was deposited in the middle Oligocene (29–34 Ma). The age of the (hydrothermally) altered Unit V and of the igneous basement is middle Oligocene or older. Radiometric dating of the igneous rocks will be attempted during shore-based investigations.

The basement lavas are massive flows with intercalated hyaloclastite and breccia layers. They are dominantly porphyritic, plagioclase-orthopyroxene-clinopyroxene andesites, with high aluminum, early oxide-mineral precipitation and concomitant iron depletion. They are less enriched in low-field-strength elements such as K, Rb, Sr, and Ba than are most arc lavas. Ratios between the high-field-strength elements (e.g., $Zr/Y = ~1.9$) are consistent with a depleted mantle source. The presence of quartz xenocrysts, along with other geochemical evidence, may indicate that magmas from two distinct sources were mixed during a high-level fractionation process to produce the andesites.

The most extensively altered pore water of seawater origin ever sampled by the Deep Sea Drilling Project (DSDP) or ODP (except for Site 793) is located from 500 to 700 mbsf, with characteristic concentrations of sulfate = 15, magnesium = 0–4, calcium = 155, and silica = 0.1–0.4 (all in mM). The maximum calcium concentration (170 mM) at 600 mbsf is the highest ever recorded, except at Site 793 and in evaporite settings. This unique geochemistry is not a basement alteration effect but is the result of low-temperature alteration of the volcanogenic sediments. It is reflected in the marked downward increase (below 350 mbsf) in smectite and zeolite at the expense of the volcanic glass in Units III and IV. This alteration releases Ca and consumes Mg, Si, and Na. Below 500 mbsf, the pore waters are saturated with respect to gypsum, which by precipitation lowers the sulfate concentration. The concentration of organic carbon decreases exponentially from a near-surface high of 0.76% to <0.15% in Unit II and below.

Magnetic inclinations on cores younger than 15 Ma show no latitudinal shift, but some northward motion is required for cores older

than 25 Ma. The inclination and declination records of the Brunhes-Matuyama reversal show a double transition during a period of decreased field intensity lasting about 3000 yr. This polarity transition period is about five times longer than at Site 791, but this may be an averaging affect caused by the threefold decrease in sedimentation rate (120 m/m.y.).

Physical property measurements indicate that (1) average bulk density values increase downward from 1.7 to 1.9 g/cm^3 in Unit I, then decrease from 2.1–1.9 g/cm^3 in Unit II to 1.85 g/cm^3 in Unit III; (2) average porosity values decrease from 65% at the top of Unit I to 55% at its base, then increase through Unit II to 65% at the base of Unit III; (3) sonic velocity data average 1.59, 1.85, and 1.87 km/s in Units I–III respectively; and (4) carbonate values range from 1%–36% at the top to 3%–21% at the base of Unit I, from 0%–4% at the top to 3%–22% at the base of Unit II, and are commonly 20%–67% in Unit III. The physical property measurements of Unit IV vary downward in concert with the lithologic changes. We defined four subunits of Unit IV, which broadly correspond to alternating finer (first and third) and coarser (second and fourth) material, subdivided at 514, 590, and 715 mbsf. In order of increasing depth, the average values in the four subunits (and Units V and VI) are (1) bulk density: 1.87, 2.16, 2.09, 2.28, 2.02, and 2.64 g/cm^3; (2) porosity: 58%, 44%, 50%, 42%, 50%, and 17%; and (3) sonic velocity: 2.3, 2.7, 2.2, 2.6, 2.2, and 4.3 km/s. Carbonate contents are 1%–10% (and rarely as high as 25%) in the upper subunit, and are typically <1%–2% below, except for thin nannofossil-rich layers with values of 10%–20%. Thermal conductivities increase downward, averaging 1.01, 1.02, 1.05, and 1.61 W/m · K in Units I–III and VI. Three excellent Uyeda-probe temperature measurements down to 110 mbsf, together with the bottom-water temperature, define a linear geothermal gradient of 55°C/km. The heat flow is 56 mW/m^2.

Although the downhole measurement logs are excellent, they mostly require shore-based analysis before final interpretation. The *in-situ* geophysical measurements show physical properties similar to the laboratory measurements. All of the lithostratigraphic and physical property unit boundaries can be recognized in the logs. The FMS clearly imaged features such as ash layers <1 cm thick. The temperature and caliper records identify permeable zones at 400–430 mbsf and at the top and bottom of Unit V, which are most likely fault zones. The borehole is slightly elongated in a direction 020° throughout the sedimentary section, but is circular in basement.

The principal results of this site are:

1. the characterization of varying rates of volcanogenic input to the forearc (extremely rapid prior to 27 Ma, minimal between 27 and 13 Ma, and from moderate to increasingly fast between 13 Ma and the present);
2. the documentation of ongoing explosive volcanism since the late Pliocene;
3. the correlation between coring results and seismic stratigraphy by means of VSP and logging, indicating sedimentary filling of the basin between the frontal arc and outer-arc highs in the middle Oligocene;
4. the first recovery of igneous basement beneath such an intraoceanic forearc basin and initial description of its unusual trace-element chemistry, characterized by weak enrichment in low-field-strength elements and depletion in high-field-strength elements (the latter indicates derivation from a refractory mantle source);
5. benthic foraminiferal evidence of 1–2 km of basement uplift since 29 Ma;
6. microstructural evidence of extensional deformation;
7. pore-water indications of low-temperature alteration of the volcanogenic sediments, producing fluids extremely enriched in calcium and depleted in magnesium, silica, and sulfate;
8. paleomagnetic evidence that the Brunhes-Matuyama reversal involved a double polarity transition during a period of decreased field intensity lasting 3000 yr or less; and
9. measurement of heat flow at 56 mW/m^2.

BACKGROUND AND OBJECTIVES

Site 792 (proposed Site BON-4) is located at 32°23.96'N, 140°22.80'E, and 1787 m below sea level (mbsl) in the western half of the Izu-Bonin forearc sedimentary basin, about 60 km east of the arc volcano Aoga Shima ("Blue Island") and 170 km west of the axis of the Izu-Bonin Trench (Fig. 1). It is located between two forks of Aoga Shima Canyon (Fig. 2). Beneath the site, the normally >3-km-thick section of forearc-basin turbidites laps onto the edge of a basement high (Fig. 3).

By drilling at this site we sought to determine the following:

1. The stratigraphy of the forearc, and hence the temporal variations in sedimentation, depositional environment, and paleoceanography, and the history of the intensity and chemistry of arc volcanism.
2. The uplift/subsidence history across the forearc to provide information on forearc flexure and basin development.
3. The nature of the forearc igneous basement, to resolve problems concerning the nature of volcanism in the initial stages of subduction and the formation of the 200-km-wide forearc crust, including the possibility of later forearc volcanism.
4. The microstructural deformation and the large-scale rotation and translation of the forearc terrane since the Eocene.

The first of these objectives was addressed partly through detailed studies of sediments retrieved at Site 792. The type of sedimentation and style of deposition in the forearc basin was expected to change with time as the proximity to arc volcanoes changed, as the volume and eruptive style of arc products varied, as the basin filled, and as the development of submarine canyons eroded and redistributed sedimentary material. Geostrophic currents, such as the paleo-Kuroshio, and changes in global sea level may also affect the pattern of sedimentation, and their effects may be deciphered from the stratigraphic record.

These sediments also contain a temporal record of the variations in the intensity and composition of arc volcanism. Studies of the chronology and nature of tephras at this site tested various conflicting models concerning the complex relationships between tectonic and volcanic phenomena in island arcs (e.g., changes in subduction rate, periodicity in backarc rifting and spreading, pulses of arc volcanism, and variations in arc geochemistry; see "Introduction" chapter, this volume, for elaboration).

The second objective was investigated through a combination of paleontological estimates of paleobathymetry, backstripping of the sedimentation history using the physical property and logging data, and seismic stratigraphic analyses of interconnecting multichannel seismic (MCS) profiles. Determining the forearc vertical-displacement history should provide some of the information necessary to decide if (1) fairly stable conditions have prevailed since the mid-Tertiary, as suggested by the well-developed submarine canyon system and lower-slope terrace of serpentinite seamounts; (2) the frontal-arc and outer-arc high resulted from igneous construction or from differential uplift; (3) the intervening forearc basin was formed by spreading or by differential subsidence; and (4) flexural loading of the forearc (by arc volcanoes or by coupling with the subducting plate) is an important process.

The third objective was investigated through studies of the basement rocks retrieved at this site. Basement beneath the thickly sedimented upper-slope basin (between the frontal-arc and outer-arc highs) had never been sampled in this or any other intraoceanic arc-trench system. From the available data, it appears that the present 150–230-km-wide Bonin-Mariana forearc formed, in large part, by volcanism during the initial stages of arc development in the Eocene and early Oligocene (see "Introduction" chapter, this volume, for elaboration). Similar volcanism has not occurred since and cannot be studied as an active phenomenon anywhere on earth at present. Studies of the basement rocks permitted evaluation of the three main alternative
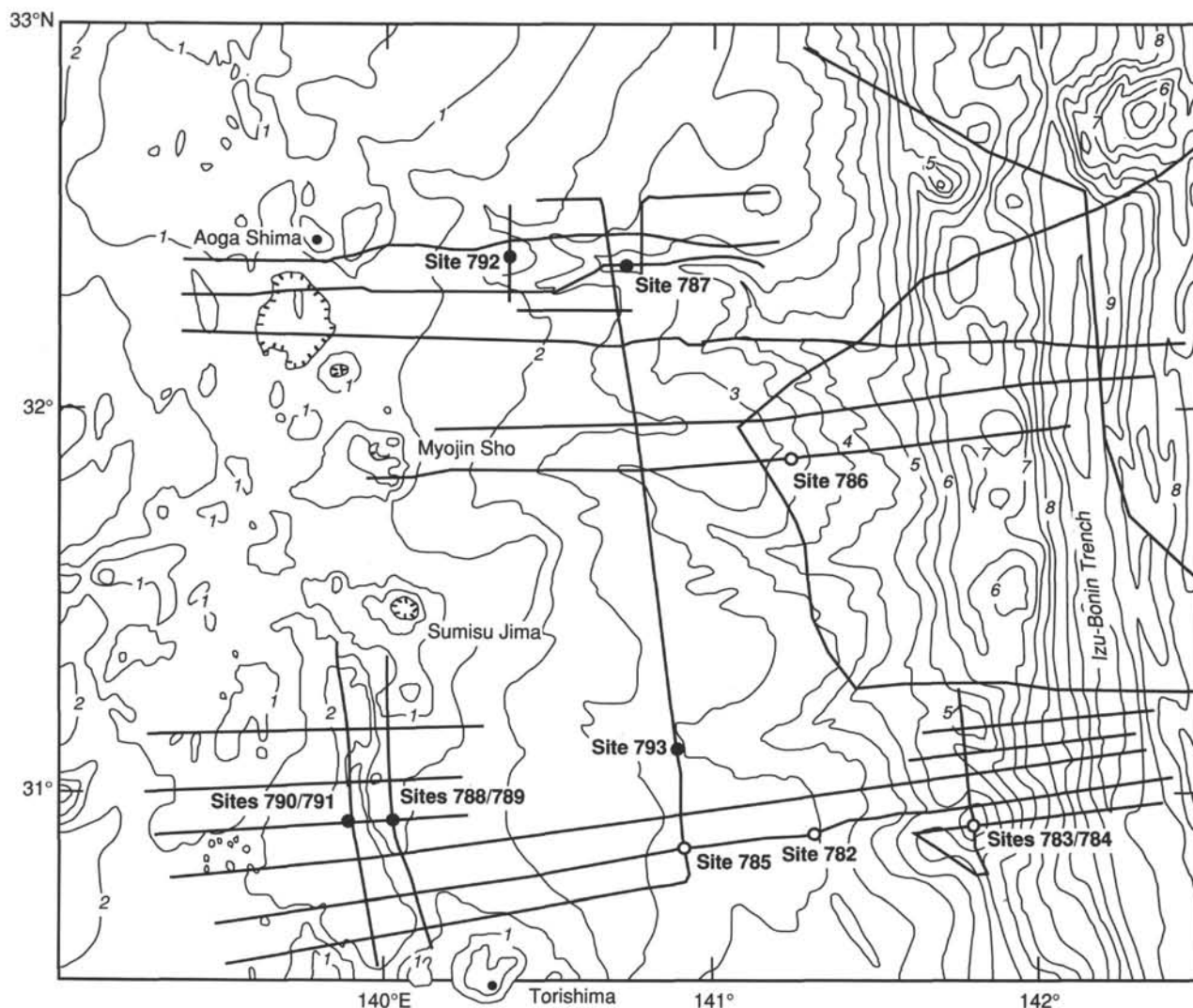
Figure 1. Bathymetric map (0.5-km contour interval) of the Izu-Bonin arc-trench system between 30.5° and 33°N. The locations of sites drilled on ODP Legs 125 (open circles) and 126 (filled circles) are shown on the map, as are the locations of site survey multichannel seismic lines.

hypotheses for the origin and evolution of this forearc terrane, namely: (1) the frontal arc and outer-arc highs could have originally been continuous and subsequently separated by forearc spreading; (2) the frontal-arc and outer-arc highs could have been built separately but nearly synchronously on former West Philippine plate crust; or (3) the terrane could form part of a continuous Eocene arc volcanic province, possibly with overprints of later forearc volcanism. Each scenario of forearc basement development implies a different crustal structure for the forearc.

The fourth objective of the site, the study of microstructures and plate rotations, was addressed through a study of FMS images and of the structural and paleomagnetic properties of the cored materials. Microstructures in the cores and on the FMS images of the borehole wall helped us to determine the intensity of faulting in space and time across the forearc terrane, as well as to define the syndepositional structures. Measurements of the paleomagnetic properties of subaerial portions of the Izu-Bonin and Mariana forearcs have shown at least 20° of northward drift and from 30° to >90° of clockwise rotation since the

Eocene (see "Introduction" chapter, this volume, for more details). Studies of the paleomagnetism of the cores constrained the numerous different models for the nature and timing of these motions, and their relationship to the overall structural evolution of the forearc. The FMS data helped orient the rotary cores so that declinations, and hence rotations, could be determined.

SEISMIC STRATIGRAPHY

The correlation of site-survey multichannel seismic (MCS) reflection data to recovered core material (Fig. 4) was accomplished by using physical property velocity data, averaged over each lithologic unit (see "Physical Properties," this chapter), to convert depths (mbsf) into two-way traveltimes. The site chosen lies on *Fred Moore* 3505, line 10, at 0134Z. The reflector sequence can be divided into five seismic units:

1. Seismic Unit 1 (2.4–2.72 s) consists of numerous subparallel, divergent (lenticular near Site 792), high-amplitude reflectors, and corresponds to lithologic Unit I and the upper portion
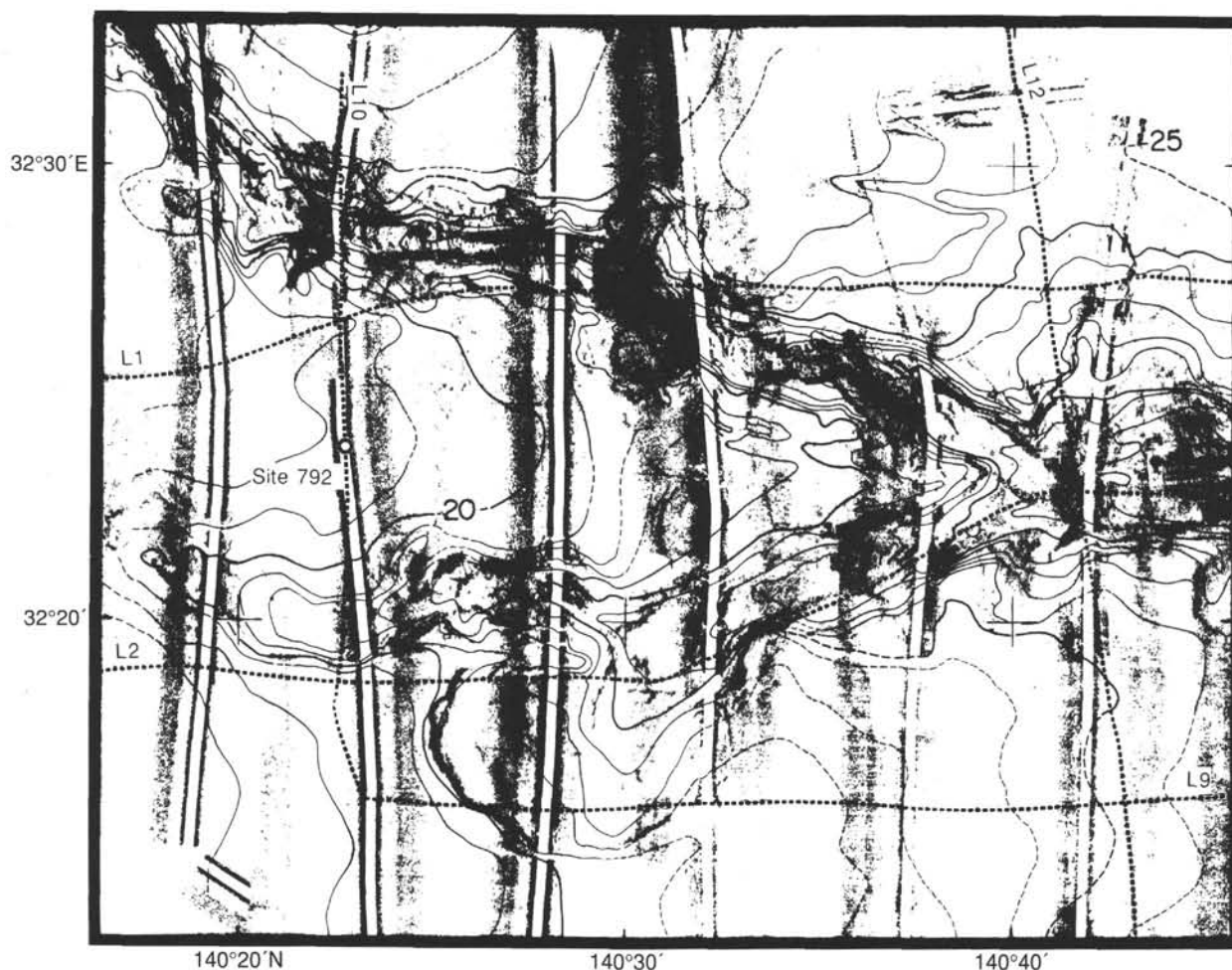
Figure 2. SeaMARC II sidescan and bathymetry (100-m contours) of Aoga Shima canyon (Klaus and Taylor, in press.). The locations of MCS site survey tracks and Site 792 (open circle) are also shown.
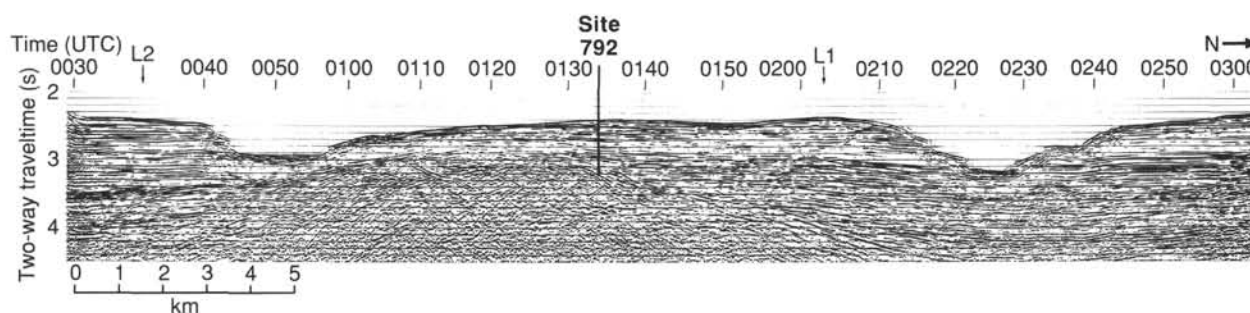

Figure 3. MCS profile 10 (Taylor et al., this volume) across the Izu-Bonin forearc sedimentary basin, crossing both forks of Aoga Shima canyon (see Fig. 2 for location). Site 792 is in the western half of the forearc basin, located where the deeper sedimentary section laps onto a basement high.

of Unit II. The lenticular reflector package may be interpreted as either channel deposits or as a bottom-current-induced depositional feature.

2. Seismic Unit 2 (2.72–2.88 s) consists of parallel, continuous, undulating, low-amplitude reflectors, and corresponds to the lower portion of lithologic Unit II and Unit III.

3. Seismic Unit 3 (2.88–3.12 s) is characterized by northward divergent, high-amplitude reflectors, offset by normal faults. It corresponds to the turbiditic lithologic Unit IV.

4. Seismic Unit 4 (3.12–3.2 s) laps off the basement in the vicinity of Site 792 and is present only as a thin horizon above basement. Subparallel to discontinuous, medium-amplitude reflectors characterize this unit farther east. The onlap of reflectors onto seismic Unit 4 indicates that a major unconformity is present near 715 mbsf at Site 792.

5. Acoustic basement (>3.2 s) at this site on the western margin of the forearc basin is characterized by chaotic, discontinuous reflectors of low to medium amplitude.
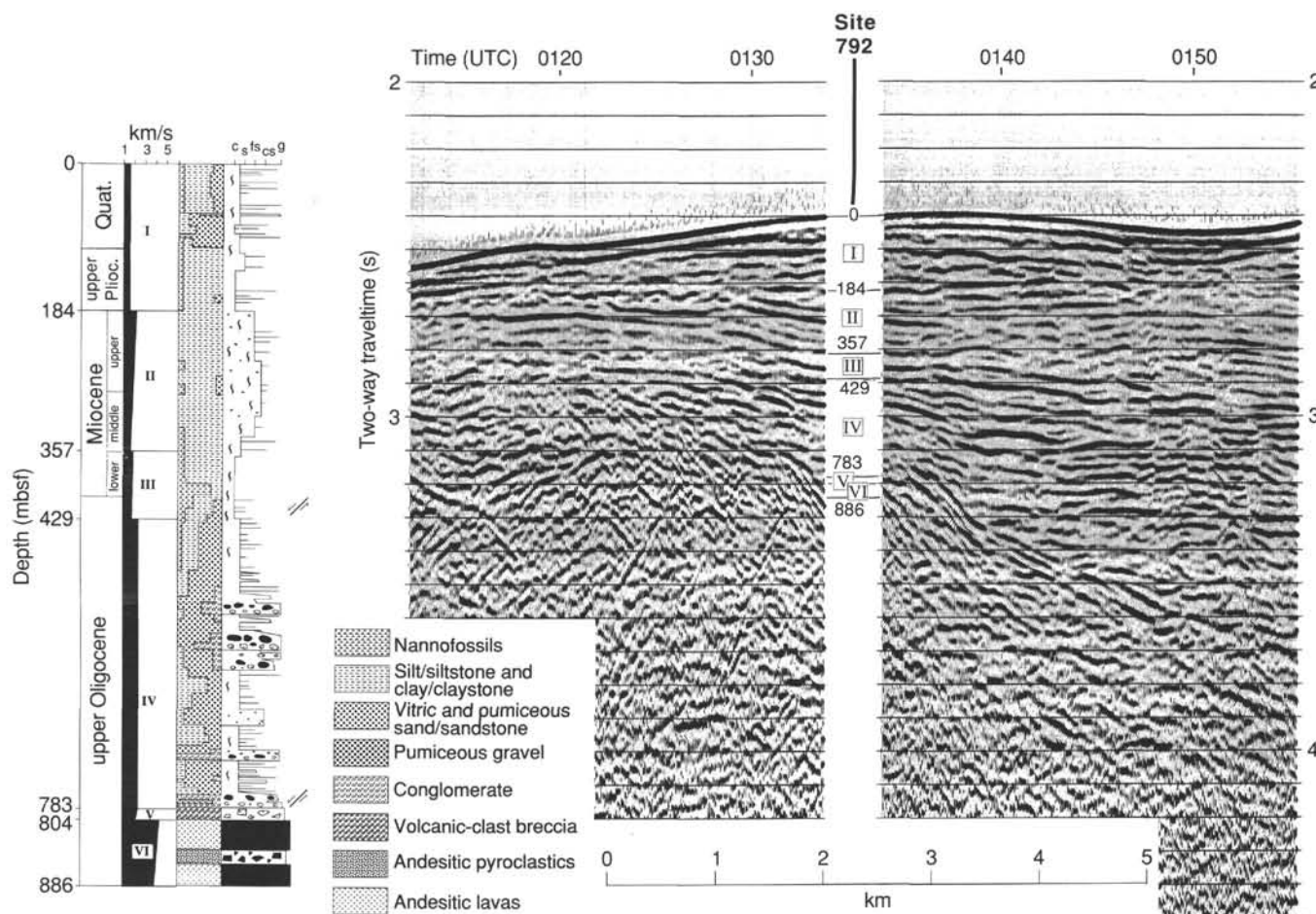
Figure 4. Correlation of Site 792 lithostratigraphy with site-survey multichannel seismic reflection data. The lithologic column for this site (see "Lithostratigraphy and Accumulation Rates" section, this chapter) appears on the left-hand side of the figure (c = clay, fs = fine sand, cs = coarse sand, and g = gravel). The location of the *Fred Moore* seismic line (MCS profile 10) is shown in Figure 2; lithologic units are identified on the seismic section, and unit boundaries are given in mbsf. The seismic section has been stacked (48-fold), deconvolved, migrated, and filtered 10–60 Hz. Vertical exaggeration is about 4×.

OPERATIONS

Site 788 to Site 792

JOIDES Resolution departed from Site 788 at full speed for Site 792 at 0330 hr (all times given in UTC) on 16 May 1989 and arrived in the vicinity of the new site at 1215 hr the same day. After a 4.5 hr survey, the first beacon was deployed at 1636 hr. Within 30 min, this beacon exhibited erratic pulse-time behavior, and a second unit had to be launched.

Site 792A

Hole 792A

A standard six-collar APC/XCB BHA with a nonmagnetic drill collar was lowered to just above the mud line, and the first APC core was shot at 2130 hr on 16 May. Although the retrieved core was 9.7 m in length, it was used to establish mud-line depth at 1797.8 mbsl. After the fifth piston core was cut, a Uyeda heat-flow experiment was conducted, and piston coring resumed. Another heat flow experiment was conducted after Core 126-792A-10H was cut. Recovery for the first 10 APC cores averaged 76% (Table 1).

The eleventh piston core was shot at 95.1 mbsf, but the core barrel resisted all efforts to extract it from the formation until

an overpull of 170,000 lb was applied. The piston rod severed at the rod connection and the inner core barrel, and 5 m of piston rod remained in the hole. The remnants of the APC prevented any further coring efforts, so the BHA was short-tripped above the mud line. The BHA cleared the mud line, officially ending Hole 792A operations at 0825 hr on 17 May.

Hole 792B

The ship was offset 20 m farther south of the beacon, and Hole 792B was spudded at 0925 hr on 17 May. The mud-line core established the seafloor at 1798.2 mbsl. The drill string was then washed to 50 mbsf, where a second piston core was shot, followed by another heat-flow experiment. The third and last piston core was shot at 59.6 mbsf. The APC core barrel was retracted, and XCB coring was initiated at 78.8 mbsf. Cores 126-792B-4X through -10X averaged <28% recovery. When Core 126-792B-11X was tripped to the surface, we discovered that the cutting shoe had broken off near the 1/4-in. radius immediately behind the cutting structure.

Because the fractured shoe in the hole could have destroyed the rotary cones if coring had been continued, we ended operations at the hole and pulled out the BHA. The BHA cleared the seafloor at 2310 hr, thus ending Hole 792B and commencing Hole 792C.

Table 1. Coring summary, Site 792.

Core no.	Date (May 1989)	Time (UTC)	Depth (mbsf)	Cored (m)	Recovery (m)	Recovery (%)
126-792A-						
1H	16	2145	0.0–9.7	9.7	9.72	100.0
2H	16	2225	9.7–19.1	9.4	5.74	61.0
3H	16	2300	19.1–28.4	9.3	9.75	105.0
4H	16	2325	28.4–37.8	9.4	9.79	104.0
5H	17	0010	37.8–47.2	9.4	8.72	92.7
6H	17	0155	47.2–56.6	9.4	7.49	79.7
7H	17	0225	56.6–66.0	9.4	7.46	79.3
8H	17	0335	66.0–75.6	9.6	3.46	36.0
9H	17	0415	75.6–85.3	9.7	4.54	46.8
10H	17	0450	85.3–95.0	9.7	5.42	55.9
Coring totals				95.0	72.09	75.9
126-792B-						
1H	17	0935	0.0–4.3	4.3	4.28	99.5
2H	17	1205	50.0–59.6	9.6	8.60	89.6
3H	17	1425	59.6–69.2	9.6	10.05	104.7
4X	17	1545	69.2–78.8	9.6	4.76	49.6
5X	17	1640	78.8–88.5	9.7	0.38	3.9
6X	17	1720	88.5–98.2	9.7	0.15	1.5
7X	17	1810	98.2–107.9	9.7	0.37	3.8
8X	17	1900	107.9–117.5	9.6	6.22	64.8
9X	17	1955	117.5–127.1	9.6	2.08	21.6
10X	17	2100	127.1–136.8	9.7	4.66	48.0
11X	17	2210	136.8–146.4	9.6	2.04	21.2
Coring totals				100.7	43.59	43.3
126-792C-						
1X	18	0745	136.8–146.4	9.6	0.59	6.1
Coring totals				9.6	0.59	6.1
126-792D-						
1X	18	1355	136.0–145.6	9.6	0.84	8.8
Coring totals				9.6	0.84	8.8
126-792E-						
1R	19	0540	135.6–145.2	9.6	1.04	10.8
2R	19	0630	145.2–154.8	9.6	0.48	5.0
3R	19	0710	154.8–164.5	9.7	2.84	29.3
4R	19	0755	164.5–174.1	9.6	3.25	33.8
5R	19	0830	174.1–183.7	9.6	0.93	9.7
6R	19	0915	183.7–193.4	9.7	1.43	14.7
7R	19	0950	193.4–203.1	9.7	0.40	4.1
8R	19	1025	203.1–212.6	9.5	0.30	3.2
9R	19	1055	212.6–222.2	9.6	5.54	57.7
10R	19	1130	222.2–231.9	9.7	5.28	54.4
11R	19	1205	231.9–241.5	9.6	2.65	27.6
12R	19	1240	241.5–251.2	9.7	4.34	44.7
13R	19	1315	251.2–260.9	9.7	1.85	19.1
14R	19	1345	260.9–270.5	9.6	0.24	2.5
15R	19	1420	270.5–280.2	9.7	3.49	36.0
16R	19	1455	280.2–289.9	9.7	2.66	27.4
17R	19	1530	289.9–299.5	9.6	5.30	55.2
18R	19	1600	299.5–309.0	9.5	5.95	62.6
19R	19	1635	309.0–318.6	9.6	3.91	40.7
20R	19	1710	318.6–328.3	9.7	3.88	40.0
21R	19	1740	328.3–337.9	9.6	2.22	23.1
22R	19	1810	337.9–347.6	9.7	4.71	48.5
23R	19	1845	347.6–357.3	9.7	2.07	21.3
24R	19	1925	357.3–367.0	9.7	1.30	13.4
25R	19	2005	367.0–376.6	9.6	1.74	18.1
26R	19	2045	376.6–386.3	9.7	1.28	13.2
27R	19	2130	386.3–396.0	9.7	5.32	54.8
28R	19	2225	396.0–405.6	9.6	3.03	31.5
29R	19	2310	405.6–415.2	9.6	3.03	31.5
30R	20	0030	415.2–424.9	9.7	8.29	85.4
31R	20	0125	424.9–434.6	9.7	4.41	45.4
32R	20	0240	434.6–444.2	9.6	4.84	50.4
33R	20	0355	444.2–453.9	9.7	4.13	42.6
34R	20	0520	453.9–463.5	9.6	5.12	53.3

Table 1 (continued).

Core no.	Date (May 1989)	Time (UTC)	Depth (mbsf)	Cored (m)	Recovery (m)	Recovery (%)
126-792E- (Cont.)						
35R	20	0655	463.5–473.2	9.7	2.68	27.6
36R	20	0800	473.2–482.8	9.6	6.93	72.2
37R	20	0910	482.8–492.5	9.7	9.82	101.0
38R	20	1020	492.5–502.2	9.7	9.02	93.0
39R	20	1125	502.2–511.9	9.7	6.98	71.9
40R	20	1225	511.9–521.6	9.7	8.80	90.7
41R	20	1330	521.6–531.2	9.6	6.80	70.8
42R	20	1435	531.2–540.6	9.4	9.39	99.9
43R	20	1555	540.6–550.3	9.7	9.71	100.0
44R	20	1725	550.3–560.0	9.7	6.59	67.9
45R	20	1840	560.0–569.7	9.7	5.70	58.7
46R	20	2010	569.7–579.4	9.7	9.75	100.0
47R	20	2150	579.4–588.6	9.2	4.66	50.6
48R	20	2300	588.6–597.8	9.2	9.60	104.0
49R	21	0130	597.8–607.4	9.6	9.72	101.0
50R	21	0230	607.4–617.1	9.7	9.61	99.1
51R	21	0340	617.1–626.8	9.7	4.86	50.1
52R	21	0440	626.8–636.4	9.6	7.97	83.0
53R	21	0600	636.4–646.1	9.7	0.00	0.0
54R	21	0725	646.1–655.7	9.6	8.33	86.8
55R	21	0835	655.7–665.4	9.7	3.57	36.8
56R	21	0945	665.4–675.1	9.7	8.77	90.4
57R	21	1055	675.1–684.8	9.7	8.95	92.2
58R	21	1200	684.8–694.4	9.6	5.20	54.1
59R	21	1500	694.4–704.0	9.6	8.21	85.5
60R	21	1610	704.0–713.6	9.6	9.83	102.0
61R	21	1720	713.6–722.9	9.3	5.98	64.3
62R	21	1830	722.9–732.5	9.6	9.88	103.0
63R	21	1940	732.5–742.2	9.7	4.73	48.7
64R	21	2140	742.2–751.8	9.6	3.55	37.0
65R	21	0005	751.8–761.5	9.7	2.27	23.4
66R	22	0110	761.5–771.2	9.7	7.77	80.1
67R	22	0255	771.2–780.9	9.7	4.92	50.7
68R	22	0435	780.9–790.6	9.7	2.69	27.7
69R	22	0610	790.6–800.2	9.6	7.68	80.0
70R	22	0830	800.2–809.9	9.7	0.19	2.0
71R	22	1135	809.9–819.5	9.6	3.05	31.8
72R	22	1435	819.5–829.2	9.7	1.45	14.9
73R	22	1700	829.2–838.8	9.6	2.31	24.0
74R	22	1900	838.8–848.2	9.4	2.15	22.9
75R	22	2110	848.2–857.7	9.5	1.57	16.5
76R	22	2245	857.7–867.1	9.4	1.24	13.2
77R	23	0110	867.1–876.6	9.5	0.40	4.2
78R	23	0445	876.6–885.9	9.3	1.36	14.6
Coring totals				750.3	361.89	48.2

Hole 792C

The vessel was offset an additional 20 m farther south of the beacon. The bottom of the drill string "felt" the seafloor at 1798.2 mbsl and was washed down to 137 mbsf, where another XCB attempt was made. The cutting shoe failed again, in the same manner as at Hole 792B. At this point, we decided that the two cutting shoe failures may have been caused by a defect in the fabrication of the entire lot of cutting shoes. A diamond-impregnated, three-bladed cutting shoe was selected for the next attempt. The drill string was short-tripped above the seafloor. The BHA cleared the seafloor at 0845 hr on 18 May, thus ending Hole 792C and initiating Hole 792D.

Hole 792D

The center bit was run down to the drill bit, and the drill string was lowered to the mud line at 1798.2 mbsl. We washed the drill string down to 136 mbsf and made another attempt to cut the core. After coring for 52 min, the driller noticed that penetration had stopped. We retrieved the core barrel and found that the cutting shoe had separated in the same manner as in the other two incidents.

The drill string was pulled out of the hole, and the BHA cleared the mud line at 1535 hr on 18 May.

Hole 792E

Hole 792E was spudded with a standard nine-collar RCB BHA and drilled to 135.6 mbsf, at which depth normal rotary coring was initiated. No problems were encountered at the level where the three XCB cutting shoes had previously fractured. We cut 78 cores to a depth of 885.9 mbsf during the next 83 hr.

After cutting Core 126-792E-78R, a multishot survey was conducted from the bottom (885.9 mbsf) up to 60 mbsf at 100-m increments. This survey took about 30 min, during which time there was no circulation or drill-pipe rotation. The survey indicated that the hole never exceeded 2.5° from vertical.

After retrieving the survey and just before removing the sinker bars, the formation started to flow into the bit and the hole began to slough in, trapping the BHA. From 0425 to 0940 hr on 23 May a successful (albeit temporary) effort was conducted to save the BHA and the hole. After mud treatment and some minor hole reaming, we decided that luck had been pushed long enough and it was time to withdraw to the logging depth.

The bit was lifted just off bottom and released at 1110 hr. The drill string stuck at 286 mbsf, at which point overpulls of 230,000 lb proved futile in moving the pipe farther up the hole. We then decided to start the downhole measurement program.

With the uncertainty of downhole conditions a prime consideration, the first log was a reduced geophysical combination (DIT/LSS/NGT-TEMP) without the density tool (HLDT). The tool was run in the hole at 2245 hr on 23 May to a depth of 877.1 mbsf, and returned at 0345 hr on 24 May. The results of this log were excellent and provided a good match with the shipboard physical property data.

The formation microscanner (FMS-NGT-TEMP) was rigged up for its maiden voyage with ODP. The tool was deployed at 0445 hr on 24 May and was successfully used to log the hole from 285 to 878.6 mbsf. All conductivity curves were visibly active and promised to yield first-class images. Both calipers showed that the borehole was cylindrical to slightly elliptical, with a typical diameter of 10 in. throughout the hole, except between 370 and 400 mbsf, where the radius exceeded 15 in.

In spite of the rough going while trying to retrieve the drill string, the hole was in excellent shape, and the absence of fill suggested that the zone that sloughed in on the pipe was essentially sealed off by the BHA.

The FMS was rigged down at 0845 hr, and the geochemical (GST-ACT-NGT-TEMP) logging suite was prepared. Between 0945 and 1830 hr on 24 May, the GST logged the borehole including through the pipe up to the mud line, with excellent results.

Completing the standard suite of logs was a rerun of the geophysical combination with the density tool (HLDT-LSS-NGT-TEMP), which also completed a successful excursion of the hole between 2000 on 24 May and 0200 hr on 25 May, although the short-spacing density sensor failed downhole. The final log at this site was a vertical seismic profile (VSP), which obtained a high-grade log. Apparently, the firm anchoring of the drill pipe in the sediment caused the ambient noise level of the log to be extremely low.

After the logging program was completed, the top drive was put up and a final attempt was made to free the stuck pipe. When this proved unsuccessful, we decided to sever the pipe. A 31-pellet severing charge was run in the hole and fired.

The pipe was tripped to the surface, and the string cleared the mud line at 1945 hr and the rotary table at 2140 hr on 25 May, ending Site 792E. An unsuccessful attempt was made to recall the commandable beacon. Finally, the thrusters and hy-drophones were pulled and the *JOIDES Resolution* made way at full speed to Site 793 at 2230 hr on 25 May.

LITHOSTRATIGRAPHY AND ACCUMULATION RATES

We drilled five holes at Site 792. The upper part of the sedimentary sequence was cored primarily in Holes 792A and 792B; the middle and lower portions were penetrated by Hole 792E. We recognized six lithologic units at this site (Table 2 and Fig. 5). A composite section incorporates data from Hole 792A for the interval from 0 to 98.2 mbsf, from Hole 792B for the interval from 98.2 to 135.6 mbsf, and from Hole 792E for the rest of the section (see Fig. 30, "Biostratigraphy" section, this chapter). The upper five units are composed of volcanogenic and biogenic sediments and sedimentary rocks, and the lowest unit is igneous rock. Contacts between adjacent units were recovered, with the exception of the Unit I/II and Unit III/IV contacts.

Although defined by lithologic changes, two contacts between lithologic units at Site 792 roughly coincide with unconformities suggested by biostratigraphic data. The Unit I/II boundary is marked by a hiatus between upper Pliocene and upper Miocene sedimentary rocks, and the Unit II/III boundary is also characterized by a hiatus between upper and lower Miocene sedimentary rocks. The Unit IV/V boundary is marked by a fault.

Biostratigraphic data suggest that three more hiatuses occur within Units I, II, and III. The oldest discontinuity coincides with a fault between the upper Oligocene and the lower Miocene in Unit III, in Core 126-792E-29R, and the middle discontinuity corresponds to a color change in the middle part of Unit II in Section 126-792E-15R-1 at 20 cm.

Unit I

Intervals: Cores 126-792A-1H through -10H, Cores 126-792B-1H
    through -11H, Core 126-792C-1X, Core 126-792D-1X, and
    Cores 126-792E-1X through -5R
Age: Holocene to late Pliocene
Depth: 0–183.7 mbsf

Unit I extends from the sediment/water interface to 183.7 mbsf, where there is a change from unconsolidated deposits, mainly nannofossil-rich fine-grained sediments, to lithified sedimentary rocks, mainly sandy mudstone and muddy sandstone. This contact was not recovered and is placed at the top of Core 126-792E-6R.

Unit I consists predominantly (62%) of dark gray (5GY 4/1) and olive gray (5Y 4/1), nannofossil-rich clayey silt and nannofossil-rich silty clay, which is composed of nannofossils, volcanic glass, and clay. Calcium carbonate contents in the highly bioturbated nannofossil-rich deposits range from 10% to 30%. Minor sediment types include foraminifer-rich silty clay (5%), nannofossil-rich vitric silt (2%), and clay (1%).

Interbedded with the nannofossil-rich muddy sediments are beds of vitric sand (19%), vitric silt (8%), and scoriaceous and pumiceous gravel (3%). These beds, which compose 30% of the core, are generally <20 cm thick, but locally exceed 100 cm in thickness (Table 3). Several layers show planar lamination and normal grading, but scoured bases are rare. The sediments are variably mafic and dark colored (dark gray, N3, 5Y 4/1; black, 5Y 3/1; brownish black, 5YR 2/1), or felsic and light colored (light gray, N6; gray, 5Y 6/1) (Figs. 6 and 7); however, the total thickness of mafic sand is almost twice that of felsic sand. Mafic vitric sand and silt are mainly composed of brown and opaque glass with variable amounts of orthopyroxene, clinopyroxene, and plagioclase crystals, whereas the felsic sediments consist of translucent bubble-wall and pumice-type glass shards with only minor crystals. Many intervals are mixtures of mafic

Table 2. Lithologic units, Site 792.

Unit	Lithology	Sedimentary structures	Interval (mbsf)	Age	Occurrence
I	Nannofossil-rich vitric silty clay and nannofossil-rich clayey silt, interbedded with vitric silts, vitric sands, and pumiceous and scoriaceous gravels. Locally rich in foraminifers and/or biogenic silica.	Vitric silt and sand layers show plane-parallel lamination, graded bedding, and burrowed tops.	0–183.7	Quaternary to late Pliocene	126-792A-1H through -10H, 126-792B-1H through -11H, 126-792C-1X, 126-792D-1X, 126-792E-1R through -5R
II	Sandy mudstone, muddy sandstone, silty claystone, vitric sandstone, and vitric siltstone, all with nannofossil-rich intervals. Nannofosil content increases irregularly with depth. Local granule- and pebble-rich intervals.	Vitric siltstone beds show plane-parallel lamination and sharp bases. Finer lithologies are strongly burrowed. Trace fossils include *Zoophycos* and *Chondrites*.	183.7–357.4	late Miocene to middle Miocene	126-792E-6R to -24R-1, 10 cm
III	Nannofossil-rich claystone, nannofossil claystone and nannofossil chalk. Rare crystal-vitric siltstone and crystal-vitric sandstone.	Some intervals show dewatering fractures and sandstone dikes. Fault zone at 407 mbsf.	357.4–429.3	early Miocene to late Oligocene	126-792E-24R-1, 10 cm through -31R
IV	Vitric sandstone, volcanic and intraclastic sandy conglomerate, with minor silty claystone, nannofossil-rich silty claystone, nannofossil-rich claystone and claystone.	Vitric sands show plane-parallel lamination, cross-lamination, scoured bases, load casts, and frame structures. Claystone cobble intraclasts are associated with scours and may be reversely graded. Microfaults, fractures, and clastic dikes occur locally. *Zoophycos* and *Chondrites* burrows are present.	429.3–783.4	late Oligocene to early Oligocene	126-792E-32R through -68R-2, 100 cm
V	Altered volcanic sandstone with claystone intraclasts.	Mottled and brecciated, possibly in association with hydrothermal alteration.	783.4–804	?	126-792E-68R-2, 100 cm through -70R-CC
VI	Plagioclase-orthopyroxene-clinopyroxene andesite.		804–885.9	?	126-792E-70R-CC to -78R

and felsic vitric material. Scoriaceous and pumiceous pebble to granule gravel beds, from 6 to 180 cm in thickness, occur mainly in the upper part of Unit I (Cores 126-792A-1H through -10H).

Sediments of Unit I are unconsolidated, except for a thin bed of dark gray (5Y 4/1) vitric siltstone in Interval 126-792E-5R-1, 25–32 cm, and lack tectonic deformation.

Unit II

Interval: Cores 126-792E-6R through Section 126-792E-24R-1 at 10 cm
Age: late to middle Miocene
Depth: 183.7–357.4 mbsf

The uppermost recovered sediment of Unit II is a poorly sorted sandy mudstone containing granules and pebbles (Fig. 8). The lower boundary of Unit II is the lithologic change from nannofossil-rich sandy mudstone/muddy sandstone to finer grained sediment types, which have much higher nannofossil contents and are assigned to Unit III. This boundary occurs in Section 126-792E-24R-1 at 10 cm, at the base of a black, fine-grained sandstone layer.

Unit II consists mainly of olive black (5Y 2/1) to dark gray (5Y 4/1, 5GY 4/1) vitric sandy mudstone (37%), vitric muddy sandstone (30%), and silty claystone (15%), all of which have nannofossil-rich intervals and minor sandstone (10%), siltstone (5%), and claystone (3%). Disseminated sand and silt grains are predominantly brown scoria, clear volcanic glass shards, and volcanic rock fragments. Bioclasts include nannofossils, foraminifers, radiolarians, and sponge spicules. Granules scattered throughout the muddy sandstone include rhyolitic pumice in Cores 126-792E-9R to -15R, and basaltic scoria in Cores 126-792E-12R to -20R. Below Core 126-792E-22R, granules of scoria are absent, and the sequence is composed mainly of very

dark gray to dark gray (5Y 3/1 to 5Y 4/1), nannofossil-rich vitric silty claystone and vitric silty claystone.

The muddy sandstone and sandy mudstone layers are burrowed, and trace fossils include *Zoophycos* (Fig. 9). These poorly sorted, bioturbated units are lithified primarily by recrystallization of matrix minerals, predominantly clay minerals and carbonate. In better sorted ash layers, thin birefringent rims of hydrated glass and/or clay minerals bind the sediments. Calcium carbonate contents of the muddy sediments generally increase downhole, from 5%–15% to 10%–20% (Fig. 5), whereas the color of the sedimentary rocks abruptly changes from olive black (5Y 2/1) to dark gray (N3) in Section 126-792E-15R-1 at 20 cm. Very dark green (5GY 2/1), glauconite-bearing, fine-grained sandstone (see X-ray diffraction [XRD] analysis that follows) is present just below this boundary.

The vitric sandstone and siltstone layers of Unit II, mostly dark colored (N2, 5Y 2/1), are 1–10 cm thick (Figs. 10 and 11). Rare, light-colored (5R 2/1, N7), siltstone beds are limited to the upper part of the unit. A pumiceous granule-to-pebble conglomerate bed is present in Interval 126-792E-9R-3, 96–103 cm.

No tectonic deformation was observed in Unit II. Unconsolidated vitric siltstone and vitric sandstone beds rarely occur in the upper part of the unit (above Core 126-792E-11R).

Unit III

Interval: Section 126-792E-24R-1 at 10 cm through Core 126-792E-31R
Age: early Miocene to late Oligocene
Depth: 357.4–429.3 mbsf

The upper boundary of Unit III is placed at the top of a dark gray (5Y 4/1) layer of nannofossil claystone that underlies the lowest black sandstone bed of Unit II. The lower boundary of
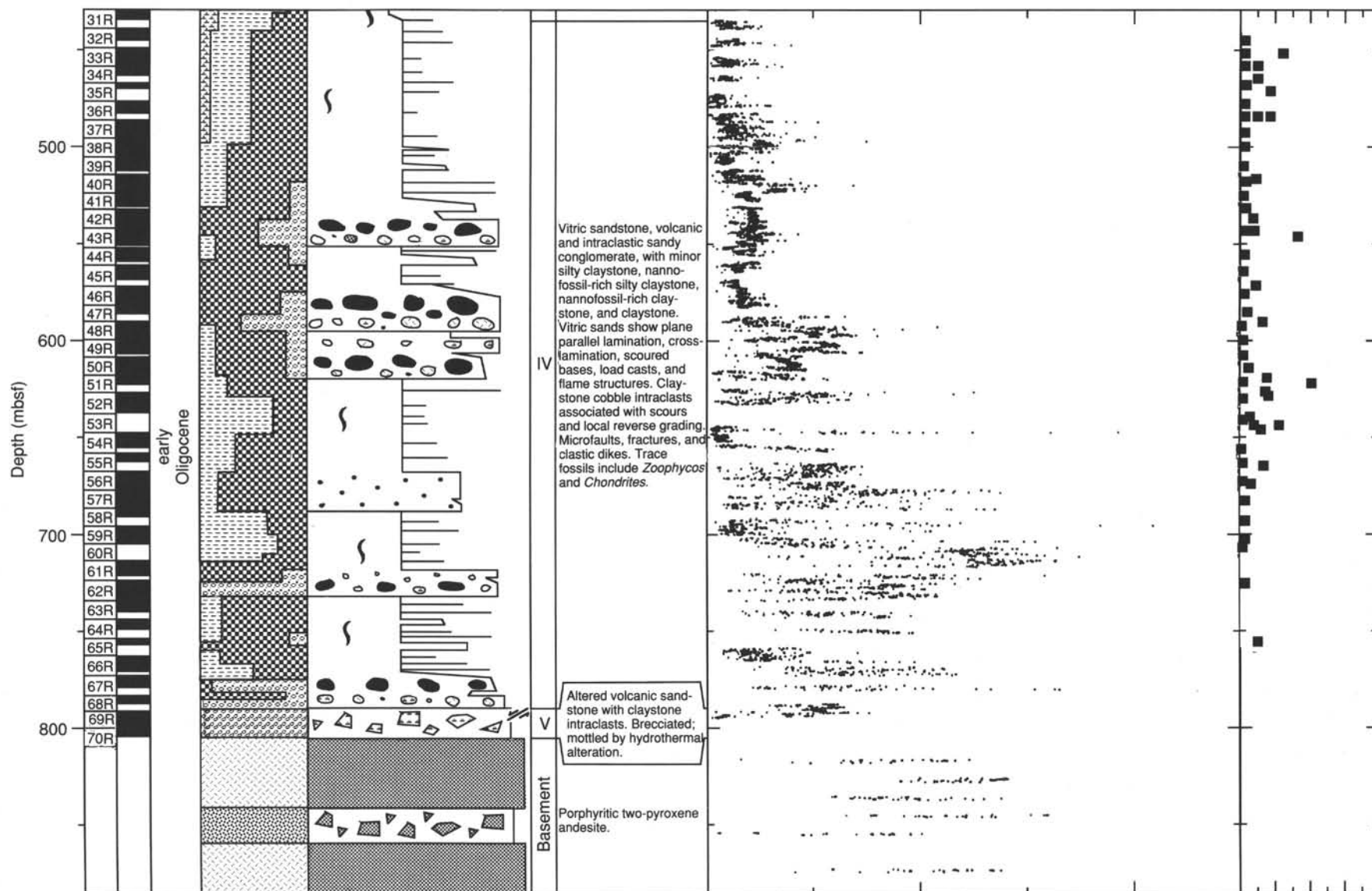
Site 792

Figure 5. Composite stratigraphic section for Site 792 showing unit boundaries and downhole variations in magnetic susceptibility and total carbonate. (See Fig. 4 for legend.)

The text labels within the figure read:

Vitric sandstone, volcanic and intraclastic sandy conglomerate, with minor silty claystone, nannofossil-rich silty claystone, nannofossil-rich claystone, and claystone. Vitric sands show plane parallel lamination, cross-lamination, scoured bases, load casts, and flame structures. Claystone cobble intraclasts associated with scours and local reverse grading. Microfaults, fractures, and clastic dikes. Trace fossils include *Zoophycos* and *Chondrites*.

Altered volcanic sandstone with claystone intraclasts. Brecciated; mottled by hydrothermal alteration.

Porphyritic two-pyroxene andesite.

Depth (mbsf)

early Oligocene

IV

V

Basement

Table 3. Ash layers, Site 792.

Core, section, interval (cm)	Thickness (cm)	Description and remarks
126-792A-		
1H-1, 0–19	19	Fine scoria (dispersed in silty clay)
1H-1, 34–42	3/5	Light brownish gray (5YR6)/very light gray (N8); silt-clay/sand
1H-1, 57–58	1	Coarse sand-granule scoria
1H-1, 63–64	1	Coarse sand-granule scoria
1H-1, 67–69	1	Coarse sand-granule scoria
1H-1, 80–82	2	Black; fine sand
1H-1, 124–130	6	Brownish black (5YR2/1); fine scoria lapilli (maximum diameter = 4 mm)
1H-2, 30–34	4	Medium light gray (N6); coarse sand (pumice and lithic)
1H-2, 51–79	9/12/7	Light gray (N7)/dark gray (N3); silt-clay/fine sand/coarse sand-granule
1H-2, 120–124	4	Dark gray (N3); fine sand
1H-2, 125–132	7	White; fine ash (dispersed)
1H-2, 139–140	1	Brownish black (5YR2/1); scoria; very coarse sand (maximum diameter = 1 mm)
1H-3, 4–5	1	Scoria; coarse sand
1H-3, 24–25	1	Olive gray (5Y4/1); medium sand
1H-3, 73–80	4/3	Brownish gray (5YR4/1); silt/coarse sand (pumice and scoria)
1H-3, 126–145	19	Light gray (N7) (purple); clay-fine sand (grading)
1H-4, 144–146	2	Olive black (5Y2/1); silt
1H-5, 15–16	1	Medium light gray (N6); silt
1H-5, 28–32	2/2	Black/black; medium sand/scoria (maximum diameter = 2 mm)
1H-5, 32–38	4/2	Medium light gray (N6)/white; clay/silt-clay
1H-5, 47–52	3/2	Black/black; fine sand/scoria (maximum diameter = 2 mm)
1H-5, 60–62	2	Dark gray (N3); scoria (maximum diameter = 1 mm)
1H-5, 80–83	2/1	Medium light gray (N6)/gray; silt/coarse sand
1H-5, 98–99	1	Dark gray (N3); scoria; coarse sand (dispersed)
1H-6, 44–55	11	Dark gray (N3); fine coarse sand (graded)
1H-6, 81–110	29	Dark gray (N3); fine coarse sand with granules (graded)
1H-6, 118–122	4	Medium light gray (N6); fine sand
1H-6, 122–124	2	Black; fine sand
1H-6, 131–132	1	Black; fine medium sand
1H-6, 144–147	1/2	Grayish green (10GY5/2)/medium light gray (N6); silt-clay
1H-7, 37–39	2	White; fine ash (dispersed)
2H-1, +0–90	+60/14/16	Medium dark gray (N4)/grayish black (N2); silt/fine sand
2H-1, 100–105	5	Grayish black (N2); fine sand
2H-1, 140–150	18/22	Medium dark gray (N4)/light olive gray (5Y6/1); pumiceous very coarse
2H-2, 10–30		Sand (pumice maximum diameter = 2 cm)/medium sand
2H-2, 64–74	8/2	Light olive gray (5Y6/1)/grayish black (N2); coarse tuff (pumice and granules)/scoria; coarse sand
2H-2, 82–94	7/3/2	Light gray (5Y6/1)/olive gray (5Y4/1)/brownish gray (5YR4/1) (purple); clay/sand/silt
2H-2, 133–150	12/13	Light olive gray (5Y6/1); pumiceous lapilli (pumice maximum diameter = 2 cm, lithic maximum diameter = 5 mm)/ pumiceous sandy lapilli (pumice maximum diameter = 1 cm)
2H-3, 0–8		
2H-3, 40–46	6	Dark gray (N3); silt-medium sand (graded)
2H-3, 59–64	5	Light gray; clay
2H-3, 90–98	8	Dark gray (N3); silt-fine sand (graded)
2H-4, 27–113	98+	Fine sand-pumiceous gravel (pumice maximum diameter = 1 cm, two kinds of pumice, white porous and gray dense)
2H-CC 0–12+		
3H-1, 27–39	12	Gray; pumice lapilli tuff (pumice maximum diameter = 2 cm)
3H-1, 50–52	2	Medium gray (N5); lithic tuff, silt-very fine sand (graded)
3H-1, 69–70	1	Lithic tuff coarse sand
3H-1, 80–94	10/4	Medium light gray (N6)/medium gray (N5); silt-very fine sand/ pumice coarse sand, crystal (plagioclase) rich (diameter = 1 mm)
3H-1, 108–113	5	Medium gray (N5); tuff; medium very fine sand
3H-1, 122–127	4/1	Medium light gray (N6)/medium gray (N5); silt/very fine sand
3H-2, 3–6	1/2	Grayish green (5G5/2)/light gray (N7); silt
3H-2, 25–27	2	Grayish black (N2); silt
3H-2, 81–84	3	Medium light gray (N6); silt
3H-2, 97–117	20	Olive gray (5Y4/1); clayey silt
3H-2, 147–148	1	White; fine tuff
3H-3, 55–57	7	Medium dark gray (N4); silt-very fine sand
3H-3, 65–73	8	Gray; pumice lapilli (pumice maximum diameter = 2 cm)
3H-3, 102–115	12/1	White; silt/pumiceous coarse sand (lithic tuff)
3H-4, 2–6	4	Grayish black (N2); fine sand
3H-4, 17–22	5	Dark gray (N3); silt
3H-4, 77–78	1	Black; very fine sand (dispersed)
3H-4, 99–104	4/1	Dark gray (N3); very fine sand/scoria, very coarse sand (maximum diameter = 2 mm)
3H-4, 141–147	6	Medium dark gray (N4); silt-medium sand (grading)
3H-5, 15–19	2/2	Olive gray (5Y4/1)/dark gray (N3); very fine sand/very coarse sand; lithic tuff (lithic maximum diameter = 1 mm)
3H-5, 54–57	2/1	Dark gray (N3); silt/scoria; coarse sand (maximum diameter = 1 mm)

Table 3 (continued).

Core, section, interval (cm)	Thickness (cm)	Description and remarks
126-792A- (Cont.)		
3H-5, 67–76	9	Grayish black (N2); very coarse silt
3H-5, 78–79	1	Medium light gray (N6); silt
3H-5, 110–114	4	White; fine tuff pocket
3H-6, 29–32	3	Light olive gray (5Y6/1); silt
3H-6, 47	<1	Pumice tuff (maximum diameter = 1 mm)
3H-6, 58–60	2	Grayish black (N2); scoria; coarse sand (maximum diameter = 2 mm)
3H-6, 82–88	3/3	Light gray (N7)/very light gray (N8); silt
3H-6, 100–115	15	Medium dark gray (N4); silt medium sand
3H-7, 16–17	1	Olive gray (5Y4/1); silt
3H-7, 42–45	17	Light gray (N7); silt
3H-CC, 0–14		
4H-1, 10–16	6	Dark gray (N3); silt/very fine sand
4H-1, 115–120	5	Dark gray (N3); silt
4H-2, 8–15	4/3	Olive gray (5Y4/1)/grayish black (N2); silt/fine sand
4H-2, 19–23	3/1	Grayish black (N2); silt/coarse sand
4H-2, 33–46	13	Light olive gray (5Y6/1); silty/coarse-medium sand
4H-2, 50–53	3	Grayish black (N2); very coarse sand with granules (maximum diameter = 4 mm)
4H-2, 73–80	7	Dark gray (N3); silt-very fine sand (graded)
4H-2, 101	<1	Dark gray (N3); lithic tuff (5 mm thick)
4H-2, 123–131	8	Dark gray (N3); silt
4H-3, 10–15	5	Black; coarse sand (burrowed)
4H-3, 30–33	3	Olive gray (5Y4/1); pumice pebble (maximum diameter = 5 mm)
4H-3, 50–52	2	Dark gray (N3); silt
4H-3, 79	<1	Dark gray (N3); silt
4H-3, 100–104	4	Dark gray (N3); silt-fine sand (graded)
4H-3, 128–129	1	Grayish black (N2); medium sand
4H-4, 6–7	1	Light olive gray (5Y6/1); fine sand
4H-4, 31–32	1	Gray; fine tuff
4H-4, 35	<1	White; fine tuff (dispersed)
4H-4, 39	<1	Dark gray (N3); fine tuff (5 mm thick)
4H-4, 48–50	2	Light olive gray (5Y6/1); fine sand
4H-4, 90–91	1	Dark gray (N3); fine sand
4H-4, 94–103	8/1	Light olive gray (5Y6/1); silt/medium sand
4H-5, 10–17	7	Grayish black (N2); scoria; coarse sand
4H-5, 28–30	2	Grayish black (N2); scoria; coarse sand
4H-5, 38–43	5	Grayish black (N2); scoria; granule
4H-5, 49–64	13/2	Dark gray (N3); silt/medium sand
4H-5, 81	<1	Grayish black (N2); scoria; coarse sand (5 mm thick)
4H-5, 102–105	3	Grayish black (N2); scoria; coarse sand (maximum diameter = 2 mm)
4H-5, 108–110	2	Grayish black (N2); scoria
4H-6, 0–2	2	Grayish black (N2); scoria; coarse sand
4H-6, 12–15	3	Light olive gray (5Y6/1); silt
4H-6, 35–36	1	Grayish black (N2); fine sand-silt
4H-6, 48–50	2	Dark gray (N3); silt with scoria (maximum diameter = 1 mm)
4H-6, 68–69	1	Dark gray (N3); medium sand
4H-6, 86–87	1	Dark gray (N3); silt
4H-6, 107–108	1	Dark gray (N3); silt
4H-6, 126–128	2	Dark gray (N3); silt
4H-6, 146–150	4	Dark gray (N3); silt
4H-7, 12–13	1	Light olive gray (5Y6/1) (reddish), silt
4H-CC 12–17	5	Dark gray (N3); silt
5H-1, +0–3	+3	Light olive gray (5Y6/1); silt
5H-1, 18–20	2	Olive gray (5Y4/1); silt
5H-1, 38–43	4/<1	Light olive gray (5Y6/1)/olive gray (5Y4/1); silt/very fine sand (5 mm thick)
5H-1, 69–72	3	Black (5Y2/1)/light olive gray (5Y4/1); silt/medium sand with pumice (5 mm thick)
5H-1, 118–119	1	Very dark gray (5Y3/1); very fine sand
5H-1, 140–142	2	Olive gray (5Y4/1); silt/very fine sand (5 mm thick)
5H-2, 20–22	2	Olive gray (5Y4/1); pumice; very coarse sand
5H-2, 31–33	2	Olive gray (5Y4/1); silt
5H-2, 40–44	4	Light olive gray (5Y6/1); silt
5H-2, 51–55	4	Very dark gray (5Y3/1); medium sand with scoria (maximum diameter = 1 cm)
5H-2, 65–68	3	Olive gray (5Y4/1); silt
5H-2, 80–89	4/5	Olive gray (5Y4/1); silt/pumice; fine sand (maximum diameter = 3 mm)
5H-2, 129–130	1	Olive gray (5Y4/2); silt
5H-2, 140–143	3	Grayish black (N2); silt
5H-3, 8–19	10/1	Olive gray (5Y4/1); silt/very fine sand
5H-3, 30	<1	Black; silt (5 mm thick, dispersed)
5H-3, 54–61	3/1/3	Light olive gray (5Y6/1)/olive gray (5Y4/1)/light olive gray (5Y6/1); silt/fine silt with a 5-mm-thick very fine sand basal part

Table 3 (continued).

Core, section, interval (cm)	Thickness (cm)	Description and remarks
126-792A- (Cont.)		
5H-3, 75–76	1	Light olive gray (5Y6/1); fine tuff
5H-3, 103–108	5	Black, fine tuff (dispersed)
5H-3, 114–150 5H-4, 0–54	11/79	Light gray (5Y4/1)/light (5Y4/1); silt/clayey silt
6H-1, 14–70	56	Olive gray (5Y4/1); pumiceous pebbly sand
6H-1, 96	<1	Black; silt (dispersed)
6H-1, 124–125	1	Grayish black (N2); silt
6H-2, 8–26	7/6/5	Light olive gray (5Y6/1)/light gray (N7)/olive gray (5Y4/1); silt/silt/pumiceous very fine sand
6H-2, 27–28	1	Olive gray (5Y4/2); very fine sand
6H-2, 38–45	5/2	Light olive gray (5Y6/1)/dark olive gray (5Y3/2); silt/medium sand
6H-2, 92–101	6/3	Olive gray (5Y4/1); silt/very fine sand (laminated)
6H-3, 4–10	6	Light olive gray (5Y6/1); silt
6H-3, 34–36	10/2	Grayish black (N2); fine sand/very fine sand (laminated)
6H-3, 58–68	10	Brownish black (5YR2/1); silt with scoria scatterd basal part (maximum diameter = 5 mm)
6H-3, 114–136	5/17	Dark olive gray (5Y3/2); grayish black (N2) silt/silt-fine sand (grading)
6H-4, 3–10	1/6	Olive gray (5YR4/1)/olive gray (5Y4/2); silt/clayey silt
6H-4, 21–24	3	Light olive gray (5Y6/1); silt pocket
6H-4, 34–85	4/47	Dark olive gray (5Y3/2); grayish black (N2); silt/medium fine sand
6H-4, 93–104	10/1	Light olive gray (5Y6/1)/olive gray (5Y4/1); silt/very fine sand
6H-4, 114–120	6	Light olive gray (5Y6/1); silt
6H-4, 140–150 6H-5, 0–7	17	Dark olive gray (5Y3/2)/olive black (5Y2/1); clayey silt silt
6H-5, 14–135	113/5/17+	Grayish black (N2); fine sand with pumice/medium coarse sand/silt
6H-CC, 0–14+	14	Medium sand
7H-1, +0–1	+1	Olive black (5Y2/1); very fine sand
7H-1, 12–13	1	Olive gray (5Y4/1); very fine sand
7H-1, 21–29	8	Light olive gray (5Y6/1); silt
7H-1, 40–57	3/6/3/5	Greenish gray (5GY6/1)/olive black (5Y2/1)/light olive gray (5Y6/1)/olive gray (5Y4/1); silt/very fine sand/silt/sandy silt
7H-1, 103–131	28	Grayish black (N2); alternation of fine sand and very fine sand
7H-2, 19–21	2	Light olive gray (5Y6/1); silt pocket
7H-2, 41–52	11	Light olive gray (5Y6/1); silt
7H-2, 112–114	2	Grayish black (N2); very fine sand pocket
7H-2, 119–121	2	Grayish black (N2); very fine sand
7H-3, 12–14	2	Brownish black (5YR2/1); very fine sand
7H-3, 27–32	5	Olive gray (5YR4/1); very fine sand
7H-3, 38–39	1	Light olive gray (5Y6/1); silt
7H-3, 46–48	2	Grayish black (N2); scoria sand pocket
7H-3, 57–67	3/5/2	Dark reddish brown (5YR2/1)/dark reddish brown (5YR2/1); very fine sand/sandy mud with scattered pumice (maximum diameter = 5 mm)/very fine sand
7H-3, 81–86	3/2	Dark reddish brown (5YR2/1)/grayish black (N2); silt/fine sand (laminated)
7H-3, 98–114 7H-4, 0–56	72	Light olive gray (5Y6/1); silt
7H-4, 87–92	1/1/3	Brownish black (5YR2/1); silt/fine sand (pumice and foraminifers included)/very fine sand with thin (2 mm) scoria base
7H-4, 101–106	3/2	Brownish black (5YR2/1)/grayish black (N2); silt/very fine sand
7H-4, 143–145	6/146/30+	Dark reddish brown (5YR3/2)/grayish black (N2); clayey
7H-5, 0–150 7H-6, 0–16 7H-CC, 0–14+		Silt/fine sand with gravel (maximum diameter = 10 mm)/scoria pebble
8H-1, +0–6	+6	Grayish black (N2); scoria; medium sand
8H-1, 33–42	9	Grayish black (N2); very fine sand
8H-1, 48–55	7	Grayish black (N2); scoria; coarse sand
8H-1, 75–77	2	Grayish black (N2); medium sand
8H-1, 85–86	1	Grayish black (N2); medium sand
8H-1, 131–137	6/47	Dark olive gray (5Y3/2)/olive black (5Y2/1); clayey silt
8H-2, 0–47		Very fine sand (medium sand pumice included)
8H-2, 66–83	2/12/3	Dark reddish brown (5YR2/1)/olive black (5Y2/1)/grayish black (N2); silt/very fine sand/sandy silt
8H-2, 93–135	4/38	Brownish black (5YR2/1)/olive black (5Y2/1); silt/fine-medium sand (graded) (pumice and foraminifers included)
8H-2, 135–148	13	Scoria pebble (maximum diameter = 7 mm) scattered in dark olive gray sandy mud)
8H-2, 148–150	2	Grayish black (N2); medium sand
8H-3, 10–12	2	Pumice; granule
8H-3, 19–21	2	Pumice; granule
8H-3, 25	<1	Pumice; granule, seam
8H-3, 30	<1	Pumice; granule, seam

Table 3 (continued).

Core, section, interval (cm)	Thickness (cm)	Description and remarks
126-792A- (Cont.)		
8H-3, 39–43	9/11+	Light olive gray (5Y6/1)/olive black (5Y2/1); sandy silt
8H-CC, 0–16+		medium sand
9H-1, +0–50	+50	Olive black (5Y2/1); scoria; pebble-granule gravel
9H-1, 60	<1	Medium sand (pumice) seam
9H-1, 60–78	18	Olive gray (5Y4/2); silt
9H-2, 29–65	36	Olive black (5Y2/1); fine sand-very fine sand (graded)
9H-2, 84–99	15	Olive black (5Y2/1); very fine sand
9H-2, 113–150	3/37	Olive black (5Y2/1); silt
9H-3, 0–3		Olive black (5Y2/1); medium sand (laminated)
9H-3, 37–54	17	Light olive gray (5Y6/1); silt
9H-3, 54–87	93	Olive gray (5Y4/1); very fine sand
9H-4, 4–64		
9H-CC, 7	1	Light olive gray (5Y6/1); silt pocket
10H-1, +0–7	+7	Grayish black (N2); scoria granule
10H-1, 16–18	2	Grayish black (N2); scoria granule
10H-1, 36–100	64	Olive gray (5Y4/1); pumiceous granule-coarse sand (pumice pebble concentrated at 65–68, 72–73, and 85–87 cm)
10H-1, 132–148	16	Olive gray (5Y5/2); pumiceous medium sand (laminated)
10H-2, 6–8	2	Olive gray (5Y4/1); silt
10H-2, 29–31	2/4	Grayish black (N2); scoria medium sand/scoria granule
10H-3, 4–8		
10H-3, 18–34	12/4	Light olive gray (5Y6/1); silt/fine sand
10H-3, 39–44	5	Light olive gray (5Y6/1); silt
10H-3, 78	<1	Medium dark gray (N4); very fine sand
10H-3, 93	<1	Medium gray (N5); silty clay
10H-3, 95	<1	Grayish black (N2); silt
10H-3, 118–124	6	Olive black (5YR2/1); scoria granules
10H-3, 129–132	3	Olive black (5YR2/1); fine sand
10H-3, 144–145	1	Medium dark gray (N4); silt
10H-4, 0–5	5	Grayish black (N2); very fine sand
10H-4, 24–84	16/44	Olive gray (5Y4/2)/olive black (5Y2/1); pumiceous medium sand/pumiceous medium sand (scoria concentrated)
10H-4, 101–150	109+	Olive black (5Y2/1); pumiceous medium sand (pumice maximum diameter = 6 mm, laminated in the upper part)
10H-5, 0–40		
10H-CC, 0–20+		

Unit III is defined by a change in lithologic character from finer grained rocks with high calcium carbonate contents to interbedded coarser vitric sandstone, clayey siltstone (generally with 0%–20% calcium carbonate), and sandy conglomerate. This contact was not recovered and is placed just below Core 126-792E-31R (see "Downhole Measurements" section, this chapter).

The high calcium carbonate contents (15%–60%) of Unit III rocks are mainly attributed to calcareous nannofossils. The principal sediment types are nannofossil-rich claystone (42%), nannofossil claystone (22%), and nannofossil chalk (14%); the minor sediment types include claystone (10%), vitric sandstone (7%), vitric siltstone (5%), and breccia (1%). Calcium carbonate contents are reflected in the color of the rocks: nannofossil chalk is white (5Y 8/1) to light gray (5Y 7/1); nannofossil clay is yellowish gray (5Y 7/2); and nannofossil-rich claystone is dark gray (5Y 4/1). The nonbiogenic component is primarily clay, with low contents of volcanic glass compared with those of fine-grained sediments in other units. Bioturbation is intense. The minor sediment types that make up the remaining 22% of the core are very thin to thin beds of olive black (5Y 2/1), greenish black (5G 2/1), and brownish black (5YR 2/1) vitric clayey siltstone, very fine-grained vitric sandstone, and vitric siltstone. Constituent grains include brown to opaque glass and feldspars. These minor sediment types rarely show planar lamination.

Dewatering veinlets occur in Unit III (Fig. 12) in Cores 126-792E-26R, -30R, and -31R, and some intervals of nannofossil chalk and nannofossil clay are highly fractured into subvertical wavy fragments along the veinlet surfaces. A fault zone in the lower part of Section 126-792E-29R-1 consists of a 30-cm-thick fault gouge characterized by highly fractured, grayish green (5GY 5/1) claystone with slickensides and lens-shaped pieces of greenish black (5GY 2/1), very fine-grained sandstone. This fault zone is clearly identified in downhole logs (see "Downhole Measurements" section, this chapter).

Unit IV

Interval: Cores 126-792E-32R through Section 126-792E-68R-2 at 100 cm
Age: late to early Oligocene
Depth: 429.3–783.4 mbsf

The lower boundary of Unit IV is a fault between sandstone and the highly altered volcanic conglomerate and sandstone of Unit V. Unit IV is composed mainly of vitric sandstone (58%) and a sandy pebble-granule conglomerate (10%). The rest of the unit is silty claystone (9%), nannofossil-rich silty claystone (6%), nannofossil-rich claystone (5%), claystone (4%), and intermediate sediment types (siltstone, 4%; nannofossil claystone, clayey siltstone, sandy mudstone, and sandy siltstone, all 1% each).

In the upper part of this unit (Cores 126-792E-32R through -40R), graded beds of vitric sandstone and vitric siltstone are interbedded with muddy intervals (Fig. 13). Parallel- and ripple-laminated beds of siltstone and very fine- to fine-grained sandstone, from one to several centimeters in thickness, predominate in Cores 126-792E-34R, -36R, -37R, and -38R. Massive sandstones beds, 60–280 cm thick, occur in Cores 126-792E-32R, -33R, -38R, and -39R.

The conglomerate is confined to the middle and lower parts of the unit; it is absent in Cores 126-792E-52R through -59R (Fig. 5). The upper conglomerates contain clasts of andesite to dacite and pumice fragments (Fig. 14). Claystone intraclasts that
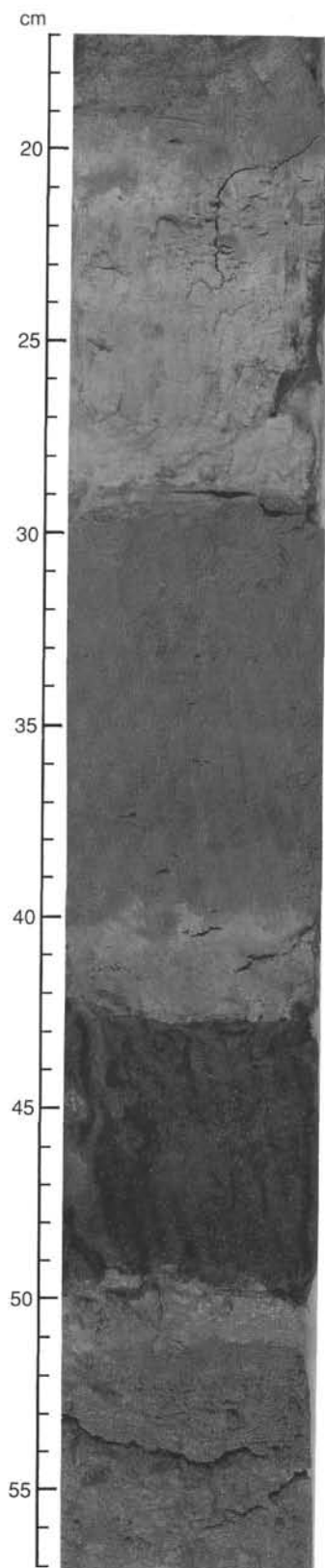
Figure 6. Interbedded light and dark colored ash, composed of vitric sand and silt and nannofossil-rich vitric clayey silt, in Unit I (Interval 126-792A-7H-1, 17–57 cm). The color of the ash layers varies from gray (5Y 6/1) in the 21–29 cm and 40–43 cm intervals, to brownish black (5YR 2/1) at 43–49 cm.
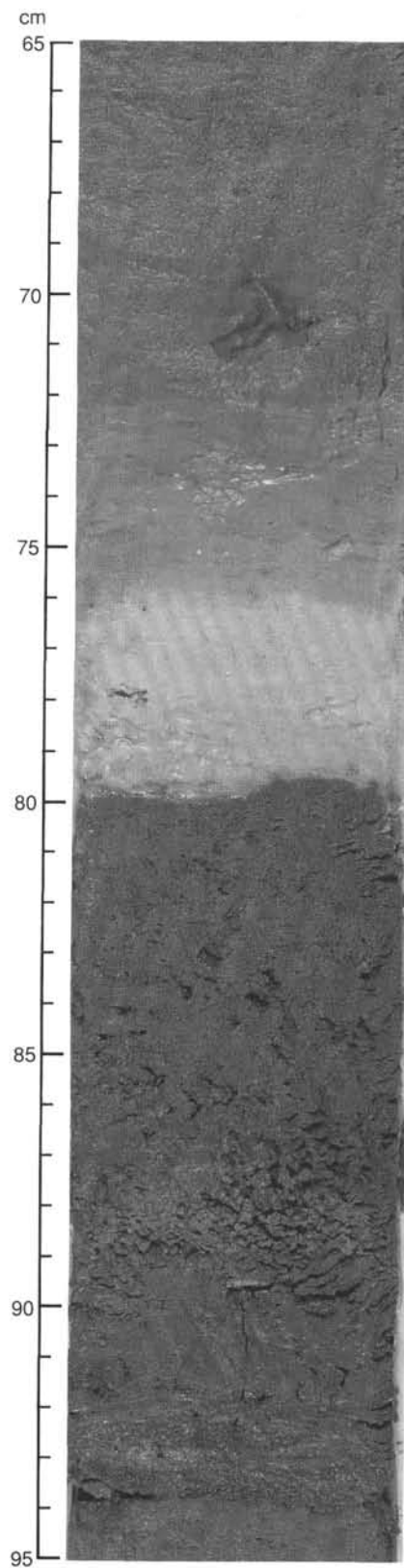
Figure 7. Interbedded light and dark ash layers of Unit I (Interval 126-792B-10X-1, 65–95 cm). The 72–75 and 75–79 cm intervals are adjacent light olive gray (5Y 6/2) and light gray (5Y 7/1) vitric silt; 79–84 cm is the host lithology (nannofossil-rich vitric silty mud); 84–89 is olive gray (5Y 4/2) pumiceous granule gravel; 89–93 cm is very dark gray (5Y 3/1) vitric silt, laminated in the basal 1 cm.
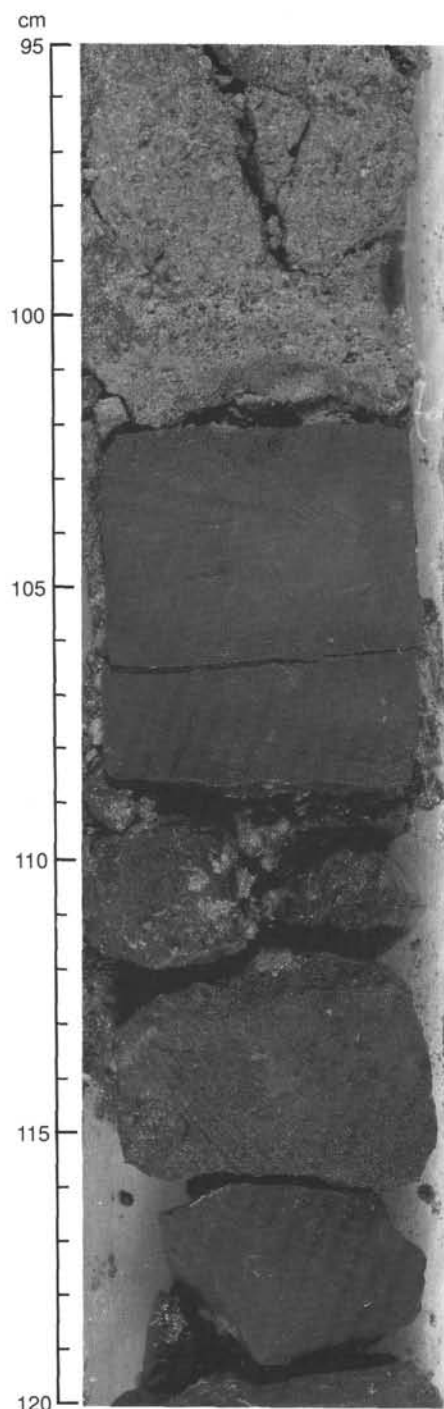
Figure 8. Lithified, poorly-sorted sandy mudstone containing granules 3 mm in diameter at the top of Unit II (Interval 126-792E-6R-1, 95–120 cm).

exceed the diameter of the core (maximum dimension about 8 cm) are present locally (Figs. 15 and 16). Intraclast sediment types resemble those of underlying units. Conglomerates below Core 126-792E-59R are greenish black (5GY 2/1, 5G 2/1) and also contain large claystone, siltstone, and sandstone intraclasts that exceed 7 cm in diameter. This lower conglomerate interval is mainly composed of thick sandstone and conglomerate beds, generally from tens of centimeters to 100 cm thick, with a maximum bed thickness of about 300 cm. In some cases, conglomer-
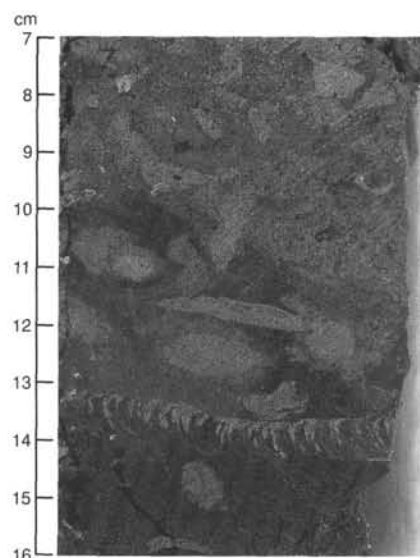
Figure 9. Intensely bioturbated nannofossil-rich vitric silty claystone in Unit II (Interval 126-792E-21R-2, 7–16 cm). The horizontal feature at 13 cm is a *Zoophycos* burrow.

ate grades upward into sandstone (Fig. 17). The grain size of the sandstone beds varies from very coarse to very fine. The thicker sandstone beds are generally massive, except for normal grading; they rarely have laminated tops. Thin- to medium-thickness beds are graded and contain a variety of sedimentary structures, including planar and cross lamination, flute casts, and flame structures (Figs. 18 and 19). Reddish brown epiclastic volcanic lithic grains occur in the thick, medium- to coarse-grained sandstones of the lower part of this unit.

Sandstones and siltstones in this unit are dominated by either felsic or mafic glass. Mixed felsic and mafic intervals are not common, and crystal contents are variable but generally low. Diagenetic products within these beds include fibroradiating zeolite cements, incipient clay-rim cements, and glass hydration rims.

The fine-grained sediments are strongly bioturbated (Fig. 20). Trace fossils include *Zoophycos* and *Chondrites*. Calcium carbonate contents are highly variable, ranging from <5% to 40%. A concentration of plant debris is present in burrowed siltstone in Section 126-792E-52R-5 (Fig. 21).

Unit IV shows moderate tectonic disturbance. Microfaults that are present in Cores 126-792E-45R, -50R, -59R and -67R rarely have slickensides, although horizontal microfaults in Section 126-792E-59R-5 show slickensides. Mineral-filled fractures (calcite and zeolite) are present in Cores 126-792E-37R through -40R, and Core 126-792E-66R, fractures in Core 126-792E-54R, subvertical fractures in Cores 126-792E-60R and -65R, and sandstone dikes (Fig. 22) in Cores 126-792E-32R, -35R, -39R, -41R, and -62R. The lowest conglomerate bed in Unit IV (Core 126-792E-67R) shows a variety of colors that are attributed to alteration (Figs. 23 and 24).

Unit V

Interval: Sections 126-792E-68R-2 at 100 cm through -70R-CC
Age: unknown
Depth: 783.4–804 mbsf

The top of Unit V is a fault. The lower contact separates the altered volcanic conglomerate of this unit from the underlying andesite lava of Unit VII (see "Igneous Petrology" section, this chapter). The lower contact occurs in Section 126-792E-70R-CC at 12 cm.
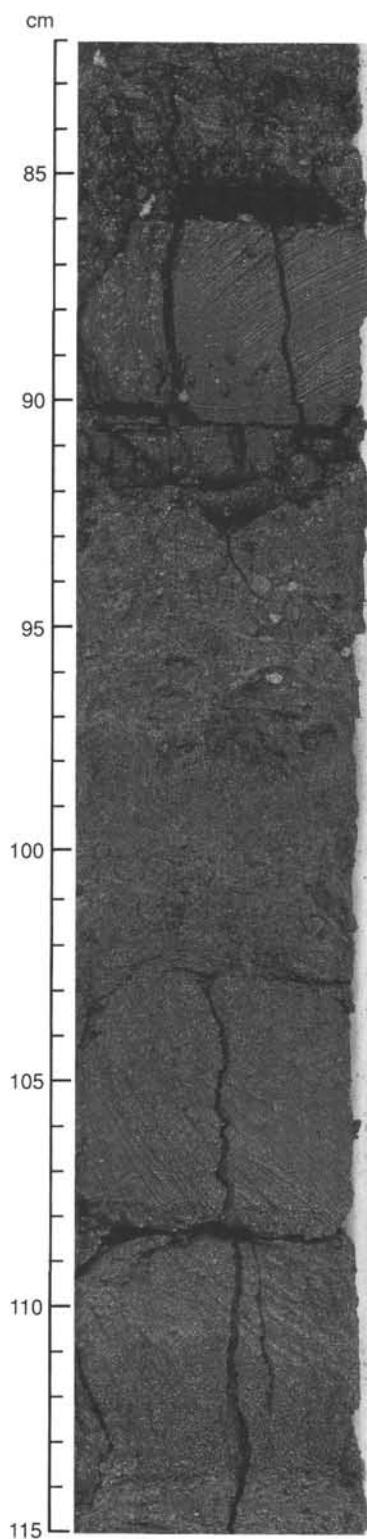
Figure 10. Dark ash beds in Unit II (Interval 126-792E-10R-2, 82–115 cm). The interval from 83–85 cm is a grayish black (N2) layer of angular to subangular, 2–4 mm granules; 85–91 cm and 102–108 cm are greenish black (5GY 2/1), laminated vitric silty claystone; 91–102 cm and 108–110 cm are intercalations of slightly bioturbated sandy siltstone.
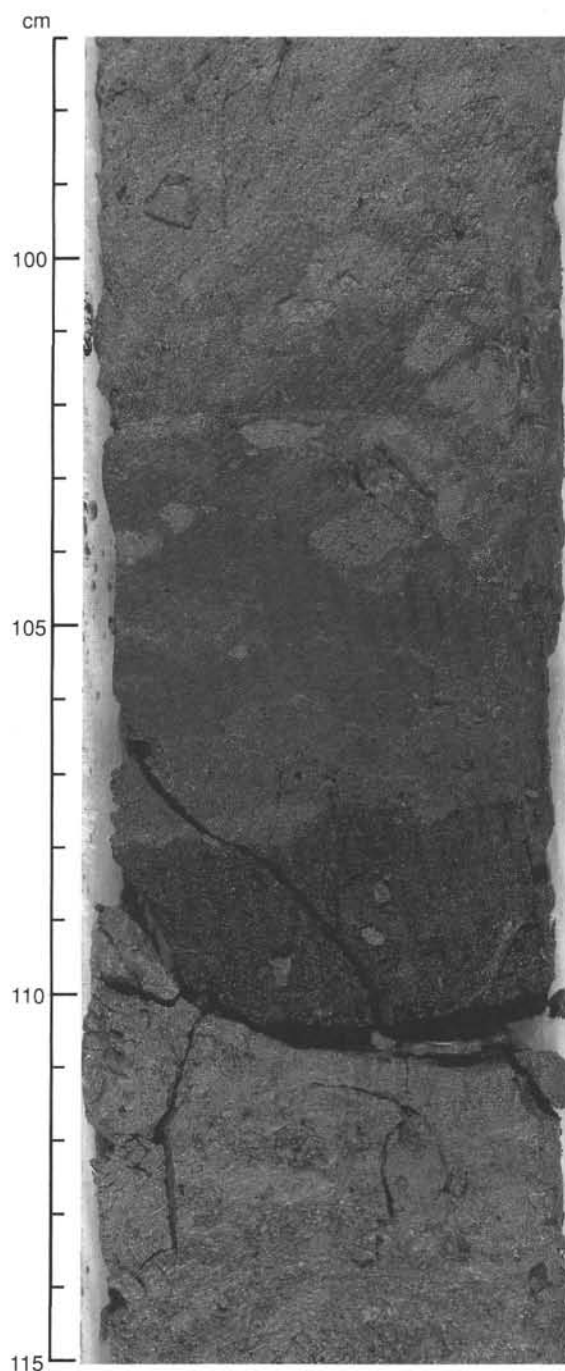

Figure 11. Grayish black (N2) ash bed of normally graded vitric sandstone to siltstone (105–111 cm), in nannofossil-rich sandy mudstone of Unit II (Interval 126-792E-18R-2, 97-115 cm).

Unit V is composed of very dark green (7.5GY 3/2) and dark grayish blue (5BG 5/1), altered volcanic pebble-granule conglomerate and sandstone. We could not determine grain sizes either visually or under the binocular microscope because of severe alteration. Greenish black (5G 2.5/1), silicified claystone and siltstone (probably clasts in the altered sandstone) and a brecciated mixture of altered volcaniclastic rock and claystone in the lower part of this unit suggest that the protolith of this material was a sedimentary rock of similar lithology to the sandstone and conglomerate in the lower part of Unit IV. Petro-
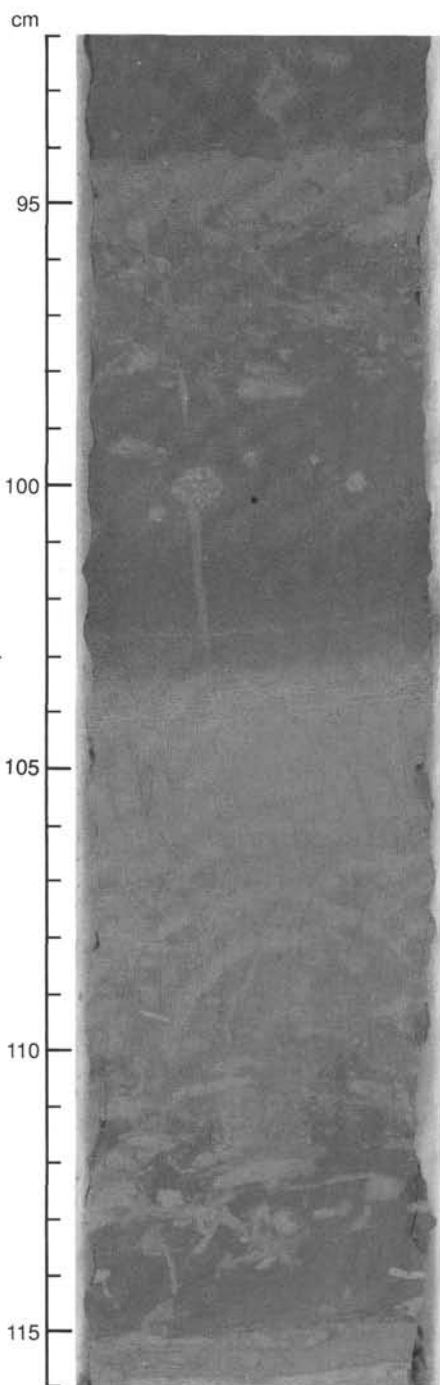
Figure 12. Intensely bioturbated nannofossil-rich claystone, medium dark gray (N4) vitric siltstone and sandstone, and grayish green (5GY 6/1) claystone of Unit III (Interval 126-792E-31R-1, 92–116 cm). Note wavy, subvertical dewatering structures (103–110 cm).

graphic examination of the unit shows it to be composed of highly altered pumiceous material, including pressure-flattened sand-size grains that are commonly wrapped around more competent crystal fragments. A pebble of highly altered andesite with a peculiar reddish color, and lumps of black manganese oxides are present within the fault that separates this unit from Unit IV (Fig. 25).
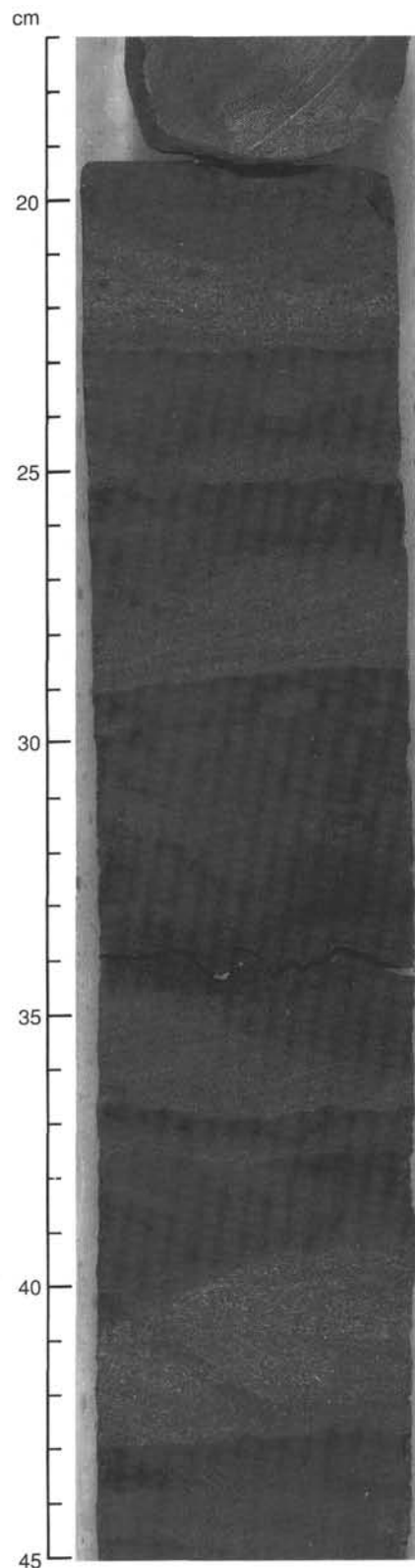
Figure 13. An interval consisting of five graded beds of very-fine-grained sandstone with parallel or cross lamination; Unit IV (Interval 126-792E-38R-1, 17–45 cm). Only the tops of these units are burrowed.
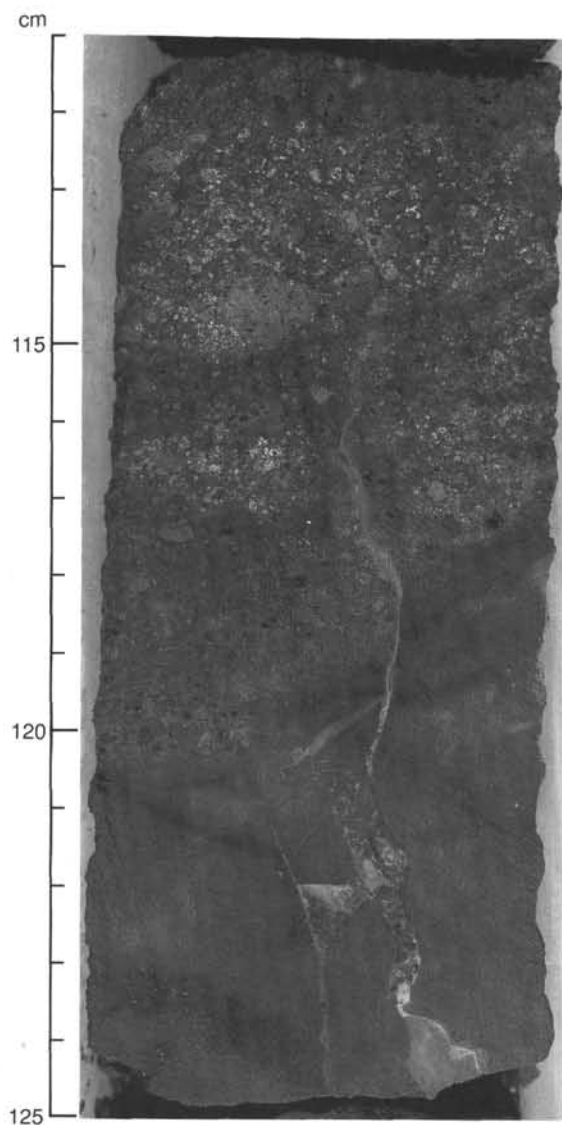
Figure 14. Pumiceous conglomerate and underlying very fine sandstone of Unit IV (Interval 126-792E-40R-2, 111–125 cm). Note the healed subvertical fracture at 114–124 cm.

Unit VI

Interval: Section 126-792E-70R-CC through -78R
Age: unknown
Depth: 804–885.9 mbsf

This unit consists of plagioclase-(± quartz)-orthopyroxene-clinopyroxene andesite lava, hyaloclastite, and breccia, with minor basaltic andesite and dacite (see "Igneous Petrology" section, this chapter).

X-Ray Diffraction Analysis

The results of XRD analyses of 44 samples from Site 792 are summarized in Table 4 and Figure 26, which present semiquantitative measurements derived from the characteristic main peaks of clay and other minerals. The quantities of calcite, reflecting the amount of microfossils in nannofossil-rich vitric silty clay, claystone, or chalk, increase irregularly with depth to 600 mbsf. The XRD calcite data are much the same as calcium carbonate values obtained from chemical analysis and display the same trends. Calcite is rare below 600 mbsf. Quartz is ubiquitous, but
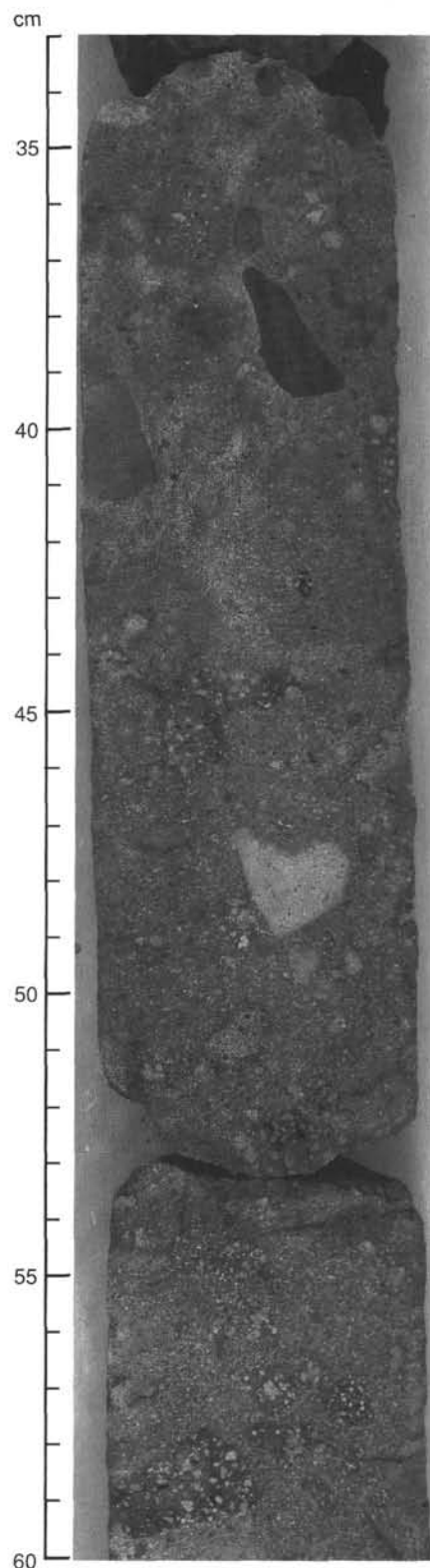

Figure 15. Matrix-supported polymictic conglomerate of Unit IV (Interval 126-792E-46R-7, 33–60 cm), with black (N1) intrabasinal clasts of claystone at 33–41 cm.
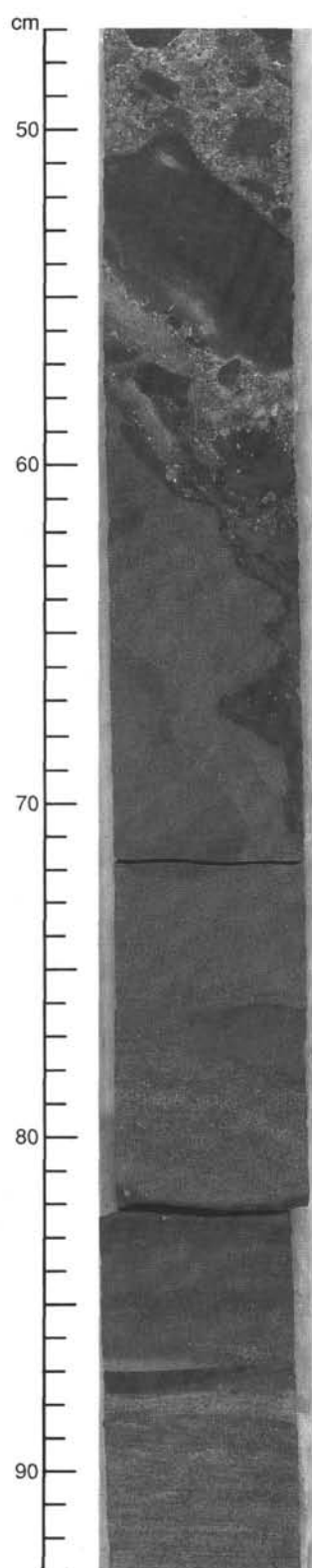
Figure 16. A sequence in Unit IV consisting of (1) the lower portion of a debris-flow deposit that has its base at 58–71 cm; (2) a plastically deformed, fine-grained sandstone (58–78 cm); (3) a medium-grained sandstone (78–82 cm); and (4) the fine-grained top and laminated portion of a graded turbidite (78–93 cm) in Unit IV (Interval 126-792E-48R-1, 47–93 cm).
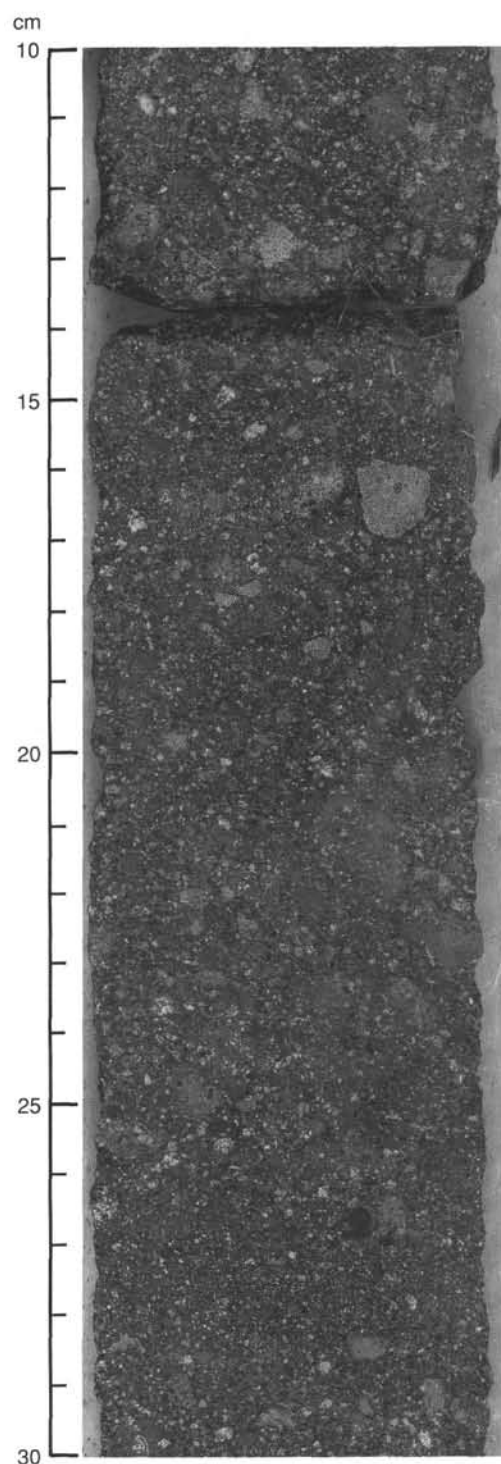

Figure 17. Volcanic granular and pebbly coarse sandstone of Unit IV (Interval 126-792E-43R-1, 10–30 cm). This is the upper part of an interval that has conglomerate at its base.

it is especially abundant in Units I and II and decreases with depth from Unit III to Unit IV. Chlorite is very rare at Site 792.

The quantity of amorphous materials, principally volcanic glass (estimated from the broad enhancement at 0.33 nm), decreases with depth, accompanied by increases in the clay mineral and zeolite contents.
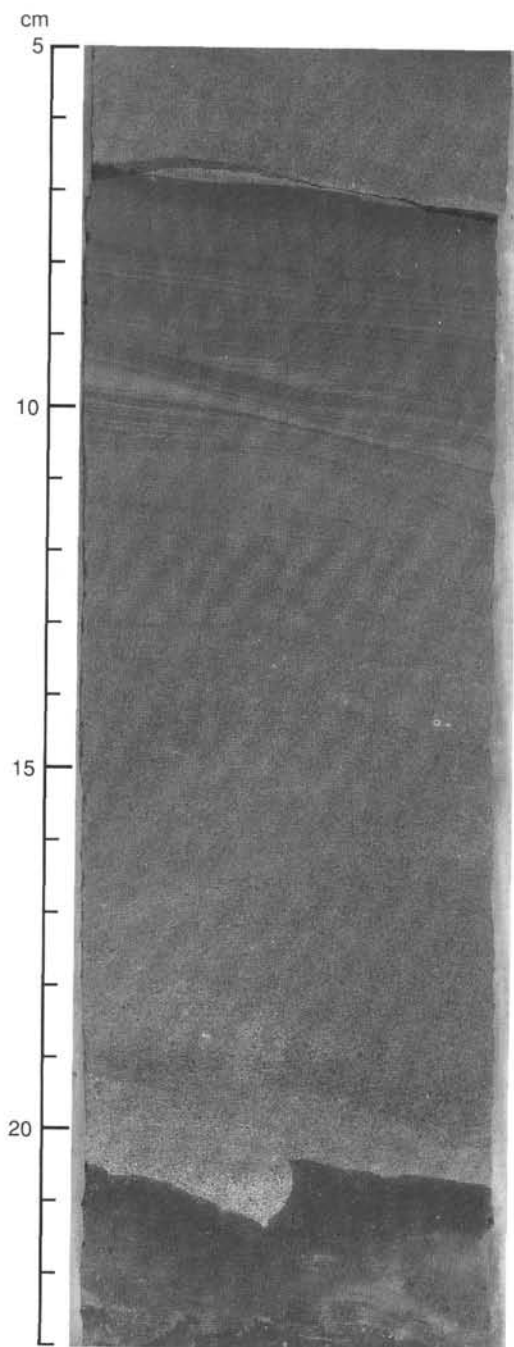
Figure 18. Turbidite bed of medium to fine-grained sandstone in Unit IV (Interval 126-792E-48R-4, 5–23 cm). The top of the turbidite (7–11 cm) is cross laminated. The bed rests with a load cast on burrowed claystone.
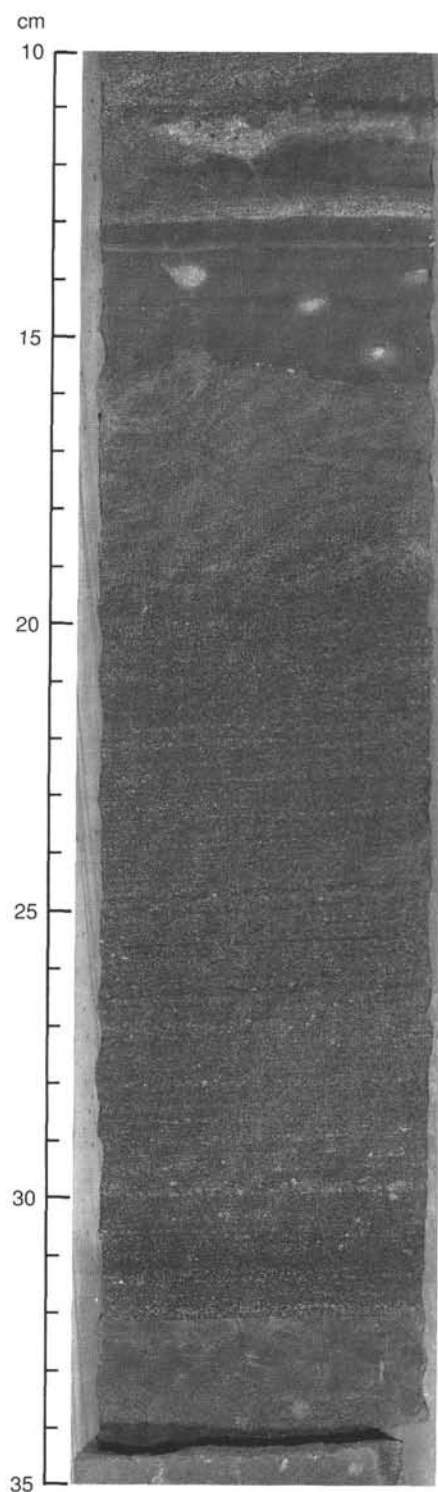

Figure 19. Laminated medium- to fine-grained sandstone turbidite (cross laminated at the top), grading into clayey siltstone, Unit IV (Interval 126-792E-56R-4, 10–35 cm).

Smectite is present in varying amounts in all the samples and increases in abundance below 350 mbsf. The glass in Units II through IV is green to brown in color and is commonly altered to smectite and palagonite. Glauconite or palagonite is present in a green, fine-grained sandstone at 270 mbsf (Section 126-792E-15R-1 at 21 cm), at a sharply defined hiatus in Unit II.

Zeolites are absent in Units I and II, but they are present in Units III–V (below 350 mbsf). The phillipsite, analcime, wairakite, heulandite-clinoptilolite, and stilbite species of the zeolite group, characterizing the earliest stages of the zeolite facies, intermediate between diagenesis and metamorphism (Coombs et al., 1959), were classified according to their characteristic peaks.

Below 400 mbsf, the zeolite minerals change downhole from phillipsite and analcime to wairakite, accompanying the increase in smectite. Heulandite-clinoptilolite and stilbite replace analcime, phillipsite, and wairakite below 670 mbsf.

In Units IV and V, minor mineral components such as gypsum, diaspore, and cristobalite are present, and numerous white to green-colored veins in Unit IV are filled with zeolite and gyp-
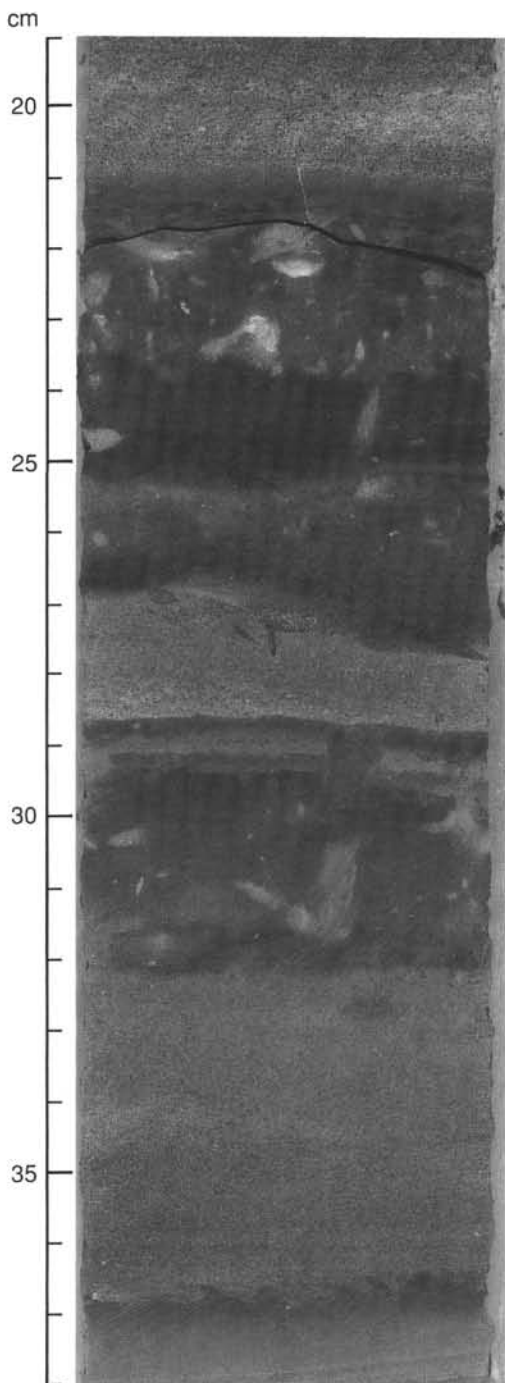
Figure 20. Bioturbated silty claystone overlying fine sandstone; Unit IV (Interval 126-792E-48R-3, 19–38 cm).

sum. A granule conglomerate layer in the middle portion of Unit IV (Section 126-792E-51R-4 at 21 cm) contains a pale reddish volcanic clast. Abundant smectite and diaspore in this clast suggests high-temperature (260°–290°C) alteration.

Sediment Accumulation Rates

We established sedimentation rates for Site 792 by using calcareous nannofossil datums and paleomagnetic reversal data (Tables 5 and 6) to construct the age-depth curves shown in Figures 27–29. The sedimentary section at Site 792 is marked by four lacunae: 1–2.2 Ma, 3.5–6 Ma, 8–9 Ma, and 13–19 Ma. The second and fourth lacunae correspond to the basal boundaries of the first two lithologic units.

Sedimentation rates in the late Oligocene (29–28 Ma) are 300 m/m.y, but they decrease almost an order of magnitude to 40 m/m.y. during the interval from 28 to 27 Ma. This sharp break
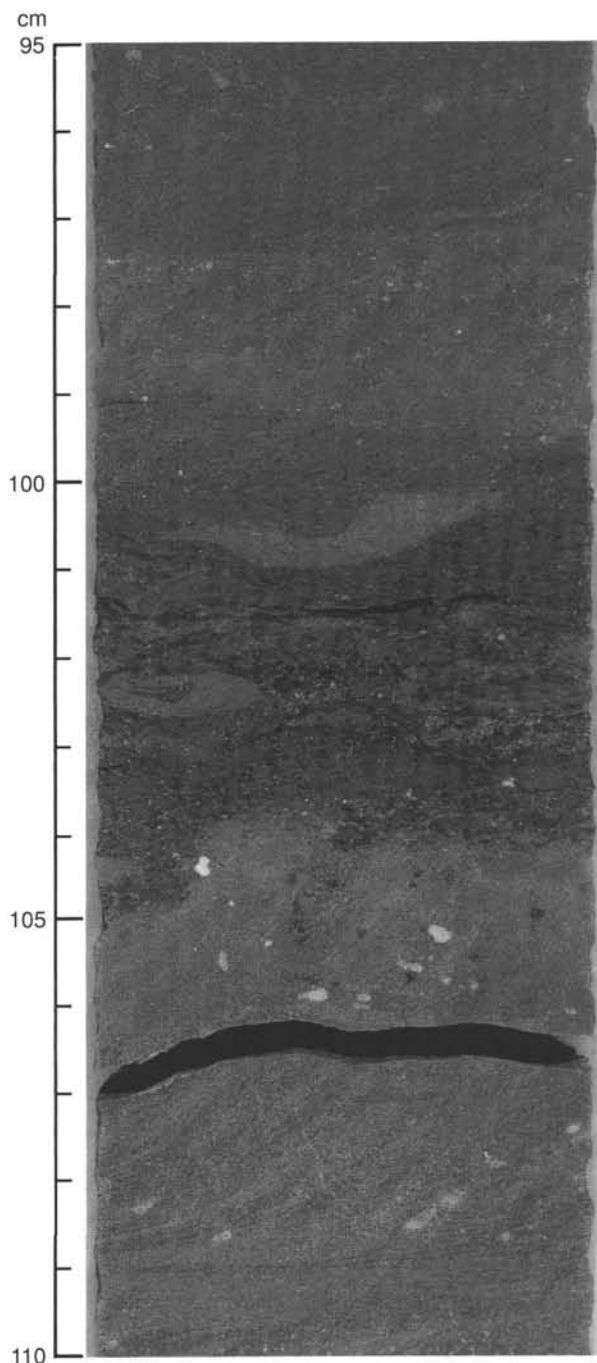
Figure 21. Concentration of carbonaceous plant debris (101–105 cm) in burrowed claystone of Unit IV (Interval 126-792E-52R-5, 95–110 cm).

occurs toward the top of Unit IV. In Unit III, sedimentation rates below and above a short normal fault that cuts out strata deposited 23–24 Ma are 4 m/m.y. and 14 m/m.y., respectively. Sedimentation rates for the Miocene section (23.7–5.0 Ma) range from 14 m/m.y. for the lower Miocene (Unit III) to values of 23 to 43 m/m.y. for the upper Miocene (Unit II).

A large increase in the sedimentation rate is apparent in the Pliocene and Quaternary sedimentary sections (Unit I). Following the early Pliocene lacuna at 6–3.56 Ma, sedimentation rates

Figure 22. Subvertical sandstone dike, 5 mm wide, invading medium- to fine-grained sandstone of Unit IV (Interval 126-792E-32R-2, 29–48 cm).

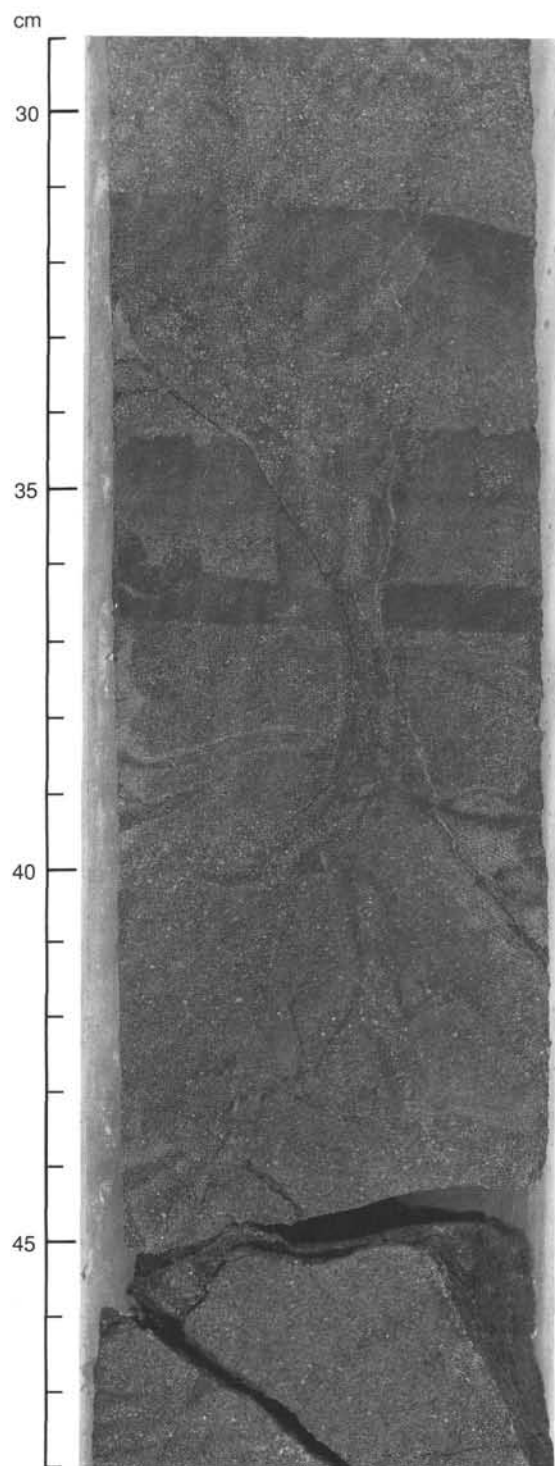increased from 40 m/m.y. to >120 m/m.y. for the late Pliocene. Similarly, sedimentation rates for the Quaternary remained high, ranging from 80 to 120 m/m.y.

Interpretation

Unit I

The nannofossil-rich clayey silt and nannofossil-rich silty clay of Unit I are interpreted as hemipelagic deposits that accu-
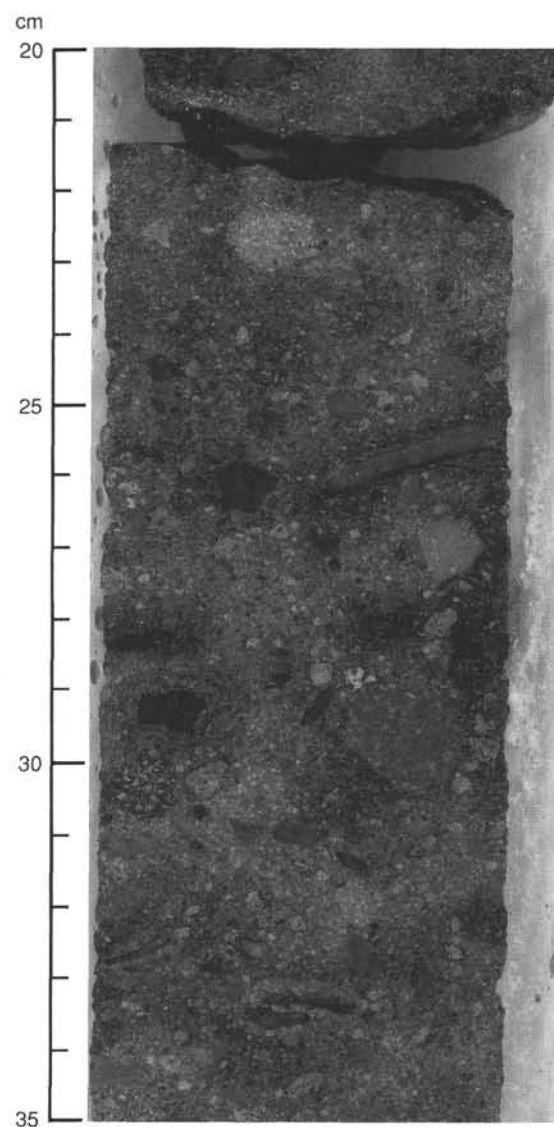

Figure 23. Polymictic, pebble conglomerate to fine-grained-sand conglomerate near the base of Unit IV (Interval 126-792E-67R-1, 20–35 cm). The mottled matrix is a result of variable hydrothermal alteration and cementation.

mulated in water depths of 1.5–3 km (see "Biostratigraphy" section, this chapter) east of the Izu-Bonin Arc. The >200 volcanic ash layers and the pumiceous and scoriaceous gravel that are interbedded with the fine-grained sediments were mostly derived from volcanoes of the Izu-Bonin Arc, either as primary airfall or, in some cases, as resedimented ash that was transported to the site by turbidity currents (Table 3). The abundance of volcanic ash layers indicates continuous explosive volcanic activity in the arc throughout the late Pliocene and Pleistocene. The wide range of grain size, bed thickness, and composition of the ash and associated volcanogenic turbidites suggest large variations of eruption styles and composition of magma for the Izu-Bonin volcanoes during this period. Some caution is required, however, because contrasts in grain size and bed thickness may also reflect multiple source volcanoes at different distances from the site.

Unit II

Muddy sandstones and sandy mudstones that characterize Unit II were probably produced by bioturbative mixing of hemi-
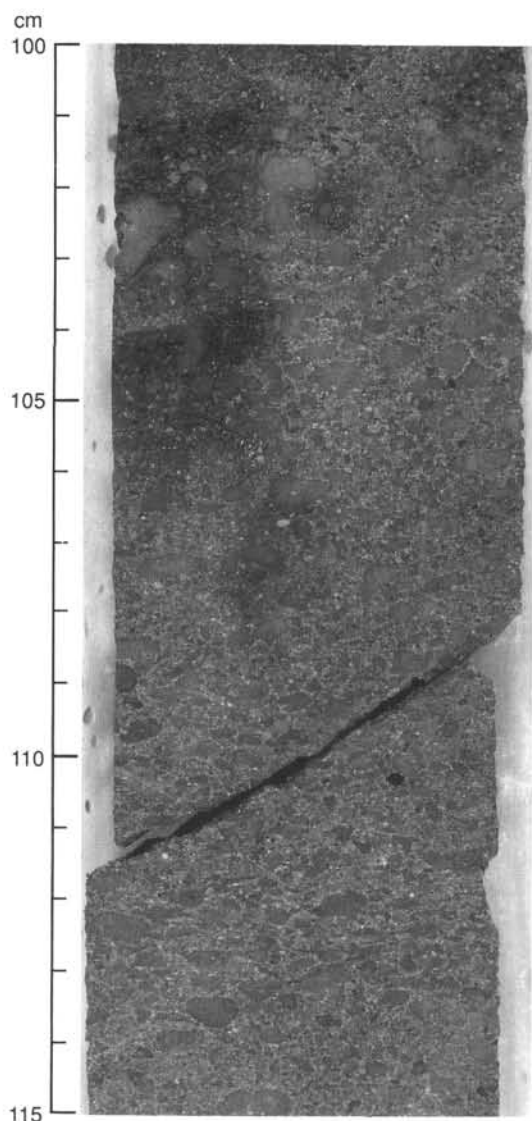
Figure 24. Polymictic granule conglomerate with a fine-grained sand matrix, near base of Unit IV (lower in the same section of Fig. 22; Interval 126-792E-67R-1, 100–115 cm). Pebbles are light red (10R 6/6), red (10R 4/6), very dusky red purple (5RP 2/2), light greenish gray (5G 8/1), greenish black (5G 2/1), medium light gray (N6), and gray (5YR 6/1); the more unusual shades are the result of hydrothermal alteration. Healed microshears displace and smear out some pebble horizons above and below the break at 108–111 cm, which is also a healed microshear fractured by drilling.

pelagic mud with thin beds of sand-size scoria grains and silt-size volcanic glass. This interpretation requires the coarser volcanic material to have been supplied at a slow rate, or as very thin beds, so that burrowers could rework and disperse the material into surrounding muds. The sedimentation rate of this unit suggests a large flux of volcanogenic material, even though instantaneous rates must have been slow.

Contrasts in ash abundance and composition from the base to the top of Unit II suggest temporal changes in volcanic supply to the site; ash is more scarce in the lower part of the unit, and lighter colored felsic ash is found only in the upper part of the unit.
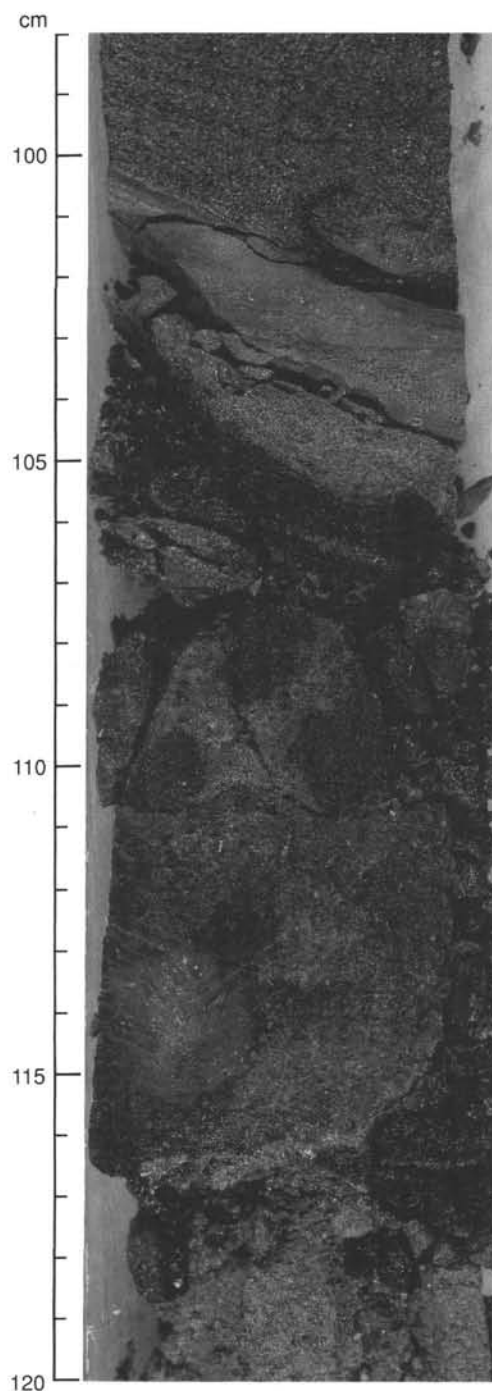
Figure 25. The fault-zone contact between Units V and IV (Interval 126-792E-68R-2, 98–120 cm). It includes a red (2.5YR 5/6) clast of altered andesite at 110 cm, and three black (N1) igneous clasts at 106–110 cm. The interval 110–116 cm is altered sandstone, mottled dark greenish gray (5G 4/1) and reddish yellow (7.5YR 6/6). Below the fault (116–120 cm) is vitric silty claystone and vitric sandy mudstone of Unit V, hydrothermally altered to mottled, very dark green (7.5 GY 3/2) and dark grayish blue (5BG 5/1) colors.

Table 4. Results of X-ray diffraction (XRD) analyses, Site 792.

Core, section, interval (cm)	Depth (mbsf)	Unit	Color	Texture	Clay minerals 1.4 nm	1.0 nm	0.7 nm	Minerals	Amorphous materials
126-792A-									
1H-1, 33	0.3	I	5GY 6/1	Vitric silt	Common	—	Present	Quartz, feldspar	Abundant
1H-3, 100	4	I	5Y 4/1	Nannofossil silty clay	Common	Present	Present	Calcite, quartz, feldspar	Abundant
1H-3, 140	4.4	I	N7	Sand, silt	Present	—	Trace	Quartz, feldspar	Abundant
1H-6, 145	9	I	10GY 5/2	Vitric silt	Trace	—	—	Quartz, feldspar	Abundant
2H-4, 100	15.2	I	N2	Sand	Trace	—	—	Calcite, quartz, feldspar	Abundant
3H-3, 100	23.1	I	5GY 4/1	Sand	Trace	—	—	Quartz, feldspar	Abundant
4H-3, 25	31.7	I	5Y 5/2	Nannofossil clayey silt	Trace	Trace	Present	Calcite, quartz, feldspar	Abundant
5H-3, 103	41.8	I	5Y 4/1	Vitric silt	Present	—	Present	Quartz, feldspar, cristobalite	Abundant
126-792B-									
1H-1, 47	0.5	I	10GY 5/2	Vitric silt	Common	Trace	Present	Calcite, quartz, feldspar	Common
3H-2, 112	62.2	I	N2	Sand	Common	—	—	Quartz, feldspar	Abundant
3H-3, 83	63.4	I	N8	Vitric silt	Trace	—	Trace	Calcite, quartz, feldspar	Abundant
3H-6, 40	67.5	I	5YR 4/1	Vitric sand	Trace	—	—	Calcite, quartz, feldspar	Abundant
8X-2, 74	110.1	I	N2	Foraminifer-rich vitric silt	Abundant	—	Common	Calcite, quartz, feldspar	Common
126-792D									
1X-CC, 10	136	I	5Y 3/2	Silty clay	Present	—	—	Feldspar	Abundant
126-792E									
14R-CC, 10	261	II	5GY 4/1	Silty sandstone	Trace	—	—	Calcite, quartz, feldspar	Common
15R-1, 21	270.7	II	5GY 2/1	Sandstone	Trace	—	—	Calcite, quartz, feldspar	Common
15R-2, 6	272.2	II	5GY 6/1	Silty sandstone	Trace	—	—	Calcite, quartz, feldspar, palagonite, glauconite	Common
16R-1, 7	280.3	II	5Y 4/1	Nannofossil sandstone	—	—	—	Calcite, quartz, feldspar, palagonite, glauconite	Common
17R-2, 14	291.5	II	5R 6/2	Pale red ash bed	—	—	—	Calcite, quartz, feldspar, palagonite, glauconite	Abundant
17R-4, 22	295.6	II	5Y 6/1	Vitric clayey silt	—	—	—	Quartz, feldspar	Common
17R-4, 29	295.7	II	5BG 3/2	Vitric clayey silt	Abundant	Trace	Trace	Feldspar, calcite, palagonite	Common
18R-2, 145	302.5	II	5YR 4/1	Tan ash	Present	—	—	Quartz, feldspar, glauconite	Common
19R-1, 123	310.2	II	5Y 2/1	Clayey siltstone	Present	—	Present	Quartz, feldspar, glauconite	Common
20R-3, 25	323.4	II	5Y 2/1	Vitric silty claystone	Present	—	Trace	Calcite, quartz, feldspar, glauconite	Common
21R-2, 16	330	II	N2	Vitric claystone	Present	—	—	Calcite, quartz, feldspar, glauconite	Common
29R-CC, 5	405.6	III	5GY 2/1	Vitric siltstone	Abundant	—	Present	Calcite, quartz, glauconite, zeolite	Common
32R-2, 130	437.4	IV	5GY 4/1	Silty claystone	Present	—	Present	Calcite, quartz, feldspar, palagonite, glauconite, zeolite	Common
32R-3, 75	438.4	IV	5G 3/2	Claystone	Abundant	Present	Present	Calcite, feldspar, palagonite, glauconite	Common
34R-1, 130	455.2	IV	5GY 4/1	Siltstone	Abundant	—	Present	Feldspar, palagonite, glauconite, zeolite	Present
35R-1, 78	464.3	IV	N3	Vein in sandstone	Abundant	—	Abundant	Calcite, feldspar, glauconite, zeolite	Present
35R-1, 77	464.3	IV	N3	Sandstone	Abundant	—	Present	Calcite, feldspar, glauconite, zeolite	Present
37R-7, 48	492.3	IV	5GY 6/1	Vein in sandstone	Present	—	Common	Calcite, feldspar, zeolite	Present
39R-2, 71	504.4	IV	N3	Vein in vitric sity claystone	Trace	—	—	Gypsum, zeolite	
39R-3, 103	506.2	IV	N2	Vein in sand	Trace	—	Present	Calcite, feldspar, zeolite	
45R-1, 137	561.4	IV	5GY 2/1	Vein in vitric sandstone	Trace	—	—	Gypsum	
46R-5, 97	576.7	IV	5GY 2/1	Pebbly sandstone	Abundant	—	Common	Feldspar, zeolite	
48R-4, 42	593.5	IV	N3	Very fine turbidites sand/shale	Abundant	—	—	Feldspar, palagonite, glauconite, celadonite	Common
49R-3, 91	601.7	IV	5G 5/2	Graded very fine sand to claystone	Abundant	—	—	Quartz, feldspar, palagonite, glauconite, celadonite	Common
51R-4, 21	621.8	IV	5G 6/2	Pale red rock	Abundant	—	—	Quartz, feldspar, palagonite, diaspore, celadonite	
56R-4, 110	671	IV	5G 5/2	Sandstone	Abundant	—	—	Feldspar, amphiboles, cristobalite, palagonite, zeolite	Present
56R-6, 110	674	IV	5G 5/2	Fine sandstone	Abundant	—	Trace	Feldspar, glauconite, zeolite	Present
58R-3, 126	689.1	IV	5GY 4/1	Silty claystone	Present	—	Trace	Zeolite	Present
69R-3, 102	794.6	V	5G 3/2	Altered sandstone	Abundant	—	Present	Feldspar, glauconite, cristobalite	Present
69R-3, 105	794.7	V	5G 5/1	Altered sandstone	Abundant	—	Present	Feldspar, glauconite, tridymite	Present

Unit III

The nannofossil chalk marks a period of slow deposition at 2–4 km water depth (see "Biostratigraphy" section, this chapter) without significant volcanic input; ash layers and terrigenous sandstone/siltstone beds are very rare. The lesser epiclastic input relative to that of the underlying Unit IV may be the result of tectonic subsidence of the source area and a significant rise in global sea level from the mid-Oligocene into the Miocene (Haq et al., 1988).

The FMS data (see "Downhole Measurements" section, this chapter) indicate that the bedding dip abruptly increases to 30° in the uppermost 1 m of Unit III, just below the bounding unconformity. This local steepening of bedding may be caused by slumping or may indicate rotation of bedding within a fault zone.

Unit IV

This unit consists mainly of sandstone, sandy conglomerate, and silty claystone. The range of bed thicknesses and grain sizes are like those found in the middle and outer parts of submarine fans, or in oversupplied basin plains (e.g., Ricci Lucchi and Valmori, 1980). Seismic data (see "Seismic Stratigraphy" section, this chapter), calibrated by the sedimentary deposits recov-

ered at Sites 787, 792, and 793, indicate that the upper Oligocene fill of the forearc basin is a rapidly deposited turbidite blanket that onlaps both the eastern and western margins of the basin. In such an oversupplied basin, individual morphological elements like submarine fans probably cannot be distinguished (Pickering, 1982).

Structural features in Unit IV include subvertical veinlets and numerous microfaults. Similar features occur in Unit III and in the Eocene and Oligocene sections at Sites 787 and 793 (see "Site 787" and "Site 793" chapters, this volume). The veinlets are identical to those described from the Middle America Trench slope by Ogawa and Miyata (1985) and from the Japan Trench by Arthur et al. (1980) and Lundberg and Leggett (1986), and are interpreted as extensional fracture cleavages formed in rapidly consolidating (wet) sediments. The microfaults in Units III and IV also formed in an extensional regime. An extensional stress field may have also facilitated injection of the clastic dikes that are common in this unit.

The conglomerate beds of Unit IV represent a spectrum of deposits, from those in which grading is absent and bed tops are sharp, to those that are normally graded. Beds of both types contain outsized, floating intraclasts as large as 7 cm in diameter. Some beds also contain scattered large pebbles of andesite, dacite, and porphyritic rocks from the Izu-Bonin Arc. The
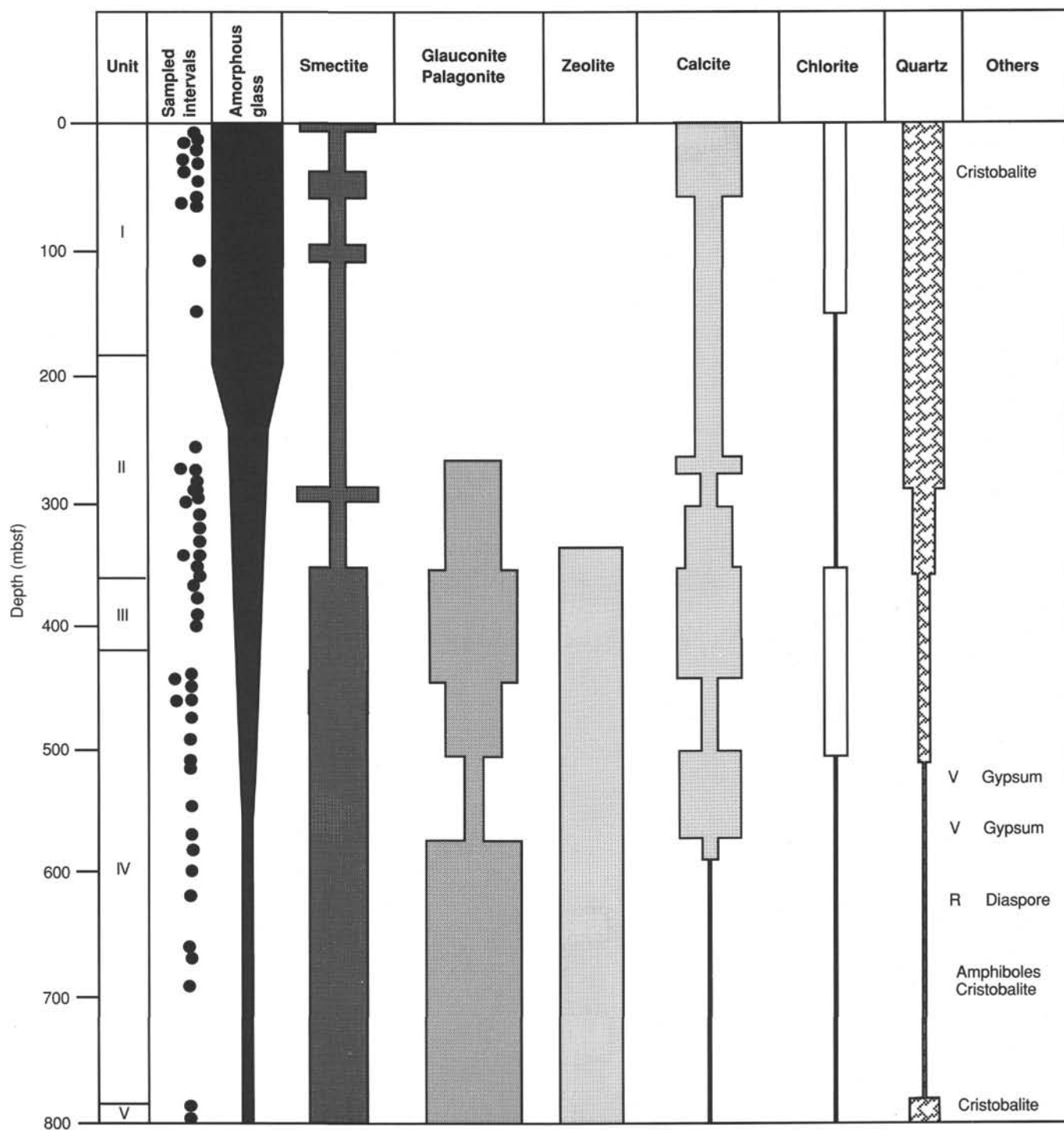
Figure 26. Summary diagram of X-ray diffraction data from Site 792 in which the relative widths of bars represent semiquantitative measurements of clay and other mineral abundances (filled circles = sampled intervals; V = vein or microfault; R = pale reddish volcanic clast).

structureless conglomerates with sharp tops and floating clasts are interpreted as debris-flow deposits. The graded beds of conglomerate are like the normally graded conglomerates of Walker (1975) and are interpreted as turbidites deposited from high-concentration flows. Thick pebbly sandstone beds and thin- to medium-bedded, graded sandstone beds with planar lamination, cross lamination, and flame structures are also turbidites.

There is no evidence that the conglomerates at this site were deposited in channels, although similar sediments in some an-

cient successions do reside in shallow channels or large scours. Conglomerates of this type are known from the inner to middle parts of ancient submarine fans, within and beyond fan channels, and from coarse-grained slope aprons (Nelson and Maldonado, 1988).

The composition of sand and gravel clasts indicates that part of the volcanogenic detritus is not the product of syndepositional volcanism, but instead was derived by the erosion of volcanoes along the nearby arc. In particular, pebble types include

Table 5. Biostratigraphic datums used to construct the age-depth curves for Site 792.

Chronostratigraphic event	Core, section, interval (cm)	Depth (mbsf)	Age (ma)
Hole 792A			
FO *F. huxleyi*	2H-CC to 3H-CC	15.55–28.40	0.275
LO *P. lacunosa*	4H-3, 40–41 to 4H-CC	31.80–37.80	0.460
LO acme *R.* Sp A	8H-CC to 9H-1, 64–65	69.46–81.41	0.830
Hole 792B			
FO *E. huxleyi*	1H-CC to 2H-CC	4.28–59.60	0.275
LO acme *R.* Sp. A	4X-CC to 5X-CC	73.96–88.50	0.830
LO *D. brouweri*	6X-CC to 7X-CC	88.65–107.90	1.890
LO *D. pentaradiatus*	7X-CC to 8X-1, 33–34	98.57–111.62	2.350
LO *D. surculus*	8X-1, 36–37 to 8X-CC	108.26–117.50	2.410
LO *D. tamalis*	11X-1, 25 to 11X-CC	137.05–146.40	2.650
Hole 792C			
LO *D. tamalis* to	1X-CC	137.39–146.40	2.65
LO *R. psuedoumbilica*			3.56
Hole 792D			
LO *D. tamalis* to	1X-CC	136.84–145.60	2.65
LO *R. psuedoumbilica*			3.56
Hole 792E			
LO *R. psuedoumbilica*	5R-CC to 6R-1, 39–40	175.03–192.37	3.56
FO *P. lacunosa*	6R-1, 39–40 to 6R-CC	185.13–193.40	3.70
LO *D. quinqeuramus*	6R-1, 39–40 to 6R-CC	185.13–193.40	5.30
FO *D. berggrenii*	15R-1, 11–12, to 15R-2, 39–40	270.16–278.6	8.20
LO *D. hamatus*	15R-1, 11–12 to 15R-39–40	270.16–278.60	8.90
FO *C. calyculus*	15R-CC to 16R-1, 40–41	273.99–287.64	10.0
FO *D. hamatus*	16R-CC to 17R-1, 40–41	282.86–294.61	10.0
FO *C. coalitus*	17R-2, 41–42 to 17R-3, 37–38	291.80–297.58	10.8
FO *D. kugleri*	20R-CC to 21R-1, 40–41	322.48–336.09	11.5
LO *S. heteromorphus*	23R-CC to 24R-1, 46–47	349.67–366.10	13.2
LO *S. belemnos*	23R-CC to 24R-1, 46–47	349.67–366.10	18.6
FO *S. belemnos*	24R-CC to 25R-1, 40–41	358.60–375.27	20.5
FO *D. druggii*	28R-CC to 29R-1, 106–109	399.03–413.26	23.2
LO *R. bisecta*	28R-CC to 29R-1, 106–109	399.03–413.26	23.7
LO *S. distensus*	36R-CC to 37R-CC	480.13–492.50	28.2

Note: Data are plotted in Figures 27, 28, and 29.

Table 6. Paleomagnetic reversal events used to construct the age-depth curves for Site 792.

Chronostratigraphic event	Interval	Depth (mbsf)	Age (Ma)
Hole 792A			
Brunhes/Matuyama	7H-1, 140	58.0–59.9	0.73
Top of Jaramillo	9H-3, 140	80.0–85.2	0.91
Base of Jaramillo	10H-1, 150	86.8–91.1	0.98
Hole 792B			
Brunhes/Matuyama	3H, 40	60.3	0.73
Top of Jaramillo	4X/5X	74.0–88.1	0.91
Top of Anomaly 2A	9X/10X	119.6–132.1	2.47
Hole 792E			
Base of Anomaly 2A	5R/6R	175.0–192.7	3.40
Top of normal between Anomalies 3A and 4	8R-1, 30	203.4–212.4	6.37
Top of Anomaly 4	9R-3, 20	215.9–219.8	6.70
Base of 1st normal in Anomaly 4	9R-3, 100	216.6–220.6	6.78
Base of 2nd normal in Anomaly 4	12R/13R	245.8–258.95	7.28
Top of Anomaly 5	15R-1, 50	271.0–277.2	8.92
Top of 2nd normal in Anomaly 5A	21R/22R	330.53–342.89	11.89
Top of 1st normal in Anomaly 8	31R-3, 140	418.45–419.86	26.86
Top of 1st normal in Anomaly 9	35R/36R	466.2–475.9	28.15
Base of 1st normal in Anomaly 9	51R/52R	621.96–628.43	28.74
Top of 2nd normal in Anomaly 9	55R-2, 50	657.7–664.33	28.80

Note: Data are plotted in Figures 27, 28, and 29.

andesite, dacite, and some porphyritic rocks; sandstones contain abundant reddish brown, epiclastic, sand-size scoria grains and local concentrations of plant debris. The pumice clasts present in the upper conglomerates suggest some contemporaneous volcanic activity in the region.
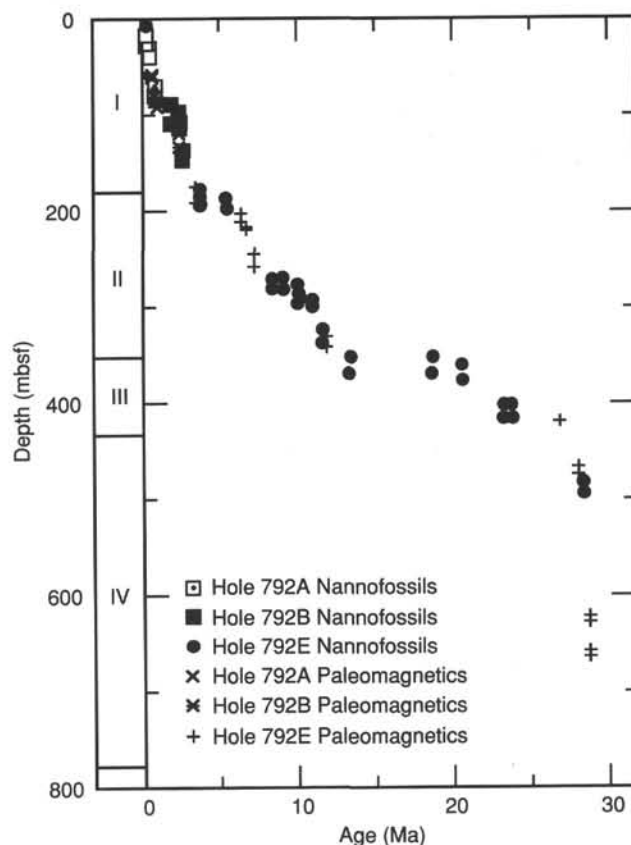

Figure 27. Age-depth plot for Site 792, constructed from the biostratigraphic datums and paleomagnetic reversal events listed in Tables 5 and 6. Lithologic unit boundaries are plotted on the right-hand side of the graph. Two data points at any one age represent possible depth range of datum or event.

Unit V

This unit is composed of severely altered volcanic pebble-granule conglomerate and sandstone. Although grain boundaries are not visible with a binocular microscope, "ghosts" of flattened pumiceous grains are visible petrographically. This alteration may be hydrothermal; the fluids responsible for it probably moved along the fault planes that bound Unit V (see "Downhole Measurements" section, this chapter). Manganese oxides that occur just below the upper fault have a hydrothermal origin. Slight alteration is also present above this fault in the lowest sandstones of Unit IV and may be the result of movement of hydrothermal fluids along the faults. The suggestion of hydrothermal circulation appears to be at odds with temperature measurements at the base of the sedimentary section that are consistently less than 30°C (see "Downhole Measurements" section, this chapter). Higher fluid temperatures may have been short lived, however, and possibly were restricted to the Oligocene or Miocene.

BIOSTRATIGRAPHY

Calcareous Nannofossils

Hole 792A

Samples 126-792A-1H-CC and -2H-CC contain *Emiliania huxleyi* and are placed within Zone CN15. The following species are also present in these samples: *Gephyrocapsa oceanica,*
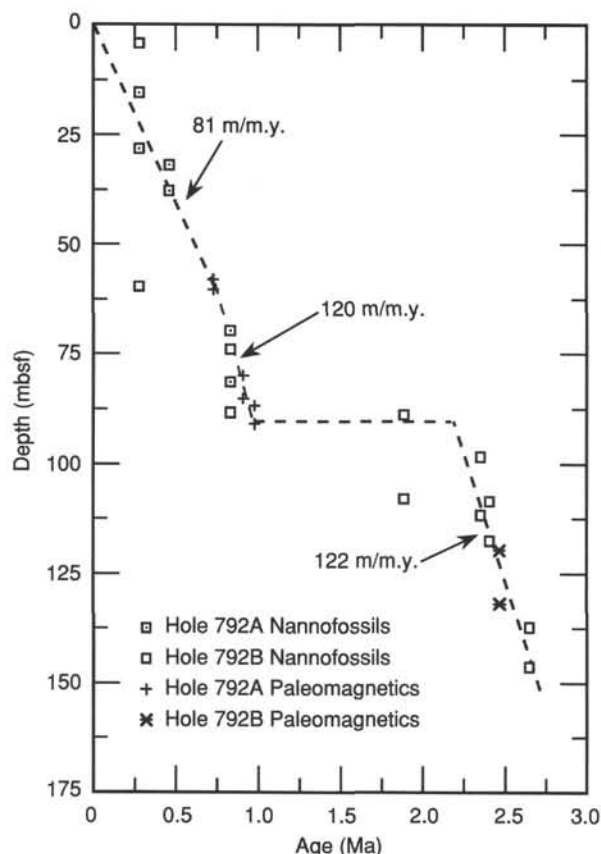
Figure 28. Expanded age-depth plot of the Pliocene-Pleistocene section, Site 792 (shown in Fig. 27), constructed from the biostratigraphic datums and paleomagnetic reversal events listed in Tables 5 and 6. Two data points at any one age represent possible depth range of datum or event. Average sedimentation rates are shown in m/m.y.
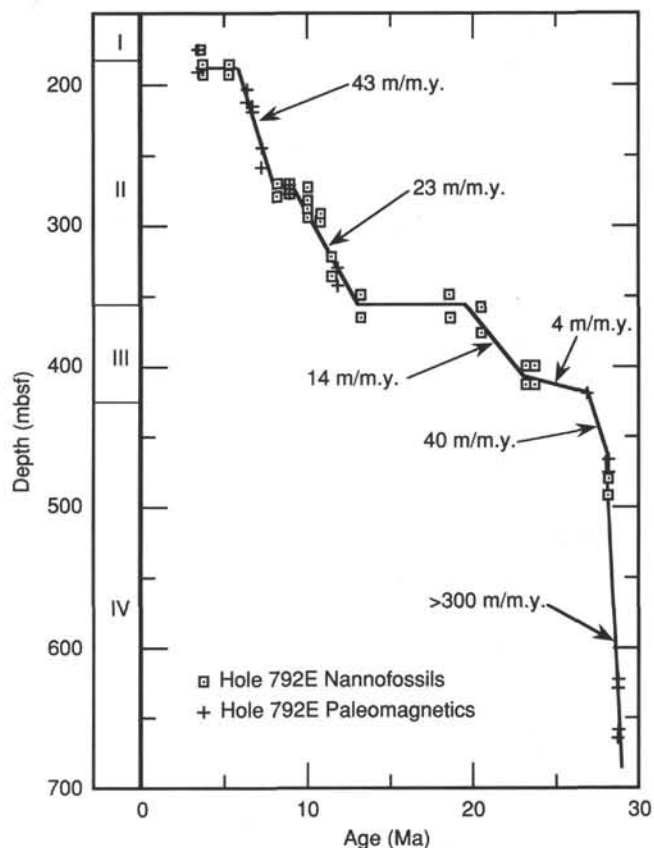

Figure 29. Expanded age-depth plot of the Miocene and Oligocene section, Site 792 (shown in Fig. 27), constructed from the biostratigraphic datums and paleomagnetic reversal events listed in Tables 5 and 6. Lithologic unit boundaries are plotted on the right-hand side of the graph. Two data points at any one age represent possible depth range of datum or event. Average sedimentation rates are shown in m/m.y.

Helicosphaera carteri, Umbilicosphaera irregularis, Rhabdospaera clavigera, and *Coccolithus pelagicus.* Reworked *Sphenolithus* sp. was found in Sample 126-792A-1H-CC.

E. huxleyi and *Pseudoemiliania lacunosa* are not present in Samples 126-792A-3H-CC, -4H-1, 40–41 cm, and -4H-3, 40–41 cm, which are placed within Zone CN14b. Other species present include *Syracosphaera* sp., *Pontosphaera japonica, Calcidiscus leptoporus, G. oceanica,* and *H. carteri.*

P. lacunosa is present in Samples 126-792A-4H-CC through -10H-CC, which are assigned to Zone CN14a. Sample 126-792A-9H-1, 64–65 cm, contains the last occurrence (LO) of the acme of *Reticulofenestra sp. A.,* which marks the 0.83 Ma datum proposed by Takayama and Sato (1987). Other species found in these samples are *G. oceanica,* small *Gephyrocapsa* sp., *Scapholithus fossilis, C. pelagicus, C. leptoporus, Thoracosphaera* sp., and *Helicosphaera* spp.

Hole 792B

Emiliania huxleyi is present in Sample 126-792B-1H-CC, which indicates that the sample falls within Zone CN15. Other species present in the sample are *C. leptoporus, G. oceanica, Ceratolithus cristatus, H. carteri,* and *Oolithotus antillarum.*

Samples 126-792B-2H-CC through -6X-CC contain *P. lacunosa* and are assigned to Zone CN14a (of Okada and Bukry, 1980). We found the *Reticulofenestra* sp. A datum (0.83 Ma) in Sample 126-792B-5X-CC. Other calcareous nannofossils in these samples are *G. oceanica, P. japonica, R. clavigera, C. leptoporus,* and *Umbilicosphaera sibogae.* Sample 126-792B-6X-CC

does not contain *Helicosphaera sellii* or *Calcidiscus macintyrei,* which suggests that this sample is younger than the LOs of both of these species (1.37 and 1.45 Ma, respectively).

We found *Discoaster brouweri* in Sample 126-792B-7X-CC, but not *Discoaster pentaradiatus,* which indicates a late Pliocene age and assignment to Zone CN12d. A hiatus or period of reduced sedimentation rate occurs within Core 126-792B-7X, between Samples 126-792B-6X-CC (Zone CN14a, <1.37 Ma) and -7X-CC (Zone CN12d, >1.89 Ma). Samples 126-792B-8X-1, 33–34 cm, and -8X-1, 36–37 cm, contain *D. pentaradiatus* and do not contain *Discoaster surculus,* which indicates Zone CN12c. Samples 126-792B-8X-CC, -9X-CC, -10X-1, 42–43 cm, and -11X-1, 25 cm, contain *D. surculus* and do not contain *Discoaster tamalis,* which indicates Zone CN12b. Sample 126-792B-11X-CC contains *D. tamalis,* but it does not contain *Reticulofenestra pseudoumbilica,* which constrains this sample to Zone CN12a. Other species present in these samples include *P. japonica, Helicosphaera sellii, Calcidiscus macintyrei, Coccolithus streckerii, Syracosphaera pulchra, D. brouweri,* and *Helicosphaera* spp.

Hole 792C

D. surculus is present in Sample 126-792C-1X-CC but *R. pseudoumbilica* is absent, which suggests a range in age from Zones CN12a to CN12b. Other species found in this sample are *D. brouweri, D. pentaradiatus, C. pelagicus, H. sellii, Thoracosphaera* sp., *P. lacunosa,* and *C. leptoporus.*

Hole 792D

Sample 126-792D-1X-CC contains *D. surculus* and does not contain *R. pseudoumbilica;* it falls within Zones CN12a to CN12b. Other calcareous nannofossils found in the sample are *D. pentaradiatus, Ceratolithus rugosus, P. lacunosa, C. pelagicus, Syracosphaera* spp., and *Discoaster asymmetricus.*

Hole 792E

D. brouweri, D. pentaradiatus, D. surculus, and *D. asymmetricus* are present in Samples 126-792E-1R-CC through -5R-CC, but *R. pseudoumbilica* is absent, which indicates Zones CN12a to CN12b. Sample 126-792E-6R-1, 39–40 cm, contains the aforementioned species plus common *R. pseudoumbilica* and is assigned to Zone CN11b. These Pliocene samples also contain common *P. lacunosa, C. leptoporus,* and *C. macintyrei.*

Samples 126-792E-6R-CC through -15R-1, 11–12 cm, contain *Discoaster quinqueramus* and *Discoaster berggrenii;* they are assigned to the upper Miocene Zone CN9. Also present within this interval are *Discoaster pansus, Sphenolithus abies,* and *Minylitha convallis.*

Zone CN7b is indicated by *Discoaster hamatus* and *Catinaster calyculus* being present in Samples 126-792E-15R-2, 39–40 cm, through -15R-CC. Zone CN8, defined as the interval between the LO of *D. hamatus* and the first occurrence (FO) of *D. berggrenii,* is either missing or is restricted to the interval between Samples 126-792E-15R-1, 11–12 cm, and -15R-2, 39–40 cm, which suggests the presence of a hiatus.

Samples 126-792E-16R-1, 40–41 cm, through -16R-CC contain *D. hamatus* but do not contain *C. calyculus;* they are assigned to the middle Miocene Zone CN7a. Samples 126-792E-17R-1, 40–41 cm, and -17R-2, 41–42 cm, contain *Catinaster coalitus* but do not contain *D. hamatus,* and are assigned to Zone CN6. Samples 126-792E-17R-3, 37–38 cm, through -20R-CC are located below the FO of *C. coalitus* and above the FO of *Discoaster kugleri,* and are assigned to Zone CN5b. Samples 126-792E-21R-1, 40–41 cm, through -23R-CC occur below the FO of *D. kugleri* and do not contain *Sphenolithus heteromorphus,* but they do contain *Cyclicargolithus floridanus* and *C. macintyrei* and thus are assigned to Zone CN5a. The middle Miocene assemblages also contain common *R. pseudoumbilica* and *C. pelagicus.*

We found *Sphenolithus belemnos* and *C. floridanus* in Samples 126-792E-24R-1, 46–47 cm, and -24R-CC but did not find *C. macintyrei,* and thus assign those samples to lower Miocene Zone CN2. The lack of an interval containing *S. heteromorphus* indicates that Zones CN3 and CN4 are missing in this hole. Samples 126-792E-25R-1, 40–41 cm, through -28R-CC are located below the FO of *S. belemnos* and above the FO of *Discoaster druggii,* and are assigned to Zone CN1c. The lower Miocene interval also contains rare to few *Reticulofenestra bisecta,* and common *C. floridanus* and *Discoaster deflandrei.*

The LO of consistently occurring, few to common *R. bisecta* in Sample 126-792E-29R-1, 106–109 cm, in the absence of any exclusively Miocene species, suggests that the top of Oligocene Zone CP19b occurs in this sample. Therefore, Subzones CN1a and CN1b do not occur in this section, indicating the presence of a short hiatus between Samples 126-792E-28R-CC and -29R-1, 106–109 cm. Samples 126-792E-29R-1, 106–109 cm, through -36R-CC contain *R. bisecta* and rare *Sphenolithus ciperoensis,* but no *Sphenolithus distentus;* they are assigned to Zone CP19b. Samples 126-792E-37R-CC through -57R-CC contain *S. distentus* and *S. ciperoensis,* and are assigned to Zone CP19a. Samples 126-792E-62R-CC, -63R-CC, and -66R-2, 99–101 cm, contain *Sphenolithus predistentus* and *S. distentus,* but they do not contain *S. ciperoensis.* We thus assigned these samples to lower Oligocene Zones CP17–CP18. *Sphenolithus dis-*

tentus and *S. ciperoensis* have rare and sporadic occurrences in this section; therefore, the boundaries between Zones CP17–18, CP19a, and CP19b are tentative. The Oligocene assemblages in Hole 792E are characterized by common *R. bisecta, C. floridanus,* and *D. deflandrei.*

Planktonic Foraminifers

Hole 792A

The faunas in Samples 126-792A-1H-CC, -2H-2, 57–62 cm, -3H-CC, -5H-CC, and 126-792A-6H-CC are dominated by *Globorotalia inflata,* dextral *Globorotalia truncatulinoides,* *Globigerinoides ruber* complex, *Globigerinoides sacculifer,* and dextral *Globigerina pachyderma.* Co-occurring species are the sinistral *Globorotalia menardii-tumida* complex, *Globigerinoides trilobus, Globigerinoides conglobatus, Globigerina bulloides, Globorotalia scitula, Globorotalia menardii flexuosa, Pulleniatina obliquiloculata,* and *Globigerinita glutinata.* The presence of *Globigerina digitata,* pink *G. ruber,* and *G. menardii flexuosa* places this sample in Zone N23 (Bielak and Briskin, 1978). Pink *G. ruber* indicates that the sample was deposited before 123 Ka (the LO of *G. ruber,* pink).

The dominant species in Sample 126-792A-7H-1, 59–61 cm, is *G. inflata;* co-occurring species include the *G. ruber* complex, *G. trilobus, P. obliquiloculata, Globorotalia crassaformi,* dextral *G. pachyderma,* dextral *G. truncatulinoides,* and sinistral *G. tumida.* The presence of *Globigerina calida* places this sample in the Brunhes Epoch (Zone N23, Blow, 1969). Sample 126-792A-8H-1, 93–97 cm, contains *G. inflata, G. sacculifer,* the *G. ruber* complex, dextral *G. truncatulinoides, G. crassaformis, G. scitula,* sinistral *G. menardii,* sinistral *G. tumida,* and dextral *G. pachyderma.* This sample is assigned to Zone N22 (Blow, 1969). Samples 126-792A-9H-CC and -10H-CC contain *G. inflata, G. truncatulinoides, Globorotalia tosaensis-truncatulinoides, Globorotalia tosaensis,* the *G. sacculifer* complex, sinistral *G. menardii, Sphaeroidinella dehiscens,* and the *G. ruber* complex, and are assigned to Zone N22 (Blow, 1969).

Hole 792B

Sample 126-792B-5X-CC is characterized by abundant *G. inflata, G. gomitulus, P. obliquiloculata,* and *G. crassaformis;* co-occurring taxa include *G. truncatulinoides-tosaensis* and *G. tosaensis.* The dominance of the sinistral *G. menardii-tumida* complex and the presence of *G. truncatulinoides* places this sample in Zone N23 (Blow, 1969; Bielak and Briskin, 1978). Sample 126-792B-7X-CC does not contain zonal markers.

Hole 792D

Sample 126-792D-1X-CC contains rare specimens of *G. tosaensis* and abundant to common representatives of the *G. ruber* complex, *G. conglobatus* and dextral *G. pachyderma.* The dominance of sinistrally coiled specimens in the *G. menardii-tumida* complex places this sample in Zone N22. However, the absence of *G. truncatulinoides* (the Pleistocene and Holocene zonal index species), generally present in low percentages, as well as the absence of such late Pliocene zonal markers as *Globigerinoides fistulosus,* make the zonal assignment of this sample tentative.

Hole 792E

Sample 126-792E-1R-CC contains about 50% sinistrally coiled *G. menardii-tumida.* Bielak and Briskin (1978) noticed a similar short-term change in the coiling direction of this species at about 1.65 Ma in a Pacific deep-sea core. Using the revised time scale of Berggren et al. (1985), we place this sample in the latest Pliocene (Zone N21). Samples 126-792E-2R-1, 13–15 cm, and -2R-CC are characterized by the predominance of sinistral *G. me-*

nardii-tumida and rare specimens of *G. tosaensis,* in addition to *Globigerinoides tenellus, Globoquadrina humerosa, G. trilobus, G. sacculifer, G. ruber, G. gomitulus, S. dehiscens,* etc., which places these samples near the top of Zone N21 in the *T. tosaensis* Subzone (Bielak and Briskin, 1978). The compositions of the foraminiferal faunas in Samples 126-792E-3R-1, 64–69 cm, and -5R-CC resemble that of the previous sample, placing them near the top of Zone N21. Sample 126-792E-6R-1, 58–60 cm, is located below an unconformity (Fig. 30). Representative taxa include *Globorotalia merotumida, Globigerinoides obliquus, Sphaeroidinellopsis sphaeroides,* and predominantly dextrally coiled *G. tumida-menardii,* placing this sample in upper Miocene Zone N17 (Bolli et al., 1985).

Samples 126-792E-7R-CC through -11R-CC are barren or contain only rare foraminiferal shell fragments unidentifiable at 100X magnification. Sample 126-792E-12R-CC contains rare foraminifers. The presence of *Globigerina nepenthes* tentatively places this sample in Zone N17. Samples 126-792E-13R-1, 30–32 cm, through -15R-1, 115–117 cm, are barren or contain rare foraminiferal fragments unidentifiable at 100X magnification. Samples 126-792E-15R-CC through -17R-CC contain *S. sphaeroides* and *G. nepenthes,* and are placed in Zone N17 (Bolli et al., 1985). Samples 126-792E-16R-CC and -17R-CC are characterized by *G. menardii* A, *Globoquadrina venezuelana, S. sphaeroides,* and *G. obliquus* and are assigned to Zone N17 (Bolli et al., 1985). Samples 126-792E-18R-CC through -20R-CC are barren or contain unidentifiable foraminiferal shell fragments.

An unconformity exists between Samples 126-792E-17R-CC and -23R-1, 59–60 cm, which contains specimens of *Globorotalia praemenardii, Globorotalia fohsi peripheronda, Globorotalia scitula, Globigerina bulloides,* and *Orbulina suturalis,* and is placed in middle Miocene Zones N8–N9 (Bolli et al., 1985; Fig. 30). Another unconformity is detected between the previous sample and Sample 126-792E-24R-CC; the latter contains specimens of *Catapsydrax stainforthi* and *Globorotalia continuosa,* and is assigned to early Miocene Zone N6 (Bolli et al., 1985). *Catapsydrax dissimilis* and *G. trilobus* were observed in Sample 126-792E-26R-CC, placing it in Zones N5–N6 (Bolli et al., 1985). Sample 126-792E-28R-1, 62–63 cm, contains *C. dissimilis, Globorotalia siakensis, Globigerina praebulloides,* and *Globigerina brevispira;* this sample is assigned to Zone N5 (Bolli et al., 1985).

The foraminiferal fauna in Sample 126-792E-28R-CC indicates an unconformity between this and the previous sample; the presence of *C. dissimilis, Globigerina quinqueloba, Globorotalia obesa, G. siakensis, Globorotalia kugleri,* and *Globorotalia opima nana* places this sample in the upper Oligocene Zone P22/N3 (Bolli et al., 1985). Sample 126-792E-29R-CC contains *G. opima nana* and *C. dissimilis,* placing this sample in Zones P18/19–P22/N3 (Bolli et al., 1985). Samples 126-792E-30R-CC through -37R-CC are barren or contain unidentifiable foraminiferal shell fragments. Sample 126-792E-40R-3, 62–64 cm, which contains *G. opima nana* and *G. venezuelana,* is placed in Zone P22/N3 (Bolli et al., 1985). Samples 126-792E-40R-CC through -57R-1, 97–99 cm, are barren or contain unidentifiable foraminiferal shell fragments. Sample 126-792E-57R-CC contains specimens of *G. venezuelana, G. opima nana* and *C. dissimilis;* this sample is assigned to Zones P18/19–P22/N3 (Bolli et al., 1985).

The preservation and abundance of species ranges from excellent to poor and very abundant to absent, respectively.

Benthic Foraminifers

We subdivided the Tertiary strata at Site 792 into twelve zonules on the basis of benthic foraminifer assemblages (Fig. 30). Our estimations of depositional water depths are mainly in comparison with (1) Holocene and Quaternary benthic fora-

minifer data from Holes 792B (1798 mbsl), 790A (2222 mbsl), 790B (2223 mbsl), 791A (2268 mbsl), 793A (2975 mbsl), and 787B (3254 mbsl; see "Biostratigraphy" sections in appropriate site chapters, this volume); (2) offshore data from Shizuoka and Shikoku, Japan (Akimoto, 1989; Yasuda, 1989) for the Pliocene and Pleistocene strata; and (3) Cenozoic benthic foraminifer data (Ingle, 1980; Woodruff, 1985; van Morkhoven et al., 1986) for the Miocene and Oligocene strata. We determined the age of each zonule on the basis of the calcareous nannofossil, radiolarian, and planktonic foraminifer zonations in this report. Dissolved oxygen contents were estimated from the ratios of aerobic to anaerobic forms of benthic foraminifers (Bernhard, 1986; Kaiho, in press).

Rhabdammina sp. Assemblage-Zonule

Characteristic species: agglutinated foraminifers such as *Rhabdammina* sp., *Rhizammina* sp., *Reophax* sp., *Thalmannamina* sp., *Subreophax* sp, and *Haplophragmoides* sp.; barren of calcareous foraminifers
Abundance: few
Samples: 126-792E-64R-1, 131–134 cm, -64R-1, 17–18 cm, and -63R-CC
Age: early Oligocene
Depositional water depth: Between 3.5 and 4.5 km
Dissolved oxygen: ?

Barren Zonule

Samples: 126-792E-62R-CC through -59R-CC
Age: early Oligocene

Stilostomella spp.–*Oridorsalis umbonatus* Assemblage-Zonule

Characteristic species: *Stilostomella* spp., *Oridorsalis umbonatus,* and *Pleurostomella* spp.
Abundance: few
Samples: 126-792E-57R-CC and -57R-1, 97–99 cm
Age: late Oligocene
Depositional water depth: between 2 and 4 km
Dissolved oxygen: high

Barren Zonule

Samples: 126-792E-56R-3, 25–27 cm, through -37R-CC
Age: late Oligocene

Rhabdammina sp.–*Stilostomella* spp. Assemblage-Zonule

Characteristic species: *Rhabdammina* sp., *Stilostomella* spp., and *Nodosaria longiscata*
Abundance: few
Samples: 126-792E-36R-CC through -30R-CC
Age: late Oligocene
Depositional water depth: between 2 and 4 km
Dissolved oxygen: ?

Oridorsalis umbonatus–*Pleurostomella* spp. Assemblage-Zonule

Characteristic species: *Oridorsalis umbonatus, Pleurostomella* spp., *Stilostomella* spp., and *Cibicidoides* spp.
Abundance: few
Samples: 126-792E-28R-CC through -24R-1, 61–63 cm
Age: early Miocene
Depositional water depth: between 2 and 4 km
Dissolved oxygen: high

Cibicidoides renzi–*Cibicidoides wellerstorfi* Assemblage-Zonule

Characteristic species: *Cibicidoides renzi, Cibicidoides wellerstorfi, Oridorsalis umbonatus, Pleurostomella* spp., and *Stilostomella* spp.
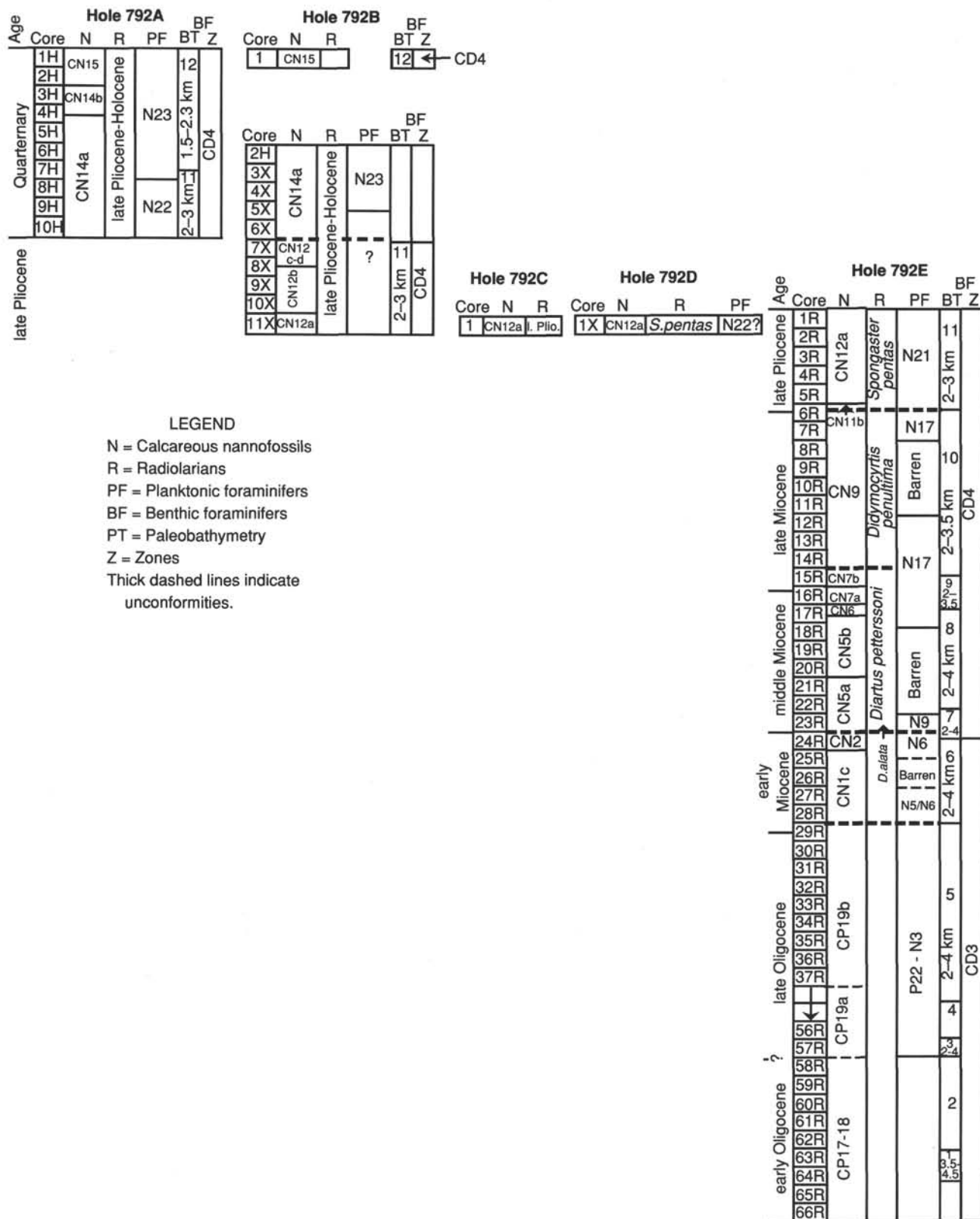
Figure 30. Summary of the biostratigraphic and paleobathymetric results for Site 792. See text for discussion of individual microfossil zones.

Abundance: few to common
Samples: 126-792E-23R-1, 59–61 cm, and -22R-CC
Age: middle Miocene
Depositional water depth: between 2 and 3.7 km
Dissolved oxygen: high

Cibicidoides spp.–Epistominella sp. Assemblage-Zonule

Characteristic species: *Cibicidoides* spp. and *Epistominella* sp.
Abundance: rare
Samples: 126-792E-22R-3, 60–65 cm, through -17R-3, 60–63 cm
Age: middle Miocene
Depositional water depth: between 2 and 3.5 km
Dissolved oxygen: high

Uvigerina sp. Assemblage-Zonule

Characteristic species: *Uvigerina* sp., *Cibicidoides* spp., *Sphaeroidina bulloides*, *Oridorsalis umbonatus*, *Gyroidinoides* sp., *Bulimina rostrata*, *Pleurostomella* spp., *Cibicidoides wellerstorfi*, *Melonis barleeanus*, and *Lenticulina* sp.
Abundance: common
Samples: 126-792E-16R-CC and -15R-CC
Age: middle Miocene
Depositional water depth: between 2 and 3.5 km
Dissolved oxygen: high

Stilostomella spp.–Cibicidoides wellerstorfi Assemblage-Zonule

Characteristic species: *Stilostomella* spp., *Cibicidoides* spp. and *Cibicidoides wellerstorfi*
Abundance: few
Samples: 126-792E-15R-1, 115–117 cm, through -7R-CC
Age: late Miocene
Depositional water depth: between 2 and 3.5 km
Dissolved oxygen: high

Stilostomella spp.–Pleurostomella spp. Assemblage-Zonule

Characteristic species: *Stilostomella* spp., *Oridorsalis umbonatus*, *Cibicidoides wellerstorfi*, *Pleurostomella* spp., *Sigmoilopsis schlumbergeri*, *Pullenia bulloides*, *Uvigerina hispidocostata*, *Uvigerina probosidea*, *Lenticulina* spp., *Amphicoryna* sp. (lower part of this zonule), and *Bolivinita* sp. (middle part of this zonule)
Abundance: abundant
Samples: 126-792E-6R-1, 58–60 cm, through -8H-1, 93–97 cm
Age: Pliocene to Pleistocene
Depositional water depth: between 2 and 3 km
Dissolved oxygen: high

Bulimina aculeata Assemblage-Zonule

Characteristic species: *Melonis barleeanus*, *Pullenia bulloides*, *Bulimina aculeata*, *Uvigerina hispidocostata*, *Oridorsalis umbonatus*, *Sphaeroidina bulloides*, *Chilostomella oolina*, *Cibicidoides wellerstorfi*, *Uvigerina hispida*, and *Globobulimina pacifica*
Abundance: abundant
Samples: 126-792A-7H-1, 59–61 cm, through -1H-CC.
Age: Quaternary
Depositional water depth: between 1.5 and 2.3 km
Dissolved oxygen: high
Remarks: The depositional age of the base of this assemblage-zonule is approximately 0.7 Ma, as determined from magnetic datums. This faunal change also occurred at the same time in Sites 790 and 791.

Samples 126-792A-1H-CC through -23R-1, 59–61 cm, contain *Cibicidoides wellerstorfi* and are correlative with the cosmopolitan benthic foraminiferal Zone CD4 (Kaiho, in press), corresponding to the post-middle middle Miocene turnover event. Samples 126-792E-24R-1, 61–63 cm, through -64R-1, 131–134 cm, are correlative with Zone CD3 given the absence of *C. wellerstorfi* and *Nuttallides truempyi*. Benthic foraminifer faunas in all the zonules below the *Bulimina aculeata* Zonule that contain *Pleurostomella* and *Stillostomella* and lack shallower fauna (e.g., *Bulimina aculeata*) indicate a deep-ocean basin environment (see Woodruff, 1985, table 5). However, the fauna in the uppermost zonule, which contains *Bulimina aculeata*, suggests a marginal ocean environment on the basis of previous studies (e.g., Kaiho and Hasegawa, 1986; Akimoto, 1989; Yasuda, 1989).

Radiolarians

Radiolarians are common to abundant and generally well preserved in Miocene to Quaternary sections of holes drilled at Site 792.

Hole 792A

Moderately diverse, well-preserved faunas are present in Samples 126-792A-1H-CC, -3H-CC, -4H-CC, -5H-CC and -9H-CC, and indicate a Quaternary age. The faunas typically include *Didymocyrtis tetrathalamus*, *Lamprocyclas maritalis*, *Botryostrobus aurita/australis* group, *Amphirhopalum ypsilon*, *Didymocyrtis tetrathalamus*, and *Spongaster tetras*. The occurrence of *Druppatractus acquilonius* in Sample 126-792A-5H-CC and *Axoprunum angelinum* in Sample 126-792A-9H-CC provides minimum age constraints of 0.3 and 0.41 Ma, respectively, for samples at and below these levels (Foreman, 1981).

Hole 792B

Moderately diverse, well-preserved radiolarian faunas are present in core-catcher samples from all cores of Hole 792B except for Samples 126-792B-4X-CC, -8X-CC, and -10X-CC. The occurrence of faunas including *Tetrapyle octacantha*, *Didymocyrtis tetrathalamus*, and *Spongaster tetras* suggest a late Pliocene to Holocene age.

Hole 792C

Upper Pliocene to Holocene radiolarians are common and well-preserved in Sample 126-792C-1X-CC and include the *Botryostrobus aurita/australis* group, *Lamprocyclas maritalis*, and *Acrosphaera spinosa*.

Hole 792D

Sample 126-792D-1X-CC contains abundant well-preserved radiolarians. The co-occurrence of *Spongaster tetras* and *Spongaster pentas* in this sample suggests assignment to the upper part of the upper Pliocene *Spongaster pentas* Zone of Sanfilippo et al. (1985).

Hole 792E

Well-preserved, lower Miocene to upper Pliocene radiolarians are common in the upper half of Hole 792E. All samples from below the level of Sample 126-792E-28R-2, 20–21 cm, are devoid of identifiable radiolarians. However, extremely poorly preserved, infilled radiolarians occur in Sample 126-792E-30R-CC and were also observed rarely below this sample.

Samples 126-792E-1R-1, 2–3 cm, through -5R-1, 19–20 cm, contain an assemblage that includes *Druppatractus acquilonius*, *Axoprunum angelinum*, *Amphirhopalum ypsilon*, *Spongaster tetras*, *Spongaster pentas*, *Pterocanium prismatium*, and *Stichocorys peregrina*. The presence of *Amphirhopalum ypsilon* and *Spongaster tetras* in these samples indicates ages less than

3.78 and 3.8 Ma, respectively (Backman, Duncan, et al., 1988). The morphotypic top of *Stichocorys peregrina*, which indicates an age greater than 2.6 Ma (Sanfilippo et al., 1985), and the presence of this species along with *Didymocyrtis avita* in Sample 126-792E-2R-1, 5–6 cm, suggests assignment to the *Spongaster pentas* Zone of late Pliocene age (Sanfilippo et al., 1985). No radiolarians were recovered between Samples 126-792E-5R-1, 19–20 cm, and -9R-1, 21–22 cm.

Sample 126-792E-9R-1, 21–22 cm, contains *Stichocorys delmontensis*, and is therefore no younger than the late Miocene (6.4 Ma; Backman, Duncan, et al. 1988). This sample is tentatively assigned to the *Didymocyrtis penultima* Zone of Sanfilippo et al. (1985).

An upper middle Miocene fauna is present in Samples 126-792E-15R-CC through -22R-CC, which includes *Stichocorys delmontensis, Cyrtocapsella japonica,* and *Didymocyrtis laticonus*. The presence of *Didymocyrtis laticonus* suggests assignment to the upper middle Miocene *Diartus petterssoni* Zone of Sanfilippo et al. (1985). *Stichocorys wolffii* is present in and below Sample 126-792E-18R-CC. The LO of this species in the latest middle Miocene was at 11.6 Ma (Nigrini, 1985).

Both *Stichocorys wolffii* and *Cyrtocapsella japonica* occur in Sample 126-792E-23R-CC. *Didymocyrtis laticonus* is absent, which suggests assignment to the lower middle Miocene *Dorcadospyris alata* Zone of Sanfilippo et al. (1985). Samples 126-792E-24R-CC through -27R-CC are barren of radiolarians.

One identifiable species, *Cyrtocapsella japonica,* is present in Sample 126-792E-28R-2, 20–21 cm, which allows the assignment of a Miocene age. This species is known to occur in the *Cyrtocapsella tetrapera* through *Diartus petterssoni* Zones (Nigrini and Lombari, 1984). No identifiable radiolarians were recovered from below Samples 126-792E-28R-2, 20–21 cm.

Summary

We recognize a sedimentary sequence from lower Oligocene through Quaternary on the basis of calcareous nannofossils, foraminifers, and radiolarians. The age of the sediment above the basement is late early Oligocene, as determined from calcareous nannofossils.

The following four hiatuses were recognized (Table 7):

1. from 5.6 Ma through 3.6 Ma (upper Miocene–upper Pliocene), CN10–CN11a and N18–N20 absent, 2.0 m.y. duration, between Samples 126-792E-6R-1, 58–60 cm, and -6R-1, 39–40 cm;

2. from 8.9 Ma through 7.0 Ma (within the upper Miocene), CN8 and *D. antepenultima* Zone absent, 1.9 m.y. duration, between Samples 126-792E-15R-2, 39–40 cm, and -15R-1, 11–12 cm;

3. from 18.6 Ma through 13.2 Ma (lower Miocene–middle Miocene), CN3–CN4 and N7–N9 absent, 5.4 m.y. duration, between Samples 126-792E-24-1, 46–47 cm, and -23R-CC; and

4. from 24.5 Ma through 21.8 Ma, (upper Oligocene–lower Miocene), CN1a, CN1b, and N4 absent, 2.7 m.y. duration, be-

tween Samples 126-792E-28R-1, 62–63 cm, and -29R-1, 106–109 cm.

Although we recognized the absence of CN13 and the lower part of CN14a (0.5 m.y. duration), we are uncertain if the absence of these biozones are due to actual hiatuses or the result of low core recovery.

Benthic foraminifer faunal changes show shallowing water depths from 3.5–4.5 km, in the late early Oligocene, to 1.5–2.3 km today. This estimate means that 1–2 km of total basement uplift has occurred since about 30 Ma in the Bonin inner forearc. The lower trench slope in the Mariana outer forearc, in contrast, has been subsiding since the Eocene (Hussong and Uyeda, 1982).

PALEOMAGNETICS

Introduction

Paleomagnetic measurements were made on the cores recovered from Site 792 to determine magnetostratigraphic ages, to estimate paleolatitude, and to observe the detailed behavior of the geomagnetic field during polarity transitions. Measurements were carried out by means of the 2G cryogenic magnetometer and the fully automatic spinner (FAS) magnetometer (see "Explanatory Notes" chapter, this volume).

Almost all archive halves (except for those highly disturbed by drilling or that consisted of gravels) were measured and demagnetized with the cryogenic magnetometer system. We made our measurements at 5- or 10-cm intervals, except in those sections that contained a polarity transition zone, for which we chose a 0.5-cm interval. The peak alternating field (AF) demagnetization level varied from 2 to 15 mT, according to the magnetic stability of each core section. During measurement, the intensity of the remnant magnetic field around the AF demagnetizing coil in the cryogenic system was periodically monitored. If the field exceeded 500 nT, the inner shield was degaussed to suppress the ambient field.

In addition to the archive half measurements, we measured a number of discrete samples to obtain a more detailed picture of the magnetic properties and to check the reliability of results from archive halves. Discrete samples were measured and stepwise demagnetized with the FAS magnetometer and the AF demagnetizer incorporated into it. Stepwise AF demagnetizations enabled us to discriminate the stable component of remnant magnetization on an orthogonal component vector endpoint plot (Zijderveld diagram). These diagrams show that most discrete samples from this site have stable directions of remanence, and also confirm the reliability of results from archive halves (Fig. 31).

Magnetostratigraphy

Hole 792A

The downhole plot of paleomagnetic direction and polarity in Hole 792A, after AF demagnetization, and the correlation of this data with the standard polarity time scale (Berggren et al., 1985) is shown in Figure 32. All cores were drilled with the APC, and the lower six cores (Cores 126-792A-5H through -10H) were oriented azimuthally with the multishot tool. The natural remanent magnetization (NRM) intensities ranged from 2 (clay) to 700 mA/m (scoria layer).

We recognized two major magnetic polarity intervals in Hole 792A (Fig. 32). The upper one, which ranges from the top of Core 126-792A-1H (0 mbsf) to the top of Section 126-792A-7H-2 (about 58.5 mbsf), is dominated by normal polarity. The lower interval, which ranges from the top of Core 126-792A-7H to the bottom of Core 126-792A-10H (95.0 mbsf), is dominated by re-

Table 7. Age and duration of hiatuses, Site 792.

Age of hiatus (Ma)	Minimum duration (m.y.)	Biozones absent
late Miocene-late Pliocene (5.6–3.6)	2.0	CN10–CN11a, N18–N20
late Miocene (8.9–7.0)	1.9	CN8, *D. antepenultima*
early Miocene-middle Miocene (18.6–13.2)	5.4	CN3–CN4, N7–N9
late Oligocene-early Miocene (24.5–21.8)	2.7	CN1a-b, N4
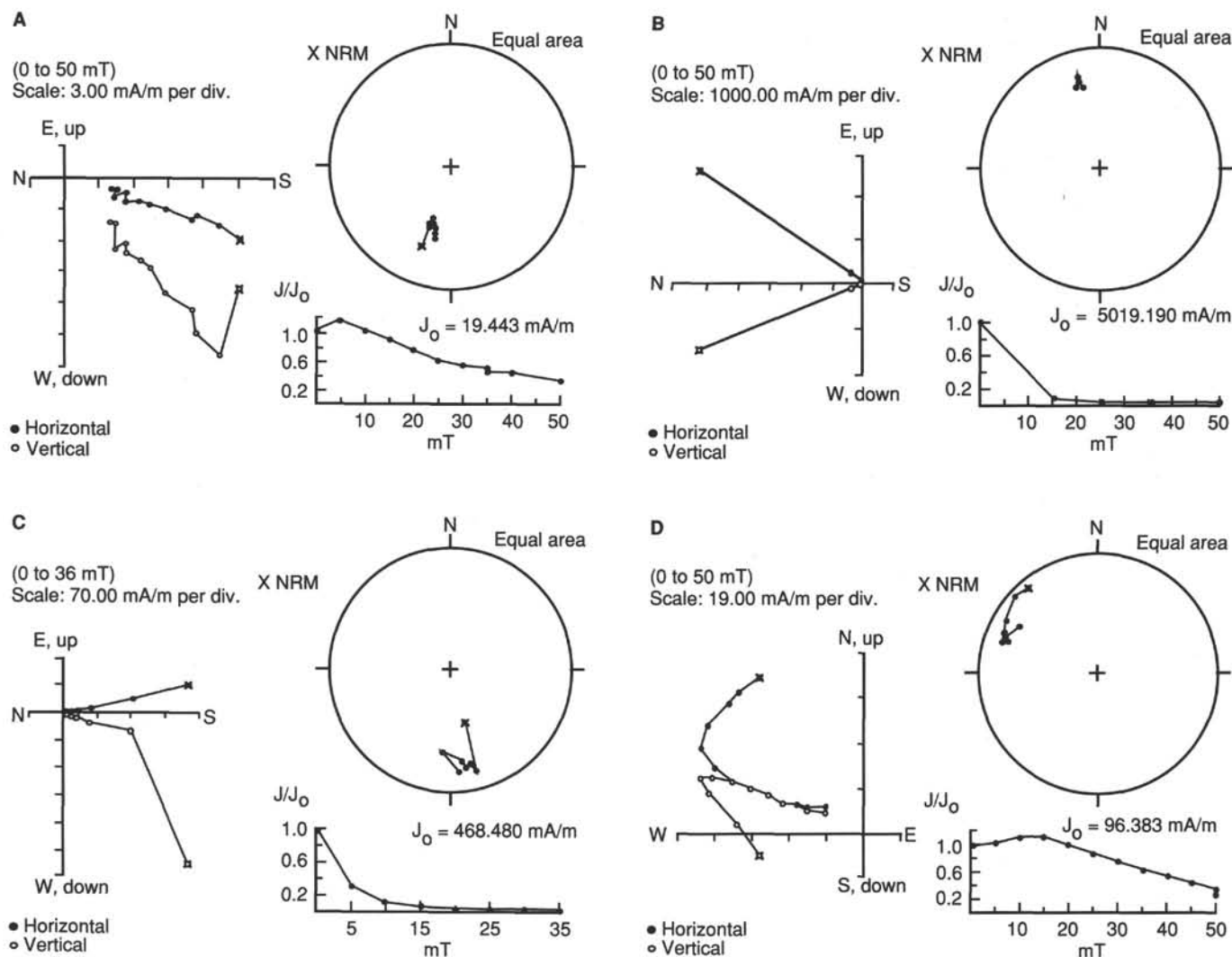
Figure 31. Examples of orthogonal component diagrams, changes of remanence vector direction, and total intensity during stepwise AF demagnetization for discrete samples from Site 792. **A.** Sample 126-792B-2H-1, 57 cm. **B.** Sample 126-792E-15R-1, 35 cm. **C.** Sample 126-792E-59R-2, 61 cm. **D.** Sample 126-792E-52R-5, 64 cm.

versed polarity. On the basis of the biostratigraphic data (see "Biostratigraphy" section, this chapter), we correlated the upper and lower intervals with the Brunhes normal and the Matuyama reversed polarity chrons, respectively. The lower interval also includes several short normal polarity intervals. We correlated the interval from the bottom of Core 126-792A-9H (~80 mbsf) to the middle part of Core 126-792A-10H (88 mbsf) to the Jaramillo normal polarity subchron on the basis of the biostratigraphic data.

Azimuthally corrected declination data were available from Core 126-792A-5H through -10H (37.8–95.0 mbsf). In Cores 126-792A-6H, -7H, -8H, and -10H, the declinations show reasonable directions, nearly aligned with north and south in the normal and the reversed polarity intervals, respectively. However, the declinations from Cores 126-792A-6H and -9H are significantly deflected, particularly from 37.8 to 47.2 mbsf, where the declination varies over 90° and approximates a sine curve. Such deflections may be caused by twisting of the core in the core liner during drilling or handling on the catwalk.

Hole 792B

The downhole plot of paleomagnetic direction and polarity in Hole 792B, after AF demagnetization, and the correlation of

this data with the standard polarity time scale is shown in Figure 33. The upper three cores (Cores 126-792B-1H through -3H, 0–69.2 mbsf) were drilled with the APC and two cores (Cores 126-792B-2H and -3H, 50.0–69.2 mbsf) were oriented azimuthally. Most NRM intensity values ranged from 2 (clay) to 200 mA/m (ash layer).

Three magnetic polarity intervals were recognized in Hole 792B (Fig. 33). The upper interval, which ranges from the top of Core 126-792B-1H to the top of Core 126-792B-3H (0–60 mbsf), is dominated by normal polarity, although the directions from Cores 126-792B-2H and -3H are scattered owing to the coarse lithology (Fig. 34). The middle interval, which ranges from the top of Core 126-792B-3H to the bottom of -9X (~59–~120 mbsf), is dominated by reversed polarity. The lower interval of normal polarity ranges from the top of Core 126-792B-10X (127.1 mbsf) to the bottom of the hole (Core 126-792B-11X). Several short, normal polarity intervals exist in Cores 126-792B-3H and -4X (59.6–78.8 mbsf, Fig. 34). Although some intervals appear to be a result of scatter in coarse materials, others (in the finer sediment types) are probably true reversal zones.

On the basis of the biostratigraphic data (see "Biostratigraphy" section, this chapter), we can correlate the upper, middle, and lower intervals with the Brunhes normal, Matuyama re-

Figure 32. Paleomagnetic data vs. depth (mbsf) for Hole 792A, and correlation with the standard polarity time scale (Berggren et al., 1985). Directional deflections are the result of coarse sediments (g = gravels, s = coarse sandstones) in some intervals.

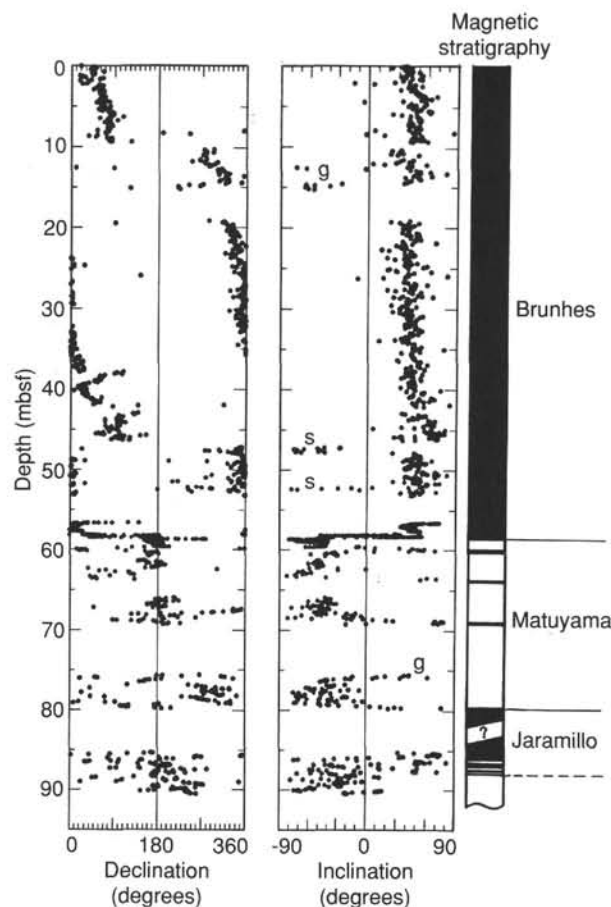Figure 33. Paleomagnetic data vs. depth (mbsf) for Hole 792B, and correlation with the standard polarity time scale (Berggren et al., 1985).

versed, and Gauss normal polarity chrons, respectively. Although normal polarity intervals do exist between 60 and 75 mbsf in the upper Matuyama Chron, the Jaramillo normal polarity subchron seems to have been missed in this hole, as the biostratigraphic datum of 0.83 Ma was not recovered between Sections 126-792B-4X-CC and -5X-CC (~74–~79 mbsf).

Holes 792C and 792D

Only one core-catcher sample was measured in each hole (Sections 126-792C-1X-CC and -1X-CC, Fig. 35). Section 126-792C-1X-CC is normally magnetized, except for the lower 10 cm, which has reversed polarity. Section 126-792D-1X-CC is normally magnetized. We correlated both sections to the Gauss normal polarity chron on the basis of the biostratigraphic data (see "Biostratigraphy" section, this chapter).

Hole 792E

The downhole plot of paleomagnetic direction and polarity in Hole 792E, after AF demagnetization, and correlation of this data to the standard polarity time scale is shown in Figure 36. All cores were drilled with the RCB, and thus the declinations are arbitrary. The NRM intensities ranged from 0.3 (clay) to 700 mA/m (conglomerate) in sedimentary rocks, and from 10 to 1000 mA/m in volcanic rocks.

In Hole 792E, NRM directions indicate that several sections between Cores 126-792E-41R and -78R have been significantly remagnetized. This is apparent from the concentration of NRM

declination values around the 0° or 360° "core north" direction, and by the systematically increasing inclination with depth within these cores (Fig. 37; e.g., Cores 126-792E-48R, 589–598 mbsf, and -50R, 607–617 mbsf). Although the remagnetization features were at least partially removed by AF demagnetization in these particular cores, in other cores they still exist after demagnetization (e.g., Core 126-792E-44R, 550–560 mbsf). The directions of discrete samples taken from these remagnetized intervals are generally concordant with the archive half results, and so the working halves also seem to be remagnetized. Because of this remagnetization problem, we chose to consider only the data from the less contaminated cores. Figure 36 shows the magnetostratigraphic results after the contaminated cores are filtered out.

The many normal and reversed polarity intervals recognized in Hole 792E have been correlated with the standard polarity time scale (Fig. 36) on the basis of biostratigraphic data (see "Biostratigraphy" section, this chapter). These data indicate four hiatuses or unconformity horizons (Fig. 36) in this hole. The polarity intervals found in Hole 792E can be correlated with the Gauss and Gilbert polarity chrons (Chrons 3 and 4, 135.6–193 mbsf), Chron 6 to 8 (193–272 mbsf), Chron 11 (or C5) to Chron C5AN (272–357 mbsf), the C6 Chrons (357–405 mbsf), and the C7 Chrons to Chron 9N (405–780 mbsf). The interval that includes Chron C9 is by far the longest, which reflects the high sedimentation rates associated with the increased abundance of turbidites toward the bottom of the hole (see "Lithostratigraphy and Accumulation Rates" section, this chapter). Although normal and reversed polarities were found in the lowest
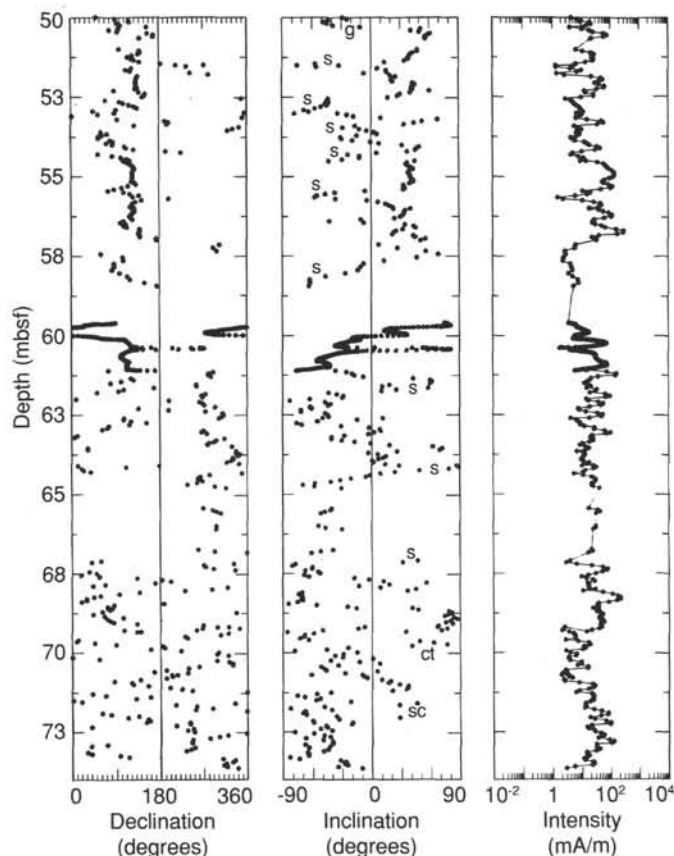
Figure 34. Paleomagnetic data vs. depth (50–74 mbsf) for Hole 792B. Directional deflections are the result of coarse sediments (g = gravels, s = coarse sandstones, ct = coarse tuffs, sc = scorias) in some intervals.

volcanic sequence, a magnetostratigraphic age assignment has not been made because of the lack of biostratigraphic data.

Figure 38 shows the magnetostratigraphic correlation of Site 792 with Site 787. Chrons C8N and C9Na exist in both sites, allowing for a precise correlation between their top and bottom horizons. Although the interval of Chron C9Na (~140 m) is longer at Site 792 than Site 787 (~60 m), the interval of Chron C8 (N + R) at Site 792 (~55 m) is shorter than at Site 787 (105 m). This indicates a sharp decrease in the sedimentation rate above ~500 mbsf at Site 792, which is near the top of a thick turbidite sequence in the upper part of Unit IV (see "Lithostratigraphy and Accumulation Rates" section, this chapter). At Site 787, the intervals that include Chrons C8 and C9 are also dominated by thick turbidites, but there is no major lithologic change near the chron boundary (see "Lithostratigraphy and Accumulation Rates" section, "Site 787" chapter).

Paleolatitude

Figure 39 shows the relationship between the age and the mean inclinations for each core. The data from the cores that display severe remagnetization, as discussed above, or from cores composed primarily of coarse sediment types (i.e., conglomerate, lapilli tuff, and volcanic breccia), were deleted from the figure. The inclinations of cores younger than 13 Ma are concordant with the axial geocentric dipole at the latitude of Site 792, whereas the inclinations for cores older than 20 Ma are generally shallower than the present mean inclination. Thus, we conclude that Site 792, along with Site 787, occupied a lower latitude in late Oligocene time. Future shore-based analyses of
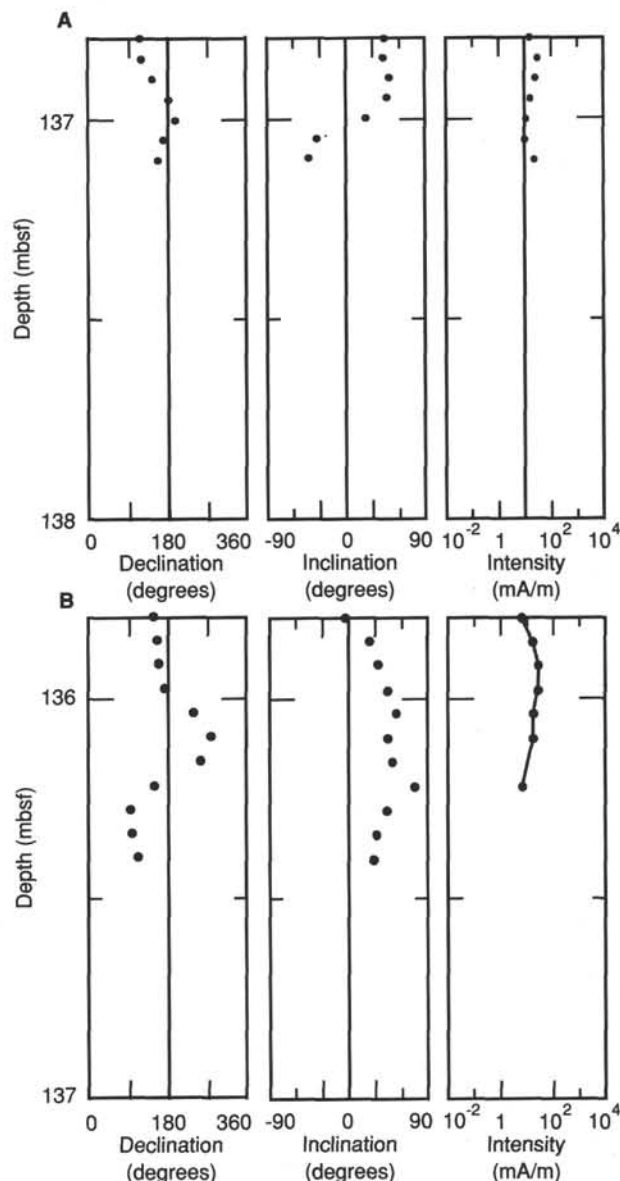
Figure 35. Paleomagnetic data vs. depth (mbsf). **A.** Hole 792C. **B.** Hole 792D.

the data and the measurement of additional discrete samples should refine this result.

The generally lower inclinations associated with the reversed (negative inclination) cores are a result of the incomplete removal of the present-field normal component, which will steepen the inclination vector for the normal cores, but will have the opposite effect on the reversed cores. Rotation of the drilling biscuits, which commonly is a result of rotary drilling into lithified sediments, will have the effect of randomizing the horizontal components of the remanence vector, which would steepen the apparent inclinations of both normal and reversed cores.

Brunhes/Matuyama Reversal Record in Holes 792A and 792B

We carried out detailed measurements on the intervals (Cores 126-792A-7H and 126-792B-3H) that included the Brunhes/Matuyama transition zone (Figure 40). Both piston cores were azimuthally oriented by the multishot tool. The transition curves
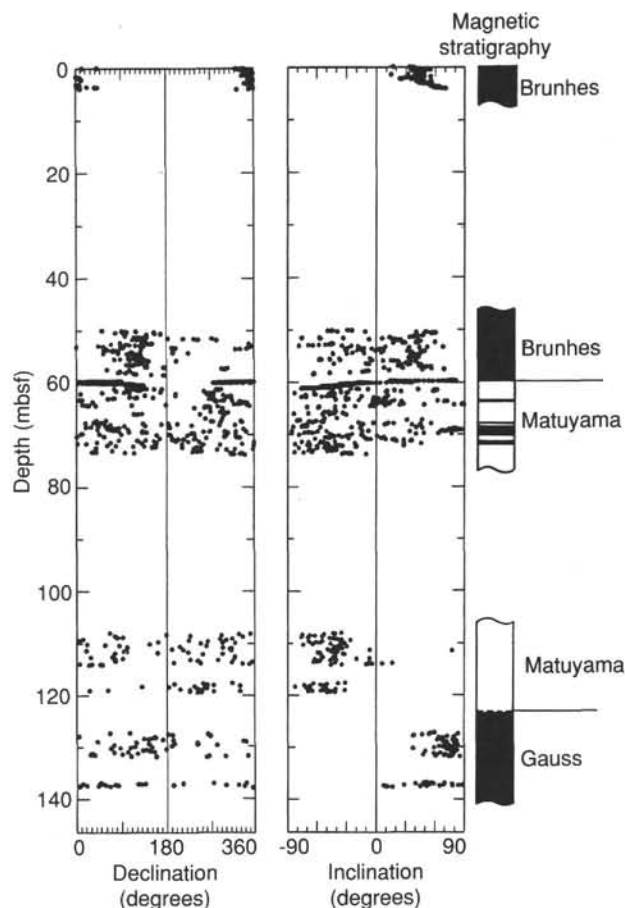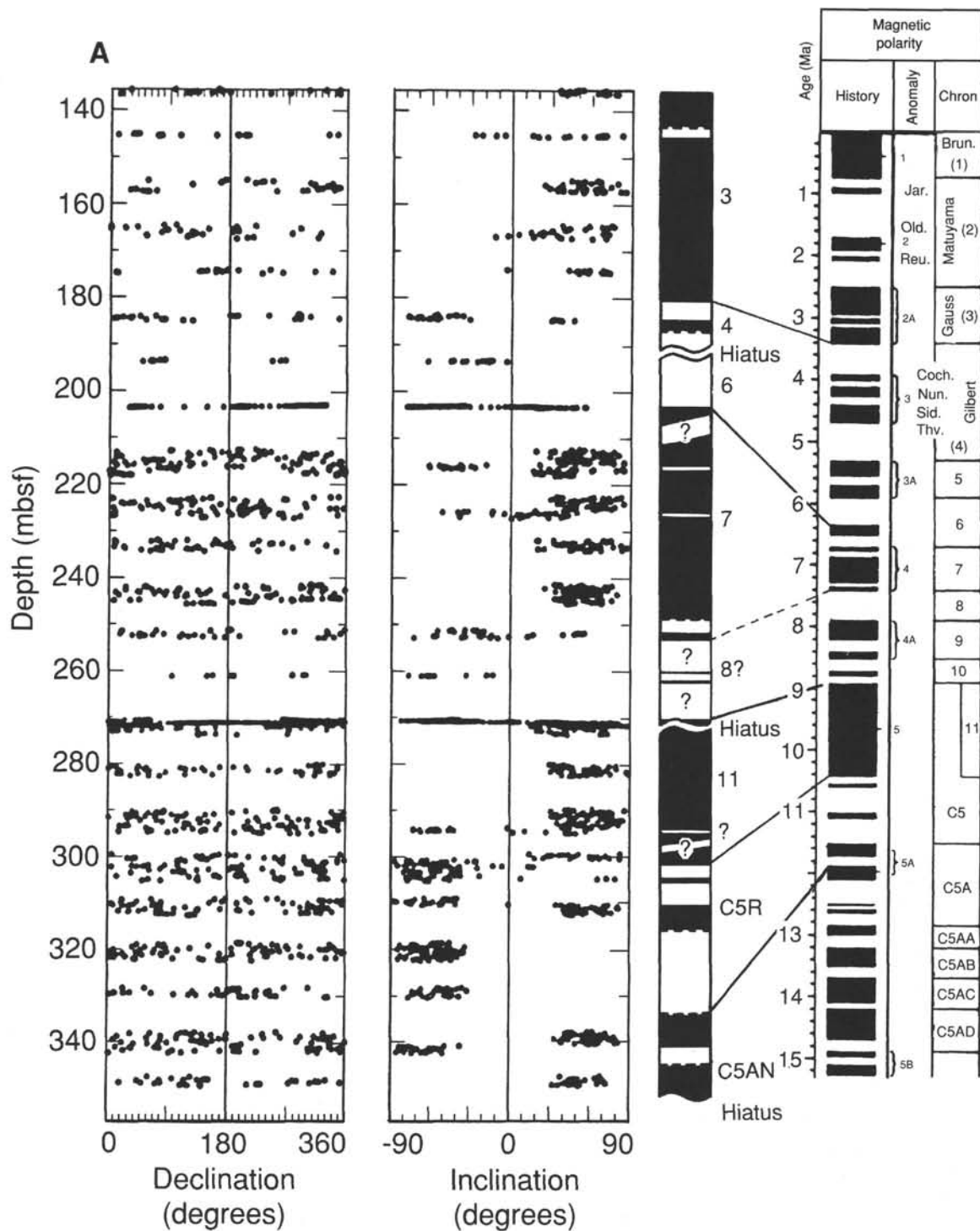
Figure 36. Paleomagnetic data vs. depth (mbsf) for Hole 792E, and correlation with the standard polarity time scale (Berggren et al., 1985). Numbers beside polarity column show chron number; hiatuses (estimated from biostratigraphic data) are indicated. **A.** Cores 126-792E-1R through -23R. **B.** Cores 126-792E-24R through -52R. **C.** Cores 126-792E-54R through -78R. Directional deflections are the result of coarse sediments (cg = conglomerates, lt = lapilli tuffs, s = sandstones) and/or alteration (= a) in some intervals.

of inclination and declination show multiple transitions in Hole 792A and possibly in 792B. Of these, the short reversed polarity interval "A" in Hole 792A and the short normal polarity interval "J" in Hole 792B are likely to be false, because they correspond to intervals disturbed by drilling.

The lithology of the transition zone is laminated clay in Hole 792A, and clay with a sandy burrow and a scoria layer in Hole 792B. The reversed intervals also correspond to an apparent decrease in remanence intensity in Hole 792A. The rapid transitions of polarity and the more extended decrease of intensity
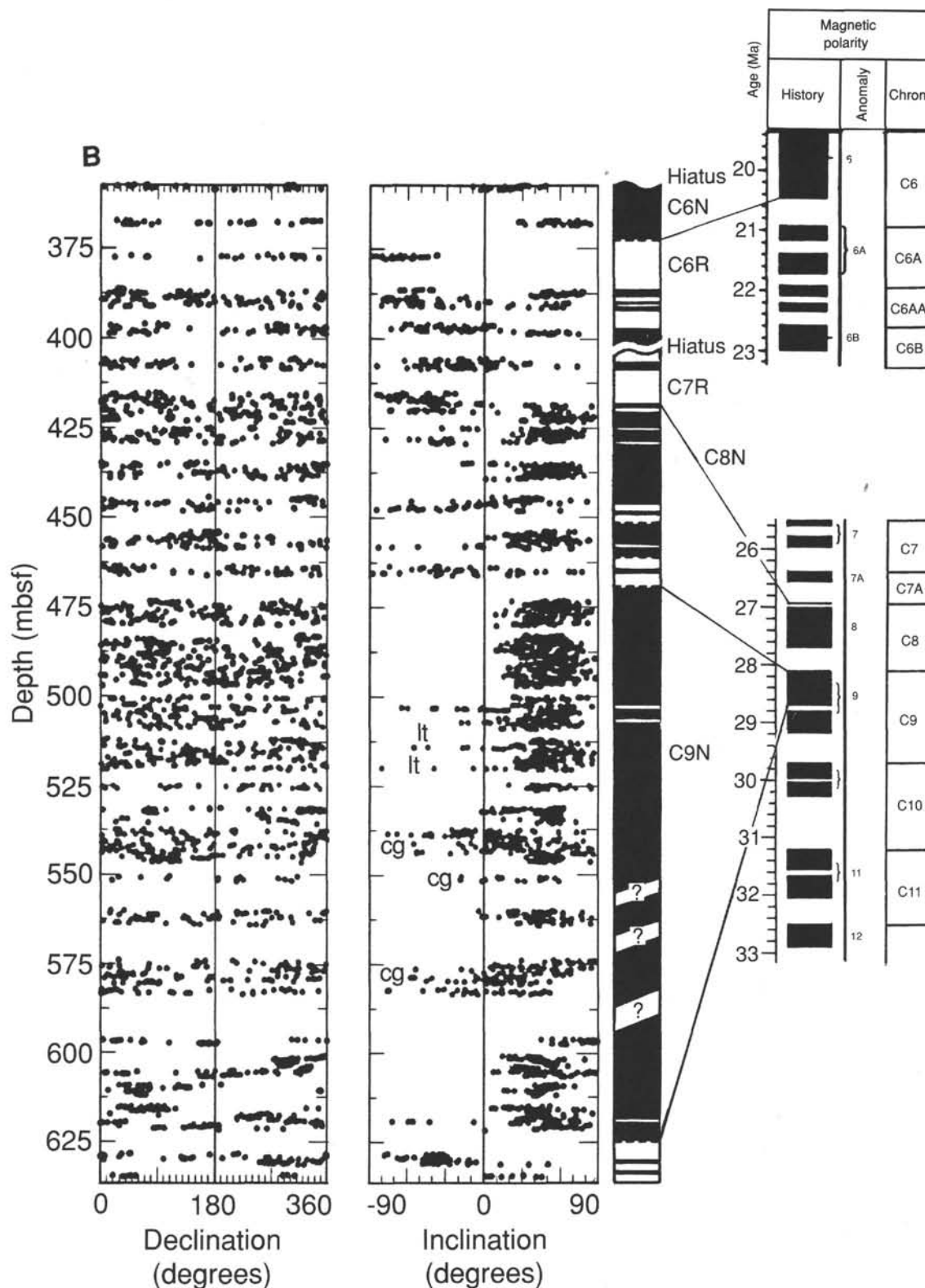
Figure 36 (continued).

were also detected at the Brunhes/Matuyama boundary in Holes 790C and 791B (see "Paleomagnetics" section, "Site 790/791" chapter, this volume). Detailed features of the reversal zone, such as double transitions and intensity decreases, are not apparent in Core 126-792B-3H, probably owing to the greater disturbance in that core.

The length of the transition zone in Hole 792A is about 40 cm, which corresponds to about 4000 yr on the basis of the average sedimentation rate for that portion of the core (see "Lithostratigraphy and Accumulation Rates" section, this chapter, and Fig. 28). Thus, the polarity transition time scale appears to be considerably longer than that for Holes 790C and 791B.
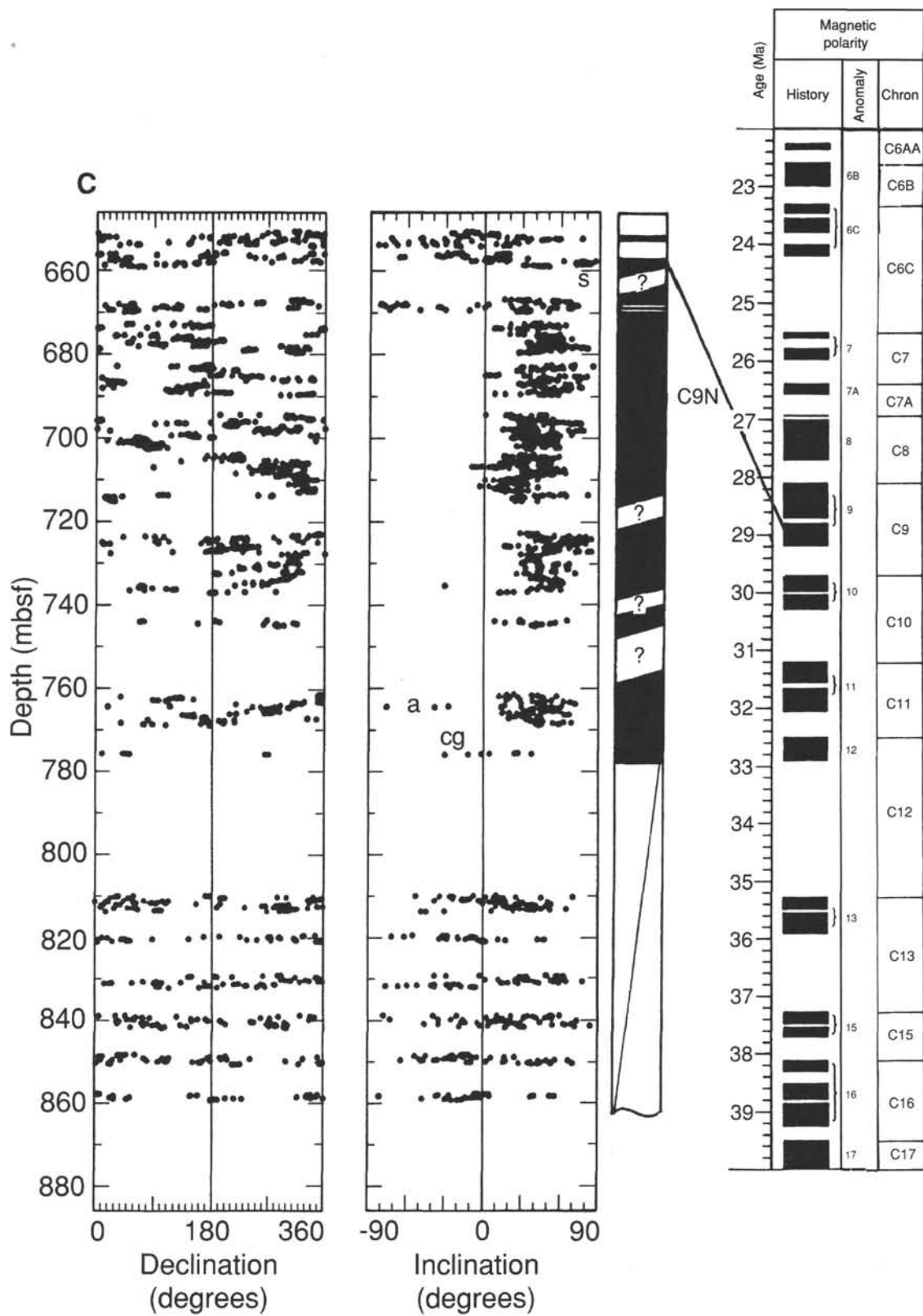
Figure 36 (continued).
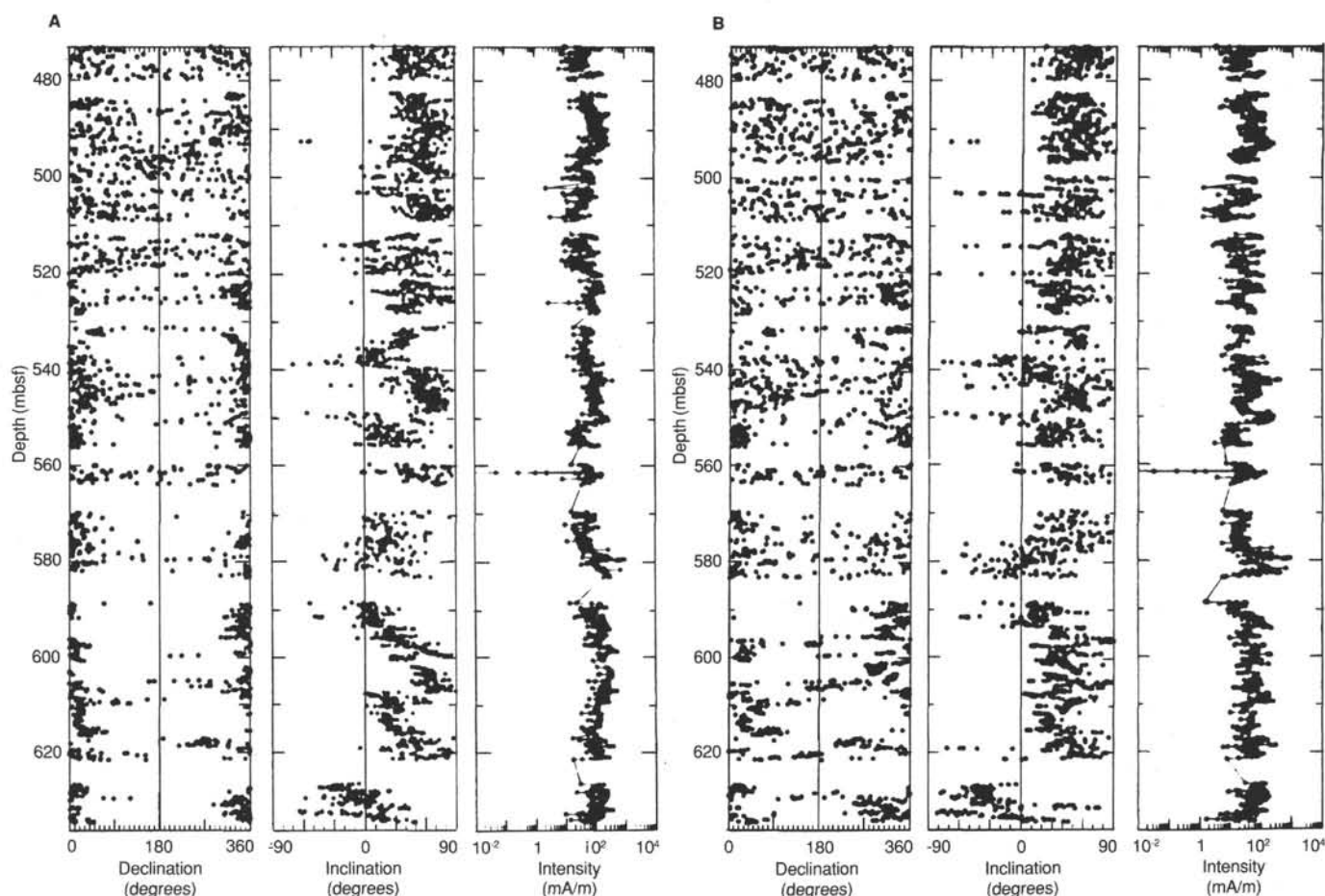
Figure 37. Comparison between the downhole plots before and after demagnetization of Cores 126-792E-36R to -52R. **A.** Before demagnetization (i.e., NRM). **B.** After AF demagnitization (AFD).

However, this may be an averaging effect caused by either the lower resolution that results from a threefold decrease in sedimentation rate (~ 100 m/m.y.) in Hole 792A as compared with Hole 791B (300 m/m.y.), or the ~ 20 cm sensing region for the Z-axis sensor of the cryogenic magnetometer. Within the transition zone in Hole 792A, each of the three "true" inclination reversals (e.g., the top and bottom of intervals C and D; Fig. 40) occur over <10 cm, which, as in Holes 790C and 791B, suggests a time scale of only hundreds of years.

Problems with Measurements

The magnetic field intensity around the AF demagnetizing coil in the cryogenic magnetometer often increased above 1000 nT during measurements on cores from this site, as it did during measurements on materials from Sites 790/791. After the transit to Site 792, the field intensity grew up to 5000 nT, which is about 10% of the total geomagnetic field intensity. The direction of the field varied over time. The correlation of the record of this change with the ship's orientation data obtained from the dynamic positioning (DP) room revealed that the magnetic field intensity in the cryogenic's shield varied with the ship's rotation. Apparently, the change of the ambient field in the laboratory magnetized the inner shield, probably owing to the poor shielding ability of the outer shield. The cause of this phenomenon is still unknown.

The remagnetization in Hole 792E cores (i.e., the clustering of declinations around the core north direction in archive and working halves) shows that the remagnetization was superim-

posed after the core barrels were lifted on deck and before the cores were split into working and archive halves rather than during drilling. This is because the orientation of RCB core barrels in a drill pipe is arbitrary. Thus, the remagnetization must have occurred in a location where the cores reside in the same orientation (e.g., in the core rack, in the GRAPE assembly, or around the super saw). The intensity of the magnetic field at the core rack in the core-cutting room was measured at >0.13 mT, larger than the ambient geomagnetic field by a factor of 3. This high field apparently results from the presence of a magnetized beam within the adjoining wall, and may be one reason for the anomalous inclination and declination trends. Remagnetization may also have occurred when the cores were split, because the ambient field within the super saw assembly was found to be horizontal, or parallel to the N-S direction in the cores.

IGNEOUS PETROLOGY

The first basement rocks ever drilled from beneath the forearc sedimentary basin of the Izu-Bonin arc-trench system were recovered at Site 792. At a depth of about 804 mbsf in Hole 792E, the drill-string penetration rate increased from 3.4 to over 8.6 m/hr, marking the transition from hydrothermally altered volcanogenic sediment to fairly unaltered volcanic rock. A further 82 m of penetration was achieved in basement, resulting in a total hole depth of 885.9 mbsf. We also found other igneous rocks as clasts in the Oligocene to Quaternary conglomerates and gravels of the sedimentary sequence.
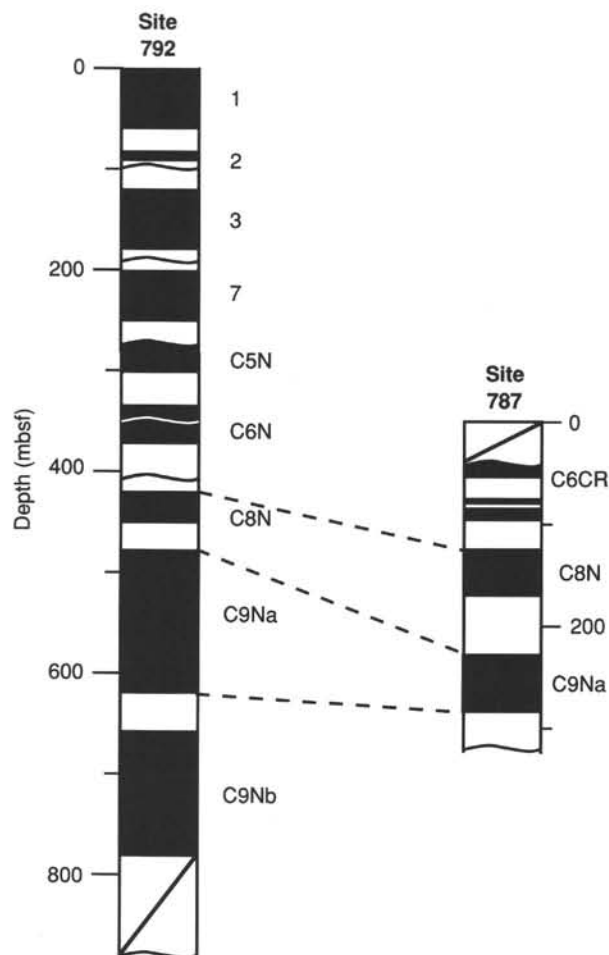
Figure 38. Magnetostratigraphic correlation of the results from Site 792 with those from Site 787. Numbers beside columns are chron numbers from in the standard polarity time scale (Berggren et al., 1985).

Basement Petrology

The dominant volcanic lithology recovered in the basal section of Hole 792E was highly porphyritic, two-pyroxene andesite, the only variant being thin layers of volcaniclastic and hyaloclastic material. On the basis of homogeneous crystallinity, long-core fragments, and the lack of any features indicative of pillow structure, the andesite was considered to be part of a sequence of massive lava flows.

Mineralogically, there is little variation in the porphyritic andesite. Plagioclase is the dominant phenocryst, forming 25%–35% of the mode, with clinopyroxenes and orthopyroxenes together usually <15%. An opaque mineral is present in all rocks as both a groundmass and phenocryst phase. In the uppermost part of Unit 1 (see below), very rare skeletal olivine pseudomorphs were recognized, now replaced by smectite and an opaque mineral. In the lower 70% of the section, from the top of Core 126-792E-73R to the base of the hole, subhedral to rounded quartz grains are present in almost all of the thin sections examined (Fig. 41). The rounded nature of most of these grains indicates dissolution at crystal apices and, therefore, disequilibrium with the original host liquid. However, only a few of the crystals show any signs of embayment. In addition to this possible xenocrystal material, evidence for lithic inclusion is found throughout the sequence. Lithic inclusions take the form of rounded clasts of diabase, quartz-bearing volcanics, and intersertal an-
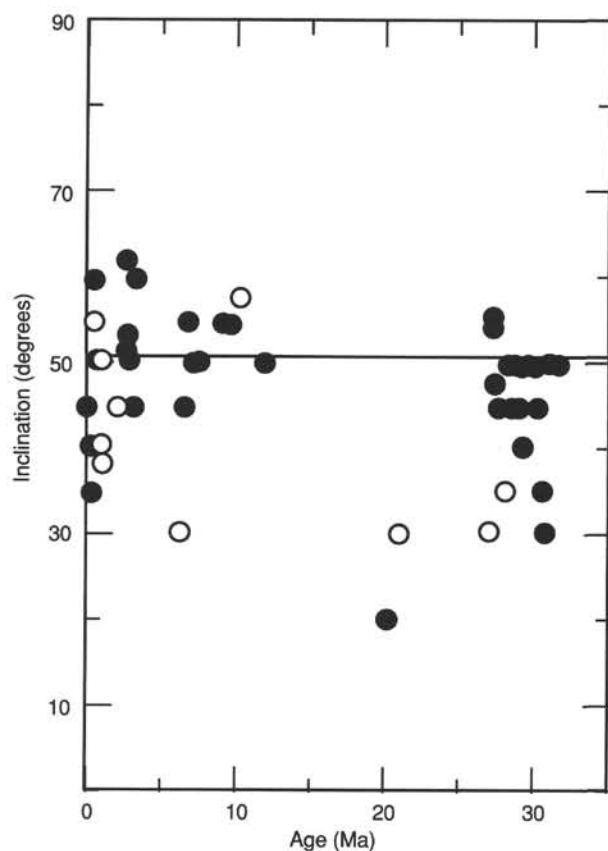
Figure 39. Plot of mean inclination of remanent magnetization from continuous core measurements vs. age (solid circle = positive inclinations, open circle = negative inclinations). Horizontal line shows the inclination value of axial geocentric dipole field at the present latitude of Site 792.

desites. Representative modal analyses of the basement rocks from Hole 792E are given in Table 8.

The groundmass texture of the lava is generally intersertal or vitric-microphyric, although at most levels in the sequence, original glass is not well preserved. Remnants of vitric material are found as pale-brown isotropic interstices in the upper 10 m of the lava and in some fragments within the interlayered hyaloclastites.

Orthopyroxene is the only member of the mineral assemblage that has been significantly affected by posteruptive alteration processes. With the exception of the uppermost 10 m of lava, orthopyroxene is totally pseudomorphed by smectite. The XRD analyses of this pseudomorph material indicate that cristobalite is also present. Some pyroxene grains in the basement and in the overlying sedimentary sequence show all the characteristics of orthopyroxene (form, cleavage, pleochroism, and birefringence), are fresh, have extinction angles ranging from 0° to 10°, and occasionally have multiple twinning. These pyroxenes may represent a late-stage form or resistant compositional variant of the dominant, altered orthopyroxenes. Alteration is most visible in the interflow hyaloclastites. Most of the original glass is now smectite, which gives these layers a green-gray tinge. Another indication of the low-temperature hydrothermal alteration is the fracturing found scattered through the basement section. The fractures are filled with a mixture of celadonite, palagonite, cristobalite, and smectite.

The age of the basement lavas is uncertain owing to the absence of intercalated fossil-bearing sedimentary horizons and
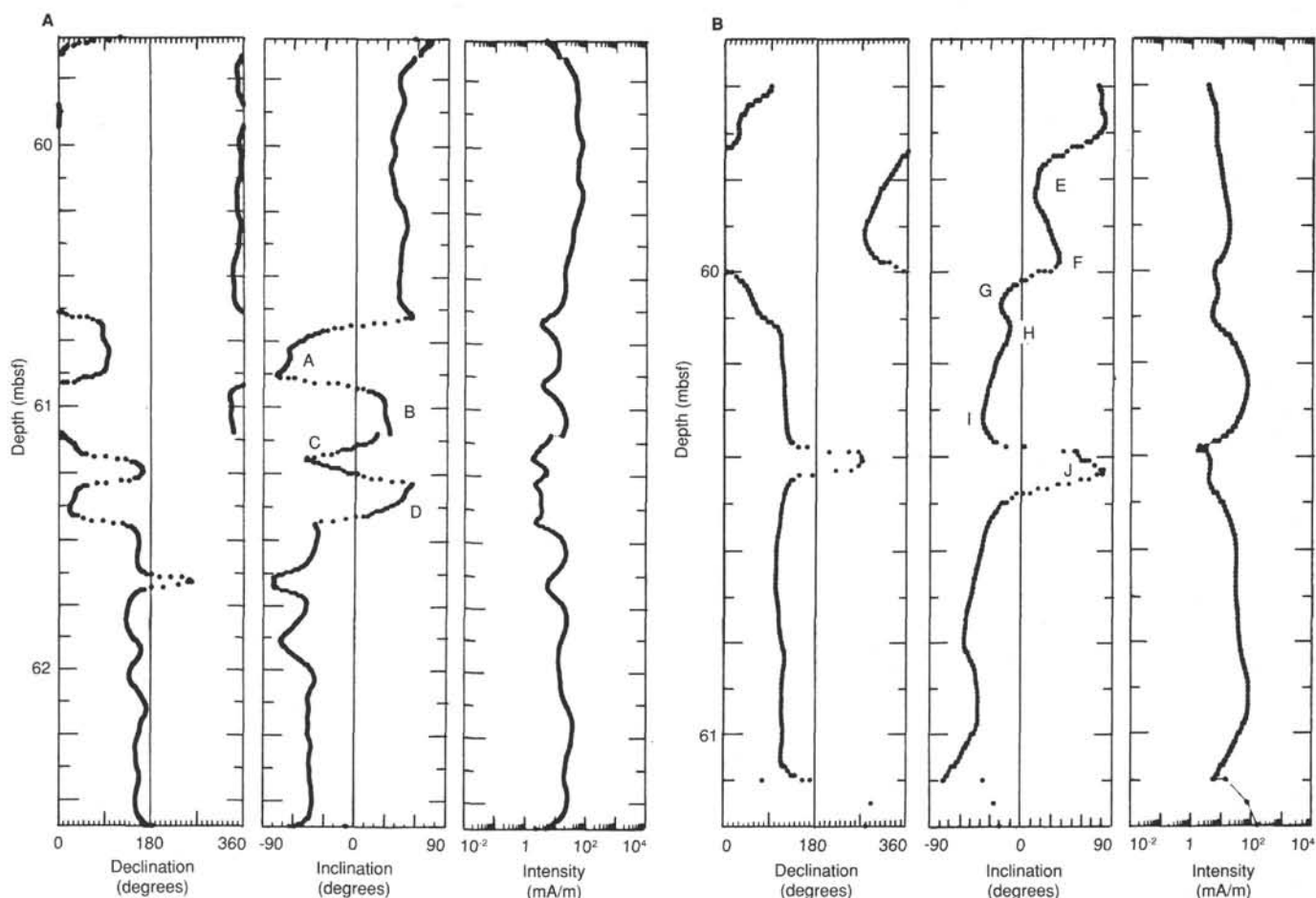
Figure 40. Azimuthally oriented paleomagnetic data vs. depth (mbsf) for the Brunhes-Matuyama polarity transition zone. Possible short polarity intervals in the transition zone are marked A–J; A and J correspond to highly disturbed zones, and probably do not represent true polarity changes. **A.** Hole 792A. **B.** Hole 792B.

barren sediments in the section immediately above basement. We obtained fossil ages that range from early to late Oligocene from the sediments of lithologic Unit IV (see "Biostratigraphy" section, this chapter). Paleomagnetic data indicate that five reversals are present in the Site 792 basement section. Such a narrow spacing of reversals within 82 m of section suggests that the lavas were erupted in a period of rapid reversals (such as the late Eocene) or that the magnetic polarity has been disrupted by hydrothermal activity.

Lava Stratigraphy

We divided the volcanic sequence into five units. This includes three levels of andesitic lava flows with intercalated hyaloclastite bands, and two major hyaloclastite-volcanic breccia horizons (Fig. 42).

Unit 1: Porphyritic Andesite Flow

Interval: Samples 126-792E-70R-1, Piece 1, through -74R-1, Piece 3
Description: pale gray-lilac porphyritic andesite lava (see Table 8 for modal analysis of lava)

This andesite unit is typical of the extrusive rocks recovered in the basement sequence. It contains about 30% euhedral fresh plagioclase, 0.5–3 mm in diameter, with <10% total pyroxenes. The feldspars show oscillatory zoning (Fig. 43) and abundant

two-phase fluid inclusions that were entrained during crystal growth. The clinopyroxenes are easily recognized as bottle-green, euhedral crystals up to 5 mm in length and are always fresh in thin section. However, the orthopyroxenes are dominantly pseudomorphed by smectite and appear as dark laths in hand specimens.

The upper section of Unit 1 (Cores 126-792E-70R and -71R) contains the only examples of fresh orthopyroxene phenocrysts. This material is present as the central portions of large crystals, and is surrounded and crosscut by smectite alteration. In some cases these orthopyroxenes are rimmed by fresh clinopyroxene (Fig. 44), which indicates a change in magma composition or crystallization pressure. The upper section of this unit (Section 126-792E-71R-1) contains rare pseudomorphs of skeletal olivine that were recognized in hand specimens and in one thin section. Toward the base of the unit, quartz first appears as a xenocrystal phase.

Xenoliths are common in the Unit 1 andesites, as well as in Units 3 and 5. All are rounded and <3 cm in diameter. In Unit 1, they consist of coarser grained variants of the andesite, notably orthopyroxene diabase, and intersertal andesite (Fig. 45).

Within Unit 1 are two layers of hyaloclastite material (Fig. 42). The uppermost band is 4 cm thick and probably represents an interflow volcanic-glass spall layer. Other similar horizons were found throughout the volcanic sequence, although it is not
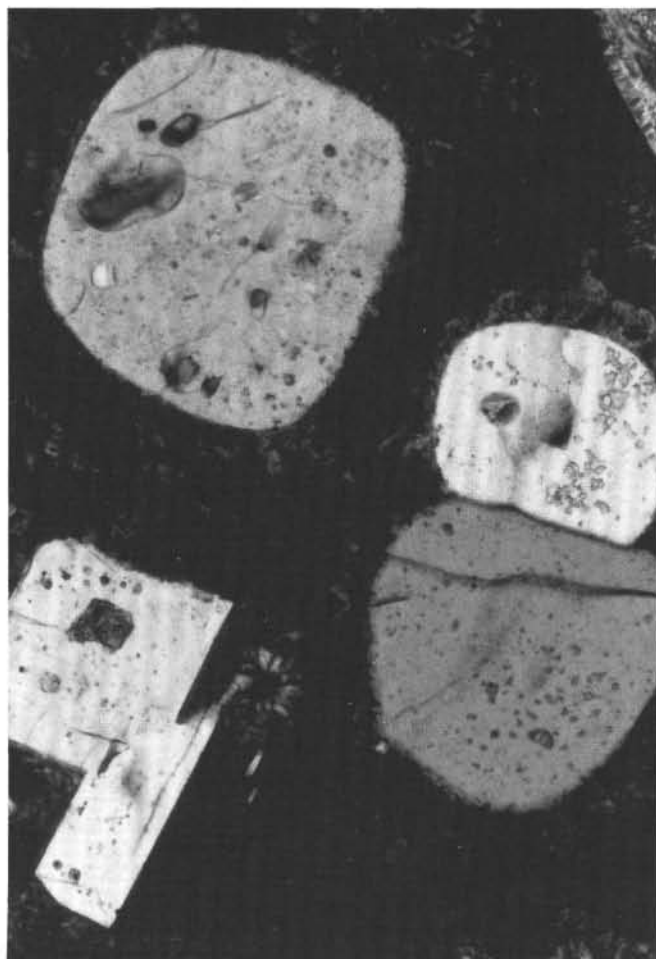
Figure 41. Rounded to subhedral quartz grains in a devitrified glassy matrix. Interval 126-792E-74R-1, 84–85 cm, Unit 2. Cross-polarized light, 95×.

clear with the limited thin sections available if all examples are genuine fragmental deposits or simply glassy sections of flows that are more susceptible to hydrothermal alteration.

Unit 2: Andesitic Hyaloclastite Breccia

Interval: Samples 126-792E-74R-1, Piece 4 through -74R-1, Piece 9

This unit is similar to the hyaloclastite bands seen in Unit 1, but it is represented by only 110 cm of recovered material. It differs from Unit I in that it has 1–4 cm clasts of dense lava sparsely distributed in a matrix of glass shards and xenocryst fragments. The mineral assemblage is similar to the andesite lavas in the lower part of Unit 1. In addition to the quartz crystals, there are clasts of dacitic lava that contain euhedral phenocrysts of quartz (Fig. 46). The majority of the clasts present in the unit and, in particular, the larger clasts are porphyritic andesite similar to the adjacent lavas. The core appears to have numerous dark porphyritic clasts in the crystal-bearing matrix, but on close inspection we found many of these "clasts" to be less-altered sectors of the matrix.

At the base of the unit we observed a contact with the underlying andesite flow. A 3-mm-layer, rich in a fragmented opaque mineral, is present above the contact (see modal analysis B in Table 8, and Fig. 47). We extracted samples from this layer and analyzed them by XRD. Figure 48 presents part of the XRD patterns of the ore-bearing layer and a normal andesite. These

Table 8. Modal mineralogy of basement rocks, Hole 792E.

Core, section, interval (cm)	Depth (mbsf)	Plag	Opx	Cpx	Qtz	Opaques
126-792E-						
71R-CC, 10[a]	812.9	36.5	5.0	3.5	—	1.7
74R-1, 146[b]	840.3	23.1	0.1	6.3	—	8.9
74R-1, 146[c]	840.3	30.7	5.9	1.8	—	2.4
76R-1, 61[d]	858.3	35.5	6.5	1.2	1.5	1.2
78R-1, 134[e]	877.9	32.8	6.5	4.4	1.3	1.3

Note: all analyses performed by point counting (>400 counts per section). Reported values are percentages, with groundmass the residual percentage (including microphenocrysts of plagioclase, pyroxene, and opaques).
[a] Porphyritic andesite, Unit 1.
[b] Basal 1.4-cm-thick layer of hyaloclastite breccia, Unit 2 (upper half of thin section).
[c] Top of porphyritic andesite flow, Unit 3, in contact with Unit 2 (lower half of thin section).
[d] Porphyritic quartz-bearing andesite, Unit 5.
[e] Porphyritic quartz-bearing andesite, Unit 5.

data suggest that the opaque mineral present at the base of Unit 2 is ilmenite, as indicated by the characteristic peak at 0.28 nm, which is notably much less intense in the analysis of normal andesite. The accumulation of ilmenite at the base of Unit 2 indicates that a gravity-settling mechanism may have operated during its formation. Hence, the unit was probably generated as a glassy debris flow in a submarine environment.

Unit 3: Porphyritic Andesite Flows

Interval: Samples 126-792E-74R-1, Piece 10, through -75R-2, Piece 9

This unit is similar to Unit 1 in phenocryst abundance and proportion. Quartz xenocrysts are present in the andesitic assemblage of Unit 3, as they were near the base of Unit 1. Two <10-cm layers of altered pale green hyaloclastite material are present in the unit and probably represent massive flow boundaries. Sample 126-792E-75R-1 (Piece 3), from directly above the lower hyaloclastite band, is a darker, apparently fresher lava. However, in thin section, the melanocratic nature can be assigned to the devitrification of glass.

Unit 4: Volcanic Breccia

Interval: Samples 126-792E-76R-1, Piece 1 through -76R-1, Piece 3

We recovered only 40 cm of this lithology. It consists of rounded, pebble-size clasts of lava in an altered, green hyaloclastic matrix. This matrix is similar to that in Unit 2, but the Unit 4 matrix contains a greater proportion and diversity of lava clasts. We found three clasts in the three pieces recovered: (1) a silicified, celadonite-stained andesitic lava; (2) a porphyritic andesite similar to the adjacent flows; and (3) a metabasaltic rock with no original mineralogy preserved. The latter clast contains abundant prehnite, chlorite, and clay minerals, which have replaced the groundmass and phenocryst assemblage. The only relics of igneous texture are minor lathlike chlorite-clay patches rimmed by smectite, which could be pseudomorphs after orthopyroxene. In hand specimens, the basaltic pebble appears to contain pseudomorphs after a pyroxene, now a mixture of hematite and a white clay mineral.

This volcanic breccia is likely to be associated with a submarine debris flow that entrained glassy debris, crystal fragments, and lava pebbles. The presence of a prehnite-grade basaltic clast suggests that an area of low-grade metamorphic basement was exposed and then entrained during the eruption of the frontal-arc andesites.
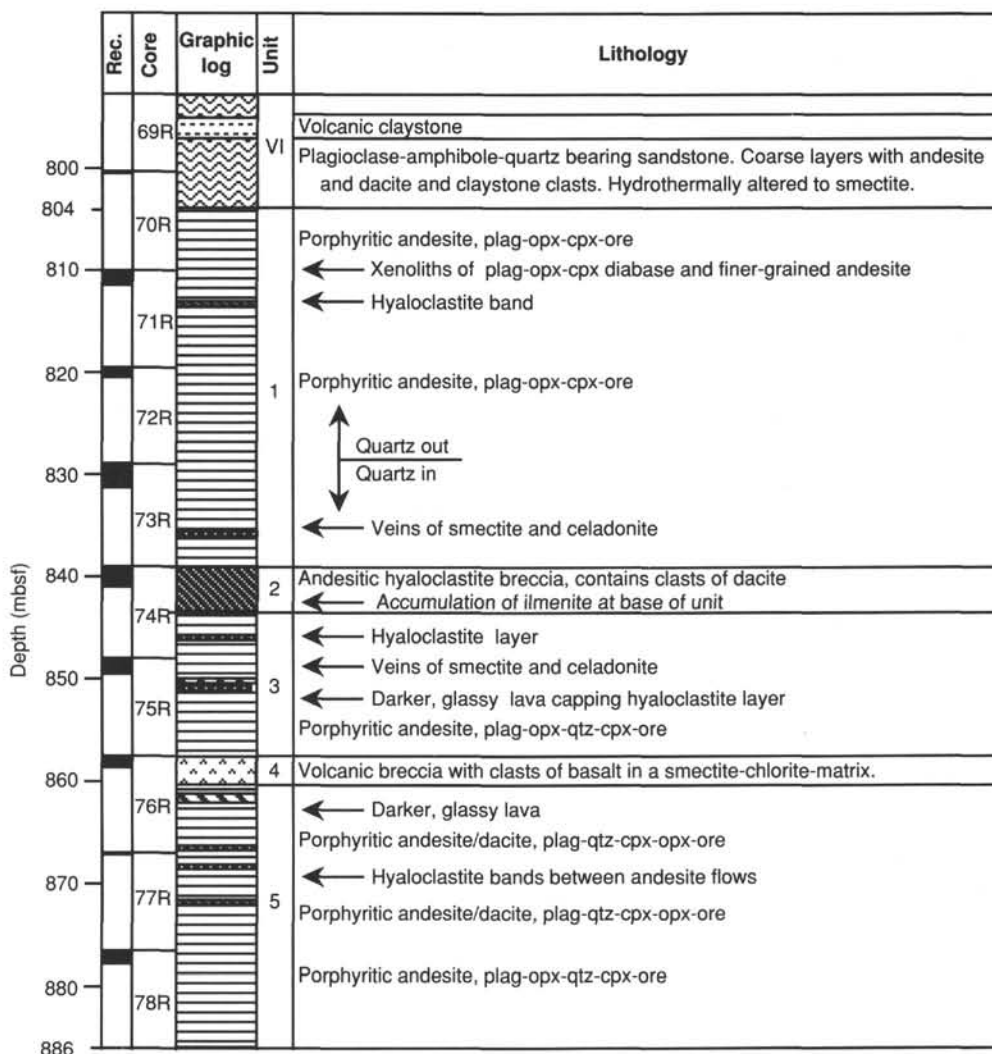
Figure 42. Stratigraphic summary of basement rock sequence at Hole 792E, Cores 126-792E-69R through -78R. Recovery within each core is proportionally expanded to fill the total core penetration.

Unit 5: Porphyritic Andesite Flows

Interval: Samples 126-792E-76R-1, Piece 4, through -78R-2, Piece 2

At the top of this unit, a contact with a 35° dip was observed between the volcanic breccia of Unit 4 and the uppermost andesite flow of Unit 5. The flow top beneath the contact has a pale, 5-mm chill zone underlain by 10 cm of andesite that contains 5-mm-diameter irregular pipe vesicles; notably, this is the only vesiculation observed in the Hole 792E basement section. Unit 5 is similar to Unit 3 in that it contains quartz, interflow hyaloclastic bands, and a darker, glassy interval amidst the porphyritic andesite flows (see Fig. 42).

IGNEOUS GEOCHEMISTRY

The 82-m basement penetration in Hole 792E revealed a sequence of andesitic massive flows with intercalated hyaloclastite bands. We analyzed 11 basement samples and 2 samples of lava clasts from the overlying sedimentary sequence with X-ray fluorescence spectrometry (XRF) for both major and trace elements. The SiO_2 content within the 11 basement samples ranged from 53.3 to 74 wt%, corresponding to a suite of compositional rock types between basaltic andesite and rhyolite (Table 9). However, a classification of individual samples on the basis of silica alone may be erroneous, owing to the presence of quartz xenocrysts

(see "Igneous Petrology" section, this chapter) and alteration (see below). Analyses of clasts from the sedimentary section are probably affected by alteration since the Al_2O_3, K_2O, and loss on ignition results are anomalously high. However, Sample 126-792E-47R-1, 15–20 cm ("Pebble A" in Table 9), shows similar characteristics to the basement lavas of Site 792. This also is true for concentrations and ratios of most trace elements in Pebble A, especially Zr, Y, Rb, Sr, Nb, and V.

Major Element Geochemistry

Low-temperature alteration has affected the Hole 792E basement rocks and must be considered in the interpretation of both major and trace elements. With the exception of Sample 126-792E-78R-1 (Piece 15) and the two silicified samples outlined below, K_2O percentages remain remarkably consistent within the sequence. Two "dacite" samples from Section 126-792E-76R-1 (Table 9) have partially silicified groundmasses; this appears to have had the effect of diluting the concentrations of most elements. However, the dacites do not merely reflect secondary addition of silica to andesite. For example, if the Zr concentration of Sample 126-792E-76R-1 (Piece 4) is increased to the same level as the average andesite from Unit 1, and if silica is proportionally decreased, the SiO_2 level is only reduced from 73.3 to 68.5 wt%, whereas the Unit 1 andesites have around 57 wt% SiO_2. However, this serves to demonstrate that

Figure 43. Typical texture of the porphyritic andesite. Oscillatory zoned plagioclase and euhedral clinopyroxene in a microphyric groundmass of feldspar and glass. Section 126-792E-71R-CC, Unit 1. Cross-polarized light, 95×.

Figure 44. Orthopyroxene phenocryst partially altered to smectite, and plucked during sectioning. This crystal is rimmed by clinopyroxene (pale), and set in a microphyric groundmass. Section 126-792E-71R-CC, Unit 1. Cross-polarized light, 95×.

the original composition lies between the average of Unit 1 andesites and the measured composition. This also may be true for all elements except Fe and V, which are too low.

In addition to the dacites, the geochemistry of most of the basement section from Hole 792E may be affected by hydrothermal alteration. Although this hypothesis must await further laboratory-based analyses, mobile elements (e.g., Rb, K, and Sr) show internally consistent values and variations, comparable to suitable fractionation schemes. The compositional range of incompatible, immobile trace elements (e.g., Ti and Zr) is narrow and presumably reflects fractionation processes. However, the Y and P variation within the sequence is not consistent with simple crystal fractionation. Further studies of the mobility of these elements in this system is required to determine whether they might have been mobilized by alteration.

Major element variation diagrams show well-defined trends with limited scatter. For example, there is a positive correlation between total iron and MgO (Fig. 49), which suggests the removal of an iron-oxide phase at an early stage of fractionation and is characteristic of a calc-alkaline suite. This association is examined further in Figure 50, which compares the Site 792 lavas with selected rock suites on an alkali-iron-magnesium (AFM) plot. The trend indicates a calc-alkaline affinity, with a typical lack of iron enrichment and an associated increase in alkali elements. However, concentrations of K_2O and Na_2O in most of

the andesites are remarkably low and increase by only a small amount as compared to normal calc-alkaline extrusives. The calc-alkaline trend of these samples is confirmed on the FeO*/ MgO-SiO_2 plot (Fig. 51), which also serves to compare the Site 792 basement with the Oligocene tholeiitic lavas drilled in the remnant arc at DSDP Site 448.

Trace Element Geochemistry

Of the 12 trace elements analyzed on the shipboard XRF, only Ce and Ba data are considered unreliable because these concentrations are close to their detection limits. The concentrations of high-field-strength (HFS) elements (Ti, Zr, Y, Nb, and P) in the samples from Site 792 basement lavas are all low relative to normal mid-ocean ridge basalts (MORB) with the same level of SiO_2 or MgO. In addition, ratios between the HFS elements are consistent with a depleted mantle source (e.g., Zr/Y ≤2) that typifies oceanic island-arc systems. The low Ti/Zr and Ti/Y ratios are unlikely to be source characteristics because of the unquantified amount and type of iron-oxide removal during crystallization processes.

The Site 792 basement lavas are low in Rb, Sr, and (as far as analytical methods will allow) Ba, relative to regional arc andesites (Table 10), concordant with the low K_2O values described above. These low-field-strength (LFS) elements normally are en-

Figure 45. Intersertal textured andesite xenolith within porphyritic andesite. Sample 126-792E-71R-3, 33–34 cm, Unit 1. Plane polarized light, 95×.

Figure 46. Dacitic clast in Unit 2 hyaloclastite. This clast contains a quartz phenocryst and a pseudomorph after a mafic phase, set in a devitrified and silicified glass. Sample 126-792E-74R-1, 84–85 cm. Cross-polarized light, 95×.

riched in supra-subduction-zone magmas and especially in calc-alkaline lavas. Thus, it is surprising that the basement lavas of Hole 792E, with such marked calc-alkaline characteristics, are comparatively unenriched in LFS elements.

The basaltic andesite flows in Units 3 and 5 (see Table 9), and the andesites and dacitic lavas from the rest of the sequence, have distinctly different Zr/Y ratios (averages of 7.3 and 1.9, respectively). In light of the major element variations between the evolved and more primitive end members of the sequence, such a difference in Zr/Y is difficult to explain by variations in the degree of partial melting or crystal fractionation. Assuming that the HFS elements are comparatively unaffected by alteration, a more likely explanation is that magmas from two distinct sources were involved.

As a whole, the Site 792 basement lavas have most of the characteristics of a calc-alkaline suite: they are porphyritic, two-pyroxene andesitic lavas, with high aluminum, early oxide mineral precipitation, and concomitant iron depletion. However, they are unusual because of their low LFS element concentrations. In Table 10, an average analysis of the four Unit 1 samples is compared with three examples of Oligocene-Miocene arc volcanic rocks from the western Pacific arc system, and with an average calc-alkaline lava from Japan. None of these lavas provide a suitable analogue for the Hole 792E basement lavas.

SEDIMENT/FLUID GEOCHEMISTRY

We obtained 26 whole-round samples (each 10 cm long) from Holes 792A, 792B, and 792E for electrical resistivity measurements, squeezing of pore water, and sediment and fluid analyses.

Sediment Resistivity

Electrical resistivity could only be measured on 17 of the whole-round samples because of the geometry of the cores. The results are presented in Table 11. The formation factor calculated from the resistivity measurements remains fairly stable from 3.1 to 341 mbsf (Core 126-792E-22R). Near 400 mbsf, the formation factor increases abruptly to a maximum of 15.8 at 620 mbsf (Core 126-792E-51R), then decreases to 7.2 by 796 mbsf (Core 126-792E-69R; see Fig. 52 and Table 11). The formation factors in the upper 350 m are typical for poorly compacted sediments, whereas the maximum readings are similar to those measured in claystones and siltstones. There is a positive correlation between the formation factor and the sonic velocity data (see "Physical Properties" section, this chapter), indicating that some of the decrease in the formation factor below 620 mbsf (Core 126-792E-51R) is the result of changes in the physi-

Figure 47. Accumulation layer at the base of Unit 2. Broken ilmenite grains in a groundmass of glass shards and fragmented phenocrysts. Contact is observed with underlying andesite flow (Unit 3), which contains only sparse opaque mineral. Sample 126-792E-74R-1, 145–148 cm. Plane polarized light, 95×.

Figure 48. X-ray diffraction patterns, Site 792. **A.** Sample 126-792E-74R-1, 146 cm, taken from the accumulation layer at the base of Unit 2. Arrows mark ilmenite d-spacings, filled circles mark feldspar d-spacings. **B.** 126-792E-75R-1, 18 cm, taken from a sample of porphyritic andesite in Unit 3.

Figure 49. Fe_2O_3–MgO variation for Site 792 basement lavas listed in Table 9. Total iron is represented as Fe_2O_3. Open circles = andesite; closed circles = dacite; closed triangles = basalt-andesite.

cal properties of the rock. However, much of the apparent decrease probably is caused by the abundance of smectites. Because of the large ion-exchange capacity of the smectites, their presence can significantly contribute to the electric conductivity of the rock (Atlan et al., 1968).

Sediment Geochemistry

Sediments from Site 792 were analyzed on board ship for inorganic carbon, total carbon, nitrogen, and sulfur (see "Explanatory Notes" chapter, this volume). Analytical results are presented in Table 12. The concentration of organic carbon decreased exponentially from a level of about 0.6%–0.8% in the upper 60 mbsf to about 0.05% below 185 mbsf (Core 126-792E-6R; Fig. 53). This change corresponds to the boundary between lithologic Units I and II (see "Lithostratigraphy and Accumulation Rates" section, this chapter). Thus, the distribution of organic carbon probably is lithologically controlled, and decomposition plays a minor role. The concentration of total sedimentary sulfur varied from less than the detection limit to 0.55%, with the highest concentrations in the interval from 4 to 26 mbsf (Cores 126-792A-1H to -3H), which corresponds to the interval where the pore waters are depleted in sulfate on account of bacterial consumption (see below).

Fluid Geochemistry

The headspace hydrocarbon analyses did not show any gases above background level and thus are not reported.

Because of a shortage of acetylene, calcium and magnesium are the only cations that we could analyze. To clean the hole, drilling mud was pumped between alternate cores. The composition of the drilling mud filtrate is presented in Table 13. On the
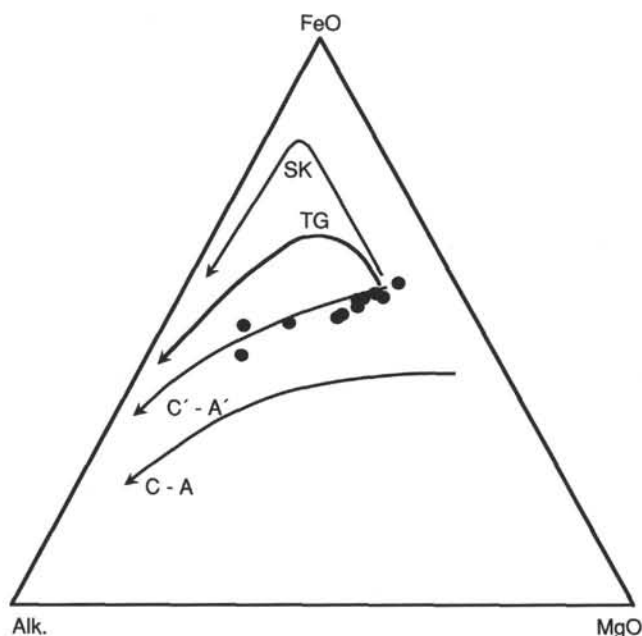
Figure 50. Na$_2$O + K$_2$O–FeO*–MgO (AFM) triangular diagram for Site 792 basement lavas and selected lava suites (SK = Skaergaard fractionation trend; TG = Thingmuli fractionation trend). C–A and C′–A′ represent typical calc-alkaline fractionation trends, and constrain the calc-alkaline lavas of New Zealand, the Cascades, and Aleutians (After Ringwood, 1974).
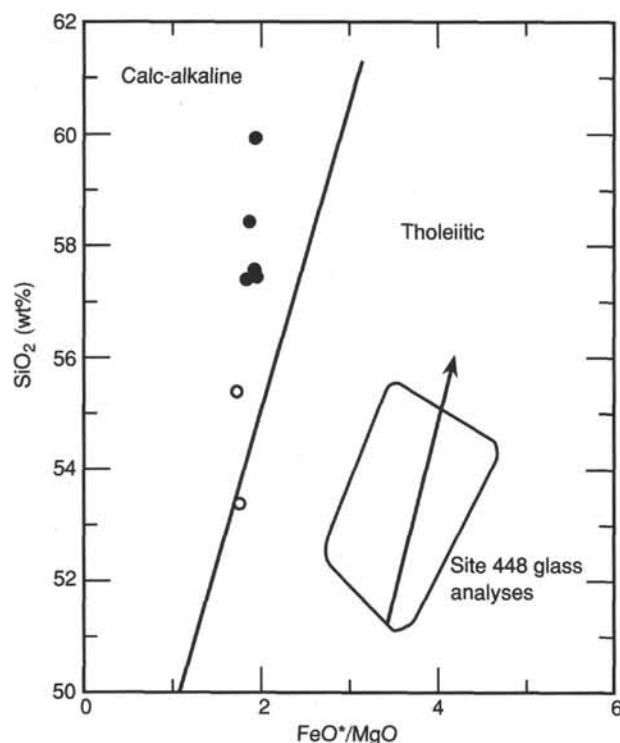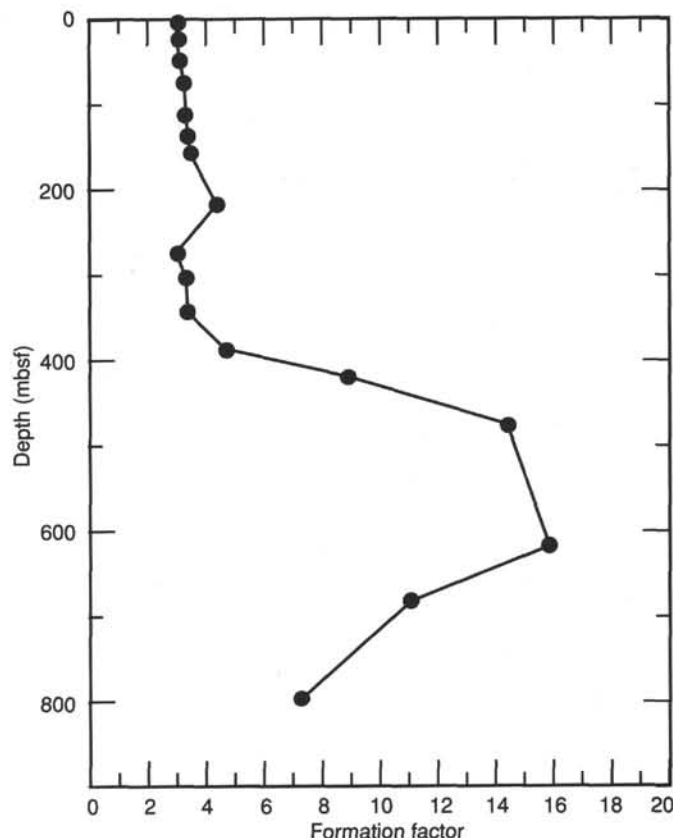
Figure 52. Formation factor of sediments from Holes 792A, 792B, and 792E.

basis of chloride analyses, we estimated that no sample contained >3% drilling-mud filtrate. The concentrations of calcium and magnesium (Fig. 54) are strongly affected by low-temperature alteration of volcanogenic material. Down to about 400 mbsf, the distribution of calcium and magnesium is typical for sediments that overlie basaltic basement, with an almost linear relationship between magnesium and calcium, and a δCa/δMg ratio of about −1.5 (e.g., McDuff, 1981). However, the continuous increase in calcium below 450 mbsf is unusual, and the pore water between 500 and 700 mbsf is the most extensively altered pore water of seawater origin ever sampled by the DSDP/ODP programs (except for pore waters sampled from Site 793). Calcium concentrations reach 170 mM at 600 mbsf (Core 126-792E-48R), which is higher than ever recorded (except at Site 793 and in evaporitic settings). Note that the reaction zone giving rise to these highly altered pore waters is not situated in the basement, but instead lies within the interval between 500 and 700 mbsf. Although some of the samples may have been contaminated by surface seawater, none of the samples below 500 mbsf contains >10% seawater and most contain <5%, if any (as determined from the magnesium data). Thus, we have no doubt that the calcium maximum is real and defines the location of the reaction zone.

There are several possible interpretations for the deep calcium maximum. It may correspond to a zone with a particularly high concentration of reactive volcanogenic components. However, unless the reactions were triggered recently, diffusion would have eliminated the downward gradient by now. It is difficult to envisage any such triggering mechanism in the middle of a sediment column. The action of a process that removes calcium in the lower part of the section seems to us a more plausible interpretation. Although we could not confirm this by shipboard

Figure 51. SiO$_2$-FeO*/MgO variation for Site 792 basement rocks listed in Table 9. Tholeiitic and calc-alkaline fields shown according to Miyashiro (1974). Site 448 data from Scott (1980). Open circles = basalt andesites; closed circles = andesites.

Table 9. Major and trace element data from XRF analysis of basement rocks and two volcanic pebbles from Hole 792E.

Core, section, interval (cm) (126-792E)	47R-1, 15-20	67R-4, 6-10	71R-1, 9-13	71R-3, 34-38	72R-1, 111-115	73R-1, 15-18	74R-2, 53-57	75R-1, 50-55
Piece #	—	—	2	2a	10	2	5	3
Depth (mbsf)	—	—	810.5	818.2	825.5	829.5	845	850.5
Unit	IV	V	1	1	1	1	3	3
Lithology	Pebble A	Pebble B	Andesite	Andesite	Andesite	Andesite	Andesite	Basalt-andesite
SiO_2	50.14	52.13	57.48	57.55	57.48	57.39	59.91	53.26
TiO_2	0.80	0.68	0.54	0.56	0.55	0.56	0.54	0.53
Al_2O_3	20.94	21.35	18.92	18.20	19.04	17.73	17.50	17.66
Fe_2O_3	6.76	8.95	6.90	8.65	7.84	9.26	7.17	12.37
MnO	0.40	0.24	0.15	0.14	0.08	0.10	0.05	0.16
MgO	5.56	5.24	3.28	4.17	3.68	4.68	3.41	6.47
CaO	10.17	6.44	9.67	9.06	9.50	8.99	8.21	7.85
Na_2O	3.41	2.59	2.31	2.21	2.18	1.98	2.57	1.80
K_2O	1.23	2.08	0.23	0.15	0.13	0.14	0.20	0.12
P_2O_5	1.07	0.31	0.11	0.05	0.13	0.04	0.04	0.02
LOI	7.04	3.67	1.01	0.81	1.05	1.10	1.44	2.23
Total	100.48	100.01	99.59	100.74	100.61	101.07	99.60	100.24
Ti	4796	4077	3237	3357	3297	3357	3237	3177
P	4666	1352	480	218	567	174	174	87
Zr	41	80	40	40	42	41	39	44
Y	22	29	20	20	28	22	18	6
Rb	2.0	10.8	1.4	1.4	1.2	1.3	2.4	1.6
Sr	174	212	176	176	188	175	166	155
Ba	20	175	31	31	16	12	28	33
V	256	150	258	258	260	244	242	186
Nb	0.7	1.1	0.9	0.9	1.3	1.1	0.6	0.5
Ni	10	5	9	9	9	9	6	5
Cr	13	n	12	12	11	12	0	0
Zn	93	77	86	86	82	93	79	134
Cu	26	30	34	34	28	27	39	18
Ce	2	6	N	N	3	N	7	N
Mg#	64.42	56.31	51.13	51.48	50.81	52.66	51.14	53.51

Note: major and minor element contents in wt%, trace element contents in ppm; N = no data.

analysis, the concentration of sodium probably increases downward from the calcium maximum to maintain the charge balance. These concentration trends are opposite to what is observed during seawater/basalt interactions and actually shift the composition of the pore waters toward seawater composition. Thus, the possibility that the downward decrease in calcium below 600 mbsf (Core 126-792B-48R) is caused by recent lateral movement of seawater in the lower part of the sediment section should be considered. Although of more recent origin, the circulating seawater must have been in the sediments for a sufficiently long time to have its magnesium removed by water/rock interactions. Unit IV consists of mottled and brecciated, highly altered, volcanic sandstone with claystone interclasts (see "Lithostratigraphy and Accumulation Rates" section, this chapter). The high porosity of this unit (average 38%, see "Physical Properties" section, this chapter) and the low formation factor (Table 11) indicate that this unit is the most permeable interval below 400 mbsf. The extensive alteration of this unit is in itself an indication of a high cumulative water/rock ratio.

The calcium gradient between 300 and 500 mbsf is much steeper than would be established by simple diffusion in a homogeneous, porous media. This is caused by the rapidly changing diffusive properties of the rocks in this region (as revealed by the formation factor; Fig. 52). Most probably, the growth of authigenic smectite at the expense of volcanic glass constitutes the major sink for magnesium. Calcium is probably derived from this reaction and from the alteration of plagioclase. Shipboard (semiquantitative) XRD analyses show that at about 400 mbsf there is a pronounced increase in the abundance of smectites, and that the zeolite facies changes downhole from phillipsite and analcime to wairakite. Heulandite, clinoptilolite, and stilbite are present at 670 mbsf (see "Lithostratigraphy and Accumulation Rates" section, this chapter). Charge balance calculations

show that the pore waters are severely depleted in sodium, although we could not confirm this by shipboard analyses. The most likely sink for sodium is the formation of zeolites (see "Lithostratigraphy and Accumulation Rates" section, this chapter).

Sulfate concentration profiles in marine sediments usually have a steep gradient close to the seafloor. However, except for a subsurface sulfate minimum at 26.55 mbsf (Core 126-792A-3H), the sulfate concentration remains close to seawater values down to 303 mbsf (Core 126-792E-18R), and then decreases to a level between 15 and 17 mM (Fig. 54). The peak in the ammonium profile at 26.55 mbsf (Core-126-792A-3H; Fig. 54) suggests that the subsurface sulfate minimum is the result of bacterial activity. Below this maximum, the concentration of ammonium decreases toward the bottom of the hole, indicating that the low-sulfate concentrations below about 500 mbsf are not related to bacterial activity.

Saturation index estimates (determined on the basis of thermodynamic data from National Bureau of Standards) demonstrate that below about 500 mbsf, pore waters are saturated with respect to gypsum (Fig. 54). Evidently, the sulfate concentrations are controlled by the precipitation of gypsum in response to the release of calcium by the low-temperature alteration of volcanogenic material. Thus, the fracture-filling gypsum observed below 500 mbsf (see "Lithostratigraphy and Accumulation Rates" section, this chapter) is not necessarily linked to a previous hydrothermal event, but may be precipitating at the present time. The data presented in Figure 54 show that the reactions taking place in the alteration zone consume silica faster than it can be supplied by diffusion from above. The considerable variations in the dissolved silica concentration in this region indicate that the reaction zone may consist of subzones characterized by different reactions or reaction rates.

Table 9 (continued).

	76R-1, 43–46	76R-1, 60–64	76R-1, 85–87	78R-1, 80–85	78R-1, 131–136
	4	6	7	9	15
	860.1	861	862.2	880.2	883
	5	5	5	5	5
	Dacite	Basalt-andesite	Dacite	Andesite	Dacite
	73.24	55.28	74.04	58.41	64.87
	0.41	0.56	0.40	0.51	0.49
	14.03	19.32	14.43	18.74	17.77
	2.92	10.04	3.72	7.94	5.08
	0.02	0.14	0.02	0.07	0.03
	0.87	5.36	0.79	3.96	1.75
	6.13	8.31	6.23	8.88	8.35
	2.23	2.04	2.31	2.30	2.45
	0.24	0.14	0.22	0.14	0.37
	0.06	0.02	0.04	0.04	0.17
	1.28	3.10	1.49	1.62	0.69
	100.15	101.21	102.20	100.99	101.33
	2458	3357	2398	3057	2938
	262	87	174	174	741
	35	49	36	44	42
	15	7	22	10	31
	2.7	2.1	3.1	1.2	3.9
	134	166	138	170	162
	42	2	211	6	43
	153	247	125	260	233
	1.4	0.7	1.0	0.7	1.2
	0	7	4	5	4
	0	2	2	8	4
	41	98	78	80	55
	26	17	31	28	18
	2	N	1	N	9
	39.61	54.02	31.85	52.33	43.12

Table 10. Representative analyses of Oligocene and Miocene basalts and andesites from Philippine Sea arc systems.

	Average Unit 1 andesite Hole 792E[a]	Palau-Kyushu Ridge Hole 448A[b]	Palau-Kyushu Ridge Site 1397[c]	West Mariana Ridge Hole 451[b]	Average Japan calc-alkaline[b]
SiO_2	57.94	50.00	54.20	49.90	53.80
TiO_2	0.56	1.11	1.15	0.71	0.95
Al_2O_3	18.67	15.30	19.00	18.20	17.79
FeO^*	7.40	11.09	9.90	8.71	8.80
MnO	0.12	0.19	0.22	0.25	0.19
MgO	3.99	4.54	2.50	5.75	5.87
CaO	9.38	9.73	8.50	10.88	8.79
Na_2O	2.19	3.55	3.50	2.44	2.76
K_2O	0.16	1.38	0.45	0.73	0.62
P_2O_5	0.08	0.14		0.14	
Total	100.50	98.74	99.42	97.71	99.57
Ni	9	16	40	8	
Cr	12	25	260	31	
Rb	1	13		9	14
Sr	179	171	270	478	550
Zr	41	71		45	40
Y	23	31		19	15

Note: Major elements oxides reported in wt%, trace elements in ppm.
[a] Average of four analyses.
[b] Data from Mattey et al. (1980).
[c] Data from IGCP "Ophiolites" project (1977).

Table 11. Sediment resistivity (R_s), measurement temperature, pore-water resistivity (R_{pw}) at 25°C, and formation factor of sediments from Holes 792A, 792B, and 792E.

Core, section, interval (cm)	Depth (mbsf)	Cell constant (m)	R_s (ohm-m)	Temp. (°C)	R_{pw} (ohm-m)	F
126-792A-						
1H-5, 140–150	7.45	0.1002	0.855	11.9	0.201	3.1
3H-5, 140–150	26.55	0.1016	0.826	12.5	0.199	3.1
6H-2, 140–150	50.15	0.0997	0.952	12.6	0.198	3.1
9H-1, 89–97	76.54	0.1009	0.872	14.4	0.198	3.4
126-792B-						
8X-3, 140–150	112.35	0.1008	0.857	14.0	0.198	3.3
11X-1, 75–85	137.60	0.0996	0.866	14.2	0.199	3.4
126-792E-						
3R-2, 60–70	156.95	0.1024	0.945	11.8	0.199	3.5
9R-4, 40–50	217.55	0.1023	1.072	15.7	0.198	4.4
15R-2, 115–125	273.20	0.0978	0.697	18.8	0.199	3.0
18R-3, 115–125	303.70	0.1002	0.760	18.3	0.199	3.3
22R-2, 140–150	340.85	0.0975	0.802	16.1	0.198	3.3
27R-1, 27–37	386.62	0.0998	1.111	17.7	0.198	4.7
30R-5, 11–21	421.36	0.0998	2.185	16.6	0.201	8.9
36R-4, 67–77	478.42	0.1012	3.571	15.4	0.198	14.4
51R-2, 140–150	620.05	0.0962	3.723	16.2	0.192	15.8
57R-5, 140–150	682.55	0.1024	2.624	16.9	0.197	11.0
69R-4, 136–146	796.51	0.1007	1.814	15.6	0.202	7.2

PHYSICAL PROPERTIES

Introduction

Multi-sensor track (MST) logging, thermal conductivity, vane shear strength, electrical resistivity, Hamilton Frame (HF) compressional sonic velocity, index properties, and $CaCO_3$ content measurements were made on relatively undisturbed sections of APC and XCB cores from Holes 792A and 792B. We took only one sample for carbonate analysis from Hole 792C, and two samples from the 84 cm of sediment recovered from Hole 792D.

Thermal conductivity, HF sonic velocity, index property, and carbonate analyses were performed on rotary-drilled sections

Table 12. Concentration of carbonate, organic carbon, total nitrogen, and total sulfur in Site 792 sediments.

Core, section, interval (cm)	Depth (mbsf)	Inorg. carbon (%)	CaCO$_3$ (%)	Total carbon (%)	Org. carbon (%)	Total N (%)	Total S (%)
126-792B-1H-1, 6–7	0.06	1.32	11.0	1.90	0.58	0.05	0.11
126-792A-1H-1, 70–73	0.70	1.20	10.0	1.56	0.36	0.02	0.09
126-792B-1H-1, 113–117	1.13	1.31	10.9				
126-792B-1H-2, 47–48	1.97	2.45	20.4				
126-792B-1H-2, 47–48	1.97	2.45	20.4	3.09	0.64	0.05	0.04
126-792A-1H-2, 64–65	2.14	0.07	0.6	0.09	0.02	LD	0.2
126-792A-1H-2, 96–99	2.46	1.32	11.0	1.69	0.37	0.03	0.13
126-792B-1H-2, 102–105	2.52	1.39	11.6				
126-792B-1H-3, 50–53	3.50	1.61	13.4				
126-792B-1H-3, 95–96	3.95	1.90	15.8	2.66	0.76	0.05	0.26
126-792B-1H-3, 95–96	3.95	1.90	15.8				
126-792A-1H-3, 99–102	3.99	1.48	12.3	1.88	0.40	0.03	0.19
126-792A-1H-4, 108–111	5.58	0.95	7.9	1.33	0.38	0.02	0.11
126-792A-1H-5, 140–150	7.40	0.50	4.2	0.67	0.17	LD	0.16
126-792A-1H-6, 113–116	8.63	0.21	1.7	0.26	0.05	LD	0.08
126-792A-1H-7, 24–27	9.24	1.92	16.0	2.22	0.30	0.02	0.05
126-792A-2H-1, 129–131	10.99	3.22	26.8	3.66	0.44	0.03	0.03
126-792A-2H-2, 102–105	12.22	1.82	15.2	2.26	0.44	0.03	0.15
126-792A-2H-3, 120–122	13.90	0.59	4.9	0.72	0.13	0.01	0.14
126-792A-2H-4, 39–41	14.59	0.08	0.7	0.08	LD	LD	0.22
126-792A-3H-2, 56–59	21.16	2.10	17.5	2.49	0.39	0.03	0.55
126-792A-3H-3, 78–81	22.88	3.98	33.2	4.27	0.29	0.02	0.05
126-792A-3H-4, 122–125	24.82	1.51	12.6	1.89	0.38	0.03	0.14
126-792A-3H-5, 91–94	26.01	2.14	17.8	2.60	0.46	0.03	0.13
126-792A-3H-5, 140–150	26.50	2.08	17.3	2.43	0.35	0.03	0.09
126-792A-3H-7, 22–25	28.32	2.27	18.9	2.60	0.33	0.03	0.04
126-792A-4H-1, 99–102	29.39	1.85	15.4	2.17	0.32	0.03	0.06
126-792A-4H-2, 118–121	31.08	2.54	21.2	2.74	0.20	0.02	0.03
126-792A-4H-3, 64–67	32.04	3.29	27.4	3.59	0.30	0.02	0.05
126-792A-4H-4, 116–119	34.06	4.33	36.1	4.87	0.54	0.04	0.05
126-792A-4H-5, 89–92	35.29	3.33	27.7	3.69	0.36	0.03	0.15
126-792A-4H-7, 40–43	37.80	1.23	10.2	1.48	0.25	0.02	0.08
126-792A-5H-1, 101–104	38.81	3.00	25.0				
126-792A-5H-2, 34–37	39.64	0.59	4.9	0.63	0.04	LD	0.09
126-792A-5H-3, 93–95	41.73	2.26	18.8				
126-792A-5H-4, 129–131	43.59	2.30	19.2				
126-792A-5H-6, 62–65	45.92	2.39	19.9				
126-792A-6H-1, 117–119	48.37	2.24	18.7				
126-792A-6H-2, 67–69	49.37	0.94	7.8				
126-792A-6H-2, 140–150	50.10	1.67	13.9	1.97	0.30	0.03	0.06
126-792A-6H-3, 26–27	50.46	2.11	17.6				
126-792B-2H-1, 110–113	51.10	2.87	23.9	3.33	0.46	0.02	0.02
126-792B-2H-2, 64–67	52.14	1.45	12.1				
126-792A-6H-4, 118–119	52.88	2.56	21.3				
126-792B-2H-4, 70–73	55.20	2.03	16.9				
126-792B-2H-5, 63–66	56.63	2.46	20.5	3.00	0.54	0.03	0.05
126-792A-7H-1, 95–96	57.55	0.62	5.2	0.86	0.24	0.01	0.05
126-792A-7H-2, 91–94	59.01	3.56	29.7				
126-792B-3H-1, 12–15	59.72	2.01	16.7				
126-792A-7H-3, 74–75	60.34	1.30	10.8				
126-792B-3H-3, 83–86	63.43	0.08	0.7	0.08	0.00	LD	0.07
126-792A-8H-1, 68–70	66.68	1.11	9.2				
126-792B-3H-6, 40–43	67.50	0.03	0.2				
126-792A-8H-2, 92–94	68.29	0.60	5.0	0.68	0.08	0.01	0.06
126-792B-3H-7, 39–42	68.99	2.06	17.2	2.36	0.30	0.02	0.18
126-792A-8H-3, 35–38	69.22	0.65	5.4				
126-792B-4X-1, 24–27	69.44	1.77	14.7				
126-792B-4X-2, 130–133	72.00	0.17	1.4	0.18	0.01	LD	0.18
126-792B-4X-3, 110–113	73.30	1.06	8.8				
126-792A-9H-1, 71–74	76.31	1.42	11.8				
126-792A-9H-1, 87–97	76.47	2.01	16.7	2.28	0.27	0.02	0.06
126-792A-9H-2, 100–103	77.82	3.55	29.6				
126-792A-9H-3, 17–20	78.49	2.95	24.6				
126-792A-9H-4, 20–23	79.39	2.06	17.2	2.34	0.28	0.01	0.05
126-792A-10H-1, 112–115	86.42	3.48	29.0				
126-792A-10H-3, 108–110	88.19	3.67	30.6				
126-792A-10H-4, 95–98	89.56	1.02	8.5				
126-792B-7X-CC, 26–29	98.46	0.74	6.2	0.96	0.22	0.03	0.16
126-792B-8X-1, 38–41	108.28	1.92	16.0				
126-792B-8X-2, 38–41	109.78	0.71	5.9	0.99	0.28	0.03	0.13
126-792B-8X-3, 92–95	111.82	1.81	15.1				
126-792B-8X-3, 140–150	112.30	1.31	10.9	1.55	0.24	0.02	0.14
126-792B-8X-4, 53–56	112.93	1.08	9.0				
126-792B-9X-1, 113–116	118.63	1.56	13.0				
126-792B-9X-2, 20–23	119.20	1.24	10.3				
126-792B-10X-1, 95–98	128.05	0.50	4.2	0.73	0.23	0.03	0.19
126-792B-10X-2, 141–144	130.01	0.69	5.7				

Table 12 (continued).

Core, section, interval (cm)	Depth (mbsf)	Inorg. carbon (%)	CaCO₃ (%)	Total carbon (%)	Org. carbon (%)	Total N (%)	Total S (%)
126-792B-10X-3, 69–72	130.79	2.18	18.2	2.47	0.29	0.04	0.08
126-792E-1R-1, 36–38	135.96	1.55	12.9	1.81	0.26	0.02	0.09
126-792D-1X-1, 37–38	136.37	0.94	7.8	1.12	0.18	0.02	0.07
126-792C-1X-CC, 13–14	136.93	0.72	6.0				
126-792B-11X-1, 24–26	137.04	0.88	7.3				
126-792B-11X-1, 54–55	137.34	1.19	9.9				
126-792B-11X-1, 75–85	137.55	1.66	13.8	1.97	0.31	0.02	0.03
126-792B-11X-2, 35–37	138.00	0.62	5.2				
126-792B-11X-CC, 25–27	138.78	0.68	5.7				
126-792E-3R-1, 109–111	155.89	1.74	14.5				
126-792E-3R-2, 60–70	156.90	1.85	15.4	2.13	0.28	0.03	0.1
126-792E-3R-3, 26–29	157.26	1.83	15.2				
126-792E-4R-1, 84–87	165.34	1.11	9.3	1.33	0.22	0.02	0.14
126-792E-4R-2, 107–109	167.07	0.40	3.3				
126-792E-5R-1, 65–66	174.75	2.50	20.8	2.76	0.26	0.03	0.03
126-792E-6R-1, 13–14	183.83	0.87	7.3				
126-792E-6R-1, 120–121	184.90	0.04	0.3	0.04	0.00	0.01	LD
126-792E-8R-1, 13–15	203.23	0.42	3.5				
126-792E-9R-1, 17–19	212.77	0.19	1.6	0.23	0.04	0.01	0.04
126-792E-9R-2, 24–26	214.34	0.24	2.0				
126-792E-9R-3, 74–76	216.34	0.07	0.6				
126-792E-9R-4, 40–50	217.50	0.30	2.5	0.37	0.07	0.01	0.03
126-792E-9R-5, 31–35	217.91	0.24	2.0				
126-792E-10R-1, 48–50	222.68	0.11	0.9				
126-792E-10R-3, 6–8	225.26	0.06	0.5	0.06	0.00	0.01	0.46
126-792E-10R-3, 124–127	226.44	0.38	3.2				
126-792E-11R-1, 94–96	232.84	0.69	5.8				
126-792E-11R-2, 3–5	233.43	0.92	7.7	0.95	0.03	0.02	0.06
126-792E-11R-2, 64–66	234.04	0.08	0.7				
126-792E-12R-1, 116–119	242.66	1.43	11.9				
126-792E-12R-3, 20–22	244.70	0.97	8.1	1.04	0.07	0.01	0.15
126-792E-13R-1, 11–12	251.31	0.89	7.4				
126-792E-15R-1, 71–72	271.21	1.02	8.5				
126-792E-15R-1, 79–80	271.29	1.74	14.5	1.86	0.12	0.02	0.07
126-792E-15R-1, 99–101	271.49	0.78	6.5				
126-792E-15R-2, 16–18	272.16	1.76	14.7				
126-792E-15R-2, 115–125	273.15	0.31	2.6	0.31	0.00	0.01	0.04
126-792E-16R-1, 26–28	280.46	1.18	9.8				
126-792E-16R-2, 7–9	281.77	0.30	2.5				
126-792E-17R-1, 14–16	290.04	0.41	3.4				
126-792E-17R-1, 42–43	290.32	1.71	14.2	1.86	0.15	0.01	0.03
126-792E-17R-2, 140–142	292.80	0.05	0.4	0.06	0.01	0.01	0.05
126-792E-17R-3, 139–141	294.29	0.31	2.6				
126-792E-17R-4, 42–44	294.82	1.76	14.7				
126-792E-18R-1, 15–17	299.65	0.81	6.8				
126-792E-18R-2, 104–106	302.04	0.17	1.4				
126-792E-18R-2, 137–138	302.37	1.48	12.3				
126-792E-18R-3, 107–109	303.57	1.13	9.4				
126-792E-18R-3, 115–125	303.65	0.85	7.1	0.95	0.10	0.01	0.02
126-792E-18R-4, 124–126	305.24	2.00	16.7				
126-792E-19R-1, 47–48	309.47	0.09	0.8				
126-792E-19R-2, 21–23	310.71	0.60	5.0	0.66	0.06	0.02	0.03
126-792E-19R-3, 48–50	312.48	2.49	20.7				
126-792E-20R-1, 34–36	318.94	2.64	22.0				
126-792E-20R-2, 124–126	321.34	1.45	12.1				
126-792E-20R-3, 19–21	321.79	1.04	8.7	1.13	0.09	0.02	0.1
126-792E-21R-1, 13–15	328.43	2.61	21.7				
126-792E-21R-2, 49–51	330.29	0.96	8.0				
126-792E-22R-1, 79–81	338.69	0.77	6.4				
126-792E-22R-2, 5–7	339.45	1.87	15.6				
126-792E-22R-2, 140–150	340.80	0.87	7.3	0.96	0.09	0.01	0.02
126-792E-22R-3, 52–54	341.42	0.35	2.9				
126-792E-23R-1, 74–75	348.34	1.67	13.9				
126-792E-24R-1, 26–27	357.56	1.62	13.5				
126-792E-25R-1, 111–112	368.11	1.68	14.0				
126-792E-25R-1, 129–131	368.29	1.90	15.8				
126-792E-26R-1, 10–12	376.70	2.58	21.5				
126-792E-26R-1, 69–70	377.29	2.31	19.2				
126-792E-27R-1, 27–37	386.57	6.88	57.3				
126-792E-27R-2, 43–44	387.35	7.16	59.6				
126-792E-27R-4, 87–88	390.79	3.98	33.2				
126-792E-28R-1, 35–36	396.35	7.75	64.6	7.84	0.09	0.03	0.04
126-792E-28R-1, 69–71	396.69	5.53	46.1				
126-792E-28R-2, 42–43	397.92	8.12	67.6	8.19	0.07	0.02	LD
126-792E-29R-1, 99–100	406.59	4.71	39.2				
126-792E-29R-2, 5–6	407.15	3.03	25.2	3.05	0.02	0.02	0.07
126-792E-29R-2, 23–24	407.33	0.22	1.8				
126-792E-30R-1, 107–108	416.27	0.06	0.5				

Table 12 (continued).

Core, section, interval (cm)	Depth (mbsf)	Inorg. carbon (%)	CaCO₃ (%)	Total carbon (%)	Org. carbon (%)	Total N (%)	Total S (%)
126-792E-30R-3, 85–86	419.05	1.12	9.3	1.11	0.00	0.01	0.11
126-792E-30R-5, 10–12	421.30	0.50	4.2				
126-792E-30R-5, 11–21	421.31	0.10	0.8	0.07	0.02	0.02	0.08
126-792E-30R-7, 37–39	423.28	1.33	11.1				
126-792E-31R-1, 54–55	425.44	5.12	42.7				
126-792E-31R-1, 127–128	426.17	4.93	41.1	4.90	0.00	0.03	0.06
126-792E-31R-2, 22–23	426.62	0.11	0.9				
126-792E-31R-2, 48–49	426.88	0.05	0.4				
126-792E-31R-3, 97–98	428.87	2.47	20.6	2.38	0.00	0.02	0.06
126-792E-31R-3, 118–119	429.08	1.67	13.9				
126-792E-32R-1, 38–40	434.98	0.69	5.8				
126-792E-32R-3, 100–101	438.60	0.59	4.9				
126-792E-33R-1, 90–92	445.10	0.09	0.8				
126-792E-33R-2, 95–105	446.65	0.17	1.4	0.19	0.02	0.01	0.19
126-792E-33R-3, 60–62	447.60	0.48	4.0				
126-792E-34R-1, 67–69	454.57	3.00	25.0	3.06	0.06	0.02	0.11
126-792E-34R-2, 104–106	456.44	1.05	8.8				
126-792E-34R-3, 78–80	457.68	1.16	9.7				
126-792E-35R-1, 105–107	464.55	0.12	1.0	0.12	0.00	0.01	0.06
126-792E-35R-2, 47–49	465.47	1.00	8.3				
126-792E-36R-1, 73–75	473.93	0.82	6.8				
126-792E-36R-2, 139–141	476.09	0.62	5.2	0.67	0.05	0.01	0.04
126-792E-36R-3, 129–131	477.49	1.75	14.6				
126-792E-36R-4, 67–77	478.37	0.23	1.9	0.24	0.01	0.01	0.02
126-792E-36R-5, 92–94	479.39	0.75	6.3				
126-792E-37R-1, 73–74	483.53	2.26	18.8	2.32	0.06	0.02	0.06
126-792E-37R-1, 132–134	484.12	0.95	7.9				
126-792E-37R-3, 52–55	486.32	1.67	13.9				
126-792E-37R-5, 126–128	490.06	0.65	5.4				
126-792E-37R-7, 16–18	491.96	0.13	1.1	0.20	0.07	0.01	0.03
126-792E-38R-1, 41–43	492.91	0.16	1.3				
126-792E-38R-3, 118–120	496.68	0.04	0.3	0.05	0.01	0.01	0.09
126-792E-38R-5, 30–32	498.80	0.09	0.8				
126-792E-38R-6, 6–8	501.00	0.05	0.40	3.3			
126-792E-39R-1, 128–130	503.48	0.33	2.8	0.41	0.08	0.01	0.03
126-792E-39R-2, 115–125	504.85	0.18	1.5	0.21	0.03	0.01	0.02
126-792E-39R-3, 36–38	505.56	0.34	2.8				
126-792E-39R-5, 60–62	508.80	0.07	0.6	0.08	0.01	LD	0.03
126-792E-40R-1, 103–105	512.93	0.28	2.3				
126-792E-40R-3, 15–17	515.05	0.07	0.6				
126-792E-40R-5, 107–109	518.97	0.06	0.5				
126-792E-40R-6, 75–77	520.15	1.29	10.7				
126-792E-41R-1, 20–22	521.80	0.07	0.6				
126-792E-41R-1, 118–119	522.78	0.07	0.6	0.08	0.01	0.01	0.03
126-792E-41R-2, 56–58	523.66	0.31	2.6				
126-792E-41R-3, 82–84	525.42	0.07	0.6				
126-792E-41R-5, 99–101	528.32	0.07	0.6				
126-792E-42R-3, 118–119	535.38	0.07	0.6				
126-792E-42R-4, 140–150	537.10	0.07	0.6	0.07	0.00	0.01	0.02
126-792E-42R-5, 121–122	538.41	0.10	0.8				
126-792E-43R-1, 76–78	541.36	0.07	0.6	0.07	0.00	0.01	0.02
126-792E-43R-3, 56–58	543.97	1.17	9.8				
126-792E-43R-3, 110–111	544.51	0.85	7.1				
126-792E-43R-5, 82–84	547.25	0.11	0.9				
126-792E-43R-5, 100–101	547.43	3.91	32.6				
126-792E-43R-7, 30–32	549.63	0.06	0.5				
126-792E-44R-1, 60–61	550.90	0.07	0.6				
126-792E-44R-3, 53–54	553.84	0.08	0.7				
126-792E-44R-5, 34–35	556.65	0.08	0.7				
126-792E-45R-1, 64–65	560.64	0.10	0.8	0.08	0.00	0.01	0.05
126-792E-45R-2, 0–10	561.45	0.08	0.7	0.12	0.04	0.01	LD
126-792E-45R-3, 4–5	562.96	0.19	1.6				
126-792E-45R-4, 132–133	565.55	0.10	0.8				
126-792E-46R-1, 78–79	570.48	0.10	0.8				
126-792E-46R-3, 122–124	573.65	0.08	0.7				
126-792E-46R-5, 119–121	576.55	1.03	8.6				
126-792E-46R-7, 31–33	578.56	1.29	10.7				
126-792E-47R-1, 114–116	580.54	0.13	1.1				
126-792E-47R-3, 47–49	582.48	0.09	0.7				
126-792E-48R-1, 35–37	588.95	0.10	0.8	0.12	0.02	0.01	0.02
126-792E-48R-3, 37–39	591.27	0.22	1.8				
126-792E-48R-3, 52–53	591.42	0.64	5.3				
126-792E-48R-5, 63–65	594.21	0.05	0.4	0.08	0.03	0.01	0.02
126-792E-48R-6, 83–84	595.88	1.70	14.2				
126-792E-48R-7, 140–150	597.55	0.05	0.4	0.06	0.01	0.01	0.02
126-792E-48R-8, 19–21	597.84	0.07	0.6				
126-792E-49R-3, 63–65	601.43	0.47	3.9				
126-792E-49R-5, 112–114	604.77	0.50	4.2				

Table 12 (continued).

Core, section, interval (cm)	Depth (mbsf)	Inorg. carbon (%)	CaCO₃ (%)	Total carbon (%)	Org. carbon (%)	Total N (%)	Total S (%)
126-792E-50R-1, 23–25	607.63	0.15	1.3				
126-792E-50R-3, 7–9	610.47	0.07	0.6				
126-792E-50R-5, 16–18	613.57	0.10	0.8				
126-792E-50R-7, 11–13	616.52	0.29	2.4				
126-792E-51R-1, 32–34	617.42	0.73	6.1				
126-792E-51R-2, 106–108	619.66	0.31	2.6				
126-792E-51R-2, 140–150	620.00	0.19	1.6	0.24	0.05	0.01	0.08
126-792E-51R-3, 14–16	620.24	0.75	6.3	0.81	0.06	0.01	0.22
126-792E-52R-1, 38–40	627.18	1.92	16.0				
126-792E-52R-1, 100–102	627.80	5.10	42.5				
126-792E-52R-2, 29–31	628.59	0.11	0.9				
126-792E-52R-3, 22–24	630.02	0.07	0.6				
126-792E-52R-4, 49–51	631.79	1.77	14.7				
126-792E-52R-5, 50–52	633.30	0.10	0.8				
126-792E-52R-6, 8–10	634.38	0.09	0.7				
126-792E-54R-1, 136–137	647.46	0.08	0.7				
126-792E-54R-2, 49–50	648.09	0.76	6.3				
126-792E-54R-3, 11–12	649.21	0.17	1.4				
126-792E-54R-3, 140–150	650.50	1.07	8.9	1.12	0.05	0.01	0.05
126-792E-54R-5, 83–84	652.93	1.64	13.7				
126-792E-54R-6, 8–9	653.68	2.79	23.2				
126-792E-55R-1, 53–55	656.23	1.45	12.1				
126-792E-55R-2, 99–101	658.19	0.10	0.8				
126-792E-56R-2, 77–79	667.67	0.27	2.2				
126-792E-56R-4, 16–18	670.06	0.08	0.7				
126-792E-56R-6, 136–138	673.98	0.05	0.4				
126-792E-57R-1, 98–100	676.08	1.56	13.0				
126-792E-57R-3, 3–5	678.13	0.06	0.5				
126-792E-57R-5, 85–87	681.95	0.03	0.2				
126-792E-57R-5, 140–150	682.50	0.04	0.3	0.04	0.00	0.01	LD
126-792E-57R-6, 49–51	683.09	0.81	6.7				
126-792E-58R-1, 70–72	685.50	0.06	0.5				
126-792E-58R-2, 92–94	687.22	0.28	2.3				
126-792E-58R-CC, 20–22	689.90	0.05	0.4				
126-792E-59R-1, 65–67	695.05	0.44	3.7				
126-792E-59R-2, 49–51	696.39	0.05	0.4				
126-792E-59R-3, 101–103	698.28	0.13	1.1				
126-792E-59R-4, 72–74	699.21	0.08	0.7				
126-792E-59R-5, 47–49	700.40	0.73	6.1				
126-792E-60R-1, 121–123	705.21	0.08	0.7				
126-792E-60R-2, 71–72	706.21	0.05	0.4				
126-792E-60R-3, 16–17	707.16	0.05	0.4				
126-792E-60R-4, 140–141	709.90	0.04	0.3				
126-792E-60R-6, 27–28	711.77	0.04	0.3				
126-792E-60R-6, 140–150	712.90	0.05	0.4	0.05	0.00	0.01	0.02
126-792E-61R-2, 119–121	716.29	0.04	0.3				
126-792E-61R-3, 130–132	717.90	0.05	0.4				
126-792E-61R-4, 88–90	718.98	0.07	0.6				
126-792E-62R-1, 4–5	722.94	0.15	1.2				
126-792E-62R-2, 95–96	724.53	0.10	0.8				
126-792E-62R-4, 37–38	726.54	0.13	1.1				
126-792E-62R-7, 69–70	730.80	0.07	0.6				
126-792E-62R-8, 6–7	731.67	0.21	1.7				
126-792E-63R-1, 109–111	733.59	0.06	0.5				
126-792E-63R-3, 5–7	735.41	0.32	2.7				
126-792E-63R-3, 138–150	736.74	0.35	2.9	0.35	0.00	0.01	0.02
126-792E-64R-1, 14–15	742.34	0.27	2.2				
126-792E-64R-2, 51–53	744.16	0.05	0.4				
126-792E-65R-1, 12–14	751.92	0.07	0.6				
126-792E-65R-2, 13–14	753.36	0.06	0.5				
126-792E-66R-1, 52–54	762.02	1.17	9.7				
126-792E-66R-3, 144–146	765.94	0.08	0.7				
126-792E-66R-5, 139–149	768.91	0.14	1.2	0.15	0.01	0.01	0.03
126-792E-66R-6, 10–12	769.11	0.13	1.1				
126-792E-67R-1, 74–76	771.94	0.05	0.4				
126-792E-67R-2, 110–112	773.80	0.11	0.9				
126-792E-67R-3, 23–25	774.43	0.08	0.7				
126-792E-68R-1, 50–52	781.40	1.93	16.1				
126-792E-68R-2, 82–84	782.96	0.06	0.5				
126-792E-68R-2, 124–126	783.38	0.03	0.2				
126-792E-69R-3, 107–108	794.67	0.06	0.5				
126-792E-69R-4, 136–146	796.28	0.04	0.3	0.04	0.00	0.01	0.03

Note: Samples are listed according to depth (mbsf); LD = less than detection limit.
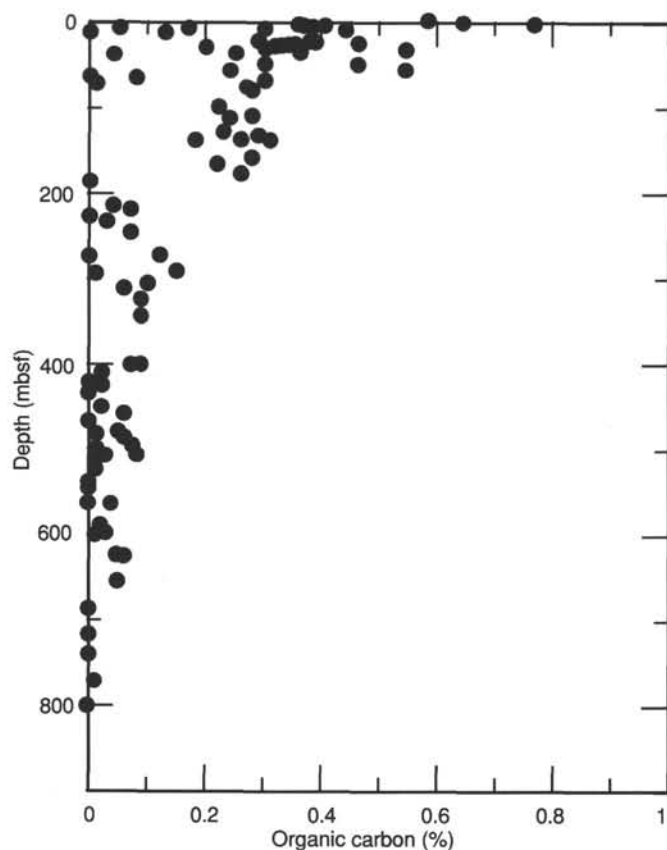
Figure 53. Organic carbon, Site 792.

from Hole 792E. We obtained MST logging from Cores 126-792E-1R through -31R, but we report only the sonic data for Hole 792E (see "Physical Properties" sections in previous site chapters, this volume, for details). Vane shear strength measurements were discontinued after five cores because of drilling disturbance. Thermal conductivity was suspended at Core 126-792E-32R, below which the material became too lithified for the needle-probe method.

We conducted HF velocity, index property, and thermal conductivity analyses on igneous rock samples. All igneous samples for physical property analyses were taken from core sections within minutes of splitting to minimize the effects of dessication. Thermal conductivity was measured on six samples with the half-space method.

Four downhole temperature measurements were attempted by means of a Uyeda temperature probe at Site 792, two in Hole 792A and two in Hole 792C. Of these, three were successful (at depths of 47.2, 67, and 110 mbsf). The fourth measurement (at 95 mbsf) produced an anomalous temperature-vs.-time plot and was not included in further analyses. Bottom-water temperature was used as a fourth data point to constrain the geothermal gradient.

Index Properties

Index property measurements overlap at two depth intervals in Holes 792A and 792B: 0–4.3 mbsf and 50–73 mbsf (Figs. 55 and 56; Table 14). Trends agree reasonably well with absolute values, although values in Hole 792A exhibit greater variability. Depth overlap between Hole 792B and Holes 792C, 792D, and 792E is minimal. The physical property measurements and lithologic units are displayed in Figure 55, and relationships among the parameters are discussed below.

Table 13. Pore-water composition, Site 792.

| Core, section, interval (cm)	Depth (mbsf)	pH	Alk. (mM)	Sal. (g/kg)	Cl^- (mM)	SO_4^{2-} (mM)	Mg^{2+} (mM)	Ca^{2+} (mM)	SiO_2 (μM)	NH_4^+ (μM)
126-792A-										
1H-5, 140–150	7.45	7.74	3.18	35.5	550	28.4	52.2	9.4	521	192
3H-5, 140–150	26.55	7.80	4.27	35.5	556	25.5	52.5	7.9	629	536
6H-2, 140–150	50.15	7.80	3.33	35.5	561	26.3	53.0	9.2	595	453
9H-1, 89–97	76.54	7.82	2.66	35.5	562	26.9	52.0	10.2	650	296
126-792B-										
8X-3, 140–150	112.35	7.60	3.09	35.5	561	27.6	51.8	11.0	710	250
11X-1, 75–85	137.60	7.69	2.64	36.0	560	27.1	50.6	15.1	794	199
126-792E-										
3R-2, 60–70	156.95	7.52	2.15	35.5	557	27.2	50.2	16.5	805	187
9R-4, 40–50	217.55	7.69	0.23	36.0	560	27.8	46.0	23.5	765	212
15R-2, 115–125	273.20	7.93	1.62	36.0	559	28.5	46.6	23.0	875	161
18R-3, 115–125	303.70	7.58	2.34	36.0	559	28.2	46.4	23.9	938	165
22R-2, 140–150	340.85	7.53	1.43	36.0	559	27.2	43.6	28.8	979	147
27R-1, 27–37	386.62	7.34	1.37	36.0	560	26.6	40.0	36.9	924	118
30R-5, 11–21	421.36	7.79	1.20	36.0	551	25.5	31.2	53.7	157	92
33R-2, 95–105	446.70	ND	ND	ND	559	23.2	22.2	71.5	135	106
36R-4, 67–77	478.42	7.94	0.12	36.5	560	19.7	12.0	98.5	118	133
39R-2, 115–125	504.90	ND	ND	ND	562	16.7	4.2	130.6	118	105
42R-4, 140–150	537.15	ND	ND	ND	578	15.2	2.6	159.0	375	114
45R-2, 0–10	561.55	ND	ND	ND	579	15.6	4.6	156.1	123	108
48R-7, 140–150	599.05	8.48	0.35	39.0	579	15.3	0.4	169.3	262	44
51R-2, 140–150	620.05	ND	ND	ND	577	15.1	3.2	153.1	343	58
54R-3, 140–150	650.55	ND	ND	ND	560	15.2	2.4	153.1	123	60
57R-5, 140–150	682.55	8.11	0.47	38.0	563	16.3	1.4	143.1	447	80
60R-6, 140–150	712.95	ND	ND	ND	568	18.8	3.2	135.6	282	82
63R-3, 138–150	736.94	ND	ND	ND	567	17.3	0.3	143.8	203	113
66R-5, 139–150	768.95	ND	ND	ND	569	16.8	5.4	121.7	146	55
69R-4, 136–146	796.51	ND	ND	ND	549	16.2	4.3	114.2	508	72
Drilling mud filtrate		9.69	0.80	ND	215	12.0	2.7	7.0	19	58

Note: ND = not determined.
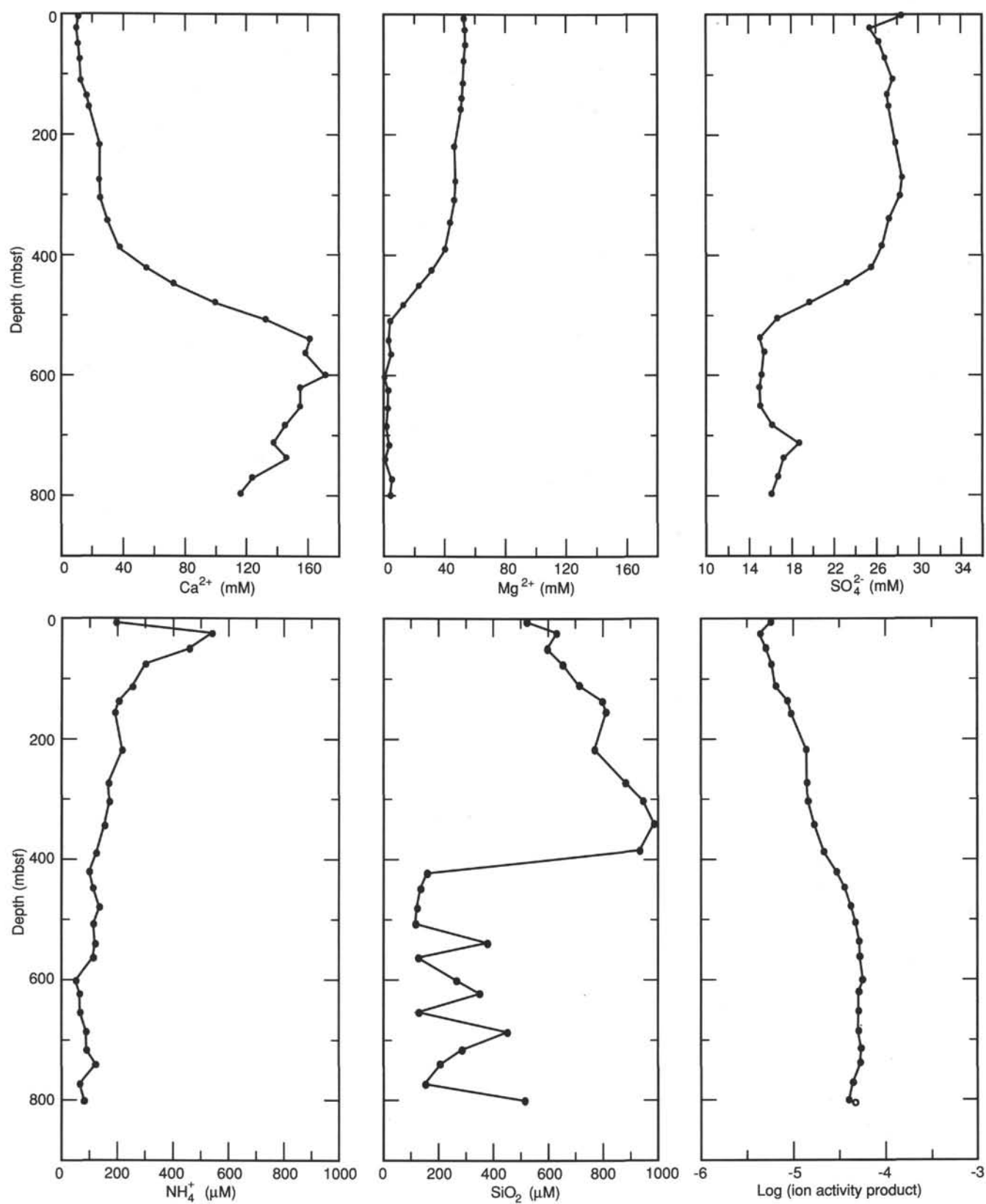
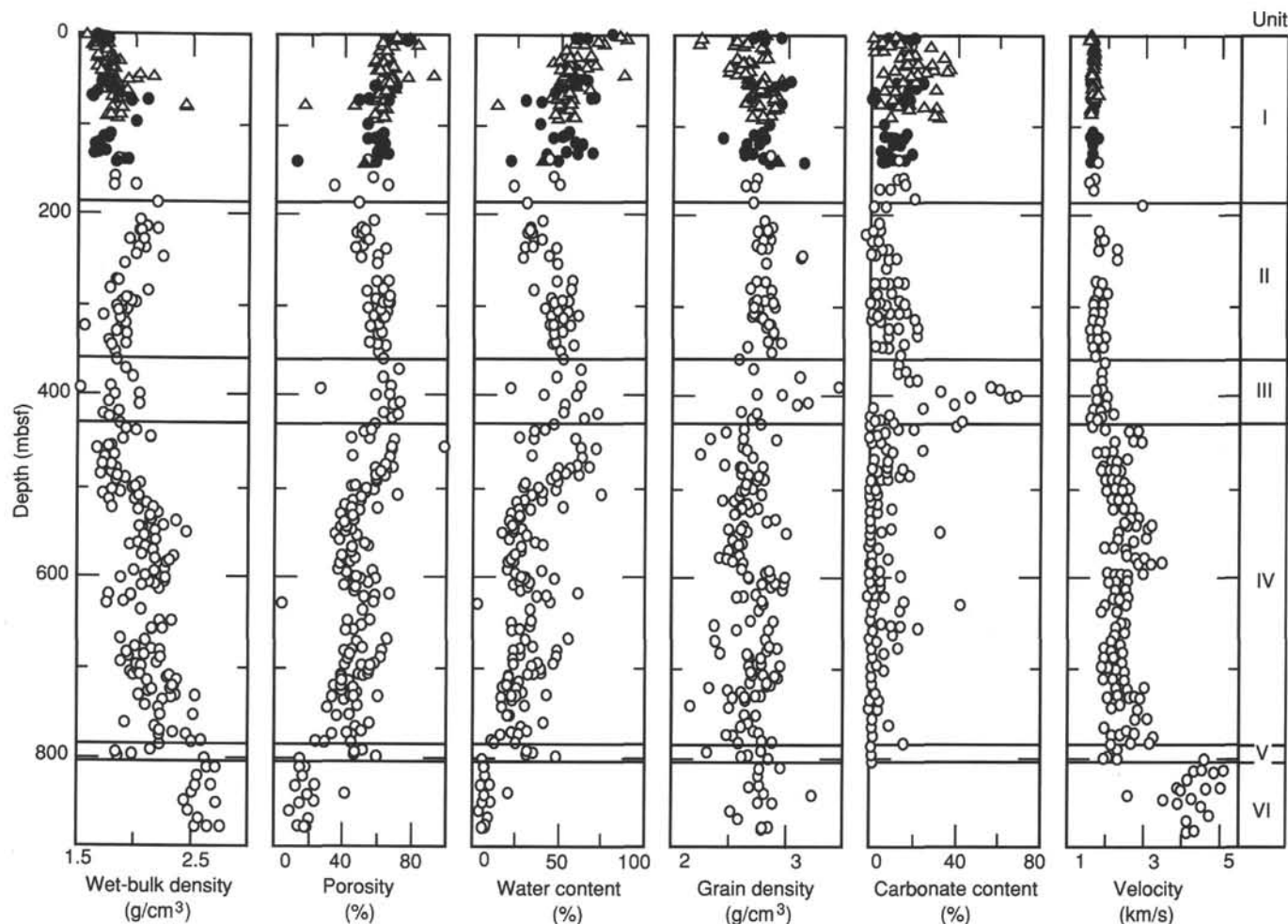Figure 54. Composition of pore waters, Site 792.

Figure 55. Downhole plots of index properties, carbonate content, and velocity for Holes 792A (open triangles), 792B (closed circles), and 792E (open circles). Horizontal lines indicate lithologic units.

In Unit I, average porosity, water content, and wet-bulk density values are 62.5%, 56.4%, and 1.8 g/cm^3, respectively. Porosity and water content values decrease downward, whereas wet-bulk density increases. Values of porosity and water content increase from Unit II (averages of 58.1% and 45%, respectively) to Unit III (averages of 66% and 58.5%, respectively). We observed a steady decrease in porosity and water content in the top 100 m of Unit IV, from average values of 61% and 52% to 43% and 24%, respectively (Fig. 55). Average porosity and water content values for the remainder of Unit IV (542–783.4 mbsf) are 46% and 29%, respectively. Wet-bulk density data mirror the trends in porosity and water content data. Wet-bulk density values in Units II and III are similar (means of 1.95 g/cm^3 and 1.86 g/cm^3, respectively). Wet-bulk density increases from about 2.0 g/cm^3 at the top of Unit IV to 2.23 g/cm^3 at approximately 535 mbsf, and then remains constant (but variable) to the base of Unit IV (averaging 2.16 g/cm^3 from 542 to 783.4 mbsf).

Smaller scale fluctuations in porosity, water content, and wet-bulk density values within the lithologic units are probably related to compositional and grain-size variations. In general, coarser grained intervals are associated with lower porosity and water content values and higher wet-bulk density values. In the upper two lithologic units, index property data correlate with variations in clay mineralogy. All four zones of high porosity above 350 mbsf (Fig. 55) correspond to smectite-rich intervals (see "Lithostratigraphy and Accumulation Rates" section, this

chapter). Smectite minerals have high water-adsorption capacities and are thus associated with high water contents and porosities (e.g., Mitchell, 1976).

Increases in porosity and water content below Unit II may be related to increased concentrations of high-porosity zeolites in the unit. Intervals of high porosity observed in Unit IV (410 and 630 mbsf) may also be associated with increased glauconite and palagonite concentrations (see "Lithostratigraphy and Accumulation Rates" section, this chapter). Furthermore, the sharp change in porosity, water content, and wet-bulk density observed at approximately 540 mbsf is most likely related to the increase in grain size at this depth (see "Lithostratigraphy and Accumulation Rates" section, this chapter).

The GRAPE wet-bulk density measurements from Holes 792A and 792B and the gravimetric values from the same depth intervals are shown in Figure 56. Agreement between the two types of measurements is good. Three intervals of low wet-bulk density are observed in the GRAPE data (at approximately 12 and 87 mbsf in Hole 792A and at 50 mbsf in Hole 792B) but not in the gravimetric measurements. These intervals are associated with drilling disturbance. Although the gravimetric samples were chosen from areas that appeared the least disturbed, the GRAPE measures continuously and thus does not discriminate disturbed and undisturbed regions of the core.

Grain density values are highly variable. The data fall into three distinct depth zones (Figs. 55 and 56). From 0 to 350 mbsf
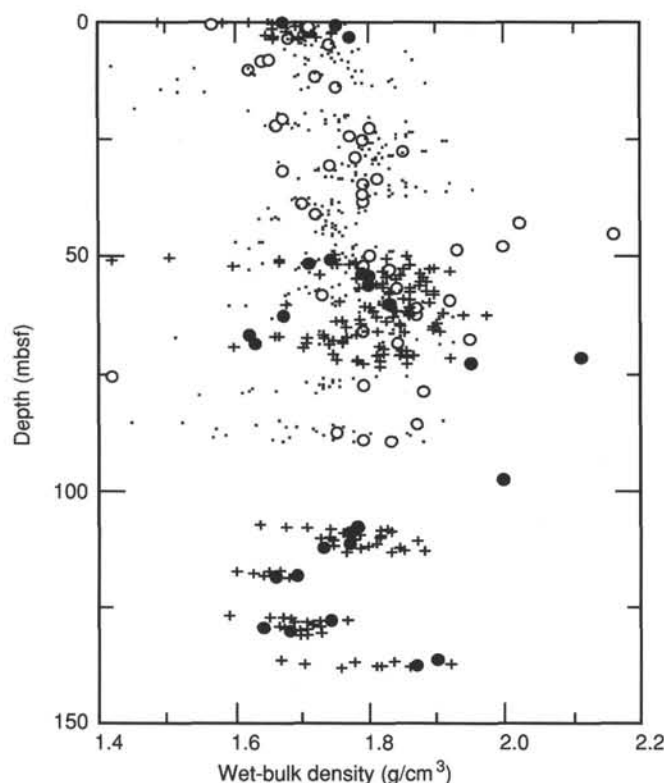
Figure 56. Comparison of gravimetric and GRAPE wet-bulk density, Holes 792A and 792B. Small closed circles = Hole 792A GRAPE; crosses = Hole 792B GRAPE; open circles = Hole 792A gravimetric; closed large circles = Hole 792B gravimetric.

(Units I and II), grain density data average 2.76 g/cm³ and have a relatively narrow range of values from 2.52 to 3.01 g/cm³. Within Unit III (from approximately 350 to 430 mbsf), grain density displays variable but high values (the range of values is 2.58–3.46 g/cm³; the average is 2.87 g/cm³). Some of this increase in grain density values can be attributed to the increased carbonate content of this unit. However, of the 13 data points within this unit, nine exceed the average carbonate density of 2.71 g/cm³. These high values are associated with increased concentrations of opaque, heavy minerals in this unit.

In the sediments below 410 mbsf, grain density variability increases, with values ranging from 2.31 to 3.0 g/cm³ (Figs. 55 and 56; Table 14). The mean (2.66 g/cm³) is lower than that in the upper 350 m. Grain density increases from the base of the sediment toward the basement, but rarely attains values as high as those observed in Unit III, which ranges from 2.51 to 3.22 g/cm³, and averages 2.79 g/cm³ in Unit VI.

Porosity and water contents in Unit V increase relative to values at the base of Unit IV (averages of 51% and 37%, respectively), whereas wet-bulk density decreases to an average of 1.97 g/cm³. These changes probably are caused by low-temperature hydrothermal alteration in this unit (see "Lithostratigraphy and Accumulation Rates" section, this chapter). Porosity and water content values decrease sharply near the Unit V/Unit VI contact and average 18.7% and 8.1%, respectively, within Unit VI. One sample, at 839.6 mbsf, has a porosity of 42% and a water content of 21%. The wet-bulk density and HF velocity (see below) are correspondingly low. This sample is from a zone of andesitic hyaloclastite breccia (see "Igneous Petrology" section, this chapter).

Calcium Carbonate

Calcium carbonate contents generally exhibit trends consistent with the lithologic unit boundaries (Fig. 55; see "Lithostratigraphy and Accumulation Rates" section, this chapter). Carbonate values in Unit I are quite variable (with a range of 0.6%–36.1% and an average of 13.8%) and represent samples of interbedded nannofossil-rich and nannofossil-poor beds (see "Lithostratigraphy and Accumulation Rates" section, this chapter). Carbonate values in Unit II correlate with irregularly increasing nannofossil contents with depth (see "Lithostratigraphy and Accumulation Rates" section, this chapter). Carbonate contents range from 0.3% at 184.9 mbsf to 22% near the base of Unit II. However, the average is relatively low (7.5%). This downward trend in carbonate content within Unit II continues through Unit III, where values range from 13.5% to a maximum of 67% at 398 mbsf (the average CaCO₃ content in Unit III is 25%). Unit IV is characterized by generally low CaCO₃ contents; the average is 4.0%. Isolated high carbonate peaks represent samples from microfossil-rich pelagic intervals. Two CaCO₃ analyses from Unit V average 0.4%.

Vane Shear Strength

Vane shear strength measurements in Holes 792A and 792B overlap in the depth intervals from 0 to 3.5 mbsf and 51 to 73 mbsf (Fig. 57; Table 15). Correlation between the two holes is good in the upper zone and below 55 mbsf. Data from Hole 792B between 51 and 55 mbsf are significantly lower than values in Hole 792A at these depths, and probably are the result of greater drilling disturbance in Hole 792B. Shear strength values are highly variable, even when one ignores anomalously low values in which disturbance is suspected. We noted three intervals displaying different strength characteristics. Shear strength values in the upper 13 m are low, exceeding 20 kPa in only two samples. The section between 13 and 78 mbsf has the highest shear strengths measured at this site, with an average of 30.8 kPa and values as high as 46.6 kPa. Below 78 mbsf, shear strength decreases, averaging 16.9 kPa and reaching values as low as those observed in the upper 13 m. Most of these low shear strength values in the deeper interval are from cores drilled by XCB or RCB operations; therefore, they are expected to display low shear strengths as a result of drilling disturbance. However, the zone of lower strengths actually starts within the APC-cored interval in Hole 792A. We noted no obvious change in porosity or wet-bulk density trends at this depth, so the origin of the low shear strengths remains unknown.

Sonic Velocity

We performed sonic velocity measurements on discrete samples from Holes 792A, 792B, and 792E with the Hamilton Frame velocimeter (Table 14; Fig. 55). In addition, we passed Cores 126-792A-1H through -10H and 126-792E-1R through -31R through the multi-sensor track (MST) and obtained sonic velocity measurements from the sonic wave (P-wave) logger (Fig. 58).

Velocity values average 1.59 km/s (with a range of 1.55–1.67 km/s) within Unit I (0–183.7 mbsf), 1.85 km/s (with a range of 1.65–2.28 km/s) in Unit II (183.7–357.4 mbsf), and 1.87 km/s (with a range of 1.76–2.05 km/s) in Unit III (Figs. 55 and 58). Two samples, near 240–250 mbsf, with velocity values exceeding 2.20 km/s, are from coarser grained lithologies (Figs. 55 and 58).

We observed a 1.0-km/s increase in velocity across the Unit III/Unit IV contact. This velocity contrast is the result of a high-velocity zone (average = 2.77 km/s; 429–450 mbsf) in the

Table 14. Physical property (index-property, velocity, and carbonate) data, Site 792.

Core, section, interval (cm)	Depth (mbsf)	Wet-bulk density (g/cm³)	Dry-bulk density (g/cm³)	Porosity (%)	Water content (%)	Grain density (g/cm³)	Void ratio	Carbonate content (%)	Velocity (km/s)
126-792A-									
1H-1, 70–73	0.70	1.57	0.87	71	86	2.78	2.42	10.0	1.55
1H-2, 60–64	2.14							0.6	
1H-2, 97–99	2.47	1.71[a]	0.94	77[a]	87[a]	2.23[a]	3.52[a]	11.0	1.55
1H-3, 99–101	3.99	1.68	1.01	68	71	2.54	2.11	12.3	1.56
1H-4, 108–111	5.58	1.74	1.13	62	57	2.64	1.62	7.9	1.61
1H-5, 140–150	7.40							4.2	
1H-6, 113–115	8.63	1.65	1.03	62	63	2.51	1.64	1.8	1.56
1H-7, 24–28	9.24	1.64[a]	0.83	82[a]	105[a]	2.22[a]	4.67[a]	16.0	1.56
2H-1, 128–131	10.98	1.62	0.95	67	74	2.59	2.05	26.8	1.60
2H-2, 102–105	12.22	1.72	1.08	65	63	2.75	1.84	15.2	1.59
2H-3, 120–122	13.90							4.9	1.59
2H-4, 39–42	14.59	1.75	1.16	60	54	2.78	1.49	0.7	
3H-2, 57–59	21.17	1.67	1.07	65	67	2.80	1.89	17.5	1.53
3H-3, 78–81	22.88	1.66	1.02	65	66	2.56	1.83	33.2	1.54
3H-3, 119–123	23.29	1.80	1.19	62	55	2.77	1.64		
3H-4, 122–125	24.82	1.77	1.14	64	59	2.58	1.76	12.6	1.62
3H-5, 91–94	26.01	1.79	1.22	57	49	2.63	1.34	17.8	1.61
3H-5, 140–150	26.50							17.3	
3H-7, 22–25	28.32	1.85	1.29	56	45	2.61	1.29	18.9	1.59
4H-1, 99–102	29.39	1.78	1.17	61	55	2.68	1.58	15.4	1.56
4H-2, 118–121	31.08	1.74	1.13	62	57	2.60	1.61	21.2	1.56
4H-3, 64–67	32.04	1.67	1.01	67	70	2.59	2.05	27.4	1.55
4H-4, 116–119	34.06	1.81	1.23	59	50	2.48	1.41	36.1	1.56
4H-5, 88–91	35.28	1.79	1.11	68	64	2.63	2.15	27.7	1.57
4H-7, 31–34	37.71	1.79	1.18	61	54	2.66	1.59		1.57
4H-7, 40–43	37.80							10.3	
5H-1, 101–105	38.81	1.79	1.18	61	54	2.62	1.56	25.0	1.57
5H-2, 35–38	39.65	1.70	1.09	62	60	2.48	1.66	4.9	1.60
5H-3, 92–96	41.72	1.72	1.10	63	60	2.55	1.71	18.8	1.57
5H-4, 129–132	43.59	2.02[a]	1.12	91[a]	86[a]	2.62[a]	10.55[a]	19.2	1.57
5H-6, 62–65	45.92	2.16[a]	1.40	76[a]	56[a]	2.78[a]	3.23[a]	19.9	1.58
6H-1, 107–109	48.27	2.00	1.34	67	52	2.65	1.99		1.62
6H-1, 117–119	48.37							18.7	
6H-2, 67–69	49.37	1.93	1.25	69	57	2.94	2.18	7.8	1.59
6H-2, 140–150	50.10							13.9	
6H-3, 26–28	50.46	1.80	1.18	63	56	2.66	1.71	17.6	1.58
6H-4, 118–119	52.88							21.3	
6H-4, 126–128	52.96	1.79	1.16	63	57	2.66	1.74		1.59
6H-5, 17–19	53.37	1.83	1.24	59	50	2.74	1.45		
7H-1, 94–96	57.54	1.84	1.23	63	53	2.73	1.67	5.2	1.59
7H-2, 91–94	59.01	1.73	1.06	68	67	2.87	2.07	29.7	1.55
7H-3, 74–75	60.34	1.92	1.30	62	50	2.74	1.65	10.8	
7H-4, 114–117	61.91	1.87	1.27	60	49	2.77	1.50		1.58
7H-5, 90–92	63.17	1.87	1.26	62	51	2.71	1.61		
8H-1, 68–70	66.68	1.79	1.17	63	56	2.88	1.68	9.3	1.58
8H-2, 92–93	68.29	1.95	1.37	59	44	2.90	1.41	5.0	1.63
8H-3, 35–37	69.22	1.84		58	48	2.64	1.40	5.4	
9H-1, 72–74	76.32	1.42	0.97	46	49	2.74	0.83	11.8	1.61
9H-1, 87–97	76.47							16.7	
9H-2, 75–77	77.57	2.44[a]	2.10	83[a]	54[a]	2.88[a]	5.09[a]		
9H-2, 100–103	77.82							29.6	1.58
9H-3, 18–21	78.50	1.79	1.18	61	54	2.69	1.56	24.6	1.59
9H-4, 20–23	79.39	1.88	1.26	63	52	2.88	1.71	17.2	1.59
10H-1, 112–114	86.42	1.87	1.30	58	46	2.85	1.37	29.0	
10H-3, 104–107	88.15	1.75	1.14	62	57	2.68	1.63	30.6	
10H-4, 94–97	89.55	1.79	1.17	63	56	2.78	1.70	8.5	
10H-5, 20–22	90.31	1.83	1.25	58	48	2.78	1.39		
126-792B-									
1H-1, 6–7	0.06							11.0	
1H-1, 113–115	1.13	1.75	1.11	65	61	2.93	1.85	10.9	1.56
1H-2, 47–48	1.97							20.4	
1H-2, 102–105	2.52	1.71	1.06	65	65	2.70	1.89	11.6	1.56
1H-3, 49–51	3.49	1.77	1.14	64	58	2.79	1.74	13.4	1.57
1H-3, 95–96	3.95							15.8	
2H-1, 110–113	51.10	1.74	1.07	68	66	3.01	2.09	23.9	1.57
2H-2, 63–66	52.13	1.71	1.12	60	56	2.67	1.52	12.1	1.62
2H-3, 29–30	53.29	1.79	1.17	63	56	2.97	1.68		
2H-4, 70–73	55.20	1.80	1.19	62	54	2.75	1.62	16.9	1.56
2H-5, 62–66	56.62	1.80	1.23	58	49	2.88	1.37	20.5	1.61
3H-1, 12–15	59.72							16.7	
3H-1, 112–115	60.72	1.83	1.27	57	47	2.81	1.33		1.62
3H-3, 81–84	63.41	1.67	1.09	58	56	2.69	1.40	0.7	
3H-6, 39–42	67.49	1.62	0.98	65	69	2.69	1.83	0.3	1.62

Table 14 (continued).

Core, section, interval (cm)	Depth (mbsf)	Wet-bulk density (g/cm^3)	Dry-bulk density (g/cm^3)	Porosity (%)	Water content (%)	Grain density (g/cm^3)	Void ratio	Carbonate content (%)	Velocity (km/s)
126-792B- (Cont.)									
3H-7, 39–42	68.99	1.73		68	67	3.00		17.2	1.57
4X-1, 24–27	69.44	1.63	0.99	64	68	2.64	1.80	14.7	
4X-2, 130–132	72.00	2.11	1.64	47	30	2.88	0.89	1.4	
4X-3, 110–114	73.30	1.95	1.42	54	39	2.93	1.16	8.8	1.67
7X-CC, 28–33	98.48	2.00	1.46	54	38	2.83	1.17	6.2	
8X-1, 37–44	108.27	1.78	1.19	60	53	2.78	1.52	16.0	1.59
8X-2, 37–40	109.77	1.77	1.18	60	53	2.70	1.47	5.9	1.60
8X-3, 92–95	111.82	1.77	1.19	59	51	2.80	1.42	15.1	1.60
8X-3, 140–150	112.30							10.9	
8X-4, 53–56	112.93	1.73	1.21	53	46	2.43	1.13	9.0	1.67
9X-1, 113–116	118.63	1.69	1.09	61	58	2.64	1.54	13.0	1.60
9X-2, 20–23	119.20	1.66	1.04	63	63	2.76	1.68	10.3	1.61
10X-1, 95–96	128.05	1.74	1.15	59	54	2.62	1.45	4.2	
10X-2, 141–144	130.01	1.64	0.99	65	69	2.62	1.86	5.8	1.59
10X-3, 70–72	130.80	1.68	1.07	62	60	2.69	1.60	18.2	
11X-1, 25–28	137.05	1.90	1.35	56	43	2.79	1.25	7.3	1.62
11X-1, 54–55	137.34							9.9	
11X-1, 75–85	137.55							13.8	
11X-2, 35–38	138.00	1.87	1.28	59	48	3.14	1.46	5.2	1.59
11X-CC, 25–26	138.78	0.7[a]	0.58	12.2[a]	21.8[a]	2.86[a]	0.14[a]	5.7	
126-792C-									
1X-CC, 13–14	136.93							6	
126-792D-									
1X-1, 37–38	136.37							7.83	
1X-1, 72–74	136.52	1.89	1.37	53	40	2.91	1.11		
126-792E-									
1R-1, 38–40	135.98	1.86	1.31	55	44	2.85	1.23	12.9	1.67
3R-1, 109–111	155.89	1.82	1.27	56	46	2.73	1.28	14.5	1.61
3R-2, 60–70	156.9							15.4	1.58
3R-3, 26–29	157.26							15.2	
4R-1, 66–67	165.16	2.00	1.36	65	49	2.63	1.82		
4R-1, 84–87	165.34							9.3	
4R-2, 106–107	167.06	1.81	1.48	33	23	2.71	0.50	3.3	1.65
5R-1, 65–66	174.75							20.8	
6R-1, 13–14	183.83							7.3	
6R-1, 120–122	184.90	2.20	1.70	51	31	2.70	1.02	0.3	2.89
8R-1, 13–15	203.23	2.04	1.48	57	40	2.80	1.31	3.5	
9R-1, 19–21	212.79	2.11	1.61	50	32	2.87	1.01	1.6	
9R-2, 25–27	214.35	2.20	1.68	52	32	2.82	1.08	2.0	1.83
9R-3, 74–76	216.34	2.06	1.56	50	33	2.83	1.01	0.6	
9R-4, 40–50	217.5							2.5	
9R-5, 31–34	217.91	2.05[a]	1.58	47[a]	31[a]	2.74[a]	0.91[a]	2.0[a]	
10R-1, 48–50	222.68							0.9	1.82
10R-3, 6–8	225.26	1.96	1.43	54	40	2.79	1.19	0.5	1.80
10R-3, 124–126	226.44	2.08[a]	1.57	52[a]	35[a]	2.86[a]	1.11[a]	3.17[a]	
11R-1, 94–96	232.84	2.07	1.57	51	34	2.74	1.04	5.8	1.80
11R-2, 2–4	233.42	2.03[a]	1.39	64[a]	48[a]	2.82[a]	1.81[a]	7.7[a]	
11R-2, 64–66	234.04	2.10	1.64	47	30	2.77	0.89	0.7	2.28
12R-1, 116–119	242.66	2.01	1.42	60	44	3.13	1.49	11.9	
12R-3, 19–21	244.69	2.26	1.76	50	29	3.12	0.99	8.1	2.24
13R-1, 11–13	251.31	1.91	1.32	60	47	2.82	1.47	7.4	
15R-1, 71–72	271.21							8.5	
15R-1, 79–81	271.29							14.5	
15R-1, 99–102	271.49	1.87	1.28	59	48	2.81	1.46	6.5	1.80
15R-2, 16–18	272.16	1.85	1.20	66	57	2.73	1.91	14.7	1.77
15R-2, 115–125	273.15							2.6	
16R-1, 27–29	280.47	1.79	1.17	63	56	2.68	1.69	9.8	1.77
16R-2, 8–11	281.78	2.12	1.59	54	35	2.87	1.15	2.5	2.01
17R-1, 15–17	290.05	1.95	1.36	59	45	2.86	1.46	3.4	1.82
17R-1, 42–43	290.32							14.2	
17R-2, 141–143	292.81	1.96		65	51	2.81	1.86	0.4	1.82
17R-3, 139–141	294.29	2.01	1.39	63	47	2.71	1.68	2.6	1.91
17R-4, 43–45	294.83	1.89	1.24	66	55	2.88	1.91	14.7	1.70
18R-1, 15–17	299.65	1.85	1.22	63	54	2.89	1.72	6.8	1.74
18R-2, 102–106	302.02	1.89	1.36	54	41	2.71	1.17	1.4	1.74
18R-2, 137–138	302.37							12.3	
18R-3, 107–109	303.57	1.93	1.32	62	49	2.74	1.60	9.4	1.75
18R-3, 115–125	303.65							7.1	
18R-4, 124–126	305.24	1.87	1.23	65	55	2.71	1.82	16.7	1.73
19R-1, 10–12	309.10	1.73	1.10	64	60	2.69	1.75		1.69
19R-1, 47–49	309.47							0.8	

Table 14 (continued).

Core, section, interval (cm)	Depth (mbsf)	Wet-bulk density (g/cm³)	Dry-bulk density (g/cm³)	Porosity (%)	Water content (%)	Grain density (g/cm³)	Void ratio	Carbonate content (%)	Velocity (km/s)
126-792E- (Cont.)									
19R-2, 21–24	310.71	1.91	1.34	58	45	2.75	1.38	5.0	1.77
19R-3, 41–51	312.41	1.88	1.26	62	52	2.79	1.66	20.7	1.71
20R-1, 36–38	318.96	1.92	1.34	59	46	2.85	1.46	22.0	1.73
20R-2, 123–126	321.33	1.57[a]	1.02	55	57	2.82	1.24	12.1	1.73
20R-3, 19–21	321.79	1.89	1.33	57	45	2.84	1.32	8.7	1.76
21R-1, 15–17	328.45	1.85	1.24	62	52	2.89	1.63	21.7	1.74
21R-2, 50–53	330.30	1.93	1.33	60	47	2.88	1.50	8.0	1.93
22R-1, 79–81	338.69	1.78	1.23	56	47	2.83	1.26	6.4	1.79
22R-2, 5–7	339.45	1.92	1.33	59	46	2.94	1.44	15.6	1.69
22R-2, 140–150	340.8							7.3	
22R-3, 52–54	341.42							2.9	
22R-3, 74–77	341.64	1.80	1.16	64	58	2.65	1.80		1.87
23R-1, 74–77	348.34	1.82	1.23	60	51	2.86	1.48	13.9	1.74
24R-1, 25–27	357.55	1.85	1.24	62	52	2.58	1.64	13.5	1.95
25R-1, 108–111	368.08	1.92	1.21	72	63	2.70	2.57	14.0	1.91
25R-1, 129–131	368.29							15.8	
26R-1, 10–12	376.7							21.5	
26R-1, 68–70	377.28	1.98	1.36	63	48	3.11	1.68	19.2	1.86
27R-1, 27–37	386.57							57.3	
27R-2, 42–44	387.34	1.80	1.13	68	62	3.46	2.08	59.6	1.80
27R-4, 88–90	390.80	1.50[a]	1.24	26[a]	22[a]	3.80[a]	0.35[a]	33.2	1.83
28R-1, 35–36	396.35								
28R-1, 69–70	396.69	1.82	1.16	67	60	2.74	2.01	64.6	2.05
28R-2, 41–43	397.91	2.04	1.46	59	42	2.95	1.41	67.6	1.79
29R-1, 97–100	406.57	1.78	1.07	72	71	3.19	2.55	39.2	1.96
29R-2, 5–7	407.15							25.2	
29R-2, 21–23	407.31	2.04	1.35	69	53	3.09	2.22	1.8	1.76
30R-1, 108–110	416.28	1.87	1.24	63	53	2.60	1.71	0.5	2.20
30R-3, 84–86	419.04	1.73	1.03	71	72	2.73	2.42	9.3	1.80
30R-5, 10–12	421.3	1.73		72	75	2.79		4.2	
30R-5, 11–21	421.31							0.8	1.78
30R-7, 37–39	423.28	1.79	1.12	68	64	2.69	2.16	11.1	1.69
31R-1, 54–55	425.44							42.7	1.67
31R-1, 127–128	426.17							41.1	
31R-2, 22–23	426.62							0.9	
31R-2, 48–49	426.88							0.4	
31R-3, 96–98	428.86	1.88	1.31	58	46	2.78	1.39	20.6	1.99
31R-3, 118–119	429.08							13.9	
32R-1, 35–37	434.95	1.93	1.38	55	41	2.62	1.22	5.8	2.60
32R-3, 98–101	438.58	2.02	1.50	52	36	2.47	1.08	4.9	2.81
33R-1, 15–17	444.35	2.14	1.59	55	36	2.62	1.22		2.80
33R-1, 89–90	445.09	2.15	1.71	44	27	2.33	0.79	0.8	2.87
33R-2, 95–105	446.65							1.4	
33R-3, 58–60	447.58	1.90	1.22	69	59	2.91	2.24	4.0	2.24
34R-1, 67–69	454.57	1.78[a]	0.81	99[a]	131[a]	1.83[a]	73[a]	25.0	1.82
34R-2, 102–104	456.42	1.80	1.13	68	63	2.61	2.10	8.8	2.15
34R-3, 79–81	457.69	1.68	1.01	68	71	2.64	2.14	9.7	2.05
35R-1, 107–110	464.57	1.83	1.38	45[a]	33[a]	2.24[a]	0.82	1.0	2.52
35R-2, 48–50	465.49	1.75	1.09	67	64	2.71	1.99	8.3	2.22
36R-1, 75–77	473.95	1.73	1.10	64	61	2.46	1.76	6.8	2.14
36R-2, 139–141	476.09	1.81	1.23	59	50	2.61	1.41	5.2	2.33
36R-3, 129–132	477.49	1.73	1.06	69	68	2.79	2.18	14.6	1.95
36R-4, 67–77	478.37							1.9	
36R-5, 91–93	479.38	1.85	1.21	65	56	2.59	1.86	6.3	2.17
37R-1, 73–74	483.53							18.8	
37R-1, 131–135	484.11	1.80	1.19	62	54	2.60	1.60	7.9	2.12
37R-3, 54–57	486.34	1.71	1.08	64	62	2.67	1.75	13.9	2.03
37R-5, 16–18	488.96	1.86	1.28	59	48	2.76	1.45		
37R-5, 128–130	490.08	1.92	1.34	59	46	2.80	1.43	5.4	2.23
37R-7, 16–18	491.96							1.1	2.33
38R-1, 43–45	492.93	1.84	1.25	59	49	2.74	1.46	1.3	2.47
38R-3, 119–121	496.69	2.04	1.57	47	31	2.64	0.89	0.3	2.63
38R-5, 30–33	498.80	2.01	1.56	45	30	2.64	0.82	0.8	2.60
38R-CC, 6–8	501.25	1.99	1.46	53	38	2.70	1.14	0.4	2.37
39R-1, 128–130	503.48	1.81	1.24	58	48	2.63	1.36	2.8	2.18
39R-2, 115–125	504.85							1.5	
39R-3, 36–38	505.56	1.88	1.35	53	41	2.60	1.13	2.8	2.21
39R-5, 63–66	508.83	2.03	1.53	50	34	2.59	1.00	0.6	2.47
40R-1, 103–106	512.93	1.79	1.29	51	41	2.55	1.03	2.3	2.36
40R-3, 15–17	515.05	2.00	1.55	45	30	2.43	0.83	0.6	2.51
40R-5, 107–110	518.97	2.11	1.70	42	26	2.66	0.73	0.5	2.67
40R-6, 75–77	520.15							10.7	
41R-, 20–22	521.80	2.17	1.73	44	27	2.76	0.79	0.6	2.48
41R-1, 118–119	522.78							0.6	
41R-2, 56–59	523.66	1.81	1.30	60	52	2.61	1.52	2.6	2.23
41R-3, 82–85	525.42	2.03	1.53	50	34	2.69	0.99	0.6	2.32

Table 14 (continued).

Core, section, interval (cm)	Depth (mbsf)	Wet-bulk density (g/cm³)	Dry-bulk density (g/cm³)	Porosity (%)	Water content (%)	Grain density (g/cm³)	Void ratio	Carbonate content (%)	Velocity (km/s)
126-792E- (Cont.)									
41R-5, 100–102	528.33	2.20	1.82	39	22	2.56	0.63	0.6	2.79
42R-1, 52–54	531.72	2.15	1.70	45	27	2.55	0.82		2.63
42R-3, 116–118	535.36	2.14	1.69	46	28	2.89	0.85	0.6	2.52
42R-4, 140–150	537.1							0.6	
42R-5, 119–120	538.39	2.38	1.98	41	21	2.83	0.68	0.8	2.75
43R-1, 77–79	541.37	2.27	1.86	42	23	2.62	0.71	0.6	2.78
43R-3, 56–58	543.97	2.04	1.66	39	24	2.50	0.63	9.8	3.10
43R-3, 110–111	544.51							7.1	
43R-5, 82–84	547.25	2.07	1.62	45	29	2.60	0.83	0.9	2.32
43R-5, 100–101	547.43							32.6	
43R-7, 30–33	549.63	2.19	1.78	41	24	2.65	0.70	0.5	3.11
44R-1, 60–62	550.90	2.46	2.11	35	17	3.00	0.54	0.6	3.09
44R-3, 52–55	553.83	2.09	1.61	49	31	2.57	0.94	0.7	2.26
44R-5, 34–36	556.65	2.19	1.82	38	22	2.53	0.62	0.7	2.73
45R-1, 65–67	560.65	2.03	1.50	53	37	2.61	1.14	0.8	2.22
45R-2, 0–10	561.45							0.7	
45R-3, 1–3	562.93	1.97	1.43	55	40	2.58	1.21	1.6	2.04
45R-4, 133–135	565.56	2.10	1.65	46	29	2.57	0.83	0.8	2.52
46R-1, 73–75	570.43	2.17	1.72	45	27	2.50	0.82	0.8	2.60
46R-3, 122–124	573.65	2.07	1.68	40	24	2.59	0.65	0.7	2.76
46R-5, 119–120	576.55	2.35	1.90	46	25	2.42	0.84	8.6	3.00
46R-7, 31–35	578.56	2.19	1.79	40	23	2.48	0.68		3.55
47R-1, 114–116	580.54	2.31	1.88	44	24	2.52	0.77	1.1	2.91
47R-3, 48–50	582.49	2.29	1.91	38	21	2.62	0.62	0.8	3.15
48R-1, 35–37	588.95	2.27	1.90	38	21	2.61	0.61	0.8	3.03
48R-3, 38–40	591.28	2.01	1.45	57	41	2.84	1.32	1.8	2.11
48R-3, 52–53	591.42							5.3	
48R-5, 63–65	594.21	2.18	1.77	42	25	2.83	0.73	0.4	2.52
48R-6, 83–84	595.88							14.2	2.33
48R-7, 140–150	597.55							0.4	2.40
48R-8, 19–21	597.84	2.10		47	30	2.67	0.89	0.6	2.32
49R-1, 120–121	599.00	2.17	1.71	46	28	2.86	0.86		2.32
49R-2, 37–41	599.67	2.28	1.77	51	30	2.67	1.05		2.55
49R-3, 63–66	601.43	1.89	1.31	58	46	2.99	1.40	3.9	2.15
49R-5, 111–114	604.76	2.13	1.67	46	28	2.89	0.84	4.2	2.34
49R-6, 37–39	605.52	2.27	1.73	55	33	2.98	1.22		2.33
50R-1, 23–26	607.63	2.18	1.78	40	23	2.79	0.67	1.3	2.48
50R-3, 8–10	610.48	2.07	1.60	48	31	2.87	0.91	0.6	2.25
50R-5, 16–18	613.57	2.22	1.76	46	27	2.97	0.86	0.8	2.35
50R-7, 11–13	616.52							2.4	2.37
51R-1, 33–35	617.43	1.79	1.14	66	61	2.73	1.96	6.1	2.26
51R-2, 106–109	619.66	2.00	1.48	52	37	2.57	1.10	2.6	2.55
51R-2, 140–150	620							1.6	
51R-3, 14–17	620.24	1.98	1.41	58	43	2.62	1.41	6.3	2.42
52R-1, 38–40	627.18	1.91	1.33	58	45	2.79	1.37	16.0	2.08
52R-1, 100–102	627.8							42.5	
52R-2, 31–34	628.61	1.78[a]	1.73	5[a]	3[a]	2.80[a]	0.05[a]	0.9	1.98
52R-3, 22–24	630.02							0.6	2.53
52R-4, 49–51	631.79							14.7	2.06
52R-5, 50–52	633.3							0.8	1.94
52R-6, 8–10	634.38	2.07	1.56	51	34	2.77	1.03	0.7	2.30
54R-1, 136–137	647.46	2.23	1.69	55	34	2.69	1.23	0.7	2.40
54R-2, 49–51	648.09							6.3	
54R-3, 11–12	649.21	2.33	1.91	43	23	2.89	0.74	1.4	2.51
54R-3, 140–150	650.5							8.9	
54R-5, 83–84	652.93	2.10	1.59	51	33	2.38	1.05	13.7	2.31
54R-6, 8–9	653.68							23.2	
55R-1, 53–55	656.23	2.17	1.72	46	28	2.57	0.85	12.1	2.37
55R-2, 99–101	658.19	2.25	1.84	41	23	2.85	0.71	0.8	2.46
56R-2, 78–80	667.68	1.89	1.25	65	55	2.82	1.89	2.2	2.16
56R-4, 16–18	670.06	2.11	1.64	48	30	2.38	0.93	0.7	2.36
56R-6, 136–138	673.98							0.4	2.00
57R-1, 96–99	679.06	2.00	1.49	51	36	2.87	1.06	13.0	2.15
57R-3, 4–6	678.14	2.16	1.71	46	28	2.92	0.83	0.5	2.42
57R-5, 84–87	681.94	2.22	1.81	41	23	2.83	0.70	0.2	2.38
57R-5, 140–150	682.5							0.3	
57R-6, 50–52	683.10	1.94	1.32	63	49	2.41	1.67	6.7	2.07
58R-1, 69–71	685.49	2.10	1.67	44	27	2.66	0.78	0.5	2.30
58R-2, 93–95	687.23	1.95	1.34	62	48	2.67	1.62	2.3	2.22
58R-CC, 19–21	689.89	2.23	1.82	42	24	2.78	0.72	0.4	2.41
59R-1, 68–68	695.05	1.89	1.31	59	47	2.78	1.41	3.7	1.96
59R-2, 46–48	696.36	2.20	1.79	41	24	2.76	0.69	0.4	2.41
59R-3, 101–103	689.28	2.03	1.48	55	39	2.67	1.24		2.25
59R-4, 73–75	699.22	2.07	1.57	51	34	2.94	1.06	0.7	2.30
59R-5, 47–50	700.40	2.03	1.49	56	39	2.77	1.25	6.1	2.07
60R-1, 121–123	705.21	1.98	1.44	55	40	2.69	1.21	0.7	2.02

Table 14 (continued).

Core, section, interval (cm)	Depth (mbsf)	Wet-bulk density (g/cm³)	Dry-bulk density (g/cm³)	Porosity (%)	Water content (%)	Grain density (g/cm³)	Void ratio	Carbonate content (%)	Velocity (km/s)
126-792E- (Cont.)									
60R-2, 70–73	706.20	2.06	1.58	49	32	2.70	0.95	0.4	2.20
60R-3, 16–19	707.16	2.01	1.50	52	36	2.80	1.06	0.4	2.03
60R-4, 140–143	709.90	2.32	1.94	38	21	2.90	0.62	0.3	2.50
60R-6, 28–30	711.78	2.29	1.91	38	21	2.92	0.62	0.3	2.54
60R-6, 140–150	712.9							0.4	
61R-1, 143–145	715.03	2.12	1.70	43	26	2.68	0.76		2.34
61R-2, 119–121	716.29	2.37	1.99	39	20	2.83	0.63	0.3	2.52
61R-3, 130–133	717.90	2.35	1.97	38	20	2.86	0.62	0.4	2.61
61R-4, 87–89	718.97	2.33	1.99	34	18	2.83	0.52	0.6	3.02
62R-1, 3–5	722.93	2.32	1.86	46	26	2.54	0.85	1.2	2.29
62R-2, 94–96	724.52	2.17	1.78	39	23	2.49	0.64	0.8	2.61
62R-4, 36–39	726.53	2.13	1.68	46	29	2.61	0.86	1.1	2.35
62R-6, 114–116	729.83	2.36	1.90	46	25	2.78	0.86		2.62
62R-7, 69–71	730.80	2.54	2.10	45	22	2.73	0.81	0.6	2.77
62R-8, 6–8	731.67	2.05	1.46	60	43	2.63	1.49	1.7	2.09
63R-1, 109–111	733.59	2.32	1.99	33	17	2.53	0.50	0.5	2.86
63R-3, 5–7	735.41	2.25	1.85	41	23	2.64	0.68	2.7	2.43
63R-3, 138–150	736.74							2.9	
64R-1, 15–17	742.35	2.10	1.62	48	31	2.15	0.92	2.2	2.17
64R-2, 51–53	744.16	2.22	1.92	31	17	2.50	0.45	0.4	2.85
65R-1, 11–13	751.91	2.23	1.87	36	20	2.63	0.57	0.6	3.07
65R-2, 16–18	753.39	2.52	2.08	44	22	2.73	0.78	0.5	2.80
66R-1, 52–54	762.02	1.92	1.38	55	41	2.67	1.21	9.7	1.96
66R-3, 144–146	765.94	2.19	1.60	47	28	2.60	0.90	0.7	2.56
66R-5, 139–149	768.91							1.2	
66R-6, 10–12	769.11	2.23	1.72	51	31	2.72	1.05	1.1	2.41
67R-1, 75–77	771.95	2.33	1.91	42	23	2.76	0.73	0.4	2.74
67R-2, 111–113	773.81	2.46	2.13	34	16	2.53	0.51	0.9	3.26
67R-3, 23–25	774.43	2.22	1.78	45	26	2.49	0.81	0.7	2.22
68R-1, 51–53	781.41	2.59	2.35	25	11	2.79	0.33	16.1	3.25
68R-2, 83–85	782.97	2.51	2.23	29	13	2.88	0.41	0.5	2.68
68R-2, 124–126	783.38	2.23	1.79	44	25	2.58	0.78	0.2	2.18
69R-1, 19–21	790.79	2.15	1.65	51	32	2.79	1.03		2.34
69R-2, 90–92	793.00	1.85	1.38	47	35	2.31	0.88		2.16
69R-3, 107–108	794.67							0.5	
69R-4, 24–26	795.16	1.99	1.53	46	31	2.67	0.86		2.37
69R-4, 136–146	796.28		1.28					0.3	
69R-5, 89–91	797.27	1.87		60	49	2.61	1.52		2.01
70R-CC, 2–5	800.22	2.62	2.48	15	6	2.85	0.18		4.59
71R-1, 52–54	810.42	2.65	2.50	15	6	2,77	0.18		4.50
71R-2, 22–24	811.55	2.71	2.53	18	7	2.94	0.22		4.39
71R-2, 83–85	812.16		2.66						5.09
71R-3, 5–7	812.88	11.10[a]	2.61	4[a]	3[a]	0.12[a]			4.88
73R-1, 68–70	820.18	2.56	2.39	17	7	2.75	0.20		4.17
73R-1, 49–51	829.69		2.67						5.03
73R-1, 123–125	830.43	2.68	2.56	12	5	2.68	0.14		4.66
73R-2, 99–101	831.64	2.54	2.30	24	11	2.77	0.31		3.94
73R-2, 141–143	832.06								3.91
74R-1, 77–78	839.57	2.51	2.09	42	21	2.81	0.71		2.62
74R-2, 28–30	840.51	3.23	3.03	20	7	3.22	0.25		4.29
74R-2, 46–48	840.69		2.21						3.58
75R-1, 71–73	848.91	2.45	2.22	23	11	2.75	0.31		3.94
75R-2, 35–37	850.05	2.72	2.58	15	6	2.88	0.18		4.47
76R-1, 96–98	858.66	2.48	2.39	9	4	2.51	0.10		4.75
77R-1, 44–46	867.54	2.57	2.37	20	9	2.58	0.25		4.16
78R-1, 22–24	876.82	2.76	2.61	15	6	2.80	0.17		4.30
78R-1, 37–39	876.97	2.53	2.37	17	7	2.77	0.20		4.12
78R-1, 61–63	877.21	2.64	2.46	18	8	2.84	0.22		4.22

[a] Data of uncertain quality.

uppermost part of Unit IV. Below this high-velocity layer, velocity data increase downward from an average of 2.15 km/s at 450–480 mbsf to 2.77 km/s at 540–590 mbsf. At 590 mbsf, we observed a velocity decrease of 0.5 km/s. From 590–708 mbsf, velocity values show little variation and average 2.28 km/s. Between 708 mbsf and the bottom of Unit IV (783 mbsf), variability increases and velocity values increase slightly (average = 2.58 km/s).

A distinct decrease (~0.5 km/s) in velocity is observed across the Unit IV/Unit V contact. The few velocity measurements made within Unit V average 2.22 km/s (with a range from 2.01 to 2.37 km/s). These lower velocities may be the result of the alteration that we observed in these sediments (see "Lithostratigraphy and Accumulation Rates" section, this chapter).

The contact of the sedimentary section with igneous basement (Unit VI; composed of andesite) at 804 mbsf is marked by a 2.58-km/s increase (from 2.01–4.59 km/s) in velocity. Velocity data in basement rocks average 4.26 km/s (range = 2.62–5.09 km/s). Velocity values decrease downward in the basement rocks, probably the result of an increase in alteration.
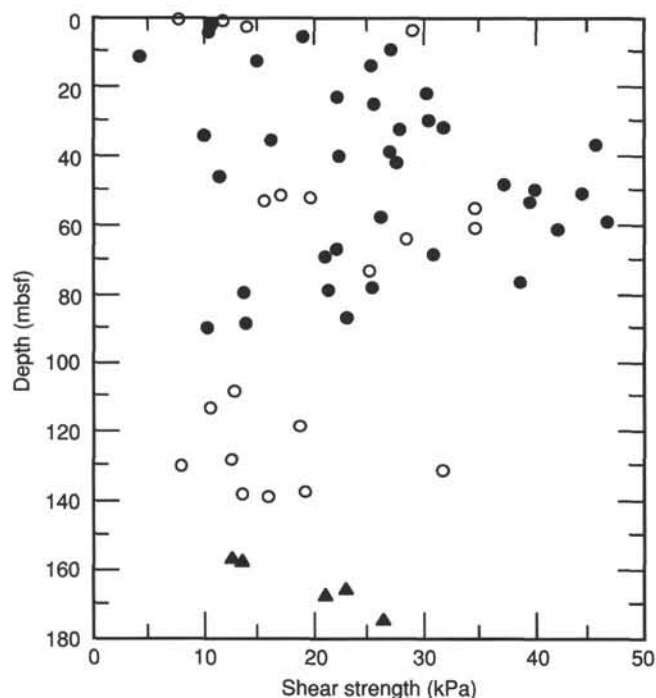
Figure 57. Plots of shear strength vs. depth for Holes 792A (closed circles), 792B (open circles), and 792E (triangles).

A comparison of MST *P*-wave and Hamilton Frame velocity data reveals a close agreement within depths drilled by the APC (Hole 792A; Fig. 58. In rotary-drilled Hole 792E, there is a large difference between MST and HF velocity measurements. This is attributed to a large annulus of air between the core and the core liner that resulted from rotary coring. This evidence, coupled with the results from previous holes (see "Physical Properties" section, "Site 787" and "Site 790/791" chapters, this volume) suggests that MST *P*-wave logging should not be attempted on rotary cores.

Thermal Conductivity

Thermal conductivity measurements were performed on as many undisturbed cores as possible from the sedimentary column, by means of the needle-probe method (Fig. 59; Table 16). In addition, thermal conductivity measurements were made on two well-lithified sedimentary samples and four igneous rock samples by means of the half-space method (Fig. 59; Table 16).

Thermal conductivity values within Units I, II, III, and IV are highly variable. However, we observed a slight increase in thermal conductivity with depth. Thermal conductivity values increase from 1.000 to 1.050 between Units I and IV, and average 1.010, 1.018, 1.047, and 1.052 W/m · K in Units I, II, III, and IV, respectively.

The two well-lithified sedimentary rocks from the lower parts of Unit IV (Sample 126-792E-67R-1, 60 cm; 771.80 mbsf) and Unit V (Sample 126-792E-69R, CC, 10 cm; 798.20 mbsf) yielded thermal conductivity values of 1.172 and 1.038 W/m · K, respectively.

Thermal conductivity data within the andesitic "basement" (Unit VI; see "Lithostratigraphy and Accumulation Rates" section, this chapter) increase sharply. Average values for this unit are 1.610 W/m · K (with a range of 1.456–1.838 W/m · K).

Heat Flow

Plots of temperature vs. time for the three successful downhole temperature runs are shown in Figure 60. These three mea-

Table 15. Shear strength data, Site 792.

Core, section, interval (cm)	Depth (mbsf)	Shear strength (kPa)
126-792A-		
1H-2, 100	2.50	10.7
1H-3, 110	4.10	10.4
1H-4, 94	5.44	19.0
1H-7, 20	9.20	26.8
2H-1, 114	10.84	4.2
2H-2, 107	12.27	14.7
2H-3, 114	13.84	25.3
3H-2, 70	21.30	30.2
3H-3, 82	22.92	22.1
3H-4, 116	24.76	25.4
4H-1, 105	29.45	30.4
4H-2, 115	31.05	31.7
4H-3, 55	31.95	27.8
4H-4, 123	34.13	10.0
4H-5, 94	35.34	16.1
4H-6, 45	36.35	45.6
5H-1, 100	38.80	26.8
5H-2, 42	39.72	22.2
5H-3, 97	41.77	27.4
5H-6, 49	45.79	11.4
6H-1, 106	48.26	37.2
6H-2, 71	49.41	39.9
6H-3, 29	50.49	44.3
6H-4, 129	52.99	39.6
7H-1, 92	57.52	26.1
7H-2, 89	58.99	46.6
7H-3, 75	60.35	42.0
7H-4, 92	61.69	42.0
8H-1, 65	66.65	21.9
8H-2, 95	68.32	30.8
8H-3, 34	69.21	21.0
9H-1, 74	76.34	38.7
9H-2, 104	77.86	25.2
9H-3, 17	78.49	21.2
9H-4, 24	79.43	13.5
10H-1, 115	86.45	22.9
10H-3, 109	88.20	13.8
10H-4, 96	89.57	10.3
126-792B-		
1H-1, 37	0.37	7.7
1H-1, 118	1.18	11.7
1H-2, 105	2.55	14.0
1H-3, 53	3.53	28.9
2H-1, 109	51.09	16.8[a]
2H-2, 63	52.13	19.6[a]
2H-3, 29	53.29	15.4[a]
2H-4, 73	55.23	34.5
3H-1, 125	60.85	34.5
3H-3, 131	63.91	28.4
4H-3, 112	73.32	25.0
8H-1, 44	108.34	12.8
8H-4, 64	113.04	10.7
9H-1, 110	118.60	18.7
10H-1, 99	128.09	12.4
10H-2, 139	129.99	7.9
10H-3, 75	130.85	31.7
11H-1, 23	137.03	19.1
11H-2, 32	137.91	13.5
11H-CC, 25	138.78	15.9
126-792E-		
3R-1, 115	155.95	12.4
3R-3, 25	157.25	13.5
4R-1, 66	165.16	22.9
4R-2, 106	167.06	21.0
5R-1, 64	174.74	26.3

[a] Data of uncertain quality.

A

B
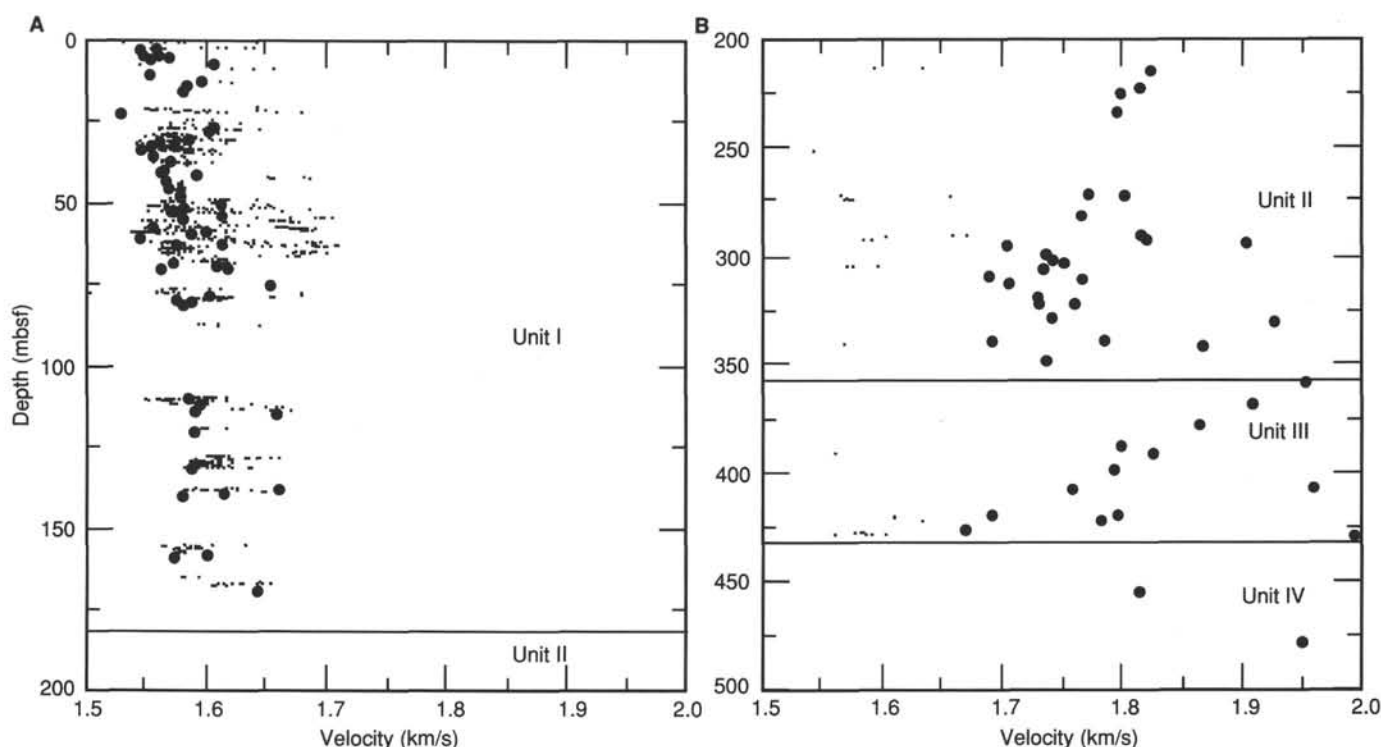
Figure 58. Comparison of sonic velocity determined by Hamilton Frame (large closed circles) and multi-sensor track (small dots) methods for Site 792. Horizontal lines indicate lithologic units. Note good correlation between methods in APC cores and poor correlation in RCB cores (shown at different vertical scales). **A.** APC cores. **B.** RCB cores.
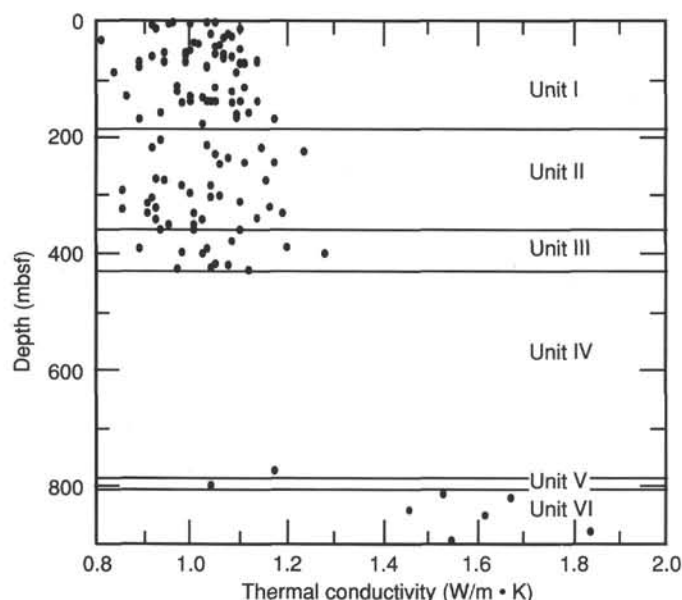
Figure 59. Plot of thermal conductivity vs. depth from Site 792. Horizontal lines indicate lithologic unit boundaries.

surements produced excellent data (Table 17) from which we made preliminary estimates of *in-situ* temperatures by extrapolation of the temperature-vs.-time data through the use of theoretical decay equations (Table 17; shipboard computer system software developed by K. Becker, unpubl. data). The linearity of the resulting geothermal gradient (0.054°C/m; Fig. 61) suggests

that no convection is occurring through this deposit. Therefore, heat flow may be calculated as

$$Q = k \, dT/dz, \qquad (1)$$

where
Q = the calculated heat flow,
k = the average thermal conductivity, and
dT/dz = the geothermal gradient.

If we use an average thermal conductivity (not corrected to *in-situ* values) of 1.012 W/m · K for the upper 110 mbsf, an average heat flow of 0.0546 W/m² (1.3 heat flow units, or HFU) is determined. Predicted heat-flow values, determined on the basis of half-space models of purely conductive flow (Davis and Lister, 1977; Parsons and Sclater, 1977) and various estimates for the age of basement, range as high as 2.19 HFU (assuming a minimum basement age of 30 Ma) to as low as 1.6 HFU (assuming a 50-Ma basement age).

DOWNHOLE MEASUREMENTS

At Hole 792E, the drill pipe became stuck at a depth of 287.0 mbsf as we attempted to pull out of the hole to the proposed logging depth of 120.0 mbsf. Thus, we decided to deploy a reduced combination of geophysical sensors in the open-hole section. The density tool was excluded to eliminate the risk of leaving a radioactive source in the hole if the tool became stuck. The first run consisted of resistivity, velocity, natural gamma, and temperature sensors. In total, we conducted a series of five experiments in Hole 792E. The second run consisted of the formation microscanner (FMS), natural gamma ray, and temperature sensors. The geochemical, natural gamma ray, and temperature sensors were deployed during the third run, whereas the density, natural gamma ray, and temperature sensors were com-

Table 16. Thermal conductivity data, Site 792.

Core, section, interval (cm)	Depth (mbsf)	Thermal conductivity (W/m · K)
792B-1H-1, 111	1.11	1.047
792A-1H-1, 119	1.19	0.958
792B-1H-2, 95	2.45	1.028
792B-1H-3, 75	3.75	0.950
792A-1H-3, 98	3.98	0.999
792A-1H-5, 104	7.04	0.913
792A-2H-3, 61	13.31	0.926
792A-2H-3, 128	13.98	1.098
792A-2H-6, 86	18.66	0.668
792A-3H-2, 45	21.05	1.074
792A-3H-3, 33	22.43	1.044
792A-3H-5, 51	25.61	1.083
792A-4H-1, 70	29.10	1.070
792A-4H-3, 69	32.09	0.813
792A-4H-6, 60	36.50	1.005
792A-5H-1, 59	38.39	1.012
792A-5H-3, 89	41.69	1.060
792A-5H-5, 25	44.05	1.049
792A-6H-1, 81	48.01	1.102
792A-6H-3, 66	50.86	0.993
792B-2H-3, 73	53.73	0.939
792B-2H-4, 73	55.23	0.986
792B-2H-5, 73	56.73	1.065
792A-7H-1, 18	56.78	1.052
792A-7H-2, 78	58.88	0.984
792A-7H-3, 55	60.15	0.918
792B-3H-1, 107	60.67	1.083
792B-3H-3, 60	63.20	1.068
792A-8H-1, 103	67.03	1.138
792A-8H-2, 102	68.39	0.892
792B-3H-7, 48	69.08	0.989
792A-8H-3, 36	69.23	0.942
792B-4X-1, 77	69.97	1.141
792B-4X-2, 123	71.93	1.099
792B-4X-3, 17	72.37	1.112
792A-9H-1, 70	76.30	1.028
792A-9H-2, 105	77.87	1.028
792A-9H-3, 34	78.66	0.893
792A-10H-1, 53	85.83	0.838
792A-10H-1, 120	86.50	1.090
792A-10H-2, 28	87.08	0.622[a]
792B-8X-2, 99	110.39	0.971
792B-8X-3, 88	111.78	1.049
792B-8X-4, 73	113.13	1.112
792B-9X-1, 102	118.52	1.082
792B-9X-2, 18	119.18	0.970
792B-10X-1, 117	128.27	0.992
792B-10X-2, 33	128.93	0.862
792B-10X-3, 94	131.04	1.026
792E-1R-1, 19	135.79	1.137
792E-1R-1, 34	135.94	1.031
792D-1X-1, 43	136.43	1.104
792B-11X-1, 10	136.90	0.993
792C-1X-CC, 14	136.94	1.049
792C-1X-CC, 32	137.12	1.043
792B-11X-2, 28	137.93	0.974
792B-11X-CC, 12	138.65	1.087
792E-3R-1, 75	155.55	0.932
792E-3R-2, 44	156.74	1.121
792E-3R-3, 33	157.33	1.092
792E-4R-1, 12	164.62	1.095
792E-4R-2, 108	167.08	1.173
792E-4R-CC, 5	167.55	0.893
792E-5R-1, 61	174.71	1.024
792E-8R-1, 24	203.34	0.932
792E-9R-1, 84	213.44	1.034
792E-9R-3, 109	216.69	0.918
792E-9R-5, 33	217.93	1.150
792E-10R-2, 48	224.18	1.232
792E-10R-4, 44	227.14	1.046
792E-11R-1, 55	232.45	1.117[a]
792E-11R-1, 126	233.16	1.073
792E-11R-2, 54	233.94	0.789[a]
792E-12R-1, 115	242.65	1.114
792E-12R-2, 67	243.67	1.175

Table 16 (continued).

Core, section, interval (cm)	Depth (mbsf)	Thermal conductivity (W/m · K)
792E-12R-3, 103	245.53	1.058
792E-13R-1, 44	251.64	1.039[a]
792E-13R-2, 24	252.94	0.673[a]
792E-15R-1, 104	271.54	0.923
792E-15R-2, 27	272.27	1.151
792E-15R-3, 20	273.70	0.943
792E-16R-1, 72	280.92	1.040
792E-16R-2, 33	282.03	0.978
792E-17R-1, 9	289.99	0.946[a]
792E-17R-2, 8	291.48	0.851
792E-17R-3, 100	293.90	0.993
792E-18R-1, 23	299.73	1.062
792E-18R-2, 13	301.13	1.038
792E-18R-4, 34	304.34	0.916
792E-19R-1, 100	310.00	1.103
792E-19R-2, 76	311.26	0.905
792E-19R-3, 22	312.22	0.896[a]
792E-20R-1, 21	318.81	1.164
792E-20R-2, 23	320.33	0.929
792E-20R-3, 46	322.06	0.850
792E-21R-1, 47	328.77	1.193
792E-21R-1, 117	329.47	1.006
792E-21R-2, 21	330.01	0.905
792E-22R-1, 15	338.05	1.138
792E-22R-2, 40	339.80	1.026
792E-22R-3, 20	341.10	0.924
792E-23R-1, 68	348.28	0.953
792E-23R-2, 21	349.31	1.004
792E-24R-1, 27	357.57	1.099
792E-24R-1, 57	357.87	0.929
792E-24R-2, 96	358.26	1.006
792E-25R-1, 87	367.87	0.951[a]
792E-26R-1, 108	377.68	1.087
792E-27R-2, 66	387.58	1.201
792E-27R-3, 105	389.47	1.032
792E-27R-4, 68	390.60	0.891
792E-28R-1, 16	396.16	0.976
792E-28R-2, 54	398.04	1.279
792E-28R-2, 115	398.65	1.024
792E-30R-2, 70	417.40	1.049
792E-30R-3, 64	418.84	1.078
792E-30R-6, 73	422.14	1.037
792E-31R-1, 96	425.86	0.971
792E-31R-2, 35	426.75	1.124
792E-31R-3, 124	429.14	1.129[a]
792E-67R-1, 60	771.8	1.172
792E-69R-CC, 10	798.2	1.038
792E-71R-1, 68	813.58	1.531
792E-72R-1, 14	819.64	1.673
792E-73R-2, 28	893.98	1.546
792E-74R-2, 61	840.91	1.456
792E-76R-2, 53	850.23	1.617
792E-78R-1, 114	877.74	1.838

[a] Data of uncertain quality.

bined for the fourth run. The velocity sensor was added to this fourth combination to obtain a second velocity profile in an attempt to reduce the noise level encountered during the first run. The last run consisted of a vertical seismic profile (VSP) experiment. The wireline heave compensator was used for downhole measurements in Hole 792E, but it failed at the beginning of the third run. A summary of the operational timing is provided in Table 18.

Prior to releasing the drill bit, we displaced the borehole fluid with KCl mud. With the exception of a short section located at the top of the open hole (297.0–317.0 mbsf), and two fault zones (407.5–430.0 and 779.0–804.0 mbsf), the borehole was generally cylindrical to slightly elliptical, with a diameter constrained to <11.0 in. The deviation of the borehole axis
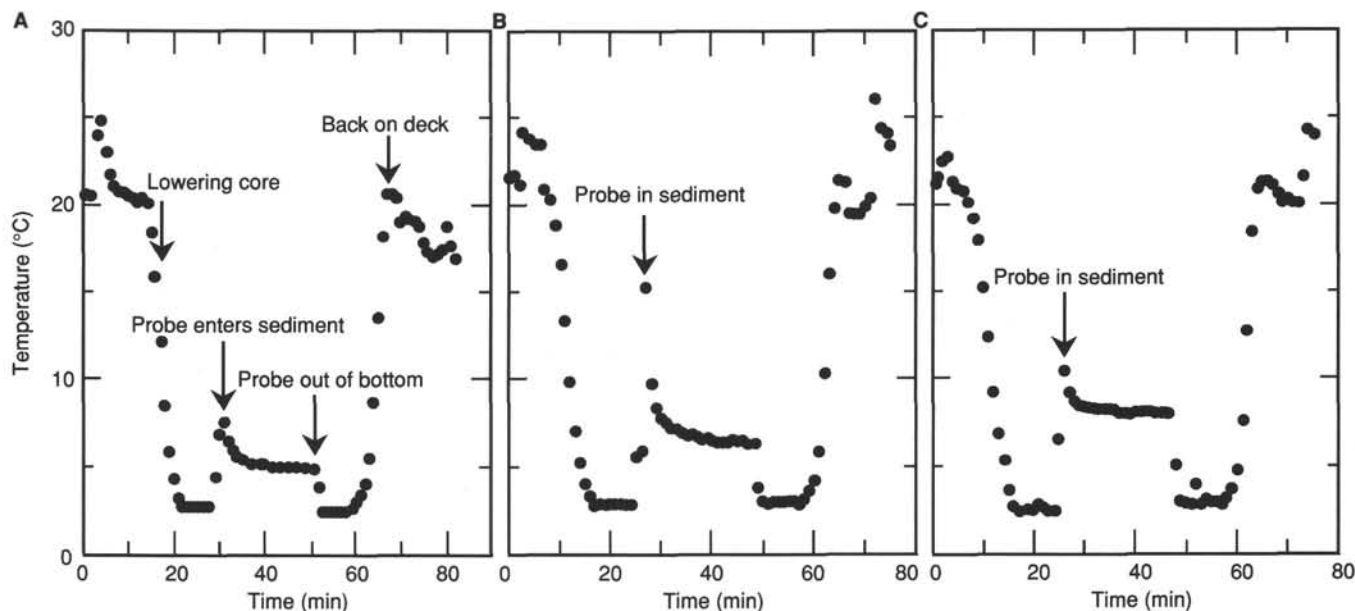
Figure 60. Plots of temperature versus time for the three Uyeda temperature probe runs. **A.** Hole 792A (47.2 mbsf). **B.** Hole 792C (67.0 mbsf). **C.** Hole 792C (110.0 mbsf).

Table 17. *In-situ* temperatures from Uyeda temperature probe runs, Site 792.

Depth (mbsf)	*In-situ* temperature (°C)
0	2.02
47.2	4.5
67	5.6
110	7.92

Table 18. Summary of downhole measurement operations, Site 792.

Date	Time[a] (UTC)	Operation	Run no.	Sensors[b]
May 23, 1989	2115	Rig-Up		
	2245	RIH tool #1	Run 1	DIL-LSS-NGT-TLT
May 24, 1989	0345	POOH tool #1		(1500 ft/hr)
	0445	RIH tool #2	Run 2	FMS-NGT-TLT
	0845	POOH tool #2		(1400 ft/hr)
	0945	RIH tool #3	Run 3	GST-ACT-NGT-TLT
	1830	POOH tool #3		(600 ft/hr)
	2000	RIH tool #4	Run 4	HLDT-LSS-NGT-TLT
May 25, 1989	0200	POOH tool #4		(1000 ft/hr)
	0330	Set-up for VSP		
	0600	RIH tool #5	Run 5	WST
	1400	POOH tool #5		(64 stations in 4.5 hr)
	1415	Rig-down		

[a] Times reported are those at which each sensor combination was run into the hole (RIH) and pulled out of the hole (POOH).
[b] Logging speed is given in parentheses.

from vertical is on the order of 3.0° (N235E), between 292.0 and 878.0 mbsf. Because of the early lithification of this sediment column, the borehole conditions were ideal for downhole experiments and, consequently, the data recorded in Hole 792E are of excellent quality. The sampling distance for FMS data is the smallest of any presently available downhole sensor (25.2 mm), whereas a VSP station was recorded every 9.45 m, and temperature data were acquired every 0.5 s. All of the other records presented in this report were sampled with a 0.152 m digitization interval. A detailed description of each of the sensors and measurement principles is provided in the "Explanatory Notes" chapter (this volume).

Run 1 (Resistivity–Sonic–Natural Gamma–Temperature)

The first run in Hole 792E consisted of a combination of two induction resistivity sensors (with deep and shallow radii of investigation for the deep-phasor induction measurement [IDPH] and the medium-phasor induction measurement [IMPH], respectively), a spherically focused resistivity sensor (SFLU), the long-

Figure 61. *In-situ* temperature vs. depth, Site 792.

$dt/dz = 0.054°C/m$

spacing sonic sensor (LSS), a spectral natural-gamma sensor (NGT), and the Lamont-Doherty Geological Observatory temperature tool (TLT). These last two sensors were included in each of the first four runs and are discussed separately at the end of this section. The NGT was included in each combination for the purpose of depth correlation. The TLT was included to record a temperature profile from seafloor to total depth for each of the four successive runs. Such consecutive profiles allowed us to evaluate the decay of the thermal anomaly introduced by drilling and extrapolate these measurements to obtain an estimate of the temperature at equilibrium for each depth level.

The resistivity data are of excellent quality, recording such features as a series of upward-fining sequences that we observed in the core from 545.0 to 580.0 mbsf (Cores 126-792E-43R through -46R; Fig. 62, 540-580 mbsf). The steplike decrease in resistivity at 587.0 mbsf occurs at the base of a thick conglomeratic bed (Core 126-792E-47R), and is also the location of a sharp increase in (1) smectite concentration observed in XRD analysis, and (2) magnetic susceptibility measured on cores (see "Lithostratigraphy and Accumulation Rates" section, this chapter). The transition from sediment to basement rock is characterized by an order of magnitude increase in resistivity at 804.5 mbsf. Within basement, we observed a series of units with near-constant resistivity values and thicknesses (about 4.1 m). These units have varying mean resistivity values, with low values that correspond to altered and/or brecciated zones observed in the core.

The main characteristic of the sonic data during acquisition was the high noise level, which interfered with the signal from the formation. This noise was primarily a result of the absence of adequate centralization of the sonic tool used aboard the *JOIDES Resolution;* it is a consequence of the small diameter of the drill pipe, which does not allow for the use of centralizers. This lack of centralization resulted in asymmetrical arrivals at the level of the receivers and in "road noise" caused by occasional direct contact between the tool and the formation. The final velocity profile (Fig. 62) was consequently computed by choosing three of the four measured transit times (LTT1, LTT2, LTT3, LTT4; Shipboard Scientific Party [Leg 105], 1987). The sonic sensor was run in the hole during Run 4 at a slower velocity (900 ft/hr instead of 1500 ft/hr) to reduce "road noise". The number of noise-related cycle-skipping events was reduced in the basement section where they were the most numerous in the earlier run.

Run 2 (FMS Images–Natural Gamma–Temperature)

The second run provided the first opportunity to record FMS images during ODP operations. The log was originally recorded from the bottom of the hole up to the drill pipe but, unfortunately, about 200 m of images from the lower part of the hole were overwritten during backup copying after the ship departed Site 792. Four continuous images (from 650.0 to 280.0 mbsf), each covering about 10% of the internal surface of the borehole, will subsequently be produced for analysis. Primary shipboard image analysis of a small interval (347.0-409.0 mbsf) shows the data to be of excellent quality. The FMS picked up features <1 cm in thickness (e.g., dark ash layers in Core 126-792E-28R; Fig. 63). We also observed a change in dip azimuth and direction at the contact between Units II and III. The average dip is 10° (N070E) in the 10.0 m located above the contact, and changes abruptly to about 30° (N250E) for a 1-m-long interval. Below this level, we observed no significant dip.

We recorded measurements pertaining to hole shape and direction (including two orthogonal measurements of drillhole diameter) from 292.0 mbsf to the bottom of the hole. The average hole diameter is approximately 10.5 in., and its shape is pre-

dominantly cylindrical to slightly elliptical. Below the fault zone located at 780.0 mbsf, the ellipticity has no preferred orientation but tends to align in a N20E-N200E direction over the rest of the sedimentary column (Fig. 64). This constrains the maximum horizontal stress direction in the sediments of Hole 792E to be approximately parallel to the relative velocity vector between the Pacific and Philippines plates in the Bonins island arc region (N110E-N290E).

Run 3 (Geochemical Combination–Natural Gamma–Temperature)

The geochemical data recorded during the third run into the drill hole are of excellent quality (Figs. 65 and 66). The data were recorded over the entire length of the drill hole, in the open hole for the lower part of the section, and in the pipe for the upper 287.0 m. Some correlations between several of the analyzed elements in the sedimentary section are shown in Figures 67 and 68, and are generally valid for the basement section as well. They show that Al, Si, Fe, and possibly S are positively correlated with the physical property data (resistivity, velocity, and density), whereas H is negatively correlated. In basement rocks, the low resistivity/velocity/density/Al/Fe/Si, high-H sections are those in which the most intense alteration was observed. The Ca curve is a mirror image of the Si curve in the sediments, and the highest Ca values in this hole are recorded in the middle section of Unit III, as observed in the laboratory core data (see "Sediment/Fluid Geochemistry" section, this chapter). The upper boundary of the Ca-rich zone is also the location of a seismic reflector identified by the VSP experiment (see Run 5, below).

Run 4 (Density–Sonic–Natural Gamma–Temperature)

The short-spacing density detector failed while going into the hole. Therefore, we present only the long-spacing density measurement (LSRH) data (Fig. 62). Because of the small size of the drill hole, however, the data are of good quality and agree with wet-bulk density core measurements. The log was run at 900 ft/hr, which yielded an improved sonic log in comparison with Run 1 (recorded at a speed of 1500 ft/hr). In combination with the velocity data, the wet-bulk density measurements permitted the computation of an impedance profile used as input to a synthetic seismogram shown in Figure 69.

Natural Gamma Spectrometry

In each of the first four runs, natural gamma data were recorded. The four records are of good quality, with a generally low uranium concentration throughout the analyzed section. In the upper part of the sediments (Units II and III), and in the basement rocks (Unit VI), the main source for natural gamma radiation is thorium. Within Units IV and V (430.0-804.5 mbsf), however, natural gamma rays are mostly generated by potassium. In this sedimentary interval, the potassium is inversely related to resistivity, velocity, density (Figs. 62 and 66), and, in some cases, grain size (430.0-500.0 and 555.0-585.0 mbsf). Throughout most of the hole, uranium and potassium are negatively correlated. Thorium and uranium are negatively correlated in the upper part of the basement section (Unit VI, 804.5-842.0 mbsf) and positively correlated in the lower section (842.0-875.0 mbsf).

Temperature Measurements

Out of the four temperature runs, only the first and last ones (Fig. 70) are presented here. The temperature data were recorded upon entering and exiting the hole, starting from a point approximately 100 m above seafloor. The temperature measured at the seafloor during the first run was 2.02°C. Upon entering the hole, the average fluid temperature inside the pipe was approximately 7.0°C. The entrance into the open hole is outlined by a
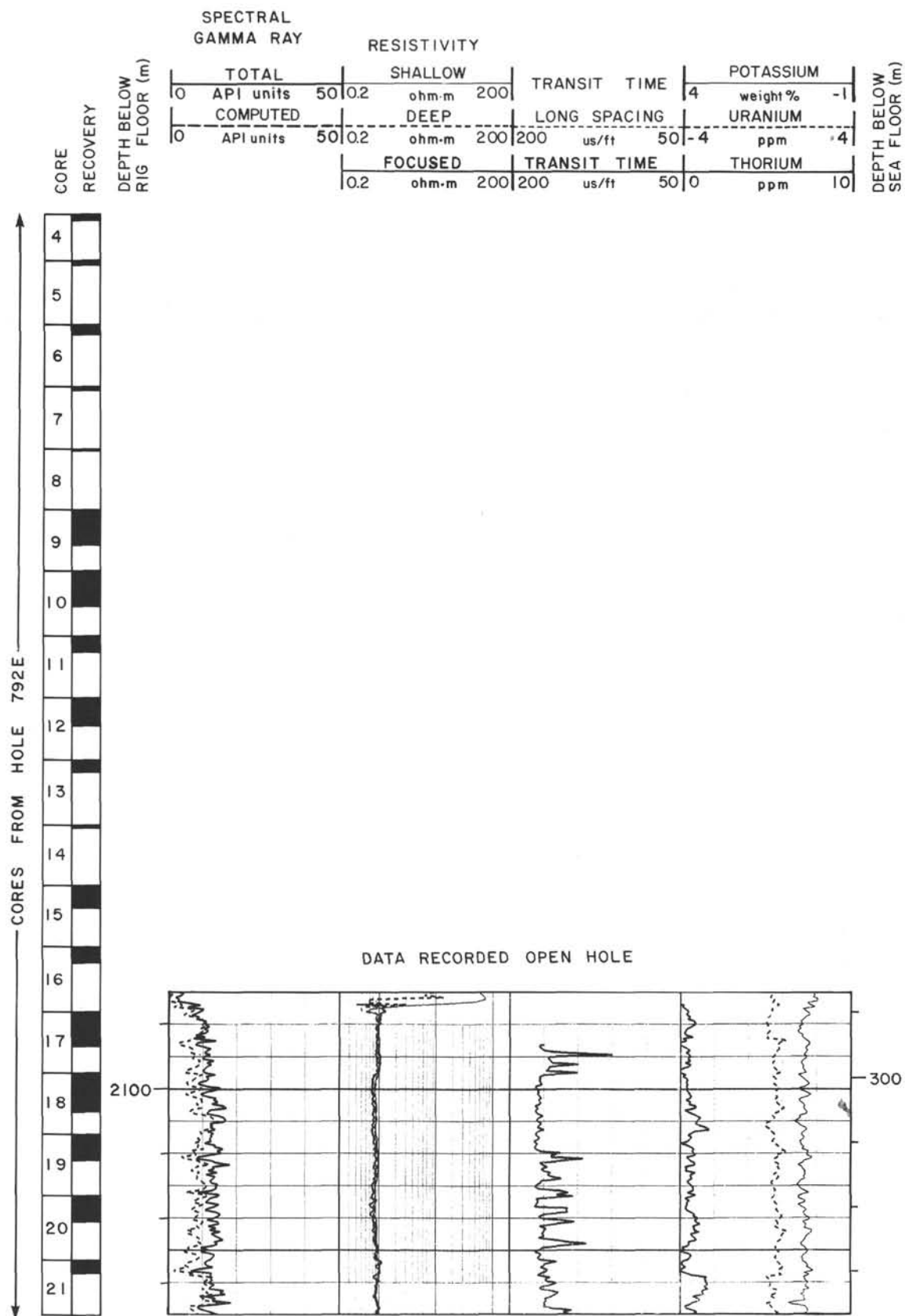
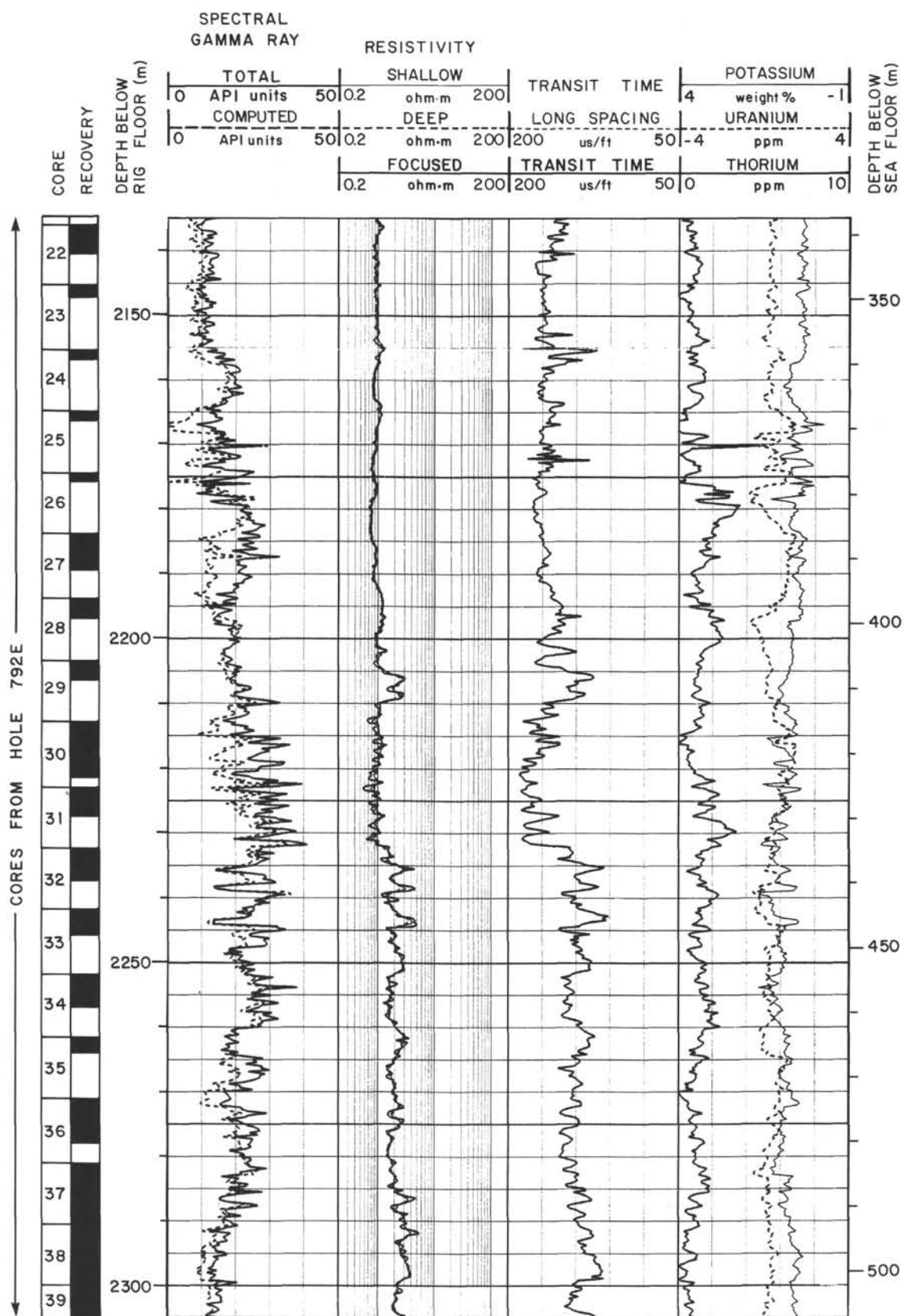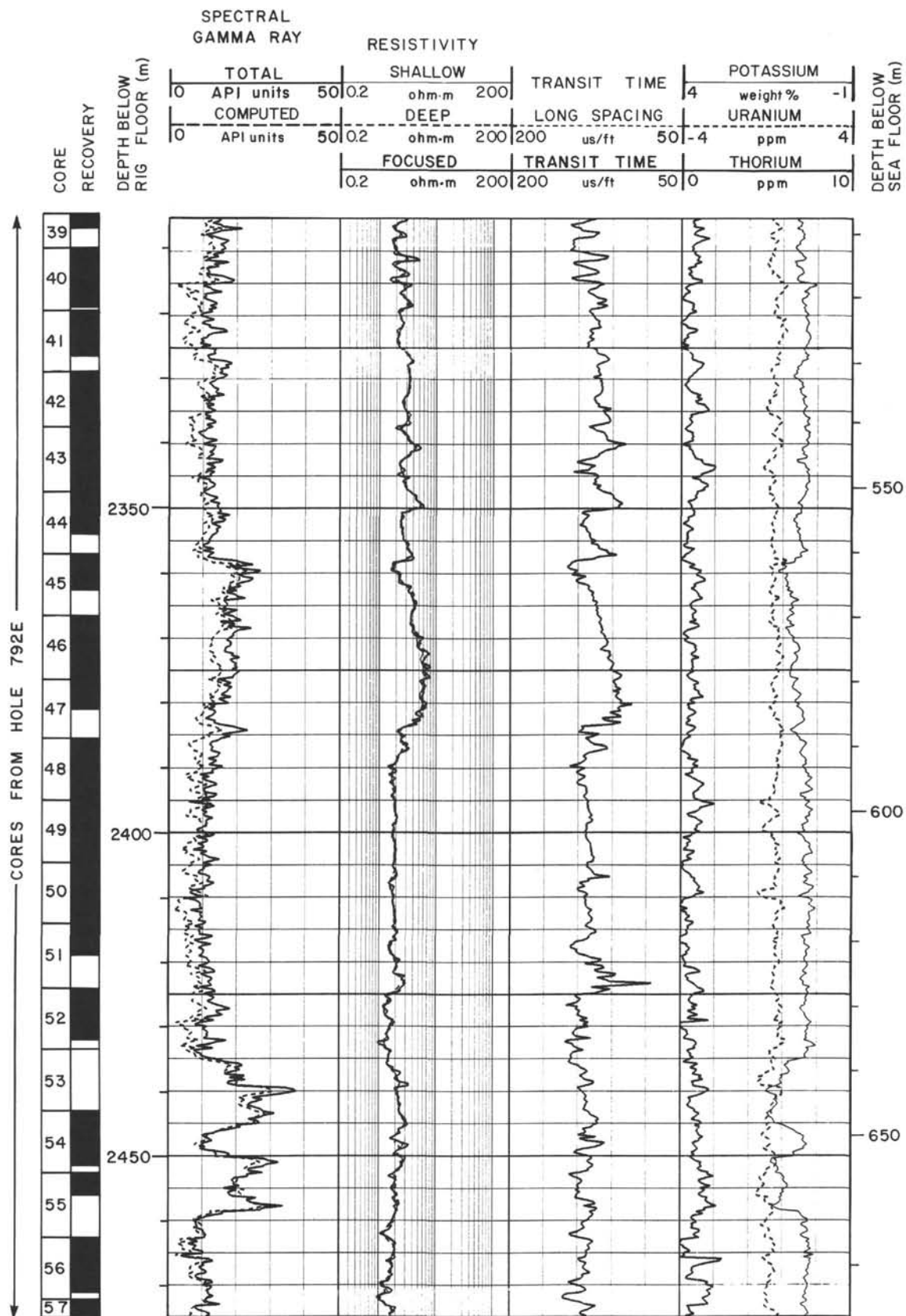Figure 62. Summary logging figure, DIT, Hole 793E.
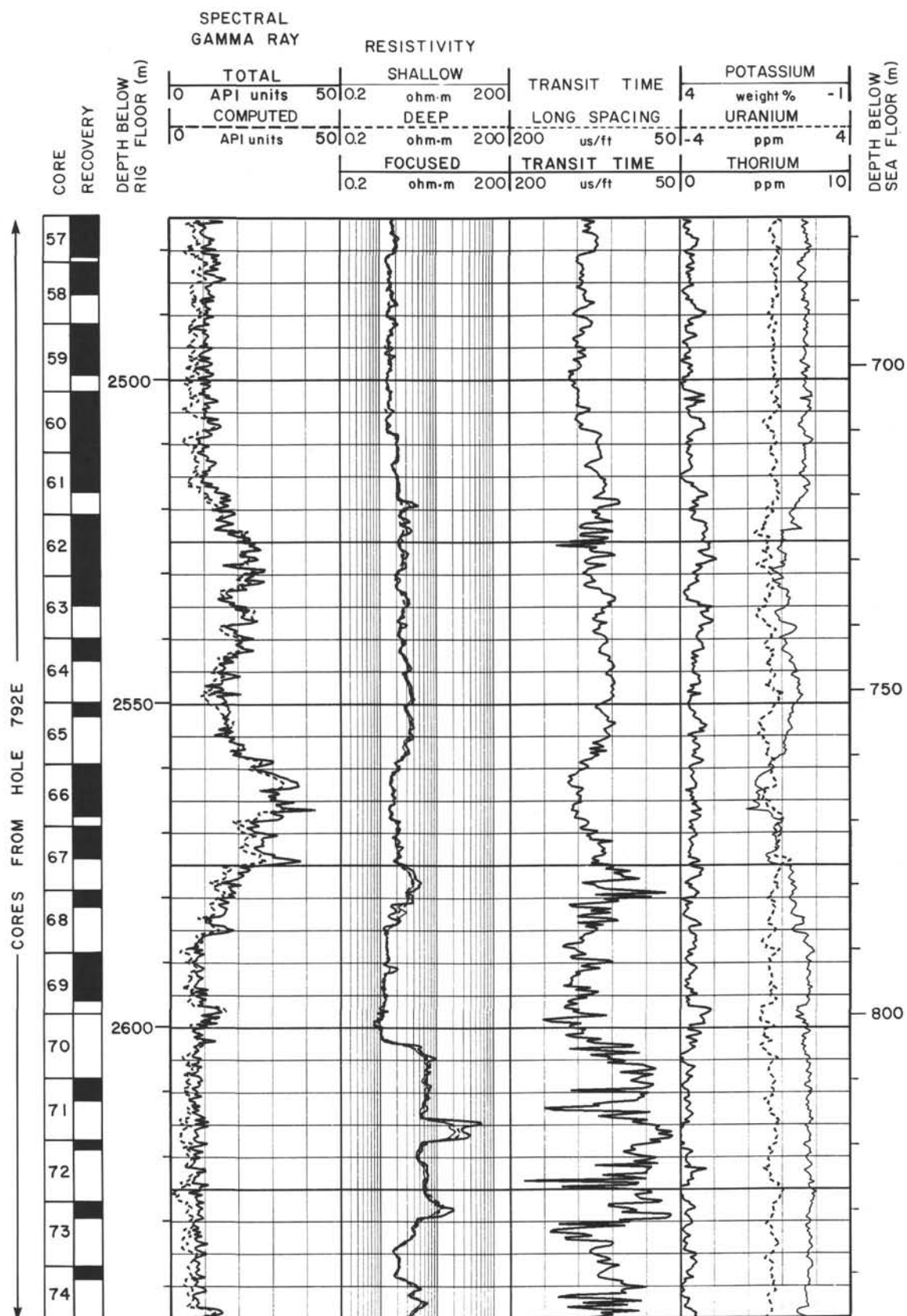
Figure 62 (continued).

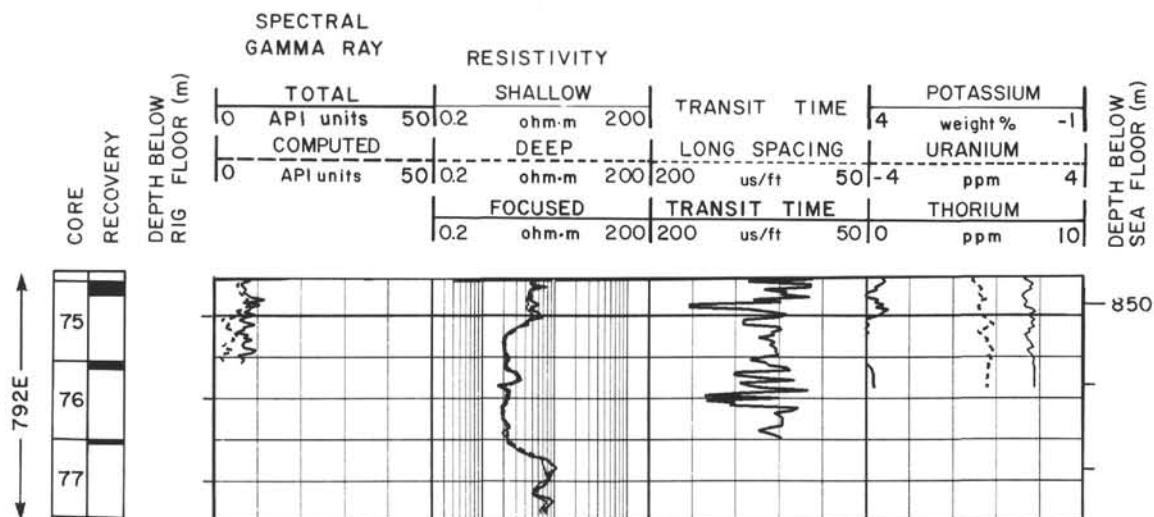Figure 62 (continued).

Figure 62 (continued).

Figure 62 (continued).

sharp temperature increase. From this depth (285.0 mbsf) to the top of the basement (804.5 mbsf), the temperature profile is generally linear. A definitive statement on the nature of the heat transfer at this site must await shore-based analysis of the dataset. We observed a linear gradient of steeper slope in basement rocks.

We observed a total of seven departures from these linear gradients in the sedimentary section, two of which represent positive temperature anomalies. We discuss these below with respect to the fourth temperature run. The profile recorded upon exiting the hole generally has less character than the one obtained upon entering the hole. This probably is caused by physical displacement and the mixing of borehole fluid by the downhole sensors. Seawater is injected into permeable zones during drilling and it flows back into the drill hole after pumping stops; thus, it is in unstable equilibrium with the denser mud placed into the drill hole prior to downhole measurements. The passage of the tool disrupts this equilibrium, and the lighter seawater is displaced upward. This mechanically generated "advective" process results in a smoothed temperature profile and an overall temperature increase of more than 2.0°C. As a consequence, warm fluid from the open-hole section was displaced into the lower section of the drill pipe (as shown by the upward smearing of the temperature anomaly located just below the drill pipe, or the upward increase in chlorine concentration detected by the geochemical measurements).

A similar flow of water from the formation into the drill hole is visible on the log recorded during the fourth run. A steeper gradient during Run 4 indicates the progressive return to thermal equilibrium over the 21 hr that separated these two runs. Only five departures from the linear gradients are visible in the fourth temperature profile. Below the drill pipe, a positive anomaly emphasizes inflow from a permeable zone within Unit 2, with water warmer than borehole fluid. At 350.0 mbsf, the anomaly turns negative, still showing inflow from a permeable zone, but with a fluid colder than borehole fluid in this case. This crossover point indicates the nearby crossing of geothermal and drilling-temperature profiles (Serra, 1984). Above the crossover point, the drilling fluid temperature is warmer than the formation temperature, and below it is colder. Below the crossover point, the temperature profile meets the linear gradient over a short interval within Unit III, and then indicates a permeable zone from which a fault zone was described (407.5–430.0 mbsf) in the cores and from geophysical logs (Figs. 62 and 66).

The amplitudes of these three anomalies are reduced between Run 1 and Run 4, indicating a slow return to equilibrium over this time interval. A fourth, small-amplitude, positive anomaly is evident in both profiles (500.0–600.0 mbsf). It remains similar between Runs 1 and 4 and may be related to a variation in thermal conductivity. The two small negative anomalies detected in the first profile, at approximately 650.0 and 700.0 mbsf, are not visible in the fourth run. The last anomaly, represented as a doublet in the first profile, is also present in the fourth, although attenuated. This doublet corresponds to two permeable zones that have larger than normal hole diameters (Fig. 66), and which may be faults bounding Unit V. Evidence for faulting was noticed in the cores (see "Lithostratigraphy and Accumulation Rates" section, this volume).

Run 5 (Vertical Seismic Profile)

The primary objectives of the vertical seismic experiment conducted in Hole 792E were to enhance velocity analysis, to identify and locate the primary reflectors, to correlate the lithostratigraphy with identified reflectors, and to tie the surface multichannel seismics to well logs for regional scale correlations.

Data Acquisition

The sound source used for the Hole 792E VSP experiment was the large-volume (400 in.[3], or 16.0 L), high-pressure (2000 psi, or 140 bar) water gun (SSI H400) aboard the *JOIDES Resolution*. The gun was suspended 15 mbsl from a buoy tethered from the drill ship's aft port crane boom, about 24 m abeam. The downhole seismic signals were received by a Schlumberger Well Seismic Tool (WST) single vertical component seismometer. The seismometer has four, series-connected, 10-Hz (F_o) geophones (Geospace Model HS-1) mounted at its base. All downhole equipment functioned flawlessly. The water-gun acoustic signals were also detected by a separate, calibrated hydrophone suspended directly from the crane boom, 3 m below the water gun. This hydrophone configuration provided a stable, zero-time reference relative to the seafloor, allowing real-time summing of the seismic records observed for the several shots fired at each seismometer clamping level. During the operation period, weather conditions were optimal and a total of 64 clamping levels were occupied, amounting to 4.5 hr of recording time.

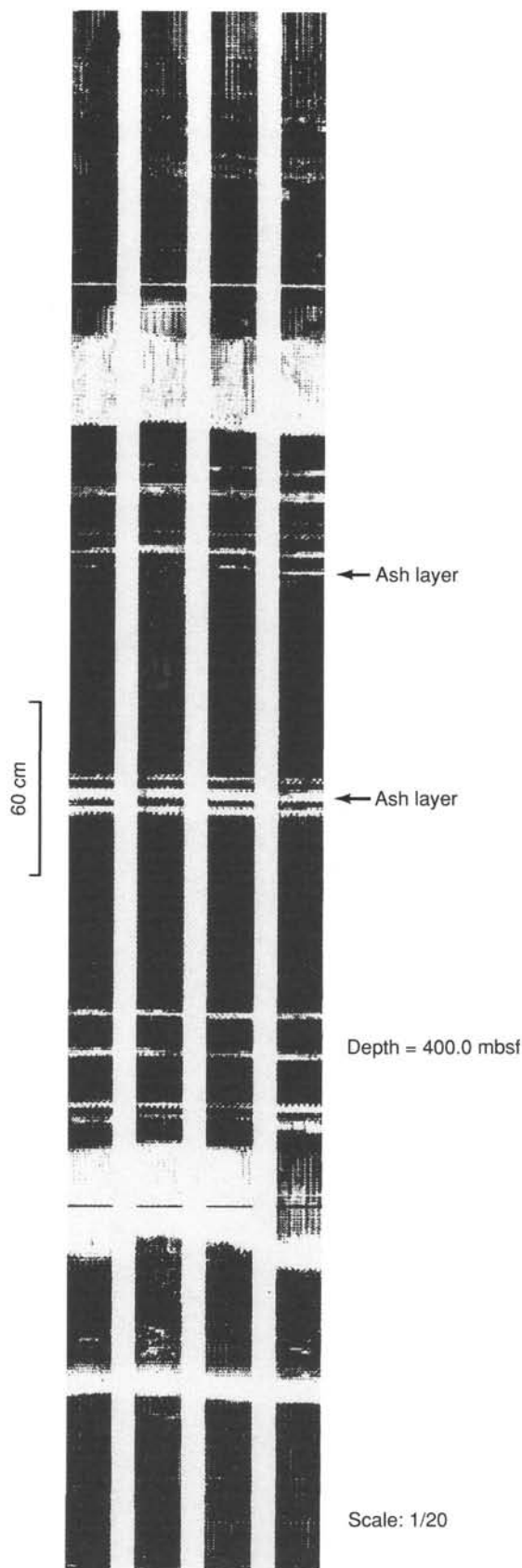The WST was lowered to the bottom of the hole (Level 1, 868.0 mbsf) and clamped to the well bore. The cable was then

Figure 63. Example of FMS images at 1/20 scale. A resistive (white) ash layer <5 mm thick in the core is imaged.
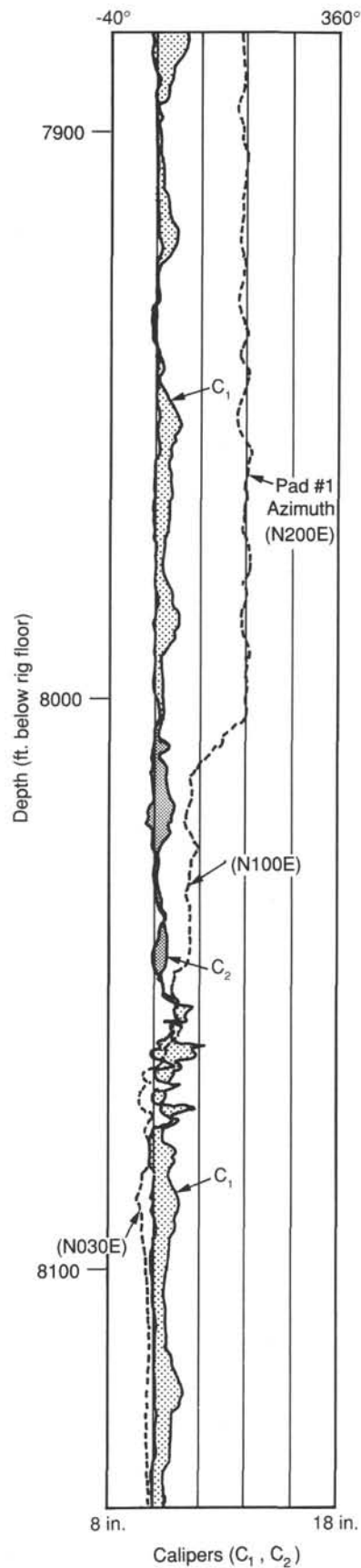

Figure 64. Example illustrating the very constant hole elongation direction as observed with FMS calipers in the sedimentary section. The tool rotated 90° at 8010.0 and 8050.0 ft below rig floor. The largest hole dimension remains oriented close to the north-south axis.
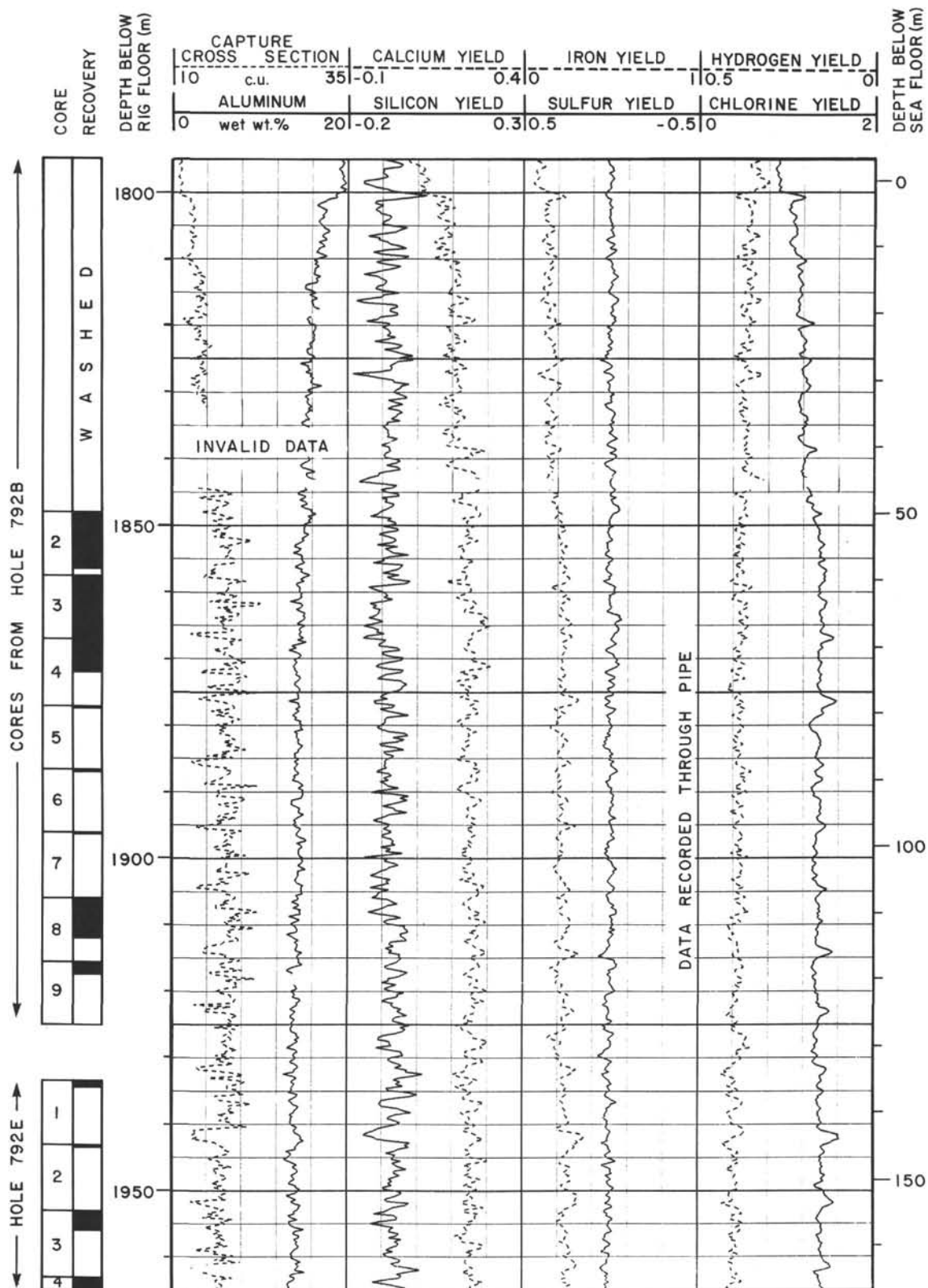
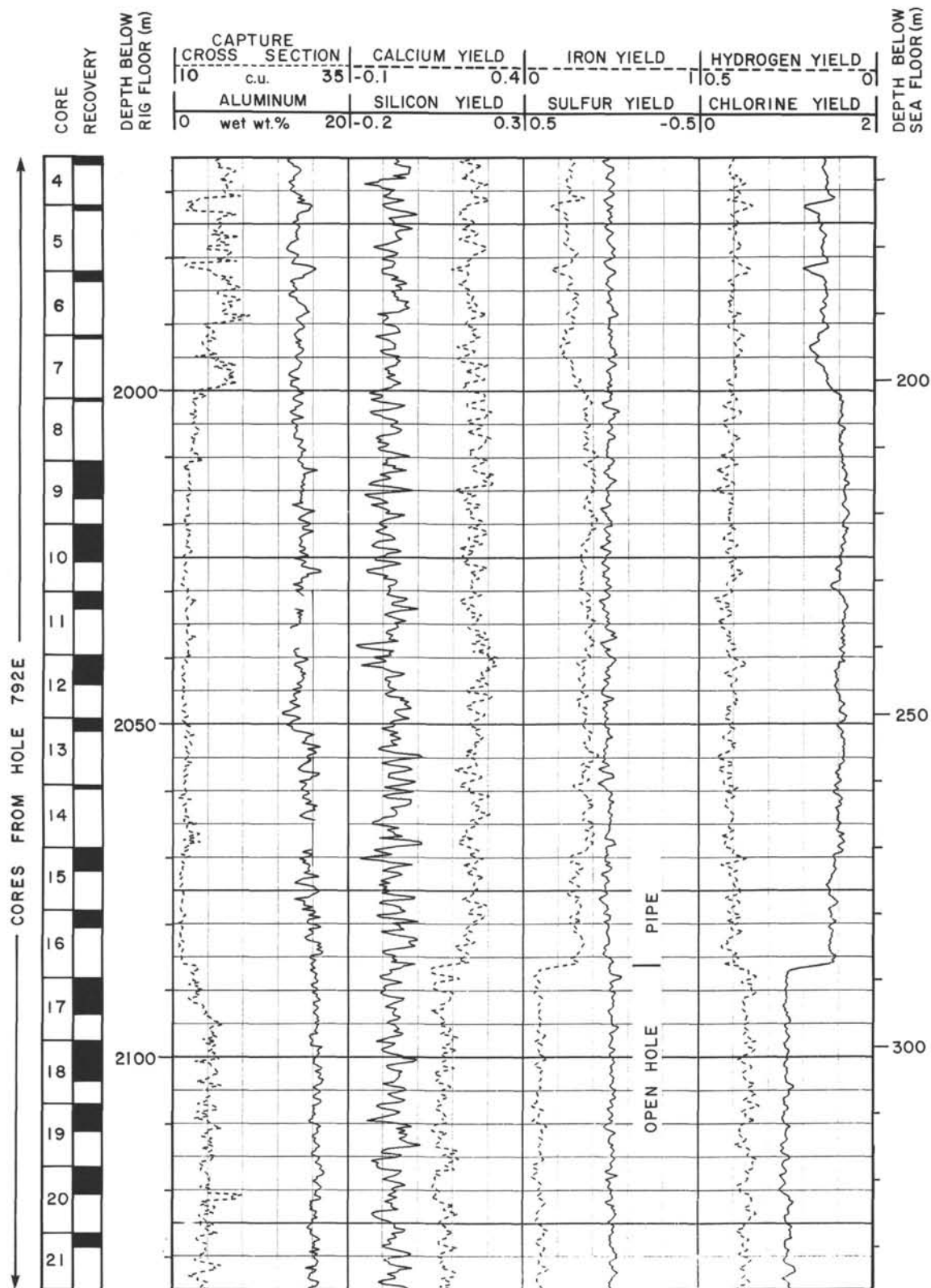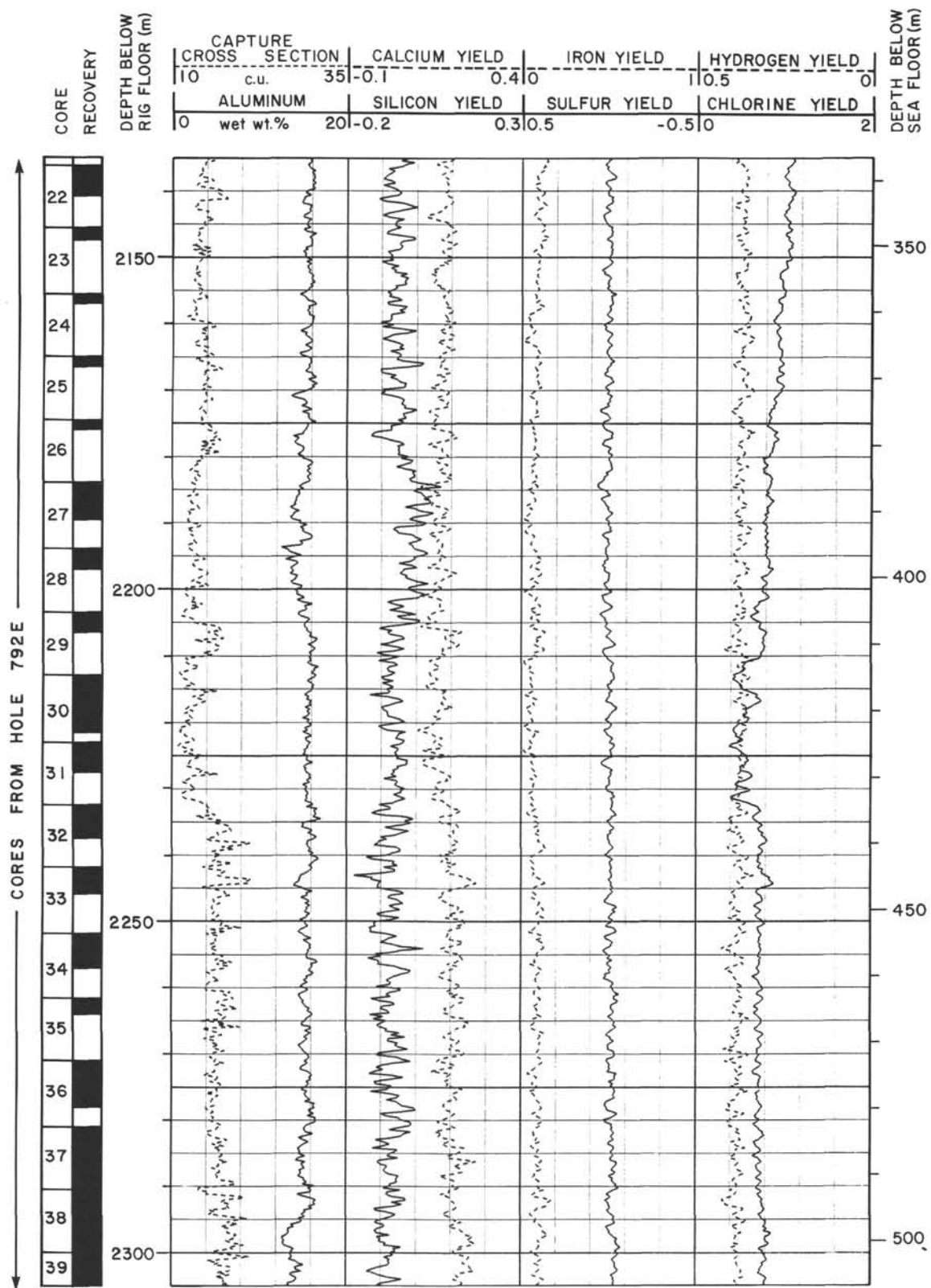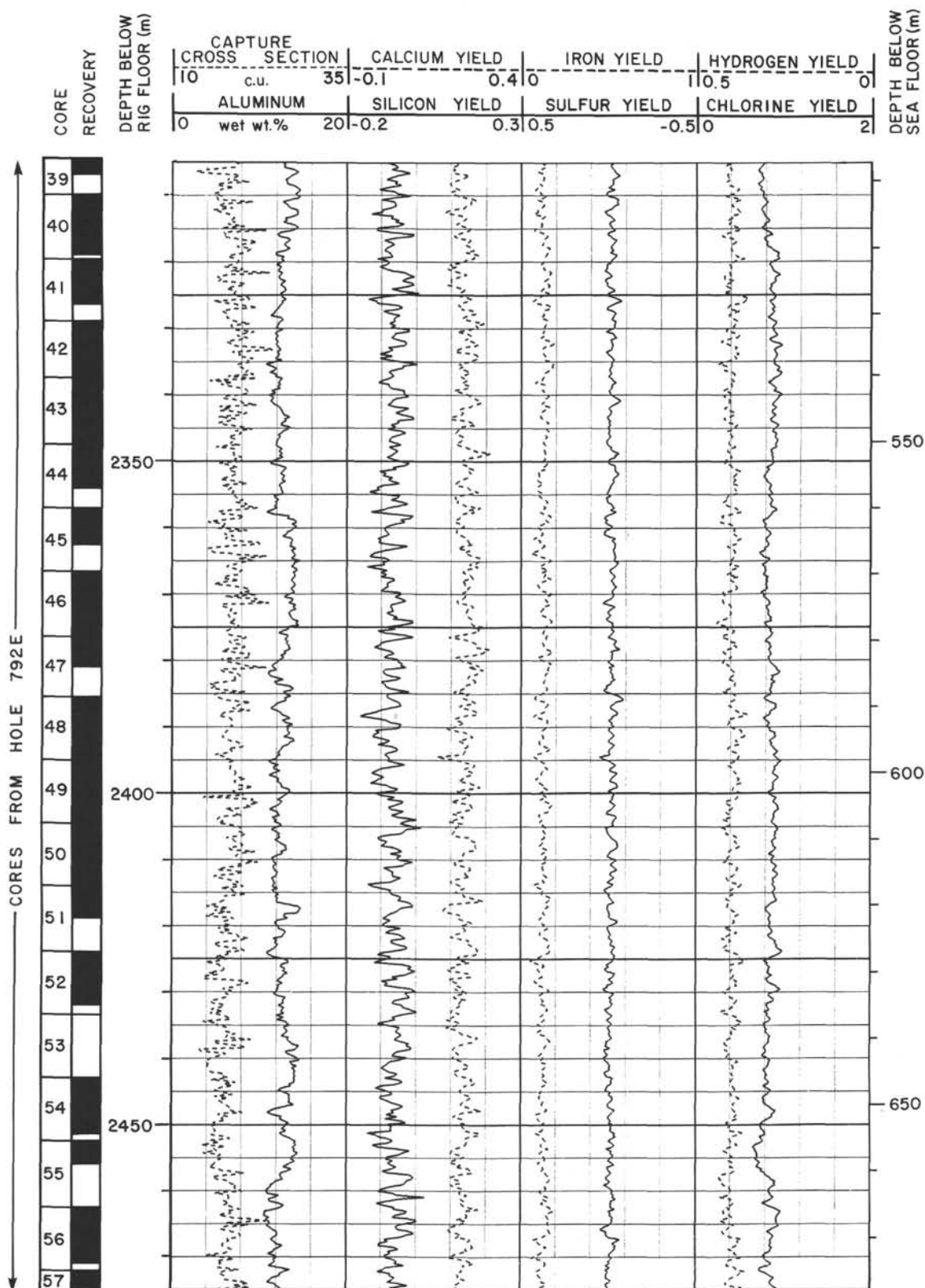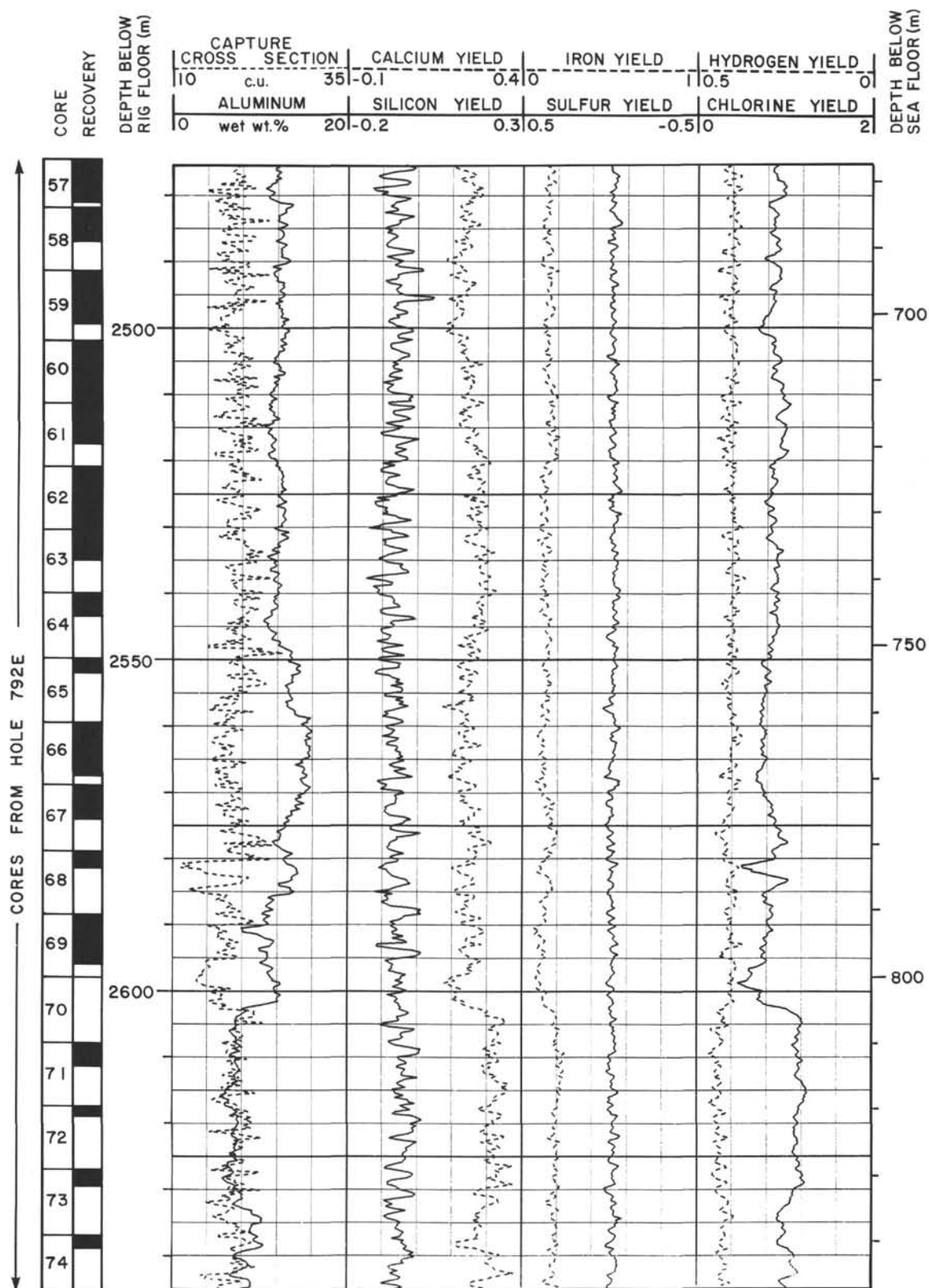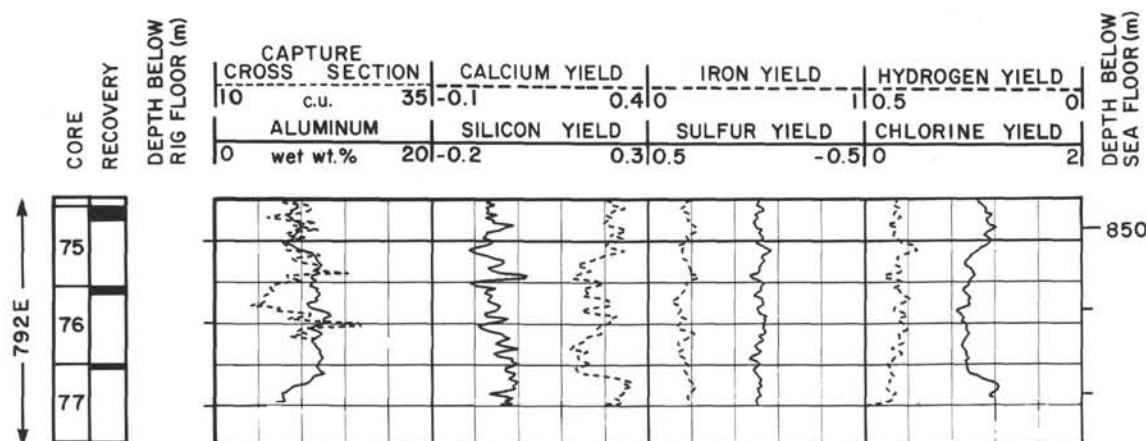Figure 65. Summary logging figure, ACT, Hole 792E.

Figure 65 (continued).

Figure 65 (continued).

Figure 65 (continued).

Figure 65 (continued).

Figure 65 (continued).

slacked 2 m, and a single shot was fired to test for noise or poor coupling to the borehole wall. The seismogram waveforms recorded for each shot were displayed in quasi-real time after the shot on a TEKTRONIX graphics terminal. After we ascertained that the seismometer was properly clamped to the well bore, additional shots were taken as deemed necessary by the operators and stacked for real-time display. Each waveform was visually inspected and either accepted for stacking or rejected. The resultant normalized stacked trace was then displayed and inspected before moving on to the next clamping level. A satisfactory signal-to-noise ratio was obtained using an average of five stacked shots per clamping level, with a maximum of seven. Following the shooting/inspection/stacking sequence, the WST seismometer package was raised 9.45 m (30 ft) and the shooting/inspection/stacking sequence was repeated at 9.45-m (30 ft) intervals to the last clamping level at 301.0 mbsf. A total of 409 shots were used. Because the drill pipe was firmly stuck in the hole, no further efforts were taken to reduce downhole seismic noise aside from adjusting the ship's heading to minimize roll and slacking the cable after clamping. The logging winch wireline heave compensator was not used, as it had failed during Run 3.

Water-gun-generated signals received by the WST borehole seismometer were preamplified downhole, transmitted up the logging cable, and digitally recorded along the hydrophone signals by the PDP-11 minicomputer and A/D converter of the Schlumberger CSU logging data acquisition system. Timing information was logged with millisecond accuracy. First-break transit traveltimes were calculated to 0.1 ms from the stacked shots at each clamping level. The data sampling rate was 1.00 ms with a record length of 3.00 s. The record delay (blanking time) ranged from 1.45 s at the maximum observation depth (868.0 mbsf) to 1.25 s at the shallowest depth (301.0 mbsf). An attempt to continue sampling inside the drill pipe was aborted because of unacceptable noise levels.

Data Processing

Shipboard seismic processing of the VSP data used the same PDP-11-based Schlumberger CSU computer used for data acquisition. The CSU system's Seismic Quick Look (SQL) software performed the primary data editing and the preliminary processing tasks immediately following the experiment. These processing steps are summarized as follows:

1. The addition or elimination of shot records from real-time, field-summed, stack trace at each clamping level. "Good" data records were re-summed to obtain a final stacked trace for each depth position.

2. Application of a static shift correction for recording delay (blanking) time and combining the final stacked traces into a composite depth vs. one-way traveltime section.

3. Application of a static shift correction equal to the first-break time of the direct wave for each stacked depth trace, to align the reflection wavetrain pattern along constant arrival times and to combine the stacked traces into a composite depth vs. two-way traveltime section.

4. Calculation of the velocity-depth profile from time differences in the direct-wave, first-break transit times for the sequential depth intervals.

5. Preliminary wavefield separation into upgoing (reflection) and downgoing (direct) waves using spatial velocity filtering (specifically, narrow-reject f-k filtering).

6. Performance of preliminary source deconvolution. A wavelet-shaping operator is derived from the downgoing waveforms of the deepest four stacked traces (1, 2, 3, and 4) and is applied to the upgoing energy.

Results

The signal-to-noise ratio was good throughout the experiment. Borehole diameter was fairly uniform except in the region of Levels 47, 48, and 49 (see Fig. 71, stacks 47–49). High-frequency tool resonance, seen in the upper level traces, increased as the tool neared the base of the drill pipe.

Figure 71 shows the one-way traveltime, stacked-trace, composite depth section for all the raw VSP data obtained at Hole 792E over the depth interval from 868.0 to 301.0 mbsf. The bottom of the drill pipe was at 287.0 mbsf, which prevented shallower seismometer clamping. The depth section includes 64 observations made in the uncased open hole. The data are unfiltered; a spreading-loss-type, 1.5-power exponential time gain factor was applied to display the weaker, deeper reflections. Each trace amplitude scale is normalized. The downgoing direct waves are the strong first arrivals with traveltime increasing with depth (Fig. 71). Note that no water-bottom multiple arrivals were seen on the section because the one-way traveltime through the water column is 1200 ms. The three-way traveltime (3600 ms) for a VSP-type, water-bottom multiple is well beyond the record length displayed. The upgoing, reflected waves are the late, weak (but coherent) events, with traveltime increasing as depth decreases. The divergence of the downgoing and upgoing wavetrains results from the decreasing range to the sound source for the direct waves and the increasing range from the reflecting interface as the seismometer is raised. The reflected wavetrains intersect the direct wave's first break arrival at the depth of the interface causing the reflection; in practice, if the direct wave is
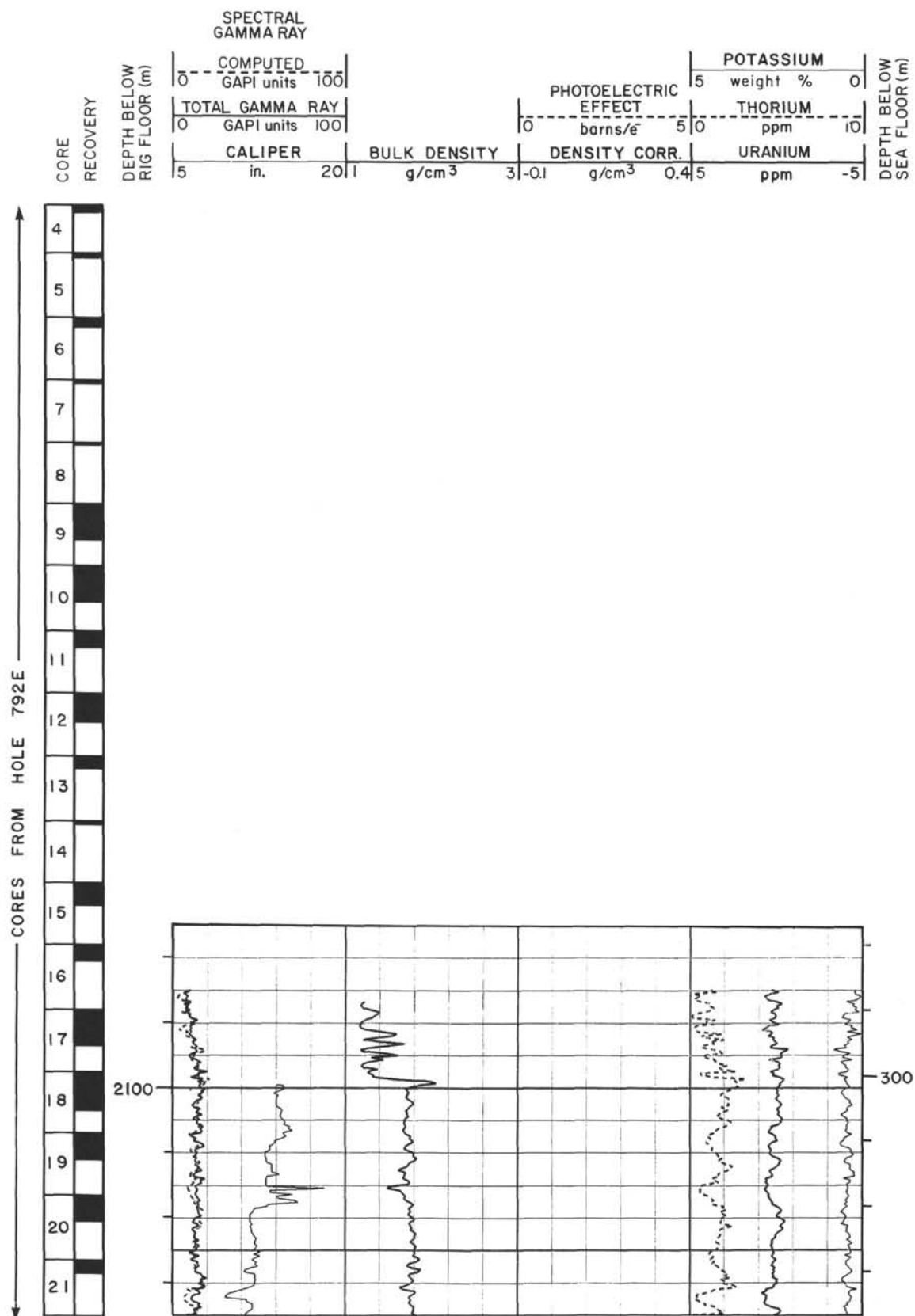
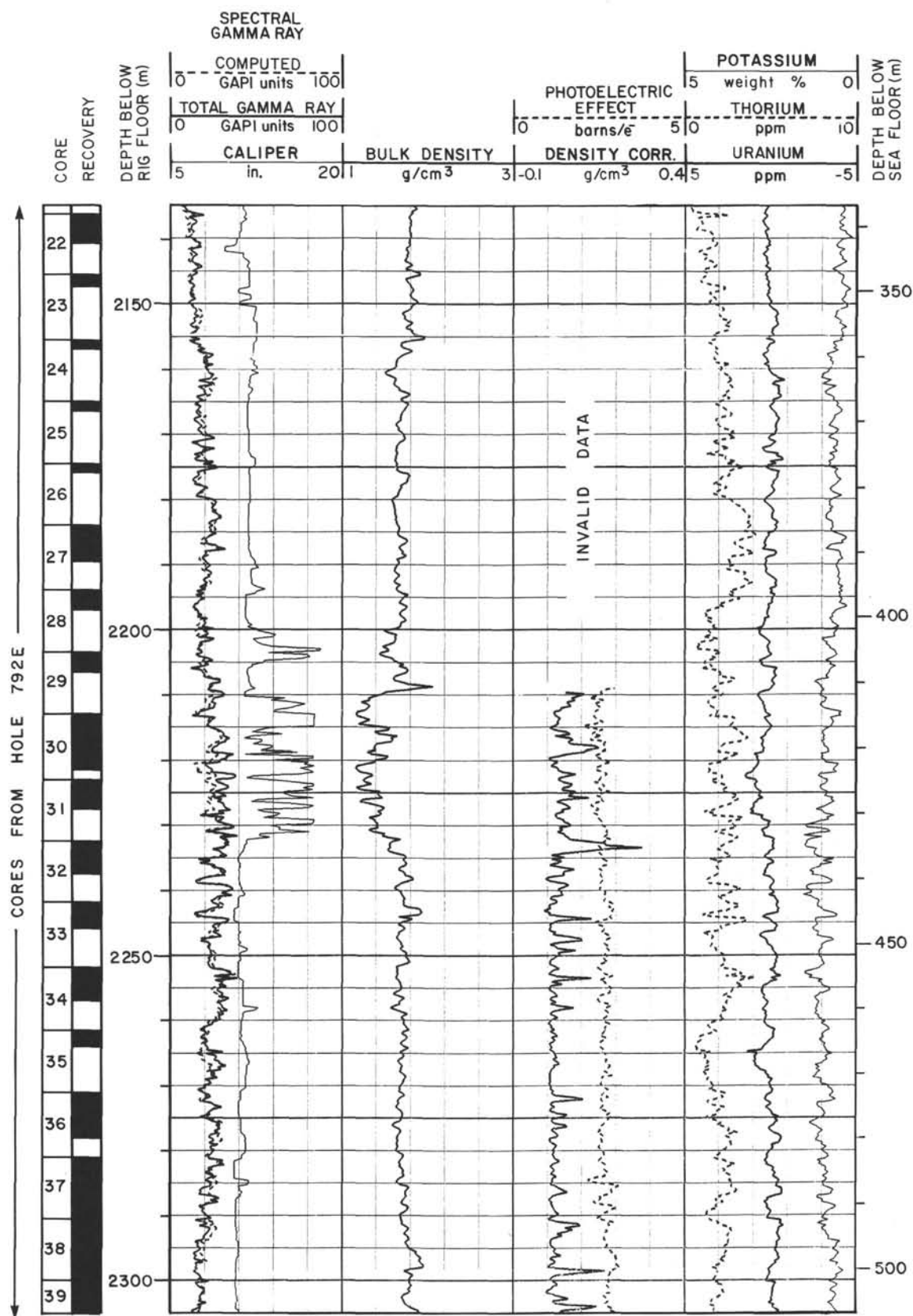Figure 66. Summary logging figure, LDT, Hole 792E.
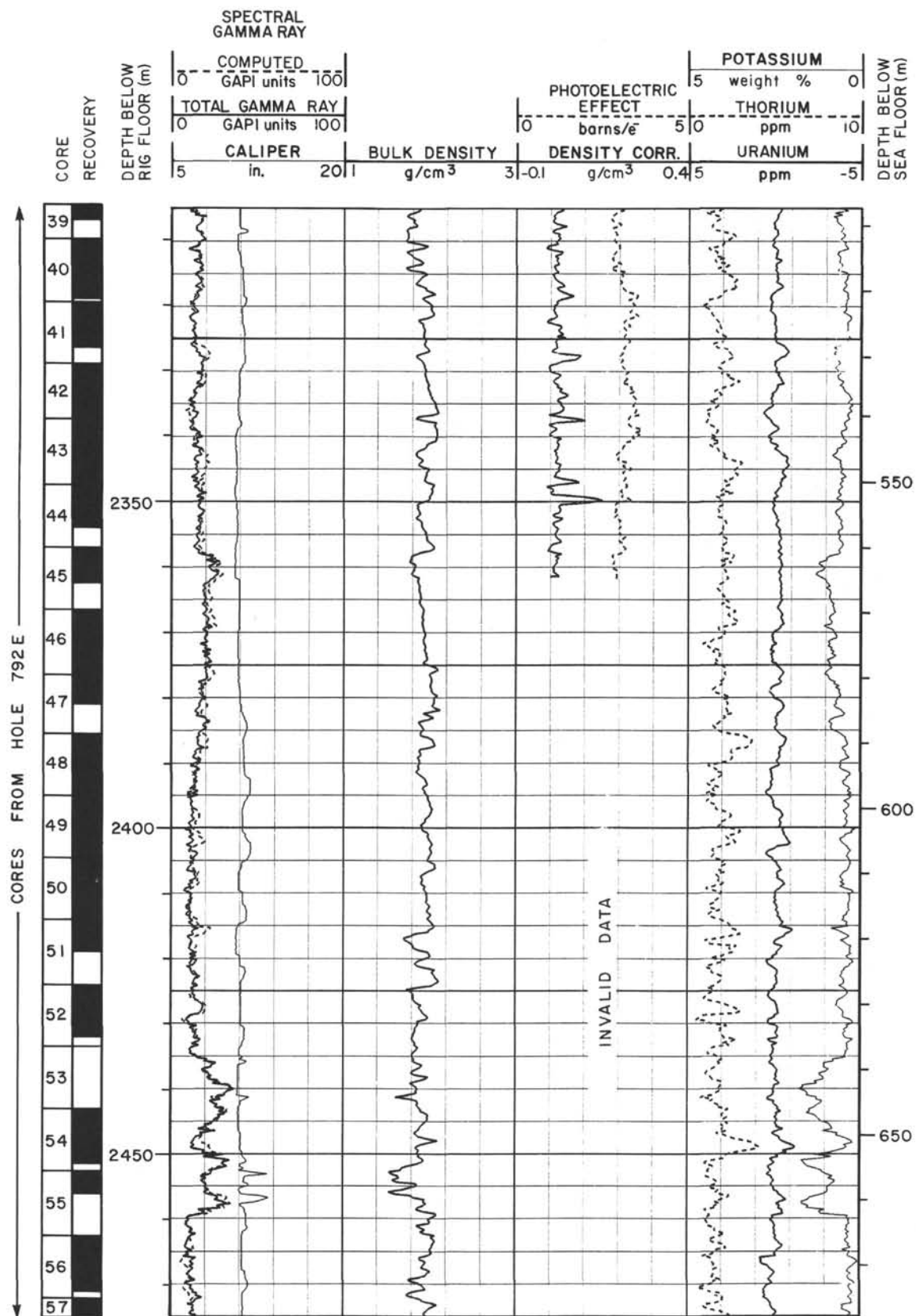
Figure 66 (continued).
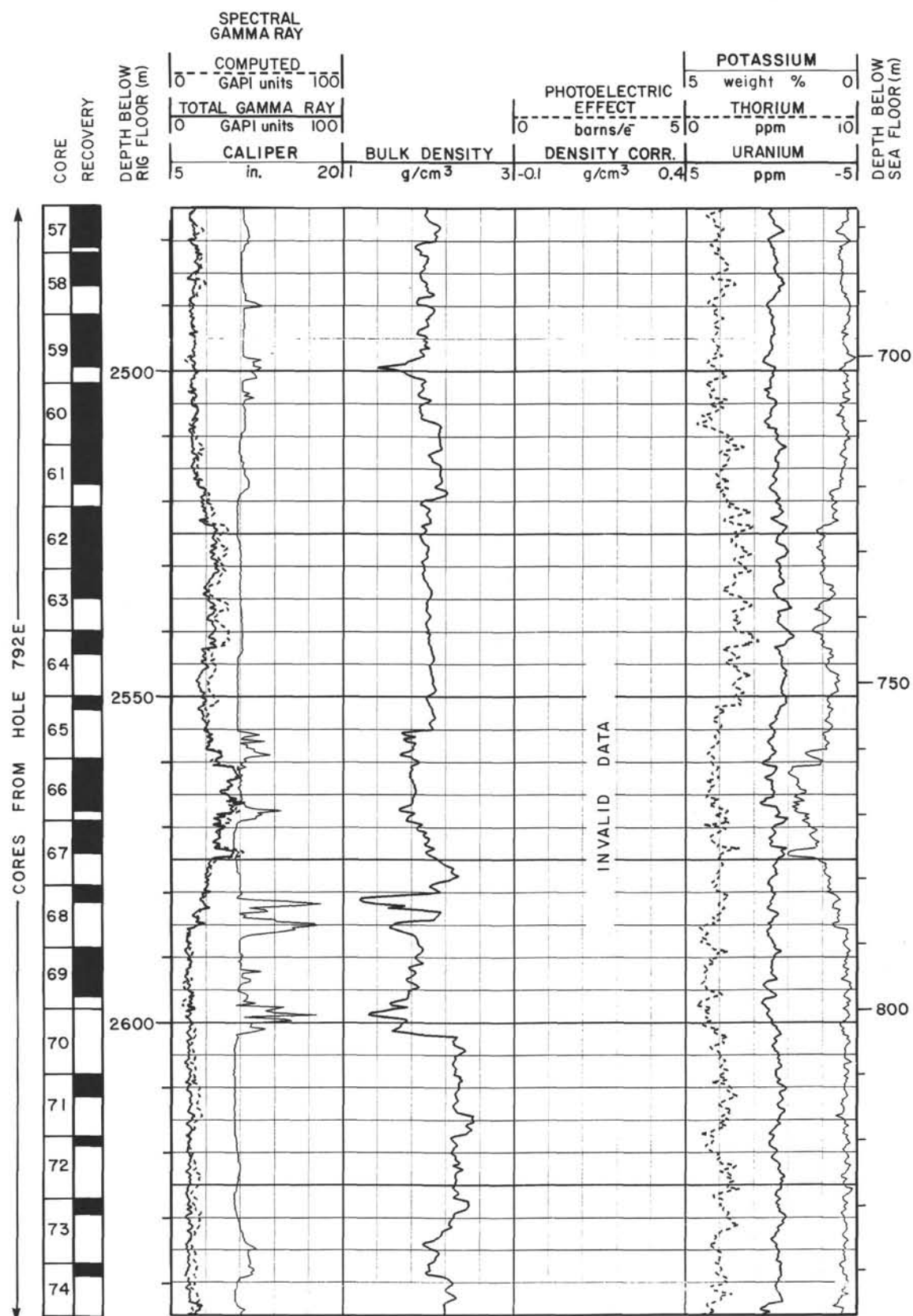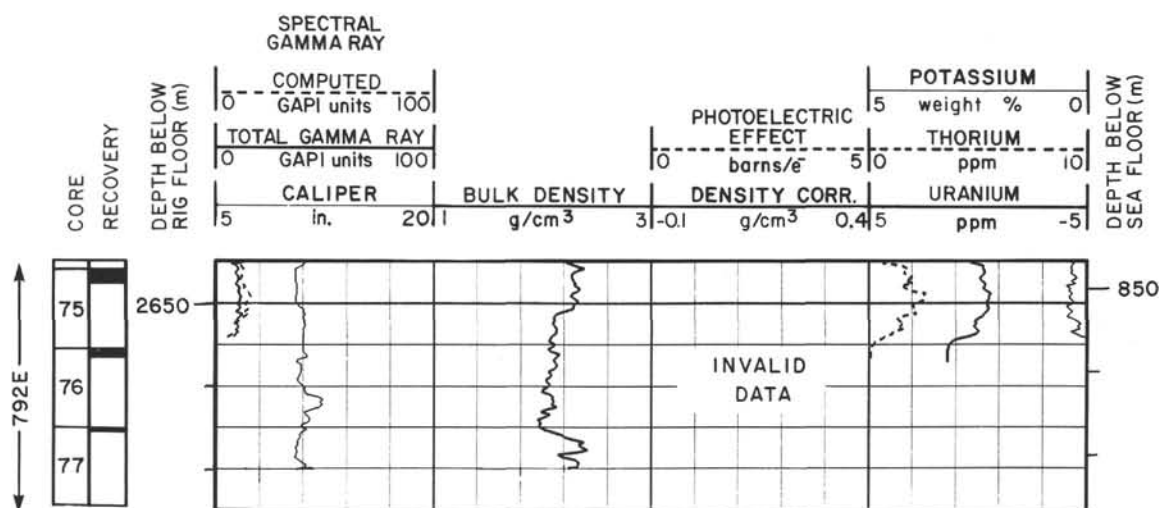
Figure 66 (continued).

Figure 66 (continued).

Figure 66 (continued).

of a complex nature, it is sometimes difficult to define that intersection. Numerous reflection events are evident in this essentially raw data display, demonstrating the overall good signal-to-noise ratio.

A preliminary determination of the interval velocity-depth structure was made by dividing the interval distance between sequential clamping levels by the difference in their direct-wave, first-break, arrival traveltimes. The results of this simple calculation are shown in Figure 72 together with the one-way traveltimes over the same depth range. Figure 73 illustrates the excellent correlation between VSP interval velocity data averaged over the designated lithostratigraphic intervals with velocity data obtained by physical properties measurements and downhole measurements.

The traces were time-shifted by an amount equal to the direct wave's first break arrival. A spatial velocity filter was then applied to the resulting partial two-way traveltime section to separate the upward propagating reflected wavetrains from the downward propagating wavetrains. The data were not corrected for the minor deviation of the borehole from vertical. Figure 74 is a display of the upgoing reflected wavetrains; prominent reflectors have been identified and, whenever possible, related to lithologic units or subunits. Reflectors defining major unit boundaries (Units III through VI) are identified on this figure and also on the multichannel data (Fig. 74). At this point in the analysis, the precision to which depths can be determined in this data is ± 1 depth level. The curvature of the deepest reflections is caused by the dip of basement beds and is analogous to the curvature often observed in CDP gathers that results from the normal moveout effect.

Preliminary Stratigraphic Results from Downhole Measurements

The downhole measurements are analyzed here with respect to the stratigraphic column defined from the cores. Because the total recovery in this hole was only 48.23%, such an analysis is necessary to define unit thicknesses and boundaries with precision, and to check if any major lithologic event was skipped as a result of partial recovery. The location of unit boundaries is discussed here in terms of variations of in-situ physical properties and in the context of VSP results. As a summary, the average value for in-situ measurements of resistivity, velocity, and density for each sedimentary unit are reported in Table 19. A comparison of laboratory and in-situ velocity data is given in Table 20.

The geochemical combination is the only sensor that recorded data through pipe within Unit I. The contact between Unit I and Unit II (183.7 mbsf, from core data) cannot be detected at present from the geochemical logging dataset. The open-hole data start within Unit II (~287.0 mbsf). Unit II is characterized by near-constant resistivity (about 0.9 $\Omega \cdot$ m) and wet-bulk density (1.76 g/cm^3; Fig. 62; Table 19). Temperature records indicate that this section is permeable.

A lacuna (a 5-m.y. gap in the middle Miocene record, at 357.4 mbsf; see "Lithostratigraphy and Accumulation Rates" section, this chapter) defines the contact between Unit II and Unit III. The wet-bulk density decreases below this depth to an average value of 1.67 g/cm^3, and the resistivity is more variable than in Unit II. We found a reflector within Unit III at 386.0 mbsf (Reflector T; Fig. 74), where the calcium concentration increases abruptly in the core and in the downhole geochemical record.

The next boundary in the hole is the top of a fault zone cored at 407.1 mbsf, and defined by large caliper values (Fig. 66), a seismic reflector in the VSP data (Reflector S; Fig. 75), and an anomaly in the temperature profiles (Fig. 70). With reference to the caliper and in-situ physical property data, this fault zone extends to approximately 430.0 mbsf, the lower contact of Unit III (Table 19). The entire fault zone is seen as permeable in the temperature records. In the upper part of Unit IV (from 430.0 to approximately 515.0 mbsf), the physical property profiles have a bimodal character, with high resistivity/velocity/wet-bulk density, low natural gamma-ray values, alternating with beds of opposite characteristics. The main source of natural gamma rays is potassium, and the low resistivity/high natural gamma values appear where we found high smectite concentrations in Core 126-792E-40R.

At about 515.0 mbsf, the overall character of physical property measurements changes, marked by an increase in average wet-bulk density, velocity, and resistivity. The profiles lose their high-frequency character below 560 mbsf as a result of the appearance of thicker, often conglomeratic units. This boundary is Reflector N in the VSP experiment (Fig. 74). In the lower part of Unit IV, the next reflector is found at about 590.0 mbsf (Fig. 74), close to the location of a sharp (1) decrease of resistivity, (2) increase in smectite content (see "Lithostratigraphy and Accumulation Rates" section, this chapter), (3) increase in magnetic susceptibility (see "Lithostratigraphy and Accumulation Rates" section, this chapter), and (4) variation in pore-water Ca^{2+} and Mg^{2+} concentrations (see "Sediment/Fluid Geochemistry" sec-
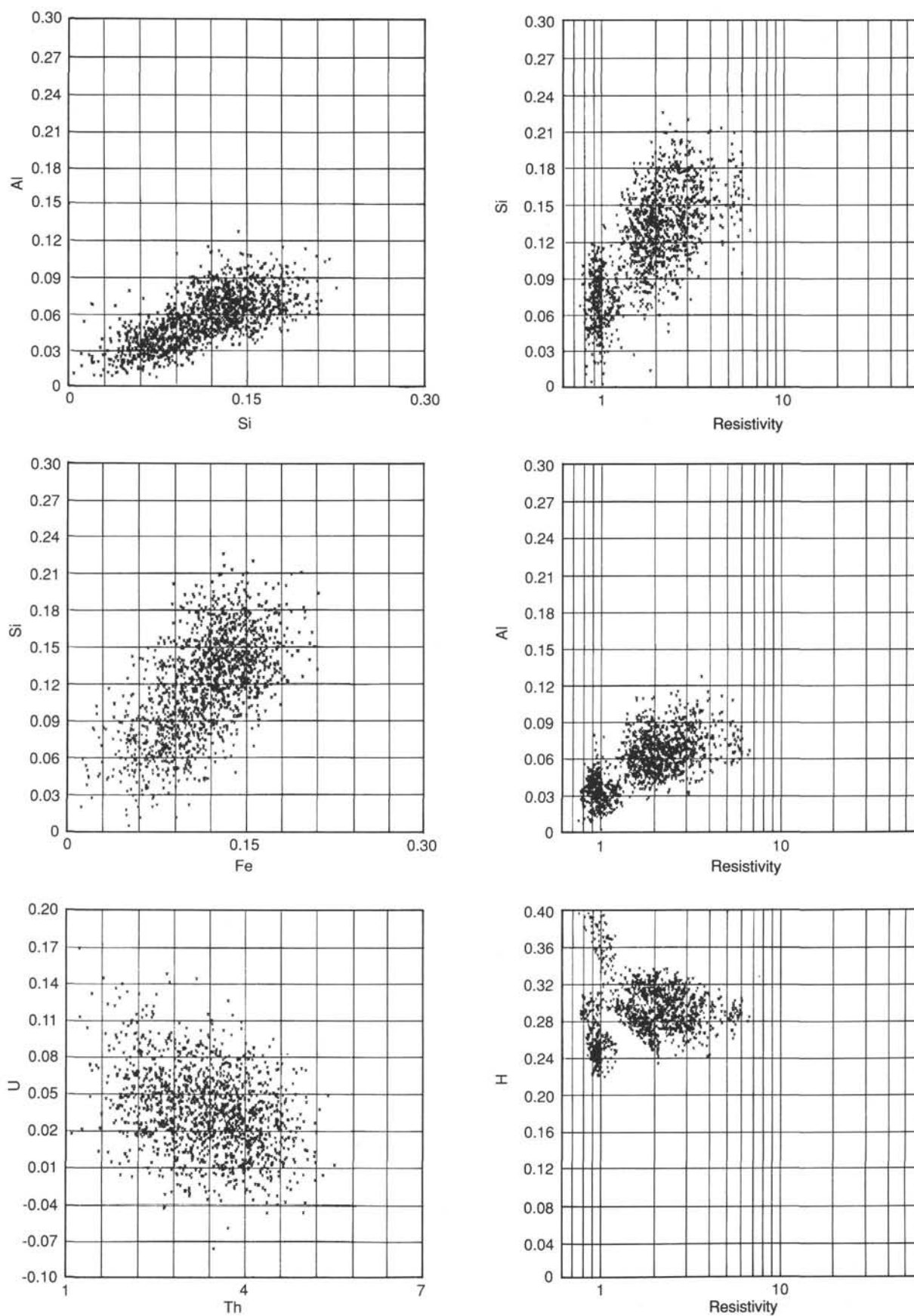
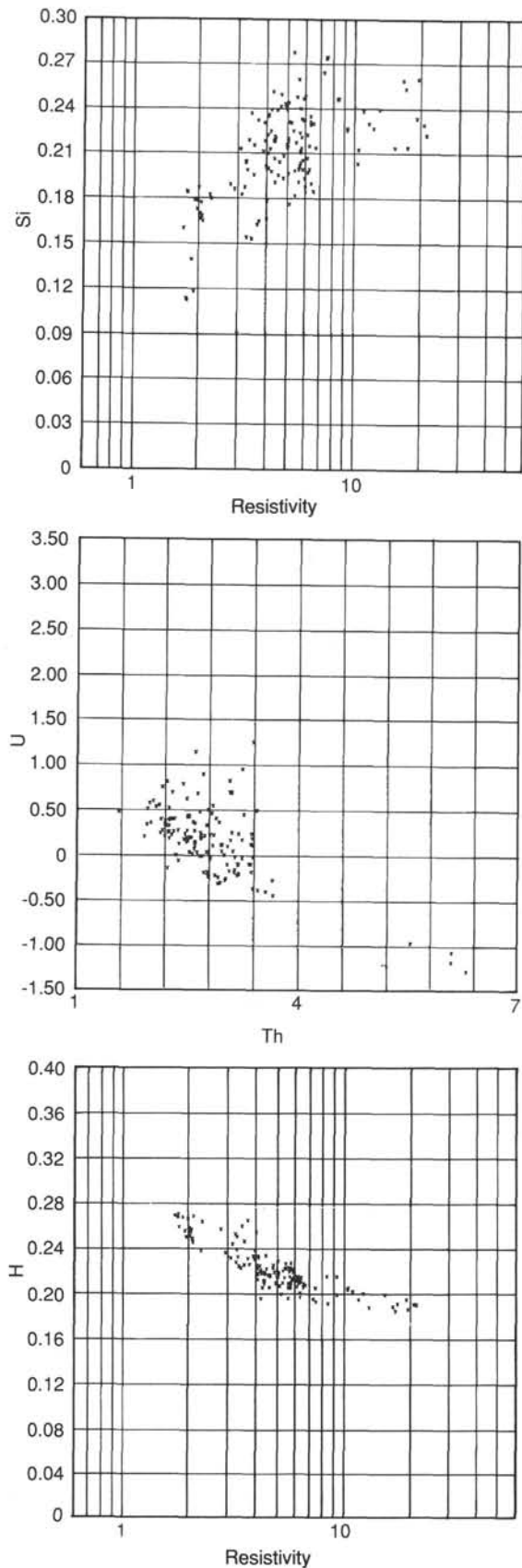Figure 67. Crossplots of *in-situ* geochemical measurements in the sediments, Site 792.

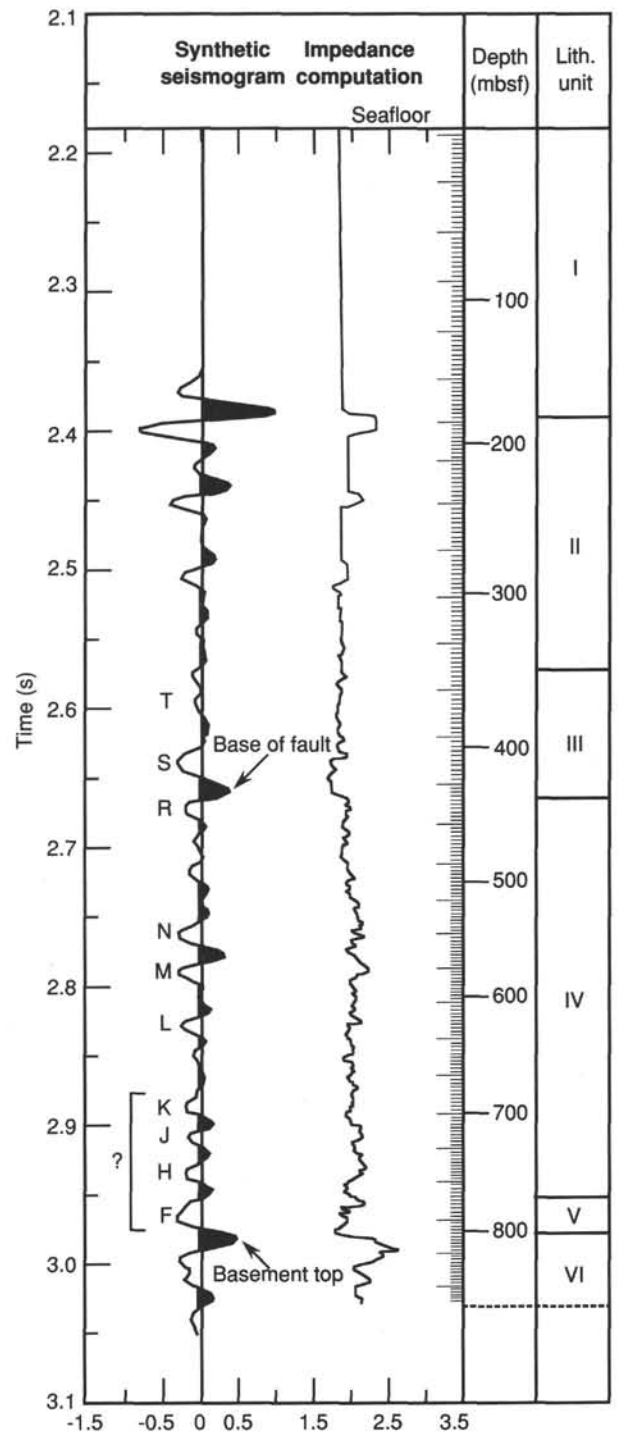Figure 68. Crossplots of *in-situ* geochemical measurements in the basement, Site 792.

Figure 69. Synthetic seismogram and impedance log for Site 792, computed from velocity and bulk density *in-situ* measurements, then convolved with a 30-Hz Ricker wavelet.

tion, this chapter). Except for a high-resistivity region associated with coarser units (717.0–758.0 mbsf), the *in-situ* physical properties remain constant to the base of Unit IV, at 780.0 mbsf.

The highly altered rocks of Unit V are characterized by low physical property values (Table 19), bounded by two permeable faults (Fig. 74), and outlined by the VSP with Reflectors F and G (Fig. 74). The top of the basement is, therefore, the site of a
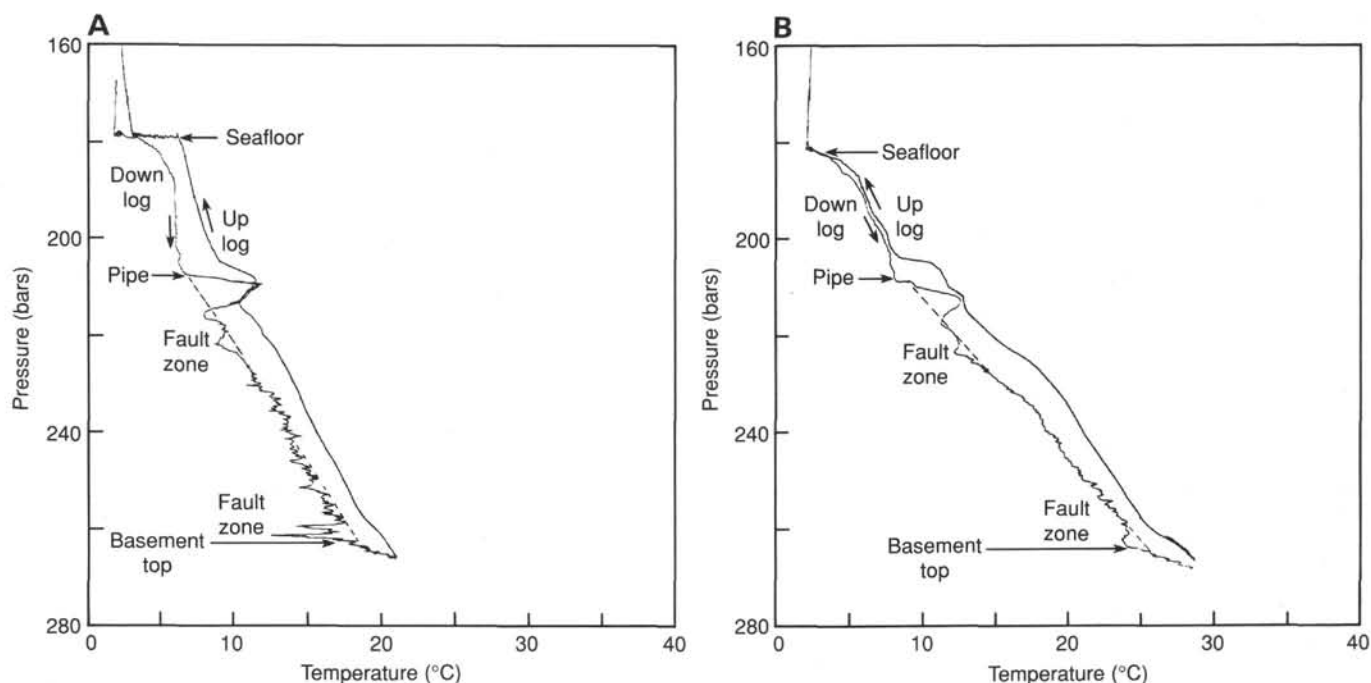
Figure 70. Temperature data (in °C) plotted against lithostatic pressure (in bars), Hole 792E. **A.** Data recorded during the first run. **B.** Data recorded during the second run (24 hr after the first run).

sharp increase in physical properties (Table 19) and of a decrease in natural gamma radiation.

Conclusions

A complete set of downhole measurements has succeeded, within the limits of shipboard analysis capabilities, in identifying the major structural and lithologic events within sediments and basement rocks. One of the most interesting results is the hole elongation seen in the sedimentary section, which shows compression aligned with the relative velocity vector between the Pacific and Philippine plates. In the basement, the FMS caliper was not able to detect any borehole breakouts, which does not rule out the possibility of a small stress anisotropy in the horizontal plane. The FMS imaged features <1 cm in thickness. We measured a geothermal gradient of 3.0°C/100 m, 30 hr after the end of the drilling operation. Further processing of geochemical, temperature, FMS, and VSP data in combination with calibrations obtained from laboratory measurements should bring more insight into the geological processes active in the inner forearc basin over the last 30 m.y.

REFERENCES

Akimoto, K., 1989. Recent foraminifera from Enshunada. *In* Takayanagi, Y., and Ishizaki, K. (Eds.), *Collected Papers on Foraminifera from the Japanese Islands:* Sendai (Toko Press), 93–104.

Arthur, M. A., Carson, B., and von Huene, R. 1980. Initial tectonic deformation of hemipelagic sediment at the leading edge of the Japan convergent margin. *In* Langseth, M., Okada, H., et al., *Init. Repts. DSDP,* 56, 57 (Pt. 1): Washington (U.S. Govt. Printing Office), 569–614.

Atlan, Y., Bardon, C., Minssieux, L., Quint, M., and Delvaux, P., 1968. Conductivite en milieu poreux argileux. Interpretation des diagraphies. Troisieme colloque de l'association de recherche sur les techniques de forage et de production. *Pau. Comm.,* No. 31.

Backman, J., Duncan, R. A., et al., 1988. *Proc. ODP, Init. Repts.,* 115: College Station, TX (Ocean Drilling Program).

Berggren, W. A., Kent, D. V., Flynn, J. J., and Van Couvering, J. A., 1985. Cenozoic geochronology. *Geol. Soc. Am. Bull.,* 96:1407–1418.

Bernhard, J. M., 1986. Characteristic assemblages and morphologies of benthic foraminifera from anoxic, organic-rich deposits: Jurassic through Holocene. *J. Foram. Res.,* 16:207–215.

Bielak, L. E., and Briskin, M., 1978. Pleistocene biostratigraphy, chronostratigraphy and paleocirculation of the southeast Pacific central water core RC 11-220. *Mar. Micropaleontol.,* 3:51–94.

Blow, W. H., 1969. Late middle Eocene to Recent planktonic foraminiferal biostratigraphy. *In* Renz, H. H., and Brönniman, P. (Eds.), *Proc. 1st Internat. Conf. Planktonic Microfossils,* 1:199–422.

Bolli, H. M., Saunders, J. B., and Perch-Nielsen, K. (Eds.), 1985. *Plankton Stratigraphy:* Cambridge (Cambridge Univ. Press).

Coombs, D. S., Ellis, A. J., Fyfe, W. S., and Taylor, A. M., 1959. The zeolite facies, with comments on the interpretation of hydrothermal syntheses. *Geochim. Cosmochim. Acta,* 17:53–107.

Davis, E. E., and Lister, C.R.B., 1977. Heat flow measured over the Juan de Fuca Ridge: evidence for widespread hydrothermal circulation in a highly heat transportive crust. *J. Geophys. Res.,* 82:4845–4860.

Foreman, H. P., 1981. Radiolaria. *In* Emiliani, C. (Ed.), *The Sea* (Vol. 7): New York (Wiley), 1121–1144.

Haq, B. U., Hardenbol, J., and Vail, P. R., 1987. Chronology of fluctuating sea levels since the Triassic. *Science,* 235:1156–1167.

Hussong, D. M., and Uyeda, S., 1981. Tectonic processes and the history of the Mariana arc: a synthesis of the results of Deep Sea Drilling Project Leg 60. *In* Hussong, D. M., Uyeda, S., et al., *Init. Repts. DSDP,* 60: Washington (U.S. Govt. Printing Office), 909–929.

Ingle, J. C., Jr., 1980. Cenozoic paleobathymetry and depositional history of selected sequences within the southern California continental borderland. *Spec. Publ. Cushman Found. Foraminiferal Res.,* 19: 163–195.

Kaiho, K., in press. Morphotype changes of deep-sea benthic foraminifera during the Cenozoic Era and their paleoenvironmental implications. *Kaseki* (Fossils).

Kaiho, K., and Hasegawa, S., 1986. Bathymetric distribution of benthic foraminifera in bottom sediments off Onahama, Fukushima Prefecture, northeast Japan. *In* Matoba, Y., and Kato, M. (Eds.), *Studies on Cenozoic Benthic Foraminifera in Japan:* Akita University, 43–52.

Klaus, A., and Taylor, B., in press. Submarine canyon development in the Izu-Bonin forearc: a SeaMARC II and seismic survey of Aoga Shima Canyon. *Mar. Geophys. Res.*

Lundberg, N., and Leggett, J. K., 1986. Structural features in cores from the slope landward of the Japan Trench, Deep Sea Drilling Project Leg 87B. *In* Kagami, H., Karig, D. E., Coulbourn, W. C., et al., *Init. Repts. DSDP*, 87: Washington (U.S. Govt. Printing Office), 809–826.

Mattey, D. P., Marsh, N. G., and Tarney, J., 1980. The geochemistry, mineralogy, and petrology of basalts from the West Philippine and Parece Vela basins and from the Palau-Kyushu and West Mariana ridges, Deep Sea Drilling Project Leg 59. *In* Kroenke, L., Scott, R., et al., *Init. Repts. DSDP*, 59: Washington (U.S. Govt. Printing Office), 753–796.

McDuff, R. E., 1981. Major cation gradients in DSDP interstitial waters: the role of diffusive exchange between seawater and the upper oceanic crust. *Geochim. Cosmochim. Acta*, 45:1705–1713.

Mitchell, J., 1976. *Fundamentals of Soil Behavior:* New York (Wiley).

Miyashiro, A., 1974. Volcanic rock series in island arcs and active continental margins. *Am. J. Sci.*, 274:321–355.

Nelson, C. H., and Maldonado, A., 1988. Factors controlling depositional patterns of Ebro turbidite systems, Mediterranean Sea. *AAPG Bull.*, 72:698–716.

Nigrini, C. A., 1985. Radiolarian biostratigraphy in the central equatorial Pacific, Deep Sea Drilling Project Leg 85. *In* Mayer, L., Theyer, F., et al., *Init. Repts. DSDP*, 85: Washington (U.S. Govt Printing Office), 511–551.

Nigrini, C., and Lombari, G., 1984. *A Guide to Miocene Radiolaria*. Spec. Publ. Cushman Found. Foraminiferal Res., No. 22.

Ogawa, Y., and Miyata, Y., 1985. Vein structure and its deformation history in the sedimentary rocks of the Middle America Trench slope off Guatemala, Deep Sea Drilling Project Leg 84. *In* von Huene, R., Aubouin, J., et al., *Init. Repts. DSDP*, 84: Washigton (U.S. Govt. Printing Office), 811–829.

Parsons, B., and Sclater, J. G., 1977. An analysis of the variation of oceanic bathymetry and heat flow with age. *J. Geophys. Res.*, 82: 803–827.

Pickering, K. T., 1982. The shape of deep-sea siliciclastic systems—a discussion. *Geo-Mar. Lett.*, 2:41–46.

Ricci Lucchi, F., and Valmori, E., 1980. Basin-wide turbidites in a Miocene, over-supplied deep-sea plain: a geometrical analysis. *Sedimentology*, 27:248–270.

Ringwood, A. E., 1974. The petrological evolution of island arc systems. *J. Geol. Soc. London*, 130:183–204.

Sanfilippo, A., Westberg-Smith, M. J., and Riedel, W. R., 1985. Cenozoic radiolarian. *In* Bolli, H. M., Saunders, J. B., and Perch-Nielson, K. (Eds.), *Plankton Stratigraphy:* Cambridge (Cambridge Univ. Press), 631–712.

Scott, R. B., 1980. Petrology and geochemistry of arc tholeiites on the Palau-Kyushu Ridge, Site 448, Deep Sea Drilling Project Leg 59. *In* Kroenke, L., Scott, R., et al., *Init. Repts. DSDP*, 59: Washington (U.S. Govt. Printing Office), 753–796.

Serra, O., 1984. *Fundamentals of Well Log Interpretation* (Vol. 1): *The Acquistion of Logging Data:* Amsterdam (Elsevier).

Shipboard Scientific Party, 1987. Site 645. *In* Srivastava, S. P., Arthur, M., et al., *Proc. ODP, Init. Repts.*, 105: College Station, TX (Ocean Drilling Program), 61–418.

Takayama, T., and Sato, T., 1987. Coccolith biostratigraphy of the North Atlantic Ocean, Deep Sea Drilling Project Leg 94. *In* Ruddiman, W. F., Kidd, R. B., Thomas, E., et al., *Init. Repts. DSDP*, 94 (Pt. 2): Washington (U.S. Govt. Printing Office), 651–702.

Van Morkhoven, F.P.C.M., Berggren, W. A., and Edwards, A. S., 1986. Cenozoic cosmopolitan deep-water benthic foraminifera. *Bull. Cent. Rech. Explor.-Prod. Elf-Aquitaine*, No. 11.

Walker, R. G., 1975. Upper Cretaceous resedimented conglomerates at Wheeler Gorge: description and field guide. *J. Sediment. Petrol.*, 45:105–112.

Woodruff, F., 1985. Changes in Miocene deep-sea benthic foraminiferal distribution in the Pacific Ocean: relationship to paleoceanography. *In* Kennett, J. P. (Ed.), *The Miocene Ocean: Paleoceanography and Biogeography:* Geol. Soc. Am. Mem., 163:131–175.

Yasuda, H., 1989. Benthic foraminifera and sedimentary facies of the lower slope basin off Shikoku, Japan. *In* Takayanagi, Y. and Ishizaki, K. (Eds.), *Collected Papers on Foraminifera from the Japanese Islands:* Sendai (Toko Press), 83–92.

Ms 126A-109

NOTE: All core description forms ("barrel sheets") and core photographs have been printed on coated paper and bound as Section 3, near the back of the book, beginning on page 421.
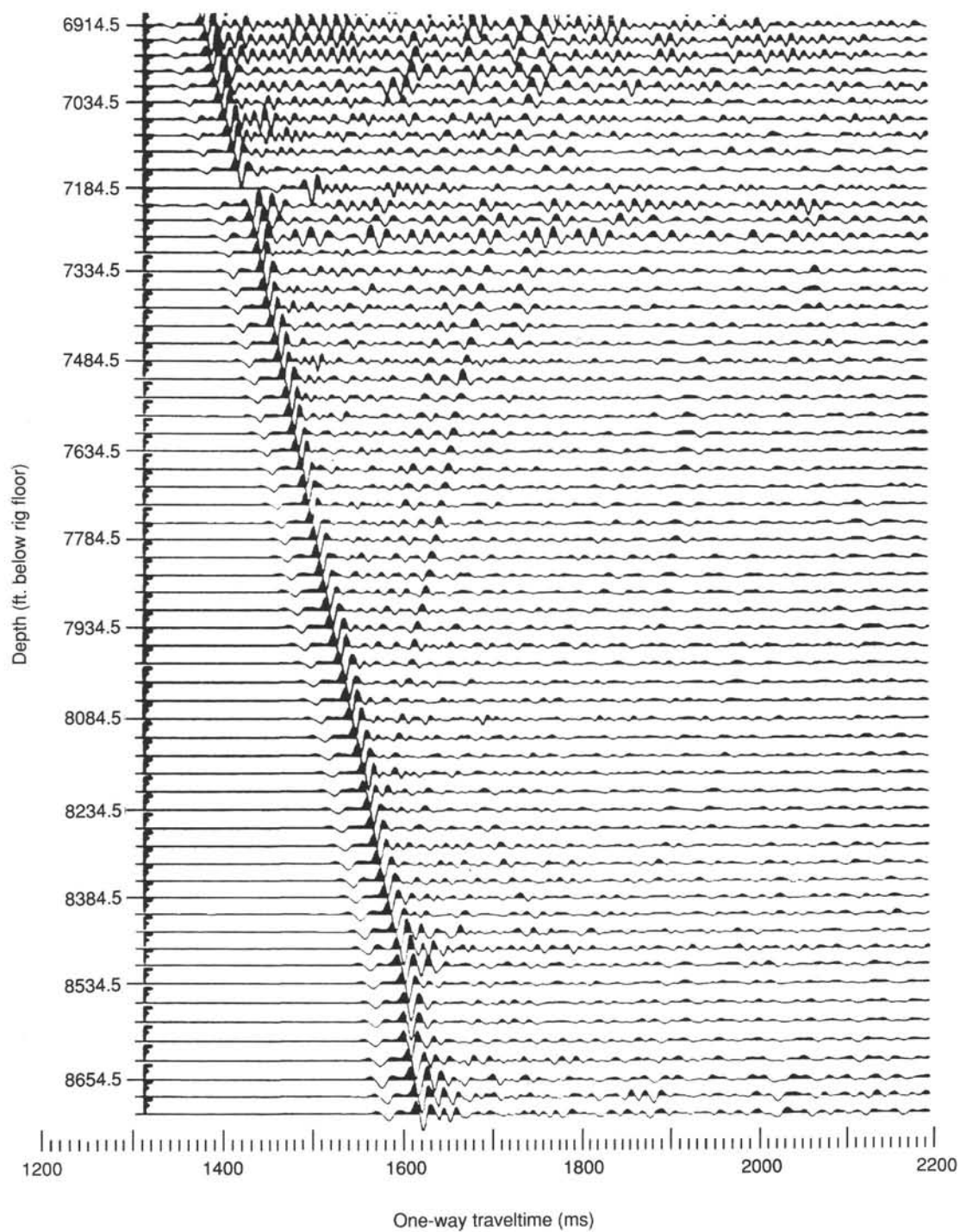
Figure 71. One-way traveltime plot of unprocessed, stacked traces, Hole 792E. Vertical scale is depth (in ft below rig floor) at which the stacked trace was obtained. The horizontal scale is one-way traveltime (in ms).

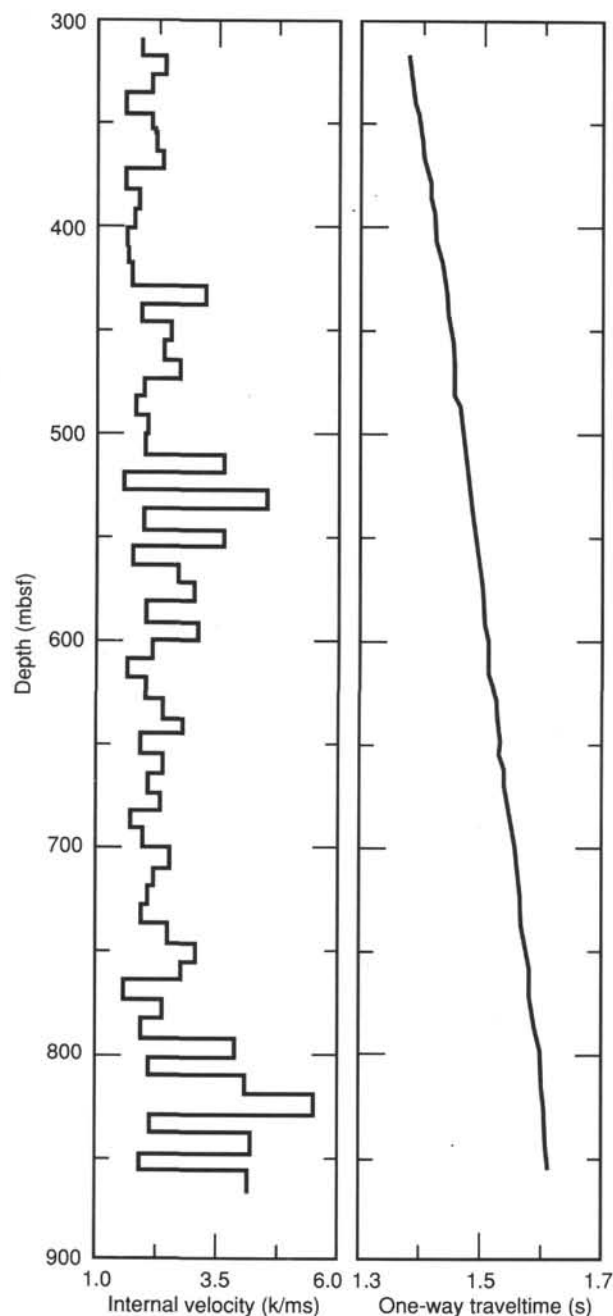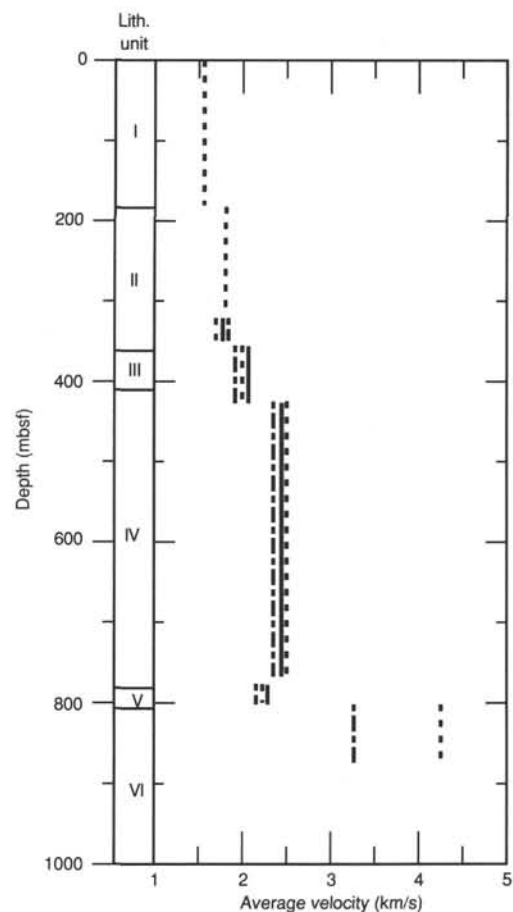Figure 72. Raw (unsmoothed) interval velocity and one-way traveltime vs. depth, Hole 792E.

Figure 73. Comparison of VSP (solid line), laboratory (dashed line), and *in-situ* (dot-and-dashed line) velocity measurements for Hole 792E. Lithologic units are shown for reference.

Table 19. Average resistivity, interval velocity, and bulk density computed for lithologic units, Site 792.

Unit/subunit	Depth (mbsf)	Resistivity[a] (Ω · m)	Interval velocity[b] (km/s)	Bulk density[c] (g/cm^3)
IIB	287.0–357.4	0.91	1.82	1.76
III	357.4–430.0	1.02	1.83	1.53
IV	430.0–783.4	2.40	2.39	1.88
V	783.4–804.0	1.21	2.21	1.79
VI (upper basement)	804.0–831.5	8.59	3.39	2.35
VI (lower basement)	831.5–878.0	3.38	2.54	2.15

Note: Values are reported from *in-situ* measurements.
[a] From deep-induction measurement (IDPH).
[b] Compressional velocity (V_p).
[c] LSRH.

Table 20. Average compressional velocity data, Site 792.

Unit/subunit	Depth (mbsf)	VSP velocity (km/s)	Laboratory velocity (km/s)	*In-situ* velocity (km/s)
I	000.0–183.7	—	1.59	—
IIA	183.7–317.0	—	1.85	—
IIB	317.0–357.4	1.80	1.76	1.82
III	357.4–430.0	2.00	1.89	1.83
IV	430.0–783.4	2.44	2.47	2.39
V	783.4–804.0	2.23	2.22	2.21
VI (upper basement)	804.0–886.0	—	4.26	3.39

Note: Data obtained from VSP transit times, laboratory measurements, and *in-situ* measurements.
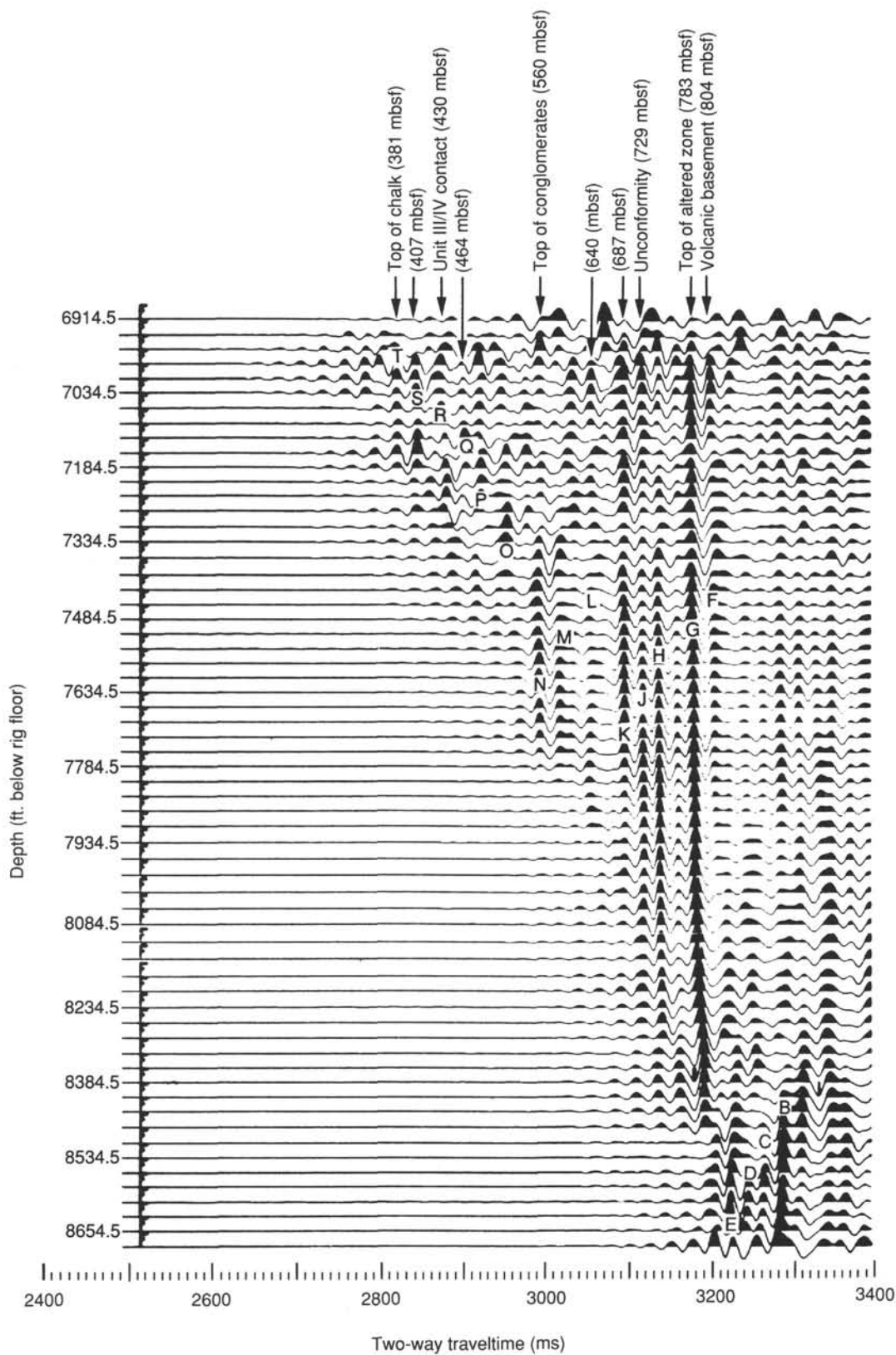
Figure 74. Two-way traveltime plot of deconvolved upgoing wavetrains, Hole 792E. The reflectors are identified by letter (for correlation with synthetic seismogram, Fig. 69, and MCS, Fig. 75) and by corresponding lithological unit (or depth) wherever possible.
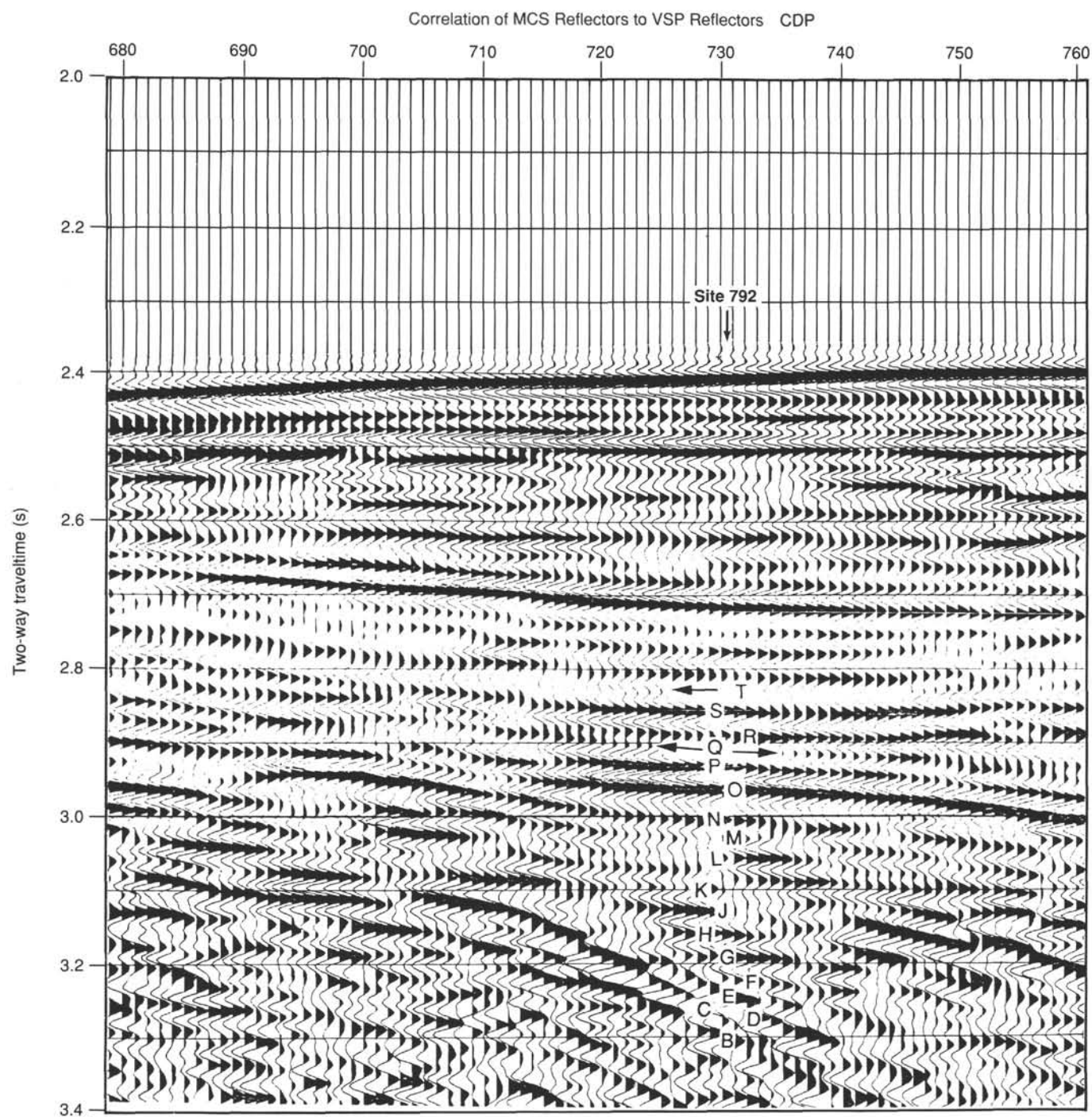
Correlation of MCS Reflectors to VSP Reflectors   CDP

Figure 75. Correlation of MCS and VSP reflectors, Site 792. See text for discussion.